

UNIVERSITY OF MODENA AND REGGIO EMILIA

Department of Physics, Informatics and Mathematics

PHD SCHOOL IN
PHYSICS AND NANO SCIENCES

XXXII Cycle

Numerical modeling of one- and two-carrier dynamics in Hall edge states and a proposal for flying-qubit quantum gates

Tutor:

Prof. Paolo BORDONE

Co-tutor:

Dr. Andrea BERTONI

Candidate:

Dr. Laura BELLENTANI

PhD Programme Coordinator:

Prof. Marco AFFRONTI

Academic Year 2018-2019

Contents

List of Publications and Contributions	II
Introduction	IV
I Numerical modeling of edge-state transport	1
1 Edge states: theoretical framework	3
1.1 The Integer Quantum Hall regime	3
1.1.1 The Symmetric gauge	4
1.1.2 The Landau gauge	5
1.2 Coherent states for electron transport	7
1.3 Chiral transport in edge channels	9
1.4 Solid-state interferometers in the IQH regime	12
2 Single-electron sources for Hall interferometers	17
2.1 Levitons	17
2.2 Mesoscopic capacitor	20
2.3 Quantum dot pumps	21
3 Numerical model for Gaussian wavepackets in 2D heterostructures	25
3.1 Gaussian wavepackets of edge states	26
3.1.1 Time-evolution of a Gaussian wavepacket	28
3.1.2 Gauge-dependent parameters and mass renormalization in the IQH regime	29
3.1.3 The wave-packet method for single and two-particle wavefunctions	29
3.2 The Split-Step Fourier method in 2D	31
3.2.1 The algorithm for 2D dynamics in IQH regime	32
3.2.2 Split-Step Fourier method for two particles in 2D	33
3.2.3 Initialization procedure for electron wavepackets	34
3.2.4 Imaginary potentials as absorbing leads	35
3.2.5 Discretization and boundary conditions	35
3.3 Parallel implementation and HPC-related performances of the Split-Step Fourier method	36
3.3.1 OpenMP parallelization of the single-particle version	37
3.3.2 MPI parallelization of the two-particle version	38
3.4 Kwant software for support calculations	41

II	Numerical simulations of Hall interferometers	43
4	A multichannel geometry for the Mach-Zehnder interferometer	45
4.1	The MZI in the IQH regime	47
4.1.1	The QPC at bulk FF 1	47
4.1.2	Phase Shifter at bulk FF 1	49
4.1.3	Visibility of the MZI at bulk FF 1	51
4.1.4	Towards a new design: multichannel geometry at bulk FF 2	53
4.2	Copropagating edge states for single-electron interferometry	54
4.2.1	A new shape for the beam splitter: the potential dip	54
4.2.2	The mesa structure for phase shifting	58
4.2.3	Electron self-interference in the multichannel MZI	59
5	Two-electron bunching in the HOM interferometer	67
5.1	State of the art	68
5.2	Effect of QPC scattering asymmetry	69
5.2.1	1D analytical model for electron bunching	70
5.2.2	2D numerical bunching probability	76
5.2.3	Two-electron detection driven by exchange	82
5.3	The role of Coulomb repulsion	84
5.3.1	Coulomb-driven antibunching	84
5.3.2	Interplay between Coulomb repulsion and exchange interaction	85
5.3.3	Effects of screening	86
5.4	Von Neumann entropy for the spatial entanglement	87
5.5	Bunching probability for alternative single-electron excitations	88
5.5.1	Lorentzian wavepackets in the energy domain	89
6	Conditional phase shifter for entanglement generation	93
6.1	A toy model with sharp barriers	95
6.1.1	Coulomb-driven scattering in the (00) configuration	96
6.1.2	Two-electron tunneling, bunching and entanglement in the (00) configuration	100
6.1.3	Screened Coulomb coupling in the (00) configuration	103
6.1.4	Coulomb-driven scattering in the (11) and (01) configurations	104
6.2	Towards a realistic conditional phase shifter	105
6.2.1	Self-electron interference for the phase factor	106
6.2.2	The γ factor in the full-scale device	107
III	Alternative frameworks for electron transport	109
7	On the incompatibility between Frensey's inflow boundary conditions and stationary Wigner distribution functions	111
7.1	Boundary conditions on a joint momentum-position space	112
7.1.1	Properties of the Wigner distribution function	112
7.1.2	Frensey's inflow boundary conditions	113
7.2	Inconsistencies for a stationary picture	114
7.2.1	Inconsistencies for a monoenergetic injection of plane waves	115
7.3	Charge localization in a time-dependent picture	118
7.4	Non-locality of the orthodox momentum	121

8. A Proposal for Evading the Measurement Uncertainty in Classical and Quantum Computing: Application to a Resonant Tunneling Diode and a Mach-Zehnder Interferometer	122
IV Conclusions	145
Conclusions	147
Acknowledgements	151
Bibliography	153

List of publications and contributions

The contents of this Thesis were partly published in the following publications:

- *Coulomb and exchange interaction effects on the exact two-electron dynamics in the Hong-Ou-Mandel interferometer based on Hall edge states*, L Bellentani, P Bordone, X Oriols, A Bertoni, Physical Review B **99**, 245415 (2019)
- *Dynamics and Hall-edge-state mixing of localized electrons in a two-channel Mach-Zehnder interferometer*, L Bellentani, A Beggi, P Bordone, and A Bertoni, Physical Review B **97**, 205419 (2018)
- *Dynamics of copropagating edge states in a multichannel Mach-Zehnder interferometer*, L Bellentani, A Beggi, P Bordone, and A Bertoni, Journal of Physics: Conference Series **906**, 012027 (2017)
- *Quantum computing with quantum-Hall edge state interferometry* P Bordone, L Bellentani and A Bertoni, Semiconductor Science and Technology **34**, 103001 (2019)

Other research activities performed during my PhD were published in the following paper:

- *A Proposal for Evading the Measurement Uncertainty in Classical and Quantum Computing: Application to a Resonant Tunneling Diode and a Mach-Zehnder Interferometer*, D Pandey, L Bellentani, M Villani, G Albareda, P Bordone, A Bertoni and X Oriols, Applied Sciences **9**, 2300 (2019)

During my PhD activity I was Co-tutor of 2 Bachelor thesis concerning the topics of my research:

- G. Forghieri, *Effetto della interazione Coulombiana sulla interferenza di pacchetti elettronici in nanodispositivi realizzati con Stati di Edge* (2019);
- C. Galeotti, *Dipendenza energetica dello scattering di quantum point contact per due particelle identiche* (2018).

I was project leader of 3 computational projects:

- **QUPIDO - HP10CPRABZ**: *Quantum Hall phase shifter In a dynamic framework*, ISCRA C project on Marconi A2 at CINECA;
- **DYNAMET - HP10C1MI91**: *Dynamics of antibunching in a two-particle interferometer in the integer quantum hall regime*, ISCRA C project on Marconi A2 at CINECA;
- **HPCEuropa3 - HPC17D8XLY**: *A parallel implementation of the Split-Step Fourier Method for the Hong-Ou-Mandel experiment with interacting electrons*, Transnational access program of HORIZON 2020 with visit (3 months) in collaboration with Barcelona Supercomputing Center;

and project collaborator of 2 computational projects:

- **CHINHEX - HP10CEMC7B**: *Coulomb-driven Hong-Ou-Mandel interferometer with single electron Hall excitations*, ISCRA C project on Marconi A2 at CINECA;
- **MINTERES - HP10CXDTX6**: *Multichannel interferometer based on copropagating edge states*, ISCRA C project on Marconi A1 at CINECA.

Introduction

In the last decade, the concrete implementation of quantum information devices is facing a notable development. Nowadays, the manipulation of the quantum bits provides a new paradigm for solving seemingly intractable problems. New applications are developed in the fields of quantum computing, quantum simulations, quantum sensing and quantum metrology. See, for example, the quantum computing facilities provided by IBM for the general audience [1].

The optimal physical implementation of the qubit is not yet well defined [2]. Although recent advancements based on superconducting and single-ion qubits showed the capability to process several qubits, alternative approaches are actively being proposed. Here, we focus on their realization in semiconductor nanodevices [3]. An electron in the Integer Quantum Hall (IQH) regime can be a very promising candidate for a qubit due to its long coherence time and its potential to be integrated into classical electron circuitry. In this regime, magnetically-driven edge states form conductive and chiral channels following the border of a confined two-dimensional electron gas (2DEG). Like classical skipping orbits, the path of an edge channel is not backscattered by an obstacle, rather it goes around the obstacle following its profile under certain conditions of smoothness and dimensionality [4].

Numerical and experimental studies [5, 6] measured the coherence length of edge channels, which is of the order of $10\ \mu m$, in absence of localized impurities, thus preventing the loss of coherence typically affecting electron states in semiconductor nanodevices. Additionally, the wide investigation of interedge scattering ensures nowadays a very high control on these devices, which has been proposed to implement logic gate operations on the qubit.

Over the years, single-qubit operations and two-electron interference have been realized in a large variety of devices, making them a possible candidate for electron quantum optics and flying qubit implementations of quantum computing architectures. One of the first interferometry devices is the electronic Mach-Zehnder interferometer (MZI), where only the first edge channel is energetically available (bulk filling factor one) [7, 8, 9]. Here, the incident beam impinges on a quantum point contact (QPC), acting as a beam splitter, and it is scattered into a superposition of the reflected and transmitted beams. The chirality of edge channels, together with a modulation of the potential landscape via top gates, leads the two beams to follow different tunable paths, where a phase difference is accumulated. Finally, the two beams are recollected on a second QPC, where they interfere. In this case, the electronic wavefunction faces a self-interference, with the phase difference being controlled by the magnetic field and by the variation of voltages applied to the top metallic gates. This device is usually exploited to observe Aharonov-Bohm oscillations in the transmission probability, which prove the coherent nature of electron transport in edge channels. This early geometry of a MZI is however affected by a fundamental topological limit that jeopardizes its viability as a quantum gate: at the second beam splitter, the reflected beam is backscattered into the area between the two channels, thus preventing concatenation in series of multiple devices and its integration into complex scalable architectures. This topological limit is the common denominator of first implementations of single-qubit interferometers.

In order to solve this issue, a new geometry has been recently proposed by Giovannetti et al. [10], where two copropagating edge channels are available (bulk filling factor two), and interchannel scattering is exploited to realize single-electron interference. Here, the beam splitter scatters the incoming electron into the first two copropagating edge channels, which are then separated by a top gate. In a first experimental implementation by Karmakar et al. [11], the electron is initialized in one of the first two spin-resolved edge channels and the beam splitter is realized with a large periodic array of magnetic nanofingers, which are rectangular top gates with a parallel sinusoidal magnetic field to rotate the spin. Ref. [12] shows Aharonov-Bohm oscillations driven by a variation of the magnetic field, whose low-visibility is caused by electron-electron interactions between the two channels, which induce charge fractionalization.

Differently from the experimental work of Karmakar et al., in our numerical simulation of self-interference we do not exploit the spin degree of freedom and consider interchannel scattering between the first two copropagating edge channels belonging to different Landau levels [13]. We design a realistic beam splitter, which is a small single potential dip, rather than an array of nanofingers, so that the length of copropagation of the two channels is reduced. The geometry of the beam splitter is tuned to produce a flat transmission probability of about 0.5 to increase the visibility of the full-scale MZI, while the smoothness of the phase shifter aims at reducing unwanted interchannel mixing.

A scalable geometry, as the one provided by the multichannel MZI, is mandatory to implement two-qubit logic gates. An example is the Hanbury-Brown-Twiss interferometer [14, 15]. At the heart of this device, which is essentially a beam splitter, exchange symmetry generates the Hong-Ou-Mandel (HOM) effect: according to their nature, two identical but counterpropagating particles impinging on a beam splitter leave the system on the opposite (antibunching) or same (bunching) outputs. The latter behavior is observed using photons [16], while the former is expected for electrons. This phenomenon is used to test the degree of indistinguishability of particles produced by different sources, which is a key requirement for the implementation of many quantum information protocols. However, despite Landauer-Büttiker formalism predicts a zero bunching probability for fermions, experiments show a nonideal behavior whose origin is still under debate [17, 18].

In particular, it is well known that energy selectivity of the beam splitter plays a crucial role in this phenomenon, together with the presence of electron-electron interactions. Regarding the first source of nonideality, the typical assumption of monoenergetic initial states in the scattering formalism is not adequate: the incident electron should be considered as a superposition of waves with a different momentum, each one scattered with a different amplitude by the central QPC, whose energy selectivity is not flat. The two outgoing states are not orthogonal and do not completely cancel each other [19, 20]. To access such phenomena, the inclusion of energy dependence of the impinging electron is a fundamental condition [21].

Two of the above MZIs [13] can be concatenated in parallel to generate a solid-state conditional phase shifter, which is a basic building block to produce entangled states for two-qubit logic gate operations [22]. This device contains four channels, two (ground and first excited) at each side of the 2DEG where the single-electron interferometers are hosted. Self-interference at each side is here affected by a selective Coulomb interaction, that couples those electron states traveling in the first excited channels only [23]. Here, indeed, the distance between the two electron paths is decreased so their mutual interaction is increased. According to its strength, Coulomb coupling affects the two-electron state at the output of the device, by selectively rotating only the component of the wavefunction with both electrons in the first excited states.

In the literature, the numerical simulation of interferometric devices in the IQH regime usually exploits the chirality of edge states to reproduce electron transport in effective 1D geometries [14, 24, 25, 26]. Moreover, as in the earliest experimental implementation of electron interferometers, the numerical modeling assumes the electrons to be injected in the edge channels as delocalized currents, so that the properties of the system, e.g. the electron bunching probability or the visibility of the self-interference pattern, are determined by ensemble measurements. With contrast to this approach, we adopt a time-dependent numerical modeling of single and two-electron transport in a Hall nanodevice by using the Split-Step Fourier method [27]. In this framework, electrons are described by localized wavepackets in the IQH regime [28, 29, 30, 31, 32] that propagate in a 2D simulation grid, where an external potential profile mimics the effect of metallic gates on top of a full-scale heterostructure. This method provides the time-dependent wavefunction for a single or two-particle system, so that we can access the dynamical properties of the system directly from the one- or two-electron state. The memory cost for its allocation in the latter case requires a parallel implementation of the algorithm in the MPI paradigm and the use of HPC resources, e.g. Marconi supercomputer at CINECA in Bologna [33] or Marenstrum Tier-0 system at BSC in

Barcelona [34].

To apply the Split-Step Fourier method, we compute the exact shape of the edge states in the heterostructure by means of **LAPACK** routines, so that the design-related performances of the device are estimated more accurately. Then, we model the localized wavefunction encoding the electron state as a Gaussian wavepacket of edge states, in order to mimic the injection of single-electron excitations in edge channels, as recently done in experimental implementations of Hall interferometers [35, 36, 17]. Despite single-electron detection is still not viable with the current nanotechnology, a large number of electron interferometers in the IQH regime have been integrated with single-electron sources (SEs) [37, 38, 39, 40], thus proving the viability of flying-qubit implementations for logic gates in the IQH regime.

Moreover, the use of a time-dependent approach to model electron transport does not require to speculate on the energy selectivity of the gates, which is exactly accounted for by the evolution of the wavefunction; additionally, the simulation of two-electron transport in a full-scale geometry allows us to include exactly electron-electron interaction and exchange correlation between the two charges, and to analyze their interplay with the realistic geometry of the device.

In this manuscript, we present in Chapter 1 the origin of edge states in the IQH regime and their theoretical description for confined 2D heterostructures. After reviewing the earliest interferometry experiments based on edge states, we describe in Chapter 2 the theoretical frameworks to simulate electron injection in the edge channels hosted by the 2DEG. Chapter 3 presents the Split-Step Fourier method that we implemented numerically to simulate single and two-electron transport in the IQH regime. The numerical modeling and performances of single and two-channel MZIs in the IQH regime are compared in Chapter 4. Chapter 5 describes two-electron bunching in an HOM interferometer and its numerical implementation in our time-dependent framework, while in Chapter 6 we simulate the selective Coulomb interaction in the active region of a conditional phase shifter, thus validating our scalable geometry of the multichannel MZI as a building block to realize two-qubit logic gates. Finally, we show in Chapter 7 how a time-dependent approach based on localized wavepackets can be adopted also in the Wigner formalism to model electron transport in nanodevices, and how it can solve the inconsistencies arising when applying the Frensky's inflow boundary condition to simulate electron injection from Ohmic contacts [41].

Part I

Numerical modeling of edge-state transport

Chapter 1

Edge states: theoretical framework

1.1 The Integer Quantum Hall regime

In the presence of a magnetic field \mathbf{B} , the linear momentum \mathbf{p} of noninteracting electrons with effective mass m^* and charge $-e$ is modified by an additional term:

$$\mathbf{p} \rightarrow \mathbf{p} + e\mathbf{A}, \quad (1.1)$$

where \mathbf{A} is called *magnetic vector potential*. The presence of an electric field further adds the *scalar potential* $-e\phi$ to the single-electron Hamiltonian, which generally reads:

$$\mathbf{H} = \frac{(\mathbf{p} + e\mathbf{A})^2}{2m^*} - e\phi, \quad (1.2)$$

where \mathbf{A} and ϕ are related to the electric and magnetic field by the following relations:

$$\mathbf{E} = -\nabla\phi - \frac{\partial\mathbf{A}}{\partial t}, \quad (1.3)$$

$$\mathbf{B} = \nabla \times \mathbf{A}. \quad (1.4)$$

The scalar and vector potential are not uniquely defined. Indeed, they can be fixed up to the gradient or time derivative of an arbitrary scalar function $\Lambda(\mathbf{r}, \mathbf{t})$:

$$\mathbf{A}' = \mathbf{A} + \nabla\Lambda \quad (1.5)$$

$$\phi' = \phi - \frac{\partial\Lambda}{\partial t}, \quad (1.6)$$

such that the new vector and scalar potential, \mathbf{A}' and ϕ' , generate the same magnetic and electric field induced by \mathbf{A} and ϕ through Eq.(1.3) and Eq.(1.4). A change of the factor $\Lambda(\mathbf{r}, t)$ in Eq.(1.5) or Eq.(1.6) is called *gauge transformation*.

By using the new potentials of Eqs.(1.5) and (1.6) in the Hamiltonian of Eq.(1.2), one proves that the eigenstate of \mathbf{H} , ψ , is modified by the application of a phase factor that leaves unchanged the physical description of the system:

$$\psi' = e^{-\frac{ie\Lambda}{\hbar}} \psi. \quad (1.7)$$

The vector and scalar potential can be represented by many different gauge choices, and gauge transformations always allow to switch from a gauge to another one. Here, we consider sub-cases of the *Coulomb gauge*, that contains all the potentials for which the following relation is true:

$$\nabla \cdot \mathbf{A} = 0. \quad (1.8)$$

In the present work, we are interested in the numerical simulation of electron transport in semiconductor heterostructures: the electrons are confined in a narrow semiconductor quantum well, that forms a 2DEG. In its perpendicular direction, the strong confinement determines a large energy level spacing, so that the electron dynamics is well approximated by a two-dimensional one in the xy -plane. Here, we consider a perpendicular magnetic field $\mathbf{B} = (0, 0, B)$ oriented along the \hat{z} -direction, and assume $\phi = 0$.

1.1.1 The Symmetric gauge

In the present framework, a possible choice is the Symmetric gauge, where the vector potential reads:

$$\mathbf{A}_S = \frac{B}{2} (-y, x, 0). \quad (1.9)$$

The Hamiltonian of the system is defined according to Eq.(1.2):

$$\hat{H}_S = \frac{1}{2m^*} (-i\hbar\nabla + e\mathbf{A}_S)^2 \quad (1.10)$$

$$= \frac{1}{2m^*} \left(\left(-\hbar^2 \frac{\partial^2}{\partial x^2} + i\hbar e B y \frac{\partial}{\partial x} \right) + \left(-\hbar^2 \frac{\partial^2}{\partial y^2} - i\hbar e B x \frac{\partial}{\partial y} \right) + \frac{e^2 B^2}{4} (x^2 + y^2) \right) \quad (1.11)$$

$$= \frac{1}{2m^*} \left((\hat{p}_x^2 - eB\hat{y}\hat{p}_x) + (\hat{p}_y^2 + eB\hat{x}\hat{p}_y) + \frac{e^2 B^2}{4} (\hat{x}^2 + \hat{y}^2) \right) \quad (1.12)$$

$$= \hat{T}_x(p_x, y) + \hat{T}_y(x, p_y) + \hat{V}_B(x, y) \quad (1.12)$$

which is diagonalized by the following 2D state:

$$\Psi(x, y) = f(x + iy) e^{-\frac{1}{4l_m^2}(x^2 + y^2)}, \quad (1.13)$$

where $f(x + iy)$ can be any analytical function (the ground state, and any other eigenstate, are therefore infinitely degenerate) and l_m is the so-called *magnetic length*. The eigenfunctions of \hat{H}_S are not factorizable, due to the symmetries in the x and y coordinates of the present Hamiltonian.

The magnetic length l_m defines the length scale on which the confining effects of the magnetic field on charged particles are relevant, according to the intensity of the magnetic field:

$$l_m^2 = \left| \frac{\hbar}{qB} \right|, \quad (1.14)$$

e.g. $l_m \simeq 11$ nm for $B = 5$ T. In the Symmetric gauge, l_m defines the standard deviation of the ground state, that is a Gaussian distribution in the \hat{x} - and \hat{y} -directions. The probability density of the excited states is instead described by a ring centered in the origin $(0, 0)$ with a quasi-Gaussian profile in the radial direction.

The center of the eigenstates can be translated from the origin to (x_G, y_G) , by applying a gauge transformation. Let us apply the vector $\mathbf{v} = (x_G, y_G)$ to the Hamiltonian of the system, \hat{H}_S . The translated Hamiltonian:

$$\hat{H}'_S = \hat{\mathcal{T}}(x_G, y_G) \hat{H}_S, \quad (1.15)$$

is diagonalized by the new eigenstates:

$$\bar{\Psi}'_n(x, y) = \hat{\mathcal{T}}(x_G, y_G) \Psi_n(x, y) = \Psi_n(x - x_G, y - y_G), \quad (1.16)$$

which must also be the eigenstates of the old Hamiltonian \hat{H}_S , for a translationally invariant system in the xy -domain, as in the case of a 2D infinite plane with a uniform magnetic field.

In the translated Hamiltonian, the new vector potential is:

$$\mathbf{A}_{S'} = \frac{B}{2} (-(y - y_G), (x - x_G), 0). \quad (1.17)$$

According to Eq.(1.5), a possible choice for Λ must therefore fulfill the condition:

$$\nabla \Lambda = \mathbf{A}_{S'} - \mathbf{A}_S = \frac{B}{2} (y_G, -x_G, 0), \quad (1.18)$$

as in the following case:

$$\Lambda(x, y) = \frac{B}{2} (y_G x - x_G y). \quad (1.19)$$

This gauge choice provides the eigenstate of \hat{H}_S centered on (x_G, y_G) :

$$\bar{\Psi}_n(x, y) = e^{-\frac{iq\Lambda}{\hbar}} \bar{\Psi}'_n(x, y) \quad (1.20)$$

1.1.2 The Landau gauge

In the Landau gauge [42], there are two possible definitions of the vector potential:

$$\mathbf{A}_L = B(0, x, 0), \quad (1.21)$$

$$\mathbf{A}_{L'} = B(-y, 0, 0). \quad (1.22)$$

The first one is typically used for free electrons in the \hat{y} -direction, while the second one is usually applied to electrons with a free motion along the \hat{x} -direction.

In the presence of a translationally invariant potential $V_{ext}(x)$ in the \hat{x} -direction, the Hamiltonian for the first gauge reads:

$$\hat{H}_L = \frac{1}{2m^*} (-i\hbar\nabla + e\mathbf{A}_L)^2 + V_{ext}(x) \quad (1.23)$$

$$\begin{aligned} &= \frac{1}{2m^*} \left(-\hbar^2 \frac{\partial^2}{\partial x^2} + \left(-\hbar^2 \frac{\partial^2}{\partial y^2} - 2i\hbar e B x \frac{\partial}{\partial y} \right) + e^2 B^2 (x^2) \right) + V_{ext}(x) \\ &= \frac{1}{2m^*} (\hat{p}_x^2 + (\hat{p}_y^2 + 2eB\hat{x}\hat{p}_y) + e^2 B^2 (\hat{x}^2)) + \hat{V}_{ext}(x) \\ &= \hat{T}_x(p_x) + \hat{T}_y(x, p_y) + \hat{V}_B(x) + \hat{V}_{ext}(x), \end{aligned} \quad (1.24)$$

whose eigenstates coincide, up to a local phase factor, with the eigenstates of the Symmetric gauge, Ψ_n , with the same energy¹, since a gauge transformation can not change the physics of the problem.

In order to switch from \mathbf{A}_S to \mathbf{A}_L , the Λ factor must fulfill the condition:

$$\nabla \Lambda = \mathbf{A}_L - \mathbf{A}_S = \frac{B}{2} (y, x, 0), \quad (1.25)$$

as, for instance,

$$\Lambda(x, y) = \frac{B}{2} xy, \quad (1.26)$$

that can be applied to Eq.(1.7) in order to compute the eigenstates of the Symmetric gauge in the Landau gauge.

¹In detail, they can be obtained as linear combinations of the “proper” eigenstates of the Landau gauge, due to the fact that they are highly degenerated.

By contrast to the Symmetric gauge, the Hamiltonian in the Landau gauge (see Eq.(1.23)) is diagonalized by eigenstates that can be factorized in the \hat{x} and \hat{y} -coordinates; an Ansatz of the associated Schrödinger equation is indeed

$$\Psi(x, y) = \chi(x)e^{iky}, \quad (1.27)$$

with a delocalized plane-wave term that describes a free motion along the \hat{y} -direction. $\chi(x)$ is instead a transverse eigenfunction, that diagonalizes the 1D effective Hamiltonian:

$$\hat{H}_L^{eff}(k) = \frac{1}{2m^*} \left(-\hbar^2 \frac{\partial^2}{\partial x^2} + 2\hbar e B x k + e^2 B^2 x^2 + \hbar^2 k^2 \right) + \hat{V}_{ext}(x) \quad (1.28)$$

$$\begin{aligned} &= -\frac{\hbar^2}{2m^*} \frac{\partial^2}{\partial x^2} + \frac{1}{2} m^* \omega_c^2 \left(x + \frac{\hbar}{eB} k \right)^2 + \hat{V}_{ext}(x) \\ &= \hat{T}(p_x) + \hat{V}_{eff}(x), \end{aligned} \quad (1.29)$$

By applying Eq.(1.27) to the Landau Hamiltonian in Eq.(1.23), one proves that

$$\hat{H}_L^{eff}(k) \chi(x) = E \chi(x). \quad (1.30)$$

\hat{H}_L^{eff} contains the kinetic energy of a free particle in the xy -domain, plus an effective potential $\hat{V}_{eff}(x)$, which is the sum of an external potential $\hat{V}_{ext}(x)$ and a parabolic magnetic confinement

$$\hat{V}_B(x, k) = \frac{1}{2} m^* \omega_c^2 (x - x_0)^2, \quad (1.31)$$

where

$$x_0(k) = -\frac{\hbar k}{eB} \quad (1.32)$$

is the center of the parable. Due to the shape of $V_{eff}(x, k)$, the eigenstates of the Landau Hamiltonian generally depend on the wavevector of the free motion, $k = k_y$, or, equivalently, on the center of the parabolic potential x_0 .

For a purely parabolic potential, i.e. when $V_{ext}(x) = 0$, the eigenenergies are identified by an additional discrete quantum number n :

$$E = E_n = \hbar |\omega_c| \left(n + \frac{1}{2} \right), \quad n \in N, \quad (1.33)$$

and are called *Landau levels*.

The transverse part of the eigenstates $\Psi_n(x, k) = \chi_n(x, k)e^{iky}$ are the ones of an harmonic oscillator,

$$\chi_n(x, k) = N_{n-1} \mathcal{A}_G \left(x - x_0, \frac{l_m^2}{2} \right) \mathcal{H}_{n-1} \left(\frac{x - x_0}{l_m} \right), \quad (1.34)$$

with \mathcal{H}_n corresponding to the Hermite polynomials [43]:

$$\begin{cases} \mathcal{H}_n(x) = (-1)^n e^{x^2} \frac{d^n}{dx^n} e^{-x^2} = 2x \mathcal{H}_{n-1}(x) - \mathcal{H}'_{n-1} \\ \mathcal{H}_0(x) = 1, \end{cases} \quad (1.35)$$

where $\mathcal{A}_G(x, \sigma)$ defines a *Gaussian probability amplitude* wavefunction:

$$\mathcal{A}_G(x, \sigma^2) = \frac{1}{\sqrt{2\pi\sigma^2}} e^{-\frac{x^2}{4\sigma^2}}, \quad (1.36)$$

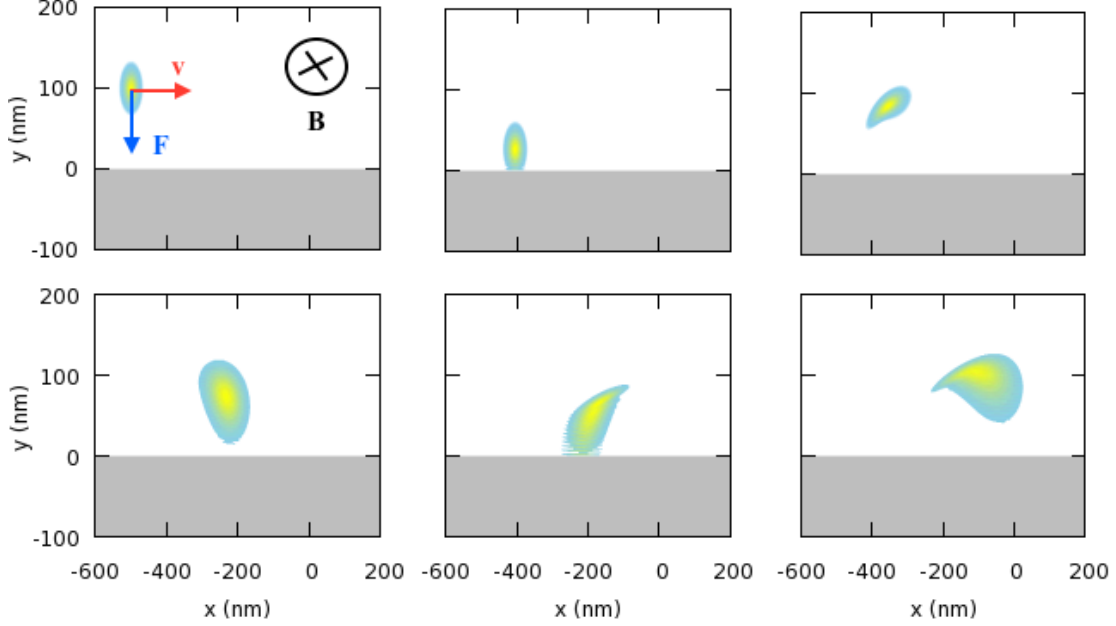


Figure 1.1: Time evolution of a coherent state with $\sigma_x = \sigma_y = l_m = 11$ nm, $x_0 = -500$ nm and $y_0 = 100$ nm in presence of translationally invariant sharp barrier at $y < 0$ nm. The wavepacket behaves as a skipping orbit. Note that the shape of the coherent state is modified due to the scattering at the barrier.

and the normalization factor N_n is given by:

$$N_n = \frac{1}{\sqrt{2^n n!}}. \quad (1.37)$$

The two directions \hat{x} and \hat{y} are still coupled by the magnetic field: the transverse part of the eigenfunction, $\chi(x, k)$, is centered along x_0 , while the wavevector k of the motion along \hat{y} is also related to the central position of the eigenfunction along the \hat{x} -direction, due to Eq.(1.32). The total energy E depends instead only on the quantum number n . The Landau levels are not dispersive in the wave-vector space k , thus determining a zero group velocity, and a zero net flow of charge in the direction given by k , thus not allowing for charge transport along the \hat{y} -direction.

Due to the presence of a plane-wave part along the \hat{y} -direction, the normalization of the eigenstates requires a spatial confinement along \hat{y} with periodic boundary conditions within L_y . The Landau state then reads:

$$\Psi_{n,k}(x, y) = \chi_n(x, k) \frac{e^{iky}}{\sqrt{L_y}}. \quad (1.38)$$

1.2 Coherent states for electron transport

For a charged particle in the symmetric gauge, the Hamiltonian in Eq.(1.11) is very similar to the one of an harmonic oscillator, except for the *mixed* term that contains the product of \mathbf{r} and \mathbf{k} parameters, thus making the Hamiltonian not factorizable.

As it happens for edge states and skipping orbits, the *coherent states* are the quantum analogue of the cyclotron orbits. Their expression is given in Ref. [44]:

$$\Psi_c(x, y) = N_0 e^{-\frac{1}{4l_m^2}((x-x_0)^2 + (y-y_0)^2 + 2\text{sgn}(B)(-ix_0y + iy_0x))}, \quad (1.39)$$

where x_0 and y_0 , the initial position of the coherent state, can be arbitrarily fixed. The expression for the state in Eq.(1.39) describes the initial position of the coherent state, which is a Gaussian wavepacket centered in (x_0, y_0) with standard deviations $\sigma_x = \sigma_y = l_m$.

Such states are characterized by the lowest possible uncertainty principle allowed by the Heisenberg's principle:

$$\langle \Delta x^2 \rangle \langle \Delta p_x^2 \rangle = \langle \Delta y^2 \rangle \langle \Delta p_y^2 \rangle = \frac{\hbar^2}{4}, \quad (1.40)$$

which confirms that this state is the maximally closed to a classical one.

The time-dependent Schrödinger Equation

$$i\hbar \frac{\partial}{\partial t} \Psi_c(x, y) = \hat{H}_S \Psi_c, \quad (1.41)$$

provides the evolved state [44]:

$$\Psi_c(x, y, t) = N_0 e^{-\frac{1}{4l_m^2}(x-x_c(t))^2 + ik_x(t)x - \frac{1}{4l_m^2}(y-y_c(t))^2 + ik_y(t)y}, \quad (1.42)$$

where

$$x_c(t) = x_0 \cos(\omega_c t) + y_0 \sin(\omega_c t) \quad (1.43)$$

$$y_c(t) = y_0 \cos(\omega_c t) - x_0 \sin(\omega_c t) \quad (1.44)$$

$$k_x(t) = -\frac{y_c(t)eB}{2\hbar} \quad (1.45)$$

$$k_y(t) = +\frac{x_c(t)eB}{2\hbar} \quad (1.46)$$

These equations describe a uniform circular motion around the origin $(0, 0)$ for the point with initial position (x_0, y_0) and velocity equal to $v = \frac{\hbar}{m^*} \sqrt{k_x^2 + k_y^2} = \frac{e|B|}{2m^*} \sqrt{x_0^2 + y_0^2}$, i.e. the center of the Gaussian wavepacket.

As visible from Eq.(1.42), in case the standard deviations are both equal to the magnetic length, the Gaussian wavepacket maintains its shape unchanged during the time evolution. An example is displayed in Fig. 1.1: here, for $\sigma_x > l_m$, the trajectory of the circular motion is the same as $\sigma_x = l_m$, but the shape of the wave-packet pulses along the \hat{x} -axis [44].

In classical physics we can choose any possible initial position and initial velocity for a particle traveling in a uniform magnetic field, while all coherent states have an orbit that is centered at the origin. To reproduce a cyclotron orbit, we therefore need to apply a gauge transform, that introduces a further degree of freedom to our system.

For a general initial position (x'_0, y'_0) , we need to translate x_0 into x'_0 and y_0 into y'_0 , that is:

$$\begin{cases} x' &= x + (x'_0 - x_0) = x + x_G \\ y' &= y + (y'_0 - y_0) = y + y_G. \end{cases} \quad (1.47)$$

The origin $(0, 0)$ is moved into (x_G, y_G) , and the translated coherent state reads:

$$\Psi'_c(x, y) = N_0 e^{-\frac{1}{4l_m^2}(x-x'_0)^2 + ik_{x0}(x-x_G) - \frac{1}{4l_m^2}(y-y'_0)^2 + ik_{y0}(y-y_G)}, \quad (1.48)$$

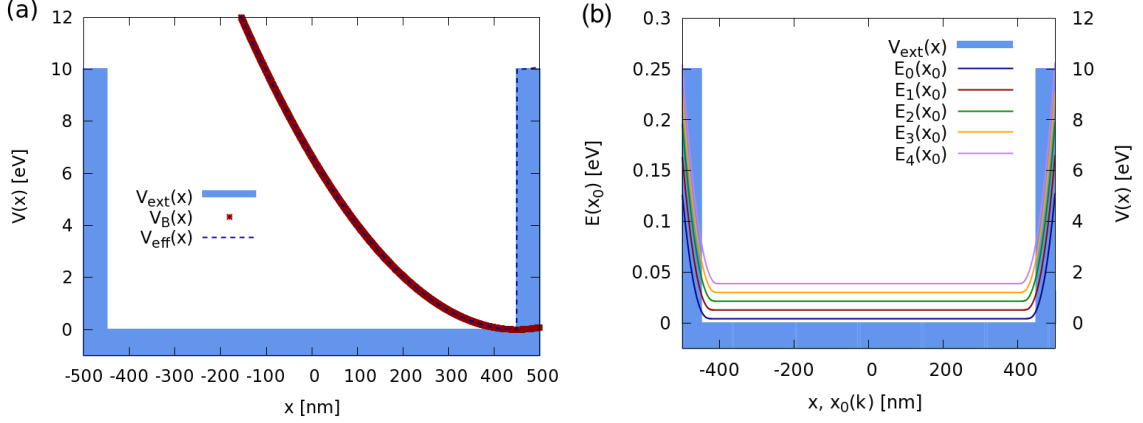


Figure 1.2: (a) Effective potential V_{eff} and its two components V_B and V_{ext} for an edge state with $x_0 = 450$ nm from Ref. [23]. V_{eff} coincides with the magnetic well term V_B in the regions far from the potential barriers, while near the barriers it changes abruptly due to the confining barrier V_{ext} . (b) Band structure $E_n(x_0(k))$ for the first five Landau Levels, computed numerically, in presence of the square external potential profile $V_{ext}(x)$ (light blue shaded area) at $B = 5$ T. Energies are displayed as a function of the parameter $x_0(k)$ by using Eq.(1.32).

which is a coherent state only for the new gauge, with:

$$\mathbf{A}_{S'} = \frac{B}{2} (-(y - y_G), (x - x_G), 0), \quad (1.49)$$

The gauge transformation is realized by a Λ that fulfills the condition $\nabla\Lambda = \mathbf{A}_S - \mathbf{A}_{S'}$. The eigenstates are then related by:

$$\Psi_c(x, y) = e^{-\frac{iq\Lambda}{\hbar}} \Psi'_c(x, y) = \quad (1.50)$$

$$= e^{i\frac{eB}{2\hbar}(y_G x - x_G y)} N_0 e^{-\frac{1}{4l_m^2}(x-x'_0)^2 + ik_{x0}x} e^{-\frac{1}{4l_m^2}(y-y'_0)^2 + ik_{y0}y} \quad (1.51)$$

$$\begin{cases} x_G = x'_0 - \frac{2\hbar}{eB} k_{y0} \\ y_G = y'_0 + \frac{2\hbar}{eB} k_{x0} \end{cases} \quad (1.52)$$

Similarly to the classical cyclotron orbit, this final state is characterized by an arbitrary couple of initial position (x'_0, y'_0) and initial wave-vector (k_{x0}, k_{y0}) , that can be chosen independently one from the other. When the coherent state is initialized near a potential barrier, a skipping orbit is reproduced only during the first bounces on the barrier: at each bounce the coherent state faces a higher deformation, and after few bounces, the original form and the coherence is completely lost.

1.3 Chiral transport in edge channels

In the presence of a confining potential $\hat{V}_{ext}(x)$ in the transverse direction, the eigenfunctions of the Landau Hamiltonian can still be factorized along the \hat{x} - and \hat{y} -directions:

$$\Psi_{n,k}(x, y) = \varphi_n(x, k) e^{iky}. \quad (1.53)$$

Here, the transverse functions $\varphi_n(x, k)$ depend on the quantum numbers n and k , but do not correspond anymore to the solutions of the harmonic oscillator. The Landau levels are so perturbed

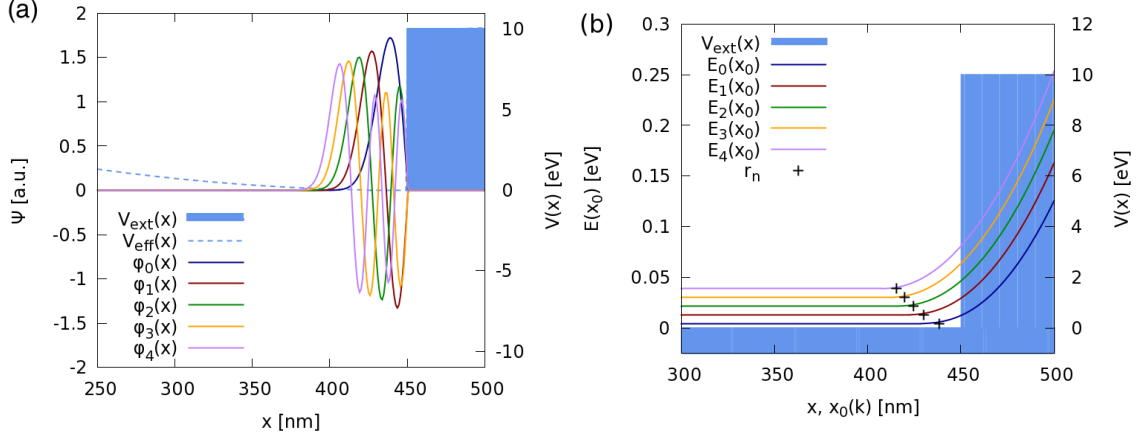


Figure 1.3: (a) Transverse component $\varphi_{n,k}(x)$ of the first two edge states ($n = 0,1$) for $x_0 = 450$ nm from Ref. [23] (b) Band structure of $E_n[x_0(k)]$ at the right border of the device.

by a positive correction $\epsilon_n(k)$, thus being now dispersive on the wavevector k :

$$E = E_{n,k} = \hbar |\omega_c| \left(n + \frac{1}{2} \right) + \epsilon_n(k). \quad (1.54)$$

The specific shape of $\epsilon_n(k)$, and therefore the dispersion relation of the energy bandstructure, depends then on the shape of the external potential $\hat{V}_{ext}(x)$.

For electrons of a 2DEG nanodevice, the external potential $V_{ext}(x)$ is typically flat in the central region, while it defines a barrier near the edges of the device itself. Far from the barrier, where $V_{ext}(x) \simeq 0$ the effect of the potential is negligible, and the solutions of the effective Schrödinger equation are the eigenstates $\chi_n(x)$ of the harmonic oscillator, and $\epsilon_n(k)$ is zero. The energy bandstructure is indeed generally flat in the center of the confined 2DEG. Near the edges, where $V_{ext}(x) \neq 0$, due to the relation between x_0 and k , the transverse confinement bends upwards the energy bandstructure and it induces a net group velocity for those states localized at the border of the device. These states are called *edge states*, and allow for coherent electronic transport in the direction given by k .

The most simple confining potential is the sharp barrier V_{ext} in Fig. 1.2(a), that is described by a sum of *Heaviside* functions

$$V_{ext}(x) = V_{max} [\Theta(-(x+L)) + \Theta(x-L)], \quad (1.55)$$

with a separation between the two edges $\Delta x = 2L$ and an height V_{max} . Here, $L = 450$ nm and $V_{max} = 10$ eV. V_{ext} adds to the parabolic confining potential V_B , which is induced by the perpendicular magnetic field in the Landau gauge.

Then, when the wavevector $k(x_0)$ approaches the barrier, $\epsilon_n(k)$ increases (see Fig. 1.2(b)), and the transverse component of the eigenstate $\varphi(x, k)$ ceases to be symmetric with respect to x_0 , as visible from Fig. 1.3(a). Note that, through the inverse of Eq.(1.32), we can express the bands $E_n(k)$ also in terms of x_0 .

The shape of $\varphi_n(x, k)$ may be then quite different from the corresponding harmonic oscillator eigenfunction $\chi_n(x, k)$. For these states, x_0 is no more the center of symmetry, but still a good quantum number. The corresponding wavevector $k(x_0)$ thus depends on the origin of the coordinate system: it is a gauge-dependent parameter. However, the difference between k and the true

wavevector of the electron is given only by a fixed constant, as we will later detail. The normalization procedure of the edge states is the same as the one for the Landau states in Eq.(1.38), and requires a spatial confinement along the \hat{y} -direction with PBC. The normalized eigenstate in 2D reads:

$$\Psi(x, y) = \frac{1}{\sqrt{L_y}} \varphi_n(x, k) e^{iky} \quad (1.56)$$

Orthogonality of Edge states In the Dirac notation, the eigenstate of the Landau Hamiltonian (Eq. (1.56)) is:

$$|\Psi_{n,k}\rangle = |k\rangle |\varphi_n(k)\rangle, \quad (1.57)$$

with $|k\rangle$ corresponding to the plane-wave contribution, such that $\langle y|k\rangle = \frac{1}{\sqrt{L_y}} e^{iky}$, and $|\varphi_n(k)\rangle$ a transverse part corresponding to the eigenfunction of the confined potential $V_{eff} = V_{ext} + V_B$, which is a parabolic well distorted by an external potential.

Landau and Edge states are characterized by the following orthogonality rules:

1. Two states $|\Psi_{n,k}\rangle$ and $|\Psi_{n',k'}\rangle$ with different values of the quantum numbers n or k are always orthogonal²

$$\langle \Psi_{n',k'} | \Psi_{n,k} \rangle = \delta_{n,n'} \delta(k - k'). \quad (1.58)$$

2. Two states with different quantum number \hat{k} but with equal quantum number \hat{n} are orthogonal in the plane wave part, while the transverse factors, $|\varphi_n(k)\rangle$ and $|\varphi_n(k')\rangle$, are in general not orthogonal.
3. Two states with the same wave-vector k but with different quantum number n are orthogonal due to the fact that the well eigenfunctions $|\varphi_n(k)\rangle$ and $|\varphi_{n'}(k)\rangle$ are orthogonal by definition.

Classical analogies and Chiral behaviour By comparing the quantum and classical expressions for energy,

$$\frac{1}{2}mv^2 = \frac{1}{2}m\omega_c^2 r^2 = \hbar |\omega_c| \left(n - \frac{1}{2} \right), \quad (1.59)$$

we can provide a relationship between the *radius* of the quantum and the classical orbit of the Landau states:

$$r_n = l_m \sqrt{2n - 1}, \quad n \in N. \quad (1.60)$$

Therefore, each eigenenergy E_n is characterized by a quantized *classical radius* of value r_n in the corresponding eigenvalue. r_n is discretized in multiples of the magnetic length, and it expresses the spatial extension of the eigenstate along the \hat{x} -direction, for a given n [42, 45].

Moreover, the classical radius can be interpreted as the effective space for the charge to behave as a free particle subject to a magnetic field only, i.e. it describes a circular orbit in the bulk, rather than contributing to a charge flux at the edge. This is clearly visible from Fig. Fig. 1.3(b): the n -th Landau level starts to bend when distance between the center of the state, x_0 , and the center of the barrier approaches r_n . The Landau state in the bulk of the confined 2DEG in the IQH regime, turns then into an edge state.

In the classical interpretation of the IQH regime, the Landau states with fixed n and x_0 correspond to linear combinations of classical cyclotron orbits with center (x_0, y) : these, indeed, have

²In the numerical simulations, for a device with finite size along \hat{y} , the Dirac delta in k of Eq.(1.58) becomes a Kronecker delta, due to the discretization of the k -space.

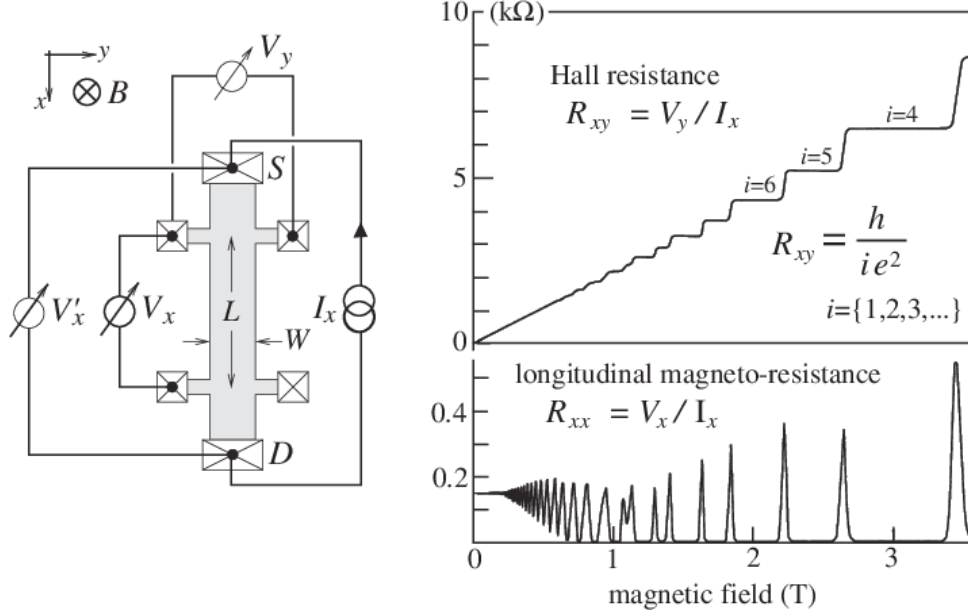


Figure 1.4: Hall resistance curve and longitudinal magneto-resistance curve measured on a two-dimensional electron system from Ref. [46]. The Hall bar geometry and the respective electrical set-up are shown on the left.

an associated zero probability current. Edge states with fixed n and x_0 are instead seen as convolutions of skipping orbits with center (x_0, y) . The latter are characterized by a non-zero probability flux and a coherent current propagation along the edge.

Charge transport in edge channels has therefore a *chiral* nature, with a direction that depends on the magnetic field: an electron initialized in an edge state contributes to charge transport only in a precise direction - which is reversed at the opposite edge of the device. Due to their immunity to backscattering, edge channels are ideal candidates for the coherent ballistic transport required in quantum computing devices [4]. Furthermore, thanks to their quasi-1D nature, the process of charge transport taking place inside them can be easily modeled by using the 1D scattering matrix formalism [42, 47].

1.4 Solid-state interferometers in the IQH regime

The first experimental observation of the IQH Effect dates back to 1980 [46]. In its experiment, Von Klitzing shows that the application of a magnetic field perpendicularly to electron current in a high-mobility 2D electron gas, e.g. the inversion layer of a MOSFET, creates a transverse potential difference in the device called *Hall potential* (see Fig. 1.4).

For any material containing a 2DEG, at low temperatures and strong magnetic fields the transverse potential is characterized by a constant resistance, which is universally quantized as follows:

$$R_H = \frac{h}{e^2 n}, \quad n \in N, \quad (1.61)$$

while the corresponding longitudinal potential and resistance go to zero. This phenomenon can be interpreted through the bending of the Landau levels, that in this condition governs ballistic transport. The finite dimensions of a real system, described as a confined 2DEG, entail indeed a

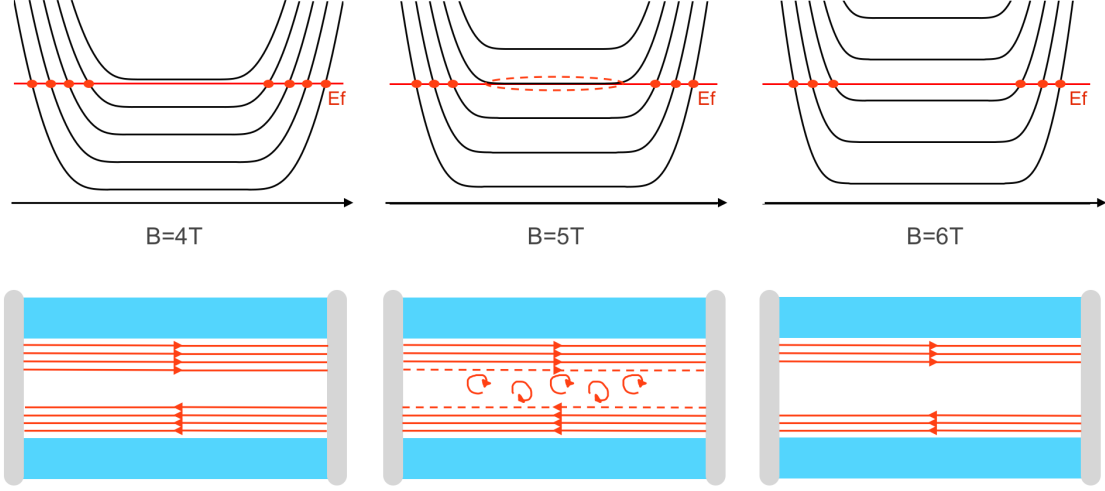


Figure 1.5: (Top) Band structure in real space of the device for the Landau levels at different values of B . (Bottom) Evolution of the edge channel paths with increasing magnetic field.

spatial confinement of the electronic wavefunction. Except for the possible presence of impurities or localized disorder producing trapped states, the unperturbed Landau levels are flat in the bulk, where there is no confinement. At the edges, instead, the Landau levels bend and intersect the Fermi level, thus becoming electron channels available for conduction.

These channels extend in the longitudinal direction of the device, following the confining edge and provide a conductive rail where electrons can propagate without being affected by backscattering, due to their chiral nature [48]. This can be interpreted semiclassically by considering the effect of the magnetic field on the charge motion: when an electron inverts its velocity due to backscattering, the Lorentz force pushes it again towards the border of the device, and the initial direction of the motion is restored. In the quantum perspective, the chirality of edge channels allow a constant electron flow only in a certain direction of the device: an eventual impurity on their path is then bypassed. This correspond to a zero longitudinal resistance and a fixed transverse resistance, that is inversely proportional to the number of edge channels that can participate in the transport.

Within this quantum picture, an increase of the magnetic field pushes the Landau levels towards higher energies, so that when one of them crosses the Fermi energy (see top panel of Fig. 1.5), the corresponding states moves towards the bulk of the device (bottom panel of Fig. 1.5). This correspond to an electron back-scattering from one edge to the opposite one, and then an increase in the longitudinal and transverse resistance. When the Landau level has totally overcome the Fermi energy, the corresponding edge channel is completely depopulated, and again electronic transport is completely characterized by a fixed number of channel without back scattering (zero longitudinal resistance and constant transverse resistance). This mechanism can be triggered by increasing or lowering the magnetic field, or by shifting directly the Fermi level, e.g. by changing the electronic density.

Electron devices operating in the IQH regime are usually fabricated in a high mobility 2DEG embedded in a semiconductor heterojunction (e.g. GaAs-AlGaAs), with Ohmic contacts connected to the edges of the structure as source/drain leads. Within this regime, a strong perpendicular magnetic field originates a new correlated state that behaves as an incompressible liquid with a

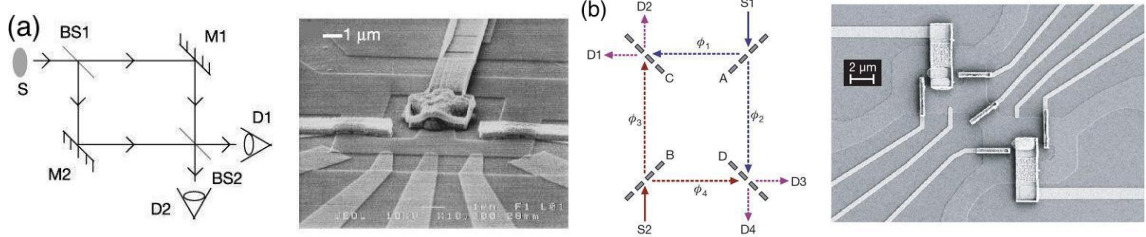


Figure 1.6: Examples of solid-state interferometers in the IQH regime. (a) Scheme of a MZI on the left and SEM picture of the device on the right from Ref. [15]. A centrally located small Ohmic contact, serving as D2, is connected to the outside circuit by a long metallic air-bridge. Two smaller metallic air-bridges bring the voltage to the inner gates of BS1 and BS2 - both serve as beam splitters for edge states. (b) Diagram of the Hanbury-Brown-Twiss interferometer of Ref. [15] on the left panel and scanning electron micrograph of the actual sample on the right. Sources S1 and S2 inject streams of particles, which are split by beam splitters A and B, later to recombine at beam splitters C and D. Each particle can arrive at any of four different drains, D1-D4.

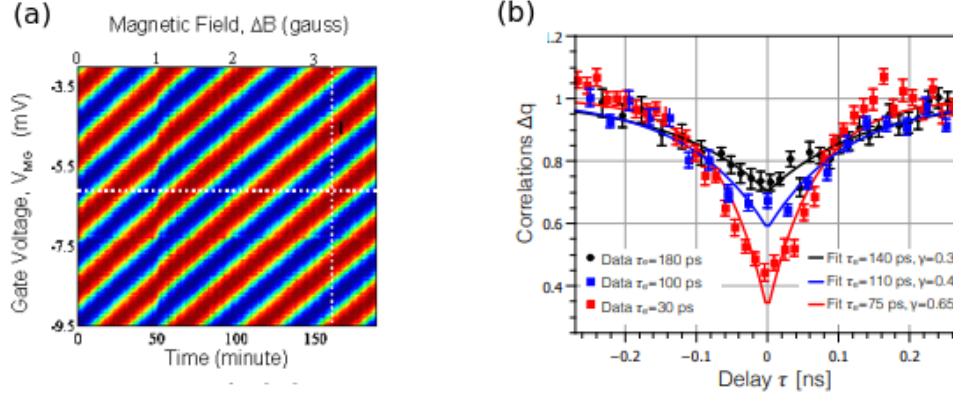


Figure 1.7: (a) Interference pattern in the Mach Zehnder interferometer of Fig. 1.6(a). The left panel displays the two dimensional color plot of the current collected by one detector as function of magnetic field and gate voltage at an electron temperature of ~ 20 mK. $B = 5.5$ T and the two QPCs were both set to transmission $T_1 = T_2 = 0.5$. Red (blue) stands for high (low) current. The visibility of the interference is 0.62. (b) HOM trace Δq from Ref. [17] as a function of the time delay between the sources τ for three values of the emission time $\tau_e = 30$ ps (red squares), $\tau_e = 100$ ps (blue squares) and $\tau_e = 180$ ps (black dots). The plain lines represent exponential fits, $\Delta q(\tau) = 1 - \gamma e^{-|\tau|/\tau_e}$.

fixed and well-defined density n [48]. Such parameter is related to the number of Landau Levels that are filled in the bulk of the confined 2DEG, which is called *bulk filling factor* (FF):

$$\nu = \frac{n\hbar c}{eB}. \quad (1.62)$$

Metallic gates on top/bottom of the heterostructure control the bulk FF by depleting the 2DEG, as in the heterostructures of Fig. 1.6. In order to control the path of the edge states in specific regions of the device, ν can also be locally varied by means of *modulation gates*, as in our multichannel implementation of the MZI presented in Chapter 4.

The long coherence length of edge states provide therefore the ideal framework to implement semiconductor logic gates for quantum computing architectures, where single-qubit transformations are realized through single-electron interferometry and qubits are coupled by Coulomb interaction. See Fig. 1.7 for an example of two of the most common interference pattern in Hall nanodevices: (a) Aharonov-Bohm oscillations in a MZI and (b) Pauli dip in the bunching probability of an HOM geometry.

Chapter 2

Single-electron sources for Hall interferometers

In the earliest experimental implementations of electron interferometry, particles are injected in the edge channels through Ohmic contacts [49, 50, 8, 15, 51, 12], and the electron wavefunction is localized only along the transverse direction of the device. Therefore, the interference is realized between currents of electrons and the quantum properties of the system are provided by ensemble measurements of noise or the detection of the transmitted current [49, 50], while its numerical modeling is based on the scattering-state formalism in a stationary framework and effective 1D geometries [14, 24, 25, 52].

In this picture, creation and annihilation operators applied to the ground state (a filled Fermi sea with negative energies) define the many-body electron state that represents the flow of electrons from the leads, while each component of the logic gate is described by a scattering matrix with properly defined reflection and transmission coefficients. Within this approach, the zero frequency cross correlation of the current fluctuations is related to the single-particle detection probability in an output or to the joint detection probability in two different outputs. This framework has been applied to study the entanglement generated by Coulomb interaction between an interferometer and a detector in Ref. [24], to predict the violation of Bell's inequality in the Hanbury-Brown-Twiss interferometer, as in Ref. [14] or to explain the unexpected increase of the visibility at large biases in multichannel implementations of the MZI in Ref. [25].

However, the current nanotechnology enables the injection of single localized carriers in the IQH regime [38, 53, 39, 36], with the qubit state encoded in the Landau index n or in the spatial localization of the edge channel. Thanks to the quasi-parabolic dispersion of the edge state, a localized wavepacket traveling in an edge channel is traditionally modeled in an effective 1D geometry as a wavepacket of plane waves [28, 37, 54, 19], while the use of a full 2D approach with time-dependent solvers is less common in literature [29, 20, 55, 13].

With contrast to the current availability of single-electron injection, the detection of a flying-qubit is still a challenging task due to the high velocity of the wavepacket with respect to the interaction time with the detector [56].

2.1 Levitons

Typically, for a system of fermions, the perturbation produced by an external voltage bias affects all states below the Fermi energy, and generates a complex superposition of particles and holes. In 1996, Levitov et al. suggested a protocol to inject single-electrons in edge channels

with a properly time-dependent perturbation $V(t)$ of Lorentzian shape [57, 58, 59]. This minimal excitation of the Fermi sea, called *leviton*, contains only one electron charge and no holes. Fig. 2.1 shows the probability density of a leviton in the real space, which is lorentzian, and in the energy domain. Only recently leviton-based SESs have been implemented experimentally and integrated into two-particle interferometers, as in Ref. [36, 60], where the electron HOM effect is demonstrated.

With contrast to alternative injection protocols, this quasi-particle is injected at the Fermi energy, and therefore it is less affected by energy relaxation processes [30]. Moreover, the generation of levitons require only the application of a properly designed voltage pulse on the source lead and no additional nanolithography of the sample. Theoretical and experimental works [36, 60] prove the generation of a minimal excitation containing a single electron charge in HOM and Hanbury-Brown-Twiss interferometers; here, a QPC partitions the leviton quasi-particle, and shot noise measurements provide the number of electron and holes in the beam. With contrast to alternative shapes of $V(t)$, this number is equal to a single electron charge for Lorentzian pulses, thus ensuring the absence of additional holes propagating in the device.

Numerical modeling in 1D

The time-dependent perturbation $V(t)$ to emit a single electron in the conduction band has a Lorentzian shape:

$$V(t) = -\frac{\hbar}{e} \frac{2\tau}{(t - t_0)^2 + \tau^2}, \quad (2.1)$$

where τ is the *emission time* and t_0 the instant of maximum voltage.

For simplicity, we initially discuss the shape of levitons in 1D, where edge states are replaced by plane waves. In the energy domain, the bias $V(t)$ produces a normalized electronic wavefunction given by [37]:

$$\Phi(E) = \sqrt{2\tau} e^{-(\tau - it_0)(E - E_F)} \Theta(E - E_F), \quad (2.2)$$

with E_F Fermi energy of the system. For a given energy dispersion $E = E(k)$, the wavefunction

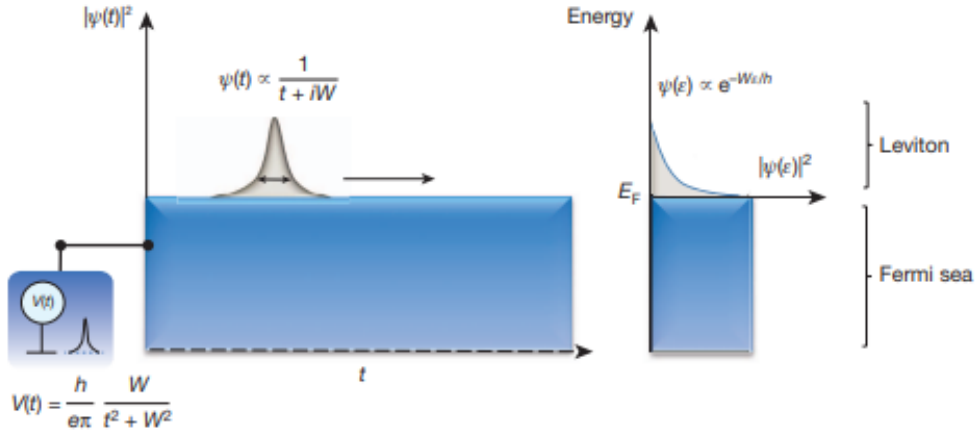


Figure 2.1: Schematic picture of a leviton in the (left) real space and in the (right) energy domain from Ref. [36]

in real space, called *Leviton*, is given by the Fourier transform of $\Phi(E)$, as follows:

$$\begin{aligned}\psi(x, t) &= \frac{1}{\sqrt{2\pi}} \int dk e^{ikx} \tilde{\psi}(k) e^{-\frac{i}{\hbar} E(k)(t-t_0)} \\ &= \frac{1}{\sqrt{2\pi}} \int dk e^{ikx} \left[\Phi(E(k)) \left| \frac{dE}{dk} \right| \right] e^{-\frac{i}{\hbar} E(k)(t-t_0)}.\end{aligned}\quad (2.3)$$

By assuming a generally parabolic dispersion $E(k) = \alpha(k - k_1)^2 + c$, with $\alpha = \hbar^2/(2m^*)$, the Leviton wavefunction in the k -space reads

$$\tilde{\psi}(k) = \sqrt{2\tau} e^{-\alpha(\tau - it_0)(k^2 - k_F^2 - 2k_1(k - k_F))} 2\alpha(k - k_1) \Theta[(k_F - k_1)(k - k_F)]. \quad (2.4)$$

Then, the real space profile in 1D is computed from the Fourier transform: $\psi(y) = \frac{1}{\sqrt{2\pi}} \int dk e^{iky} \tilde{\psi}(k)$. In the case of a linear dispersion in 1D, i.e. $E(k) = v \cdot k$, the Leviton wavefunction has a Lorentzian shape in real space [37]:

$$\psi(y, t) = \frac{1}{\sqrt{\pi}} \frac{\sqrt{\frac{\Gamma}{2}}}{(y - y_0) - v(t - t_0) + i\frac{\Gamma}{2}}, \quad (2.5)$$

where $\Gamma = 2v\tau$ is the full width at the middle height of the density probability $|\psi(y, t)|^2$.

For a small excitation in the energy space in a 2DEG, the plane waves are replaced with the edge states $\varphi(x, k) \approx \varphi(x, k_F)$, so that:

$$\psi(x, y) \approx \frac{1}{\sqrt{2\pi}} \varphi(x, k_F) \psi(y), \quad (2.6)$$

Moreover, to switch from a 1D representation to a 2DEG, we need to define the initial wavefunction ($t = t_0 = 0$) in the direction of propagation by adding the factor $\exp(ik_F y)$ (with $E(k_F) = E_F$) to give the desired group velocity to the wavepacket:

$$\psi_L(y) = \frac{1}{\sqrt{\pi}} \frac{\sqrt{\frac{\Gamma}{2}}}{(y - y_0) + i \cdot (k_F) \cdot \frac{\Gamma}{2}} e^{ik_F y}, \quad (2.7)$$

whose density profile is Lorentzian, as expected:

$$|\psi_L(y)|^2 = \frac{1}{\pi} \frac{\frac{\Gamma}{2}}{(y - y_0)^2 + \left(\frac{\Gamma}{2}\right)^2}. \quad (2.8)$$

Its Fourier transform

$$\tilde{\psi}_L(k) = \frac{1}{\sqrt{2\pi}} \int dk e^{-iky} \psi(y) = \quad (2.9)$$

$$= -ie^{-\frac{1}{2}(k - k_F)(2iy_0 + \Gamma \text{sgn}(k_F))} \sqrt{\Gamma} \Theta[(k - k_F) \text{sgn}(k_F)] \text{sgn}(k_F), \quad (2.10)$$

is exponential in the wavevector k and provides the group velocity:

$$\langle v_g \rangle = \hbar \langle k \rangle = k_F + (k_F) \frac{1}{\Gamma}. \quad (2.11)$$

Here, $\text{sgn}(k_F)$ selects the wavevectors k associated with an energy $E(k) > E_F$, as required by the Leviton energy dispersion. For parabolic bands, this corresponds to $k > k_F$ if $k_F > 0$, and $k < k_F$

if $k_F < 0$. By assuming $\varphi(x, k) \approx \varphi(x, k_F)$, the wavepacket reads:

$$\psi(x, y) = \frac{1}{\sqrt{2\pi}} \int dk \varphi(x, k) e^{iky} \tilde{\psi}(k) \quad (2.12)$$

$$\approx \varphi(x, k_F) \frac{e^{ik_F y}}{\sqrt{\pi}} \frac{\sqrt{\frac{\Gamma}{2}}}{(y - y_0) + i \cdot (k_F) \cdot \frac{\Gamma}{2}}. \quad (2.13)$$

Note that Eq.(2.13) is gauge invariant: it is indeed valid also for a limited region of wavevectors k belonging to a parabolic band ($E(k) = \alpha(k - k_1)^2 + c$), if (k_F) is replaced by $\text{sgn}(k_F - k_1)$.

2.2 Mesoscopic capacitor

The injection of localized wavepackets can also be realized by means of *mesoscopic capacitors*, i.e. dynamic quantum dots weakly connected to the lead where a single charge is injected or absorbed [61]. In 1993, Büttiker proposed their injection protocol in the IQH regime [62]. Their experimental implementation in a solid-state devices is based on a tunable QPC that controls the tunnel-coupling between the quantum dot and the 2DEG [38], as shown in Fig. 2.2. Here, due to the presence of the perpendicular magnetic field, edge states run along the boundary of the confined region and generate the discrete levels in the dot.

This source provides no DC current, but only AC current of alternated electrons and holes. The quantum dot is initially in a Coulomb blockade regime, with the same Fermi energy E_F inside and outside the source. A periodic voltage bias $V(t)$ shifts above the last occupied level E_F and a single-electron pulse, called *Landau quasi-particle*, is injected into the 2DEG. In the next semi-period, when the drive is zero, a hole is injected; indeed the depleted level drops below the Fermi energy and the quantum dot collects an electron from the 2DEG.

Ensemble measurement of the high-frequency current autocorrelation function are usually performed to estimate the quality of this SES. In particular, the experimental implementation of a mesoscopic capacitor in Ref. [63] shows the existence of a fundamental noise, called *quantum jitter*, which is entirely determined by the quantum uncertainty on the emission time of a single charge from the source.

Numerical simulations [30] prove that mesoscopic capacitors are less robust against interchannel and intra-channel interactions with respect to Lorentzian pulses in presence of a double FF. Levitons are indeed quasiclassical charge density waves that does not entangle with the environment, while the Landau quasi-particles are superpositions of such density waves, so that entanglement

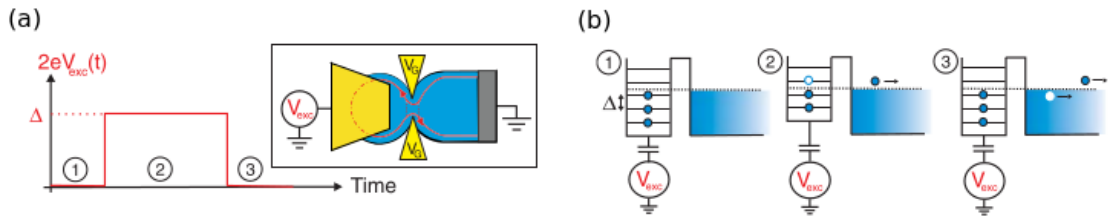


Figure 2.2: Injection protocol of a Landau quasi-particle by means of a mesoscopic capacitor from Ref. [40]. (a) Time-dependent potential applied to the quantum dot displayed in the right panel. (b) Scheme of single-electron injection and absorption for a mesoscopic capacitor connected to a 2DEG in the IQH.

with the second edge channel can destroy their coherence. These interchannel interactions at FF 2 manifest through charge fractionalization and a non-zero bunching probability in the electronic HOM interferometer [64, 65, 66, 67, 68, 69]. In detail, Ref. [17, 68] shows that, because of this source of decoherence, the minimum of the bunching probability (called Pauli dip) does not vanish for a fermionic two-particle system, but rather depends on the emission time of the Landau quasi-particle.

Numerical modeling in the energy domain

With regards to their numerical modeling, according to Ref. [70, 71], the electronic wavepacket for an initial time t_0 and position $x = x_0$ reads :

$$\psi(x) = \sqrt{\gamma} \Theta(x - x_0) e^{-ik_0(x-x_0)} e^{-\frac{\gamma}{2}(x-x_0)}, \quad (2.14)$$

and, by assuming a linear dispersion $E = \hbar v k$ with $x = vt$ [64]:

$$\psi(t) = \frac{\Theta(t - t_0)}{\sqrt{\tau_e}} e^{-i\epsilon_0(t-t_0)/\hbar} e^{-(t-t_0)/(2\tau_e)}. \quad (2.15)$$

Here, $\gamma = \frac{1}{v\tau_e}$, and τ_e is the emission time of the electron from the capacitor, while ϵ_0 is the electron energy. The wavefunction can be rewritten in the energy domain as a Lorentzian function:

$$\begin{aligned} \tilde{\psi}(\epsilon, t_0) &= N \int_{-\infty}^{+\infty} dt \Theta(t - t_0) e^{i(\epsilon - \epsilon_0)(t-t_0)/\hbar} e^{-(t-t_0)/(2\tau_e)} e^{+i\epsilon t_0/\hbar} \\ &= N e^{+i\epsilon t_0/\hbar} \int_{t_0}^{+\infty} dt e^{i(\epsilon - \epsilon_0)(t-t_0)/\hbar} e^{-(t-t_0)/(2\tau_e)} \\ &= N e^{+i\epsilon t_0/\hbar} \int_0^{+\infty} dt e^{i(\epsilon - \epsilon_0)t/\hbar} e^{-t/(2\tau_e)} \\ &= N e^{+i\epsilon t_0/\hbar} \int_0^{+\infty} dt e^{i(\epsilon - \epsilon_0 + i\frac{\Gamma}{2})t/\hbar} \\ &= \frac{N e^{+i\epsilon t_0/\hbar}}{\epsilon - \epsilon_0 + i\frac{\Gamma}{2}}, \end{aligned} \quad (2.16)$$

where $\Gamma = \frac{\hbar}{\tau_e}$ and N is the normalization factor. A typical value for the electron emission time is $\tau_e \simeq 62$ ps, and the energy ϵ_0 is of the order of half the quantum dot level spacing, $\Delta = 1.4$ K [64].

2.3 Quantum dot pumps

To avoid the decoherence effects induced by intra and interchannel interactions affecting Landau quasi-particles, the single electron should be injected at an energy much larger than the energy of the Fermi sea. In this case, single electrons are injected by quantum dot pumps, which are coupled to the source region and to the device by time-dependent confining potentials [73].

A scheme of this SES is presented in Fig. 2.3. The potential barrier connected to the electron reservoir is lowered below the Fermi sea and then it is progressively raised in order to trap one or a small number of electrons in the confined region. Then, the same potential barrier is further increased, to exceed the other confining barrier, and the trapped electrons are so injected in the 2DEG with an energy well above the Fermi energy of the 2DEG, usually 100 meV larger [74].

Ryu et al. proposed a theoretical protocol to generate and detect almost identical Gaussian wavepackets from non-identical quantum dot pumps [72]. In presence of strong magnetic fields,

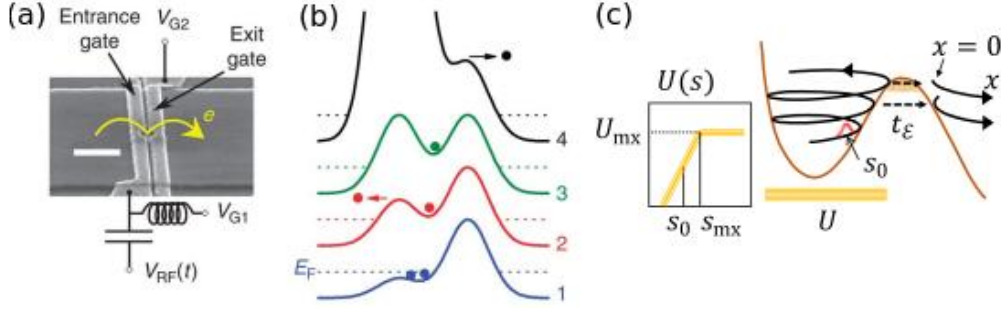


Figure 2.3: Injection protocol of a quantum dot pump proposed in Ref. [72]. (a) SEM picture of the double-well quantum dot with tunable barriers that selects and injects a single charge in the device. (b) Scheme of the injection process conveyed by the two tunable barriers. (c) Generation and injection of Gaussian wavepackets in edge channels.

the electron captured in the quantum dot evolves into a coherent state that is insensitive to details of the emission process; then, when it tunnels from the quantum dot to the 2DEG, for a small enough tunneling time, the electron state assumes the shape of a single Gaussian packet.

Due to the high energy of injection, such wavepackets are robust against inter and intrachannel interactions but will relax and loose energy, this leading to visibility loss. Regarding the relaxation processes induced by inelastic scattering with acoustic and optical phonons, recent theoretical studies [75] and experimental works [76, 77] address the specific energy distribution of the emitted carriers and analyze the magnetic and energetic regime to quench decoherence.

In the next chapter we describe our numerical modeling of localized charges in the IQH regime. In order to ensure an higher control of their dynamics, we mainly simulate wavepackets with a Gaussian shape in the real and wavevector space, as the excitations generated by quantum dot pumps. Indeed, numerical simulations of a wavepacket with a lorentzian distribution in the real space, as a Landau quasiparticle (Fig. 2.4), or an exponential distribution in energy, as a leviton (Fig. 2.5), prove that the shape of these excitations can not be easily preserved during their evolution.

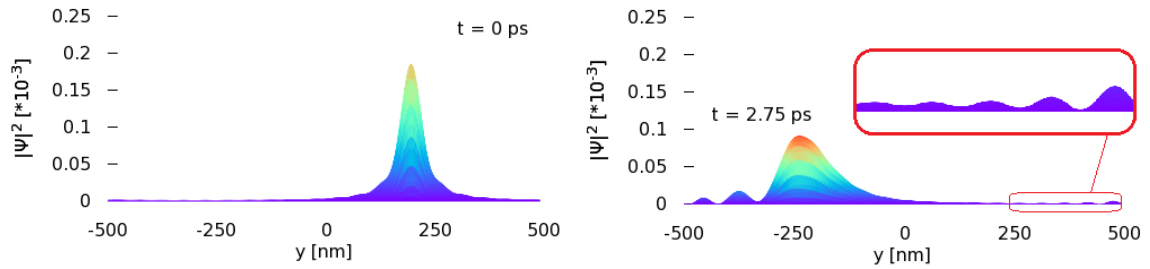


Figure 2.4: Time evolution of the density probability of leviton-like wavepacket in the longitudinal direction of a confined 2DEG. By applying our time-dependent solver for electron transport, we combine edge states at the border of the device with the weights in Eq.(2.10) and $\Gamma = 50$ nm, and evolve the localized charge with the Split-Step Fourier method. The right panel shows that, at the end of the propagation, the tails of the density probability in the real-space are strongly perturbed by the time evolution.

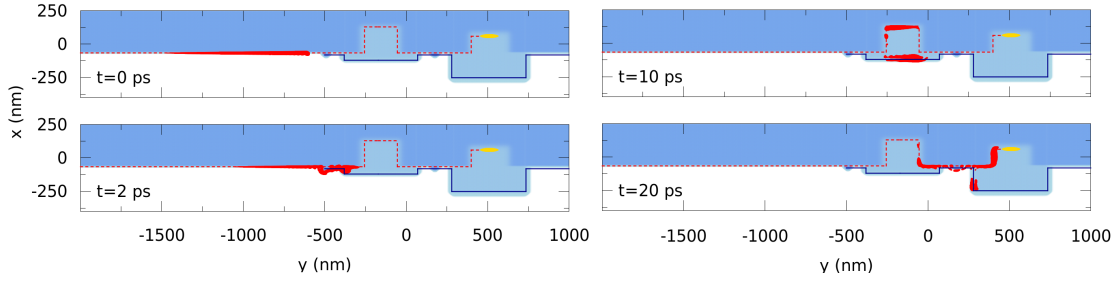


Figure 2.5: Dynamics of a single-charge wavepacket of edge states with a Lorentzian distribution in the energy domain (Eq.(2.16) with $\Gamma = 0.001$ eV) inside the multichannel geometry of the MZI [13]. The present energy distribution entails an exponential distribution in the \hat{y} direction of the 2D real-space, due to the quasi-linear bandstructure at the edge (see Sec. 4.2.3). The exponential shape of the excitation determines the presence of a large tail, also for relatively small energy broadenings, which can not be easily controlled during the time evolution.

Chapter 3

Numerical model for Gaussian wavepackets in 2D heterostructures

In the following chapters, the choice of the initial wavefunction of the propagating carrier is arbitrary. We mostly consider a minimum uncertainty wavepacket (i.e. with Gaussian shape) as the one that is generated by the protocol described in Ref. [72]; however, we also provide specific examples aimed at assessing the impact of the initial electron energy distribution on the transmission characteristics of the system.

Due to the analogy between a wavepacket of plane waves and a wavepacket of edge states, electron transport in the IQH regime is traditionally studied by means of 1D analytical models. As a reference, we adopt this scheme in our theoretical investigation of the multichannel MZI [13] and the two-particle HOM interferometer [21]. Within this simplified model, products of scattering matrices describe the effect of quantum logic gates on the system wavefunction, while the probability of detection or joint detection at the drains are obtained by integrating over the energy dispersion of the final wavepacket. However, in addition to require a number of approximations on the energy dependence of the transmission coefficient, such model does not reproduce exactly Coulomb repulsion for interacting particles. Indeed, electron-electron interactions in a 2D scenario generally differ from the 1D case [26], as proved by the computation of bunching probability of two strongly-interacting particles (see Sec. 5.3.2).

The exact simulation of single-particle or two-particle transport in wavepackets of edge states requires alternative approaches, able to describe exactly the potential background experienced by the carriers. To this aim, we implemented in-house a numerical solver of the time-dependent Schrödinger equation for a single-particle and a two-particle wavepacket in 2D, where the potential background $V_{ext}(x, y)$ affecting the traveling wavepacket mimics the effect of top gates in a realistic electron interferometer. The wavefunction is then evolved with the Split-Step Fourier Method, based on the iterative application of a properly defined evolution operator. In order to study two-particle correlations in Hall interferometers, we also developed a two-particle version of the simulator, which has been parallelized in the MPI paradigm to overcome memory occupation problems. Together with an exact simulation of electron-electron interactions in 2D, this time-dependent model provides the dynamic properties of the system from the propagating wavepacket, which is computed in real space at each iteration step and in a full-scale 2D geometry.

After presenting in Sec. 3.1 the numerical modeling of single-charge excitation in our software, we provide a detailed description of the algorithm adopted for the time evolution in Sec. 3.2.

The computational issues and numerical performances for the application of the Split-Step Fourier method in 2D are finally presented in Sec. 3.3.

3.1 Gaussian wavepackets of edge states

The numerical modeling of the single-electron excitations generated by SES (see Chapter. 2) in our time-dependent framework requires, as initial wavefunction, a localized electron state $\psi(x, y; 0)$ to evolve with the Split-Step Fourier method. Despite edge states are delocalized along the direction of propagation, \hat{y} in the present case, the bandstructure near the edge is dispersive; edge states are characterized by a non zero group velocity, that implies a net probability current propagating along the edge of the device.

Similarly to a wavepacket of plane waves in a 1D geometry, to represent a localized particle in the IQH regime we linearly combine the edge states $\varphi_{n,k}(x)e^{iky}$ on the wavevector space:

$$\Psi(x, y) = \frac{1}{\sqrt{2\pi}} \sum_n \int dk F_n(k) e^{iky} \varphi_n(x, k), \quad (3.1)$$

where $F_n(k)$ is the weight function that depends on the wavevector k and on the quantum number n . Despite we usually assume that the electron is injected selectively in one channel n and no superposition between different Landau Levels is initially present, we can in principle combine also cyclotron-resolved edge states, i.e. with different Landau index. This initialization procedure not only provides a localized wavepacket, but also a wavefunction which is normalizable to unity, so that its squared modulus can be interpreted directly as a probability.

In the previous chapter, we described three different models to reproduce the single-electron excitations generated by SES. These differ in the shape of the weight function, in the real or reciprocal space. We summarized above the numerical modeling of Landau quasi-particles and Levitons, which are characterized by a lorentzian and exponential distribution in energy, respectively. In the following, we describe our numerical modeling of Gaussian wavepackets of edge states to mimic the injection of a single-electron excitation from a quantum dot pump [72]. By selecting states from the same Landau level, the ground one in detail, the weight function reads

$$F_n(k) = \delta_{n,1} \frac{1}{\sqrt{2\pi}} \int dy e^{-iky} \psi(y) = \sqrt{\frac{2\sigma^2}{\pi}} e^{-\sigma^2(k-k_0)^2} e^{-iky_0} = F(k). \quad (3.2)$$

Here, y_0 is the initial position of the wavepacket in the direction of propagation, σ the standard deviation in the real space and $\sigma_k = 1/\sqrt{2}\sigma$ the wavepacket broadening in reciprocal space. The value of k_0 , which is the central wavevector of the Gaussian wavepacket, is computed from Eq.(1.32) by means of the transverse initial position x_0 .

Note that, as the band dispersion $E_n[k(x_0)]$, $F_n(k)$ shows also a dependence on x_0 due to the relation $k = k(x_0)$. This is equivalent to combine those states that are centered in $x_0(k)$ and near to the one centered around $x_0(k_0)$. Then, for a Gaussian distribution $F(k)$ - which is significantly different from zero only in the range $k_0 \pm 3\sigma_k$ - the states that mainly contribute to the wavepacket dynamics are contained in the range:

$$\Delta x_0 = |x_0(k_0 + 3\sigma_k) - x_0(k_0 - 3\sigma_k)| = \frac{6\sigma_k \hbar}{|eB|} = 3 \frac{l_m^2}{\sigma}. \quad (3.3)$$

As an example, we report in Fig. 3.1(a) the bandstructure of the first two Landau levels, together with the weight function $F(k)$ to combine the edge states. The parabolic bending at the

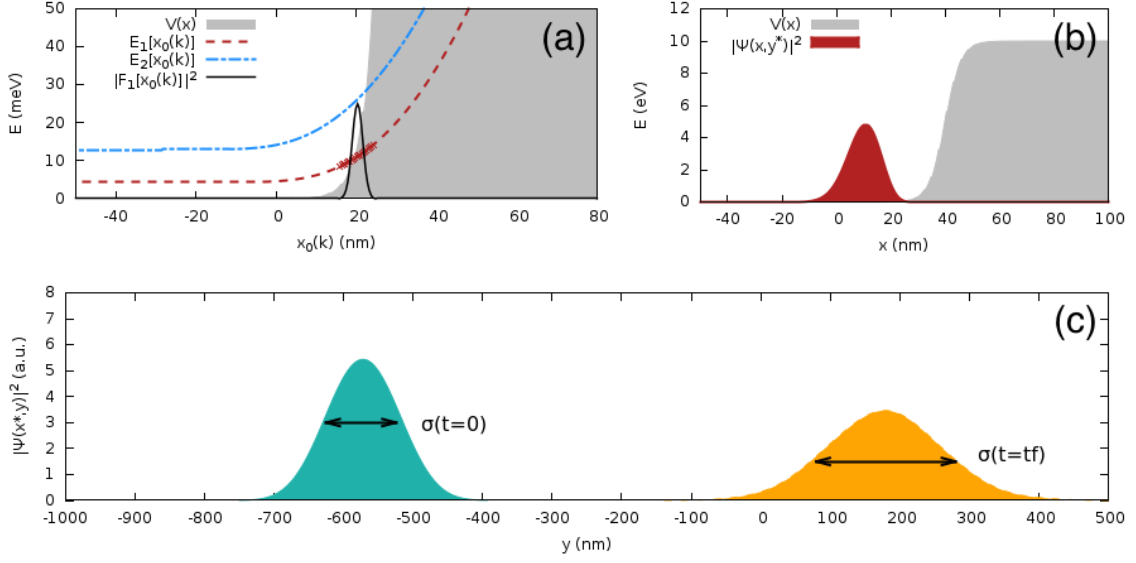


Figure 3.1: Numerical simulation of a Gaussian wavepacket of edge states at initial time $t = 0$ in presence of a translationally invariant potential as in Eq.(3.4) with $V_0 = 10$ eV, $\lambda = 3$ nm and $x_b = 0$ nm. (a) Bandstructure of the first two Landau levels at $y_0 = 350$ nm and weight function $F_n(k)$ in Eq.(3.2) with $n = 0$, $x_0 = 20$ nm. (b) Transverse profile of the single-electron wavepacket generated from the linear combination presented in panel (a). (c) Longitudinal profile of the probability density for the Gaussian wavepacket in panel (a) at initial time $t = 0$ and final time $t = t_F$. Note that the this probability is still Gaussian at the end of the dynamics and that the σ is increased due to the time evolution according to Eq.(3.11)

border of the wavevector/center space $k = k(x_0)$ is generated by the confining potential barrier $V_{ext}(x)$ modeled as follows:

$$V(x) = \frac{V_0}{1 + \exp\left(\frac{x - x_b}{\lambda}\right)}, \quad (3.4)$$

where $V_0 = 10$ eV and $\lambda = 3$ nm. The Gaussian wavepacket is initialized at a distance $x_0(k_0)$ of 20 nm from the turning point x_b of the barrier. The related profile in the transverse direction is reported in Fig. 3.1(b). The \hat{z} -direction refers to the probability distribution of the wavepacket. While, along the \hat{y} -direction, the shape is clearly Gaussian, on the \hat{x} -direction it depends on the specific profile of the edge states - and therefore, on the smoothness of the barrier.

We stress that in the IQH regime we can choose a proper space interval Δx_0 for the state to combine, so that the bandstructure of $E_0[x_0(k)]$ is almost linear. The k components have then a similar group velocity, and the edge-state packet does not spread while traveling. This differs from a Gaussian wavepacket propagating in free space, whose bending is always parabolic, so that the spreading of the distribution probability can not be avoided. Moreover, our numerical simulation of full-scale electron interferometers (see Chapter 4 for a MZI, Chapter 5 for the HOM interferometer and Chapter 6 for a Conditional Phase Shifter) prove that this wavepackets maintain all the properties of edge states, as the chirality and the long coherence length.

3.1.1 Time-evolution of a Gaussian wavepacket

To calculate analytically the time evolution of the wavepacket in Eq.(3.1), we consider a Gaussian wavepacket with a sufficiently large standard deviation σ , so that the region of states $|k\rangle$ that we are combining is very limited in the reciprocal space. As a consequence, by fixing $n = 0$:

- (1) the energy bandstructure can be locally approximated by a parable,

$$E_{0,k} = E_0(k) \simeq ak^2 + bk + c = a(k - k_1)^2 + c', \quad (3.5)$$

with $b = -2ak_1$ and $c = ak_1^2 + c'$, and a small enough due to the quasi-linearity of the band for higher energies.

- (2) the *well eigenfunctions* $\varphi_1(x, k)$ that we are combining have approximately all the same shape and the same center $x_0(k_0)$:

$$\varphi_1(x, k) \simeq \varphi_1(x, k_0) \quad \forall k. \quad (3.6)$$

Under these condition, the state described by Eq.(3.1) becomes [78]:

$$\Psi(x, y) \simeq \frac{1}{\sqrt{2\pi}} \int dk \sqrt{\frac{2\sigma^2}{\pi}} e^{-\sigma^2(k-k_0)^2} e^{-iky_0} e^{iky} \varphi_1(x, k_0) = \frac{e^{-\frac{(y-y_0)^2}{4\sigma^2}} e^{+ik_0 y}}{\sqrt[4]{2\pi\sigma^2}} \varphi_1(x, k_0). \quad (3.7)$$

This form of the wavepacket is consistent with the chiral behaviour of edge states, that act as 1D conductive channels for the device. Indeed, Eq.(3.7) can be factored along the two axes, as well as the time-evolved wavefunction. The shape of the wavepacket along \hat{x} does not change, due to the fact that the $\varphi_1(x, k)$ are the eigenstates of the effective 1D Hamiltonian. Along the \hat{y} -direction, instead, the particle travels as a free Gaussian which is governed by the parabolic band of Eq.(3.5). The time evolution of $\Psi(x, y)$ with respect to the Landau Hamiltonian \hat{H}_L is then given by:

$$\Psi(x, y; t) = e^{-\frac{i}{\hbar} t \hat{H}_L} \Psi(x, y) = \frac{1}{\sqrt{2\pi}} \int dk \sqrt{\frac{2\sigma^2}{\pi}} e^{-\sigma^2(k-k_0)^2} e^{ik(y-y_0)} \varphi_1(x, k_0) e^{-\frac{i}{\hbar} E_0(k)t}. \quad (3.8)$$

By factoring out the \hat{x} -part of the wavefunction from the integral we get the time-evolved state:

$$\Psi(x, y; t) = \varphi_1(x, k_0) \frac{e^{-\frac{ict}{\hbar}} e^{-\frac{(y-y_0+2ik_0\sigma^2+\frac{\hbar t}{\hbar})^2}{4(i\frac{\hbar}{\hbar}t+\sigma^2)}} e^{-k_0^2\sigma^2}}{\sqrt[4]{\frac{2\pi}{\sigma^2}} \sqrt{\sigma^2 + \frac{ait}{\hbar}}}, \quad (3.9)$$

with a probability density given by:

$$|\Psi(x, y; t)|^2 = \frac{1}{\sqrt{2\pi}(\sigma^2 + \frac{a^2 t^2}{\sigma^2 \hbar^2})} e^{-\frac{(y-y_0+\frac{2a(k_0-k_1)}{\hbar}t)^2}{2(\sigma^2 + \frac{a^2 t^2}{\sigma^2 \hbar^2})}} |\varphi_1(x, k_0)|^2. \quad (3.10)$$

$|\Psi(x, y; t)|^2$ describes a traveling Gaussian along the \hat{y} -axis, with a real-space spreading that is governed by the smoothness a . From $|\Psi(x, y; t)|^2$, we can further estimate the time evolution of the standard deviation, which is given by:

$$\sigma^2(t) = \left(\sigma^2 + \frac{a^2 t^2}{\sigma^2 \hbar^2} \right). \quad (3.11)$$

3.1.2 Gauge-dependent parameters and mass renormalization in the IQH regime

With contrast to a Gaussian wavefunction propagating in free space, our wavepacket of edge states is characterized by a wavevector k_0 which is a gauge-dependent parameter, and therefore can not describe a physical quantity. Note, indeed, that a rigid translation of the origin of the system along the \hat{x} -axis cannot change the physics of the problem, but it modifies the center of the well eigenfunctions x_0 , and therefore also the center of the wavepacket $k_0(x_0)$. Moreover, Eq.(3.10) contains an additional gauge-dependent parameter, k_1 , which is computed by fitting the bandstructure. $\Delta k = k_0 - k_1$ is instead a gauge-independent quantity. Therefore, it properly describes the effective wavevector for the time-evolved squared modulus of $\Psi(x, y; t)$, which is also proved to behave like the probability distribution of a Gaussian wavefunction in free-space [79, 80, 81]. Then, by computing the group velocity from the quasi-parabolic bandstructure,

$$v_g = \frac{2a(k_0 - k_1)}{\hbar}, \quad (3.12)$$

we can define an effective magnetic mass m_B^* with respect to the smoothness of the energy bandstructure (a) :

$$m_B^* = \frac{\hbar^2}{2a}, \quad (3.13)$$

so that the group velocity reads

$$v_g = \frac{\hbar(k_0 - k_1)}{m_B^*}. \quad (3.14)$$

The last equation shows that the potential barrier and the magnetic field induce a renormalization of the electron mass, which affects the group velocity of the edge state wavepacket with respect to the one of a free particle of effective mass m^* in Gallium Arsenide.

3.1.3 The wave-packet method for single and two-particle wavefunctions

According to Eq.(3.1), a generic electron wavepacket $\Psi(x, y)$ can be represented as a linear combination of edge states weighted by $F_n(k)$, generally depending on the cyclotron index n and the wavevector k . A scattering process modifies the weight function $F_n(k)$ to a new one, $F'_n(k)$, so that the scattered wavepacket reads:

$$\Psi'(x, y) = \frac{1}{\sqrt{2\pi}} \sum_n \int dk F'_n(k) e^{iky} \varphi_n(x, k), \quad (3.15)$$

In case of an *elastic scattering processes*, i.e. triggered by energy-conserving interactions, the composition of the wavefunction in terms of the wavevectors $F_n(k)$ can change, but the energy composition $F(E) = \sum_{n,k} F_n(k(E))$ of the final state $\Psi'(x, y)$ is the same as in the initial one, $\Psi(x, y)$: $F(E) = F'(E) \quad \forall E$. However, in case $\Psi'(x, y)$ is only a portion of the final state, e.g. the *reflected* or the *transmitted* part of the wavefunction coming out from the device, this does not apply. The present case requires the energy weights $F(E)$ to determine the reflection and transmission probabilities of the device for any energy component E .

In order to extract the values of $F'_n(k)$ from Eq.(3.15), we compute the Fourier Transform of $\Psi'(x, y)$ only along the \hat{y} -direction; this is equivalent to project $\Psi'(x, y)$ over the set of the plane

waves $\langle y|k \rangle = e^{iky}$ with momentum k along y :

$$\begin{aligned}
 \tilde{\Psi}'(x, k') &= \frac{1}{\sqrt{2\pi}} \sum_n \int dy e^{-ik'y} \Psi'(x, y) = \sum_n \int dk F'_n(k) \varphi_n(x, k) \frac{1}{2\pi} \int dy e^{i(k-k')y} \\
 &= \sum_n \int dk F'_n(k) \varphi_n(x, k) \delta(k - k') \\
 &= \sum_n F'_n(k') \varphi_n(x, k').
 \end{aligned} \tag{3.16}$$

By resorting to the orthogonality of the well eigenfunctions for a fixed wavevector k , we compute $F'_n(k)$ by projecting $\tilde{\Psi}'(x, k')$ over the corresponding well eigenfunction $\varphi_n(x, k)$, that is:

$$\begin{aligned}
 \int dx \varphi_m^*(x, k') \tilde{\Psi}'(x, k') &= \sum_n F'_n(k') \int dx \varphi_m^*(x, k') \varphi_n(x, k') \\
 &= \sum_n F'_n(k') \delta_{m,n} \\
 &= F'_m(k').
 \end{aligned} \tag{3.17}$$

The link between the energy E and the wavevector k is given by the bandstructure. In detail, if we call $\Psi'(x, y)$ the *transmitted state*, the *transmission probability* for the energy E between the initial, n , and the final Landau level, m , is given by:

$$T(E) = \frac{|F'_m(k')|^2}{|F'_n(k)|^2}, \tag{3.18}$$

where k and k' are, respectively, the wavevector in the input and output region of the device, which are associated with the energy E . If the confining potential has the same profile in both regions, we have $k = k'$, otherwise we have to resort to the bandstructure to find the appropriate values of the wavevectors in Eq.(3.18).

Since the wavepacket contains many components with different energy E , a single run of a simulation, followed by a Fourier analysis of the final state, provides the scattering probabilities over a broad range of energies. To this aim, we usually apply the wave packet method to characterize the scattering properties of our nanometric devices [27].

This projection can be generalized for a two-particle wavefunction in 2D as follows. The two-particle state is written as a linear combination of the eigenstates:

$$\Psi(x_1, y_1, x_2, y_2) = \frac{1}{2\pi} \sum_{n,m} \int dk_\alpha dk_\beta F'_{nm}(k_\alpha, k_\beta) \varphi_n(x_1, k_\alpha) \varphi_m(x_2, k_\beta) e^{ik_\alpha y_1} e^{ik_\beta y_2} \tag{3.19}$$

by means of a 4D weight function $F'_{nm}(k_\alpha, k_\beta)$, where n and m refers to the cyclotron index of particle 1 and particle 2 respectively, while k_α and k_β to the corresponding wavevectors.

Similarly to the single-particle case, the weight functions $F'_{nm}(k_\alpha, k_\beta)$ are computed by Fourier transform the 4D scattered wavefunction Ψ' on the $y_1 y_2$ -domain, where the edge state is a product of plane waves: $\langle y_1 y_2 | k_\alpha k_\beta \rangle = e^{ik_\alpha y_1} e^{ik_\beta y_2}$. Indeed:

$$\tilde{\Psi}'(x_1, k'_\alpha, x_2, k'_\beta) = \frac{1}{2\pi} \sum_{n,m} \int dy_1 dy_2 e^{-ik'_\alpha y_1} e^{-ik'_\beta y_2} \Psi'(x_1, y_1, x_2, y_2) \tag{3.20}$$

$$= \sum_{n,m} F'_{nm}(k'_\alpha, k'_\beta) \varphi_n(x_1, k'_\alpha) \varphi_m(x_2, k'_\beta). \tag{3.21}$$

The squared modulus of the two-particle weight function, $|F_{nm}(k'_\alpha, k'_\beta)|^2$, is therefore the probability that particle 1 is in the state with Landau index n and wavevector k'_α , and particle 2 in the state with Landau index m and wavevector k'_β . This probability is provided by projecting $\tilde{\Psi}'(x_1, k'_\alpha, x_2, k'_\beta)$ over the product of the well eigenfunctions $\varphi_i(x_1, k_\alpha)\varphi_j(x_2, k_\beta)$. Indeed:

$$\begin{aligned}
 & \int dx_1 dx_2 \varphi_i^*(x_1, k'_\alpha) \varphi_j^*(x_2, k'_\beta) \tilde{\Psi}'(x_1, k'_\alpha, x_2, k'_\beta) \\
 &= \sum_{n,m} F'_{n,m}(k'_\alpha, k'_\beta) \int dx_1 dx_2 \varphi_i^*(x_1, k'_\alpha) \varphi_j^*(x_2, k'_\beta) \varphi_n(x_1, k'_\alpha) \varphi_m(x_2, k'_\beta) \\
 &= \sum_{n,m} F'_{n,m}(k'_\alpha, k'_\beta) \delta_{i,n} \delta_{j,m} \\
 &= F'_{nm}(k'_\alpha, k'_\beta).
 \end{aligned} \tag{3.22}$$

3.2 The Split-Step Fourier method in 2D

To numerically simulate the electron dynamics in a confined heterostructure, we need to solve the time-dependent Schrödinger Equation:

$$i\hbar \frac{\partial \Psi(x, y; t)}{\partial t} = \hat{H} \Psi(x, y; t), \tag{3.24}$$

where \hat{H} is generally the Hamiltonian of our system, given by the sum of a kinetic operator and a potential one $\hat{H} = \hat{T} + \hat{V}$. For a time-independent Hamiltonian \hat{H} in a 2D real-space domain at time t , we solve Eq.(3.24) by applying the *evolution operator*

$$\hat{U}(t) = e^{-\frac{i}{\hbar} t \hat{H}}, \tag{3.25}$$

to the initial state of the system $\Psi(x, y; 0)$:

$$\Psi(x, y; t) = \hat{U}(t) \Psi(x, y; 0). \tag{3.26}$$

The evolution operator in the form of Eq.(3.25) can be applied also in case of a time-dependent Hamiltonian, provided that the time interval for the evolution, δt , is small enough with respect to all the characteristic times encoded in $\hat{H}(t)$:

$$\hat{U}(\delta t) \underset{\delta t \rightarrow 0}{\approx} e^{-\frac{i}{\hbar} \delta t \cdot \hat{H}(t)}. \tag{3.27}$$

Therefore, the evolution of $\Psi(x, y; t)$ over a time interval $t = N \delta t$ under the effect of any Hamiltonian $\hat{H}(t)$ can be obtained by N successive applications of the operator in Eq.(3.27). The Split-Step Fourier method can, in principle, be implemented numerically very easily with an iterative procedure. The difficulty lies in the representation of the evolution operator: the kinetic \hat{T} and the potential \hat{V} operators do not commute and \hat{T} contains the second derivative of the wavefunction with respect to the position, whose exponential is very difficult to calculate. As we will see in the next section, this will be solved by introducing Fourier transform in the definition of the evolution operator.

3.2.1 The algorithm for 2D dynamics in IQH regime

According to the *Trotter-Suzuki factorization* [82], the evolution operator for a short time interval δt can be written as the product of two or three exponential functions,

$$\hat{U}(t) = e^{-\frac{i}{\hbar}\delta t \cdot (\hat{T} + \hat{V})} \quad (3.28)$$

$$\simeq e^{-\frac{i}{\hbar}\delta t \cdot \hat{T}} e^{-\frac{i}{\hbar}\delta t \cdot \hat{V}} e^{o(\delta t^2)} \quad (3.29)$$

$$\simeq e^{-\frac{i}{\hbar}\delta t \cdot \frac{\hat{V}}{2}} e^{-\frac{i}{\hbar}\delta t \cdot \hat{T}} e^{-\frac{i}{\hbar}\delta t \cdot \frac{\hat{V}}{2}} e^{o(\delta t^3)}, \quad (3.30)$$

with a negligible 3rd-order correction in time [83].

The first and the last exponential factors in Eq.(3.30) depend on the potential \hat{V} , which is a scalar function of the position in real space, $\mathbf{r} = (x, y)$. The kinetic part, instead, is a second derivative in real space, and local in the Fourier space only:

$$\hat{T} = \left(-\frac{\hbar^2 \nabla^2}{2m^*} \right)_{\vec{r} \text{ space}} = \left(\frac{\hbar^2 k^2}{2m^*} \right)_{\vec{k} \text{ space}}. \quad (3.31)$$

We can introduce a sequence of direct (\mathcal{F}) and inverse (\mathcal{F}^{-1}) Fourier transforms in the evolution operator to switch from the real to the reciprocal representation:

$$\mathcal{F}\Psi(x, y) = \frac{1}{(2\pi\hbar)} \int_{-\infty}^{+\infty} e^{-\frac{i}{\hbar}\vec{p} \cdot \vec{r}} \Psi(x, y) d\vec{r} = \tilde{\Psi}(\hbar k_x, \hbar k_y) \quad (\vec{p} = \hbar \vec{k}) \quad (3.32)$$

Each factor of the evolution operator is so applied to a wavefunction which is defined in the most convenient representation. Indeed:

$$e^{-\frac{i}{\hbar}\delta t \cdot \hat{T}} \Psi(x, y) = \mathcal{F}^{-1} e^{-\frac{i}{\hbar}\delta t \cdot \hat{T}(\hat{p}_x, \hat{p}_y)} \tilde{\Psi}(p_x, p_y) = \mathcal{F}^{-1} e^{-\frac{i}{\hbar}\delta t \cdot T(\hbar k_x, \hbar k_y)} \mathcal{F}\Psi(x, y) \quad (3.33)$$

which is a scalar function in the Fourier space. This method, called indeed *Fourier Split-Step method*, finally provides the evolution operator:

$$\hat{U}(\delta t) = e^{-\frac{i}{\hbar}\delta t \cdot \frac{\hat{V}}{2}} \mathcal{F}^{-1} e^{-\frac{i}{\hbar}\delta t \cdot \hat{T}} \mathcal{F} e^{-\frac{i}{\hbar}\delta t \cdot \frac{\hat{V}}{2}}. \quad (3.34)$$

The final wavefunction after $t = N\delta t$ time-step evolution is given by the iterative application of the evolution operator for a small enough time interval δt :

$$\Psi(x, y; t) = \hat{U}(\delta t)^N \Psi(x, y; 0) \quad (3.35)$$

$$= \left(e^{-\frac{i}{\hbar}\delta t \cdot \frac{\hat{V}}{2}} \mathcal{F}^{-1} e^{-\frac{i}{\hbar}\delta t \cdot \hat{T}} \mathcal{F} e^{-\frac{i}{\hbar}\delta t \cdot \frac{\hat{V}}{2}} \right)^N \Psi(x, y; 0). \quad (3.36)$$

The computational cost for the evolution is however lowered by the following definition of the final wavefunction [83, 84]:

$$\Psi(x, y; t) = e^{-\frac{i}{\hbar}\delta t \cdot \frac{\hat{V}}{2}} \left(\mathcal{F}^{-1} e^{-\frac{i}{\hbar}\delta t \cdot \hat{T}} \mathcal{F} e^{-\frac{i}{\hbar}\delta t \cdot \hat{V}} \right)^N e^{+\frac{i}{\hbar}\delta t \cdot \frac{\hat{V}}{2}} \Psi(x, y; 0), \quad (3.37)$$

or:

$$\Psi(x, y; t) = e^{+\frac{i}{\hbar}\delta t \cdot \frac{\hat{V}}{2}} \left(e^{-\frac{i}{\hbar}\delta t \cdot \hat{V}} \mathcal{F}^{-1} e^{-\frac{i}{\hbar}\delta t \cdot \hat{T}} \mathcal{F} \right)^N e^{-\frac{i}{\hbar}\delta t \cdot \frac{\hat{V}}{2}} \Psi(x, y; 0). \quad (3.38)$$

The evolved wavefunction in the latter formulation has a numerical error of the order $o(\delta t^3)$ (one order less than Eq.(3.29)). However, the unitarity of the \hat{U} operator implies that is the norm of

the wavefunction, which described the probability distribution of the electron system, is conserved during the entire evolution.

Moreover, in presence of a magnetic field \mathbf{B} the canonical momentum \mathbf{p} is modified by the vector potential as $\mathbf{p} - q\mathbf{A}$. The kinetic energy \hat{T} contains therefore a mixed position-momentum term, that depends on the adopted gauge. In the Landau gauge for a 2DEG with $\mathbf{A} = B(0, x, 0)$, the kinetic operator reads:

$$\hat{T} = \frac{1}{2m^*} \sum_{i=x,y,z} (p_i - qA_i)^2 = \hat{T}_{p_y,x}(\hat{x}, \hat{p}_y) + \hat{T}_{p_x,y}(\hat{y}, \hat{p}_x). \quad (3.39)$$

Within this shape, we can not perform a 2D Fourier transform on the xy -domain. Indeed, $\hat{T}_{p_y,x}$ is local on the real-space in the \hat{x} direction only, and on the reciprocal space for the \hat{y} direction only:

$$\mathcal{F}_x \hat{T}_{p_y,x}(\hat{y}, \hat{p}_x) = T_{p_y,x}(y, \hbar k_y). \quad (3.40)$$

Thus, it requires the application of \mathcal{F}_y and \mathcal{F}_x^{-1} , which are 1D Fourier transforms and antitransforms in the longitudinal direction of the device. Analogously, $\hat{T}_{p_x,y}$ needs to apply the Fourier transform and antitransform in the transverse direction, i.e. \mathcal{F}_x and \mathcal{F}_y^{-1} . Finally, in presence of the magnetic field, the time-evolved wavefunction¹ is:

$$\Psi(x, y; t) = e^{+\frac{i}{\hbar}\delta t \cdot \frac{\hat{V}}{2}} \left(e^{-\frac{i}{\hbar}\delta t \cdot (\hat{V} + \hat{V}_{abs})} \mathcal{F}_y^{-1} e^{-\frac{i}{\hbar}\delta t \cdot \hat{T}_{p_y,x}} \mathcal{F}_y \mathcal{F}_x^{-1} e^{-\frac{i}{\hbar}\delta t \cdot \hat{T}_{p_x,y}} \mathcal{F}_x \right)^N e^{-\frac{i}{\hbar}\delta t \cdot \frac{\hat{V}}{2}} \Psi(x, y; 0), \quad (3.41)$$

3.2.2 Split-Step Fourier method for two particles in 2D

Let us consider the case of a two-particle Hamiltonian,

$$\hat{H}_{12} = \hat{H}_1 + \hat{H}_2 + \hat{V}_{12}, \quad (3.42)$$

where $\hat{H}_i = \hat{H}_i(x_i, y_i) = \hat{T}_i(x_i, y_i) + \hat{V}_i(x_i, y_i)$ for $i = 1, 2$ is the single-particle Hamiltonian in 2D, while $V_{12}(x_1, y_1, x_2, y_2)$ the 4D interacting potential of the two-particle system. We can rearrange the Hamiltonian as the sum of a 4D kinetic and potential operator:

$$\hat{H}(x_1, y_1, x_2, y_2) = \hat{T}(x_1, y_1, x_2, y_2) + \hat{V}(x_1, y_1, x_2, y_2), \quad (3.43)$$

where $\hat{T} = \hat{T}_1 + \hat{T}_2$ and $\hat{V} = \hat{V}_1 + \hat{V}_2 + V_{12}$.

To apply the definition of the evolution operator in Eq.(3.34), we then need a 4D Fourier transform and antitransform in the two-particle domain $\mathbf{r} = (x_1, y_1, x_2, y_2)$:

$$\hat{U}(\delta t) = e^{-\frac{i}{\hbar}\delta t \cdot \frac{\hat{V}(x_1, y_1, x_2, y_2)}{2}} \mathcal{F}_{4D}^{-1} e^{-\frac{i}{\hbar}\delta t \cdot \hat{T}(x_1, y_1, x_2, y_2)} \mathcal{F}_{4D} e^{-\frac{i}{\hbar}\delta t \cdot \frac{\hat{V}(x_1, y_1, x_2, y_2)}{2}}. \quad (3.44)$$

The presence of the magnetic field and the introduction of the Landau gauge still couple the real-space coordinates to the reciprocal ones. Therefore, in the two-particle picture, the kinetic operator is defined as:

$$\hat{T} = \sum_{i=1,2} \frac{(\hat{p}_i - q\hat{A}_i)^2}{2m^*} \quad (3.45)$$

¹The same results are valid in the Symmetric Gauge, and the decomposition given by Eq.(3.39) is still valid in any gauge in which $\frac{\partial A_i}{\partial r_i} = 0 \quad \forall i$.

However, we remark that this coupling involves the real and reciprocal-space coordinates of the same particle, i.e. \hat{p}_{y_i} and \hat{x}_i or \hat{p}_{x_i} and \hat{y}_i . Then, we can split the 4D Fourier transform/antitransform of Eq.(3.44) into two separate 2D Fourier transform/antitransforms separately acting on the $\mathbf{x} = (x_1, x_2)$ and $\mathbf{y} = (y_1, y_2)$ space. The final time-evolved wavefunction reads:

$$\begin{aligned} \Psi(x_1, y_1, x_2, y_2; t) = & e^{\frac{i}{\hbar} \delta t \cdot \frac{\hat{V}(x_1, y_1, x_2, y_2)}{2}} \left(e^{-\frac{i}{\hbar} \delta t \cdot \hat{V}(x_1, y_1, x_2, y_2)} \right. \\ & \mathcal{F}_{y_1, y_2}^{-1} e^{-\frac{i}{\hbar} \delta t \cdot (\hat{T}_{p_{y_1}, x_1} + \hat{T}_{p_{y_2}, x_2})} \mathcal{F}_{y_1, y_2} \mathcal{F}_{x_1, x_2}^{-1} e^{-\frac{i}{\hbar} \delta t \cdot (\hat{T}_{p_{x_1}} + \hat{T}_{p_{x_2}})} \mathcal{F}_{x_1, x_2} \Big)^N \\ & \left. e^{-\frac{i}{\hbar} \delta t \cdot \frac{\hat{V}(x_1, y_1, x_2, y_2)}{2}} \right) \Psi(x_1, y_1, x_2, y_2; 0). \end{aligned} \quad (3.46)$$

3.2.3 Initialization procedure for electron wavepackets

As visible from Eq.(3.46), the application of the *Split-Step Fourier method* requires as an input parameter the initial wavefunction of the system, namely $\Psi(x, y; 0)$ and $\Psi(x_1, y_1, x_2, y_2; 0)$ for the single-particle and two-particle case, respectively. However, for a nanometric device with a complicated potential landscape, the computation of the eigenstates of its 2D Hamiltonian can be very demanding. To get over this hurdle, we design in the external potential $V = V_{ext}$ an *initialization region*, which is translationally invariant in the direction of propagation, i.e. the \hat{y} -direction. Here, the wavefunction is adequately described by a strongly localized wavepacket, which mimics the single-charge excitation injected inside edge channels by SES.

The presence of a translationally invariant potential $V(x, y) = V(x)$ together with the use of the Landau gauge, implies for the 2D single-electron Hamiltonian a free term in the y -direction, $\hat{H}(x, y) = \hat{T}(x, y) + \hat{V}(x)$. For a free particle along \hat{y} , we can use the effective 1D Hamiltonian \hat{H}_L^{eff} of Sec. 1.1.2 to map the local one. The diagonalization of the effective Hamiltonian,

$$\hat{H}_L^{eff} \varphi_n(x, k) = E_n \varphi_n(x, k), \quad (3.47)$$

provides the transverse part, $\varphi_n(x, k)$, of the local edge states. To devise an electron wavepacket localized on the \hat{y} direction, we realized a properly weighted combination of the transverse eigenstates for a number of wavevectors \hat{k} .

This solution is correct only in the region where $V(x, y) = V(x)$; they generally are not the eigenstates of the whole device. However, in our time-dependent model, the probability density at initial time is non-zero in the initialization region only, where $\varphi_n(x, k)$ coincide with the true eigenstates. The application of the $\hat{U}(\delta t)$ operator modifies the shape of the wavepacket, without requiring to numerically compute the 2D eigenstates of the complex potential profile $V(x, y)$ outside the initialization region.

In case of a two-particle Hamiltonian, we initially assume the two particles to be far enough not to interact. The state of each electron, with coordinates $\mathbf{r}_i^0 = (x_i^0, y_i^0)$, is then separately designed in its initialization region. According to the local shape of $V_{ext}(\mathbf{r})$ where $\mathbf{r}_i^0 \neq 0$, each particle is well described by a single-particle wavepacket $\psi_j(x_i, y_i)$ at time $t = 0$.

For distinguishable particles, we evolve the product state of the single-charge wavepackets at initial time, which is:

$$\Psi(x_1, y_1, x_2, y_2; t = 0) = \psi_\alpha(x_1, y_1) \psi_\beta(x_2, y_2), \quad (3.48)$$

where the subindexes of ψ refers to transverse eigenstates computed in two translationally invariant regions with $V \simeq V_\alpha(x)$ and $V \simeq V_\beta(x)$, respectively. In presence of exchange symmetry, the initial

many-body wavefunction for a two-electron system is computed from the Slater determinant:

$$\Psi(x_1, y_1, x_2, y_2; t = 0) = \frac{1}{\sqrt{2}} \det \begin{pmatrix} \psi_\alpha(x_1, y_1) & \psi_\beta(x_1, y_1) \\ \psi_\alpha(x_2, y_2) & \psi_\beta(x_2, y_2) \end{pmatrix} = \quad (3.49)$$

$$= \frac{1}{\sqrt{2}} [\psi_\alpha(x_1, y_1)\psi_\beta(x_2, y_2) - \psi_\alpha(x_2, y_2)\psi_\beta(x_1, y_1)] . \quad (3.50)$$

3.2.4 Imaginary potentials as absorbing leads

Absorbing processes performed by metallic leads in the device can be simulated numerically by adding a purely imaginary potential \hat{V}_{abs} to the one \hat{V} in Eq.(3.44). To produce an absorbing effect, $\text{Im}[\hat{V}_{abs}] < 0$. The time-evolved wavefunction is [84]:

$$\Psi(x, y; t) = e^{+\frac{i}{\hbar}\delta t \cdot \frac{\hat{V}}{2}} \left(e^{-\frac{i}{\hbar}\delta t \cdot (\hat{V} + \hat{V}_{abs})} \mathcal{F}^{-1} e^{-\frac{i}{\hbar}\delta t \cdot \hat{T}} \mathcal{F} \right)^N e^{-\frac{i}{\hbar}\delta t \cdot \frac{\hat{V}}{2}} \Psi(x, y; 0). \quad (3.51)$$

This expression does not contain the imaginary potential \hat{V}_{abs} in the first half evolution; at the beginning of the evolution, the particle is localized in a region far from the absorbing contacts, where $V_{abs} \approx 0$. On the other side, the last half anti-evolution would be a positive real exponential, $\exp(+i\delta t \cdot \hat{V}_{abs}/2\hbar)$, which increases the norm, thus adding non-physical effects in the evolution. The time evolution is no more norm-conserving and \hat{U} is therefore a non-unitary operator.

3.2.5 Discretization and boundary conditions

The numerical implementation of the Split-Step Fourier method requires the discretization and bounding of direct and reciprocal space. For an area in space with dimensions L_x and L_y , the 2D grid is discretized into $N_x \times N_y$ points. The grid spacing along the two axes in the real and reciprocal space are therefore given by:

$$\begin{cases} \delta x = \frac{L_x}{N_x}, \\ \delta y = \frac{L_y}{N_y}. \end{cases} \quad \begin{cases} \delta k_x = \frac{2\pi}{L_x}, \\ k_x^{\max} = -k_x^{\min} = \frac{\pi}{\delta x}, \end{cases}$$

and similarly also for the k_y axis. This produces a simulation grid in the reciprocal space which is given by $N_x \times N_y$ points. Moreover, the *FFT algorithm* from the MKL library that is used to perform the Discrete Fourier Transforms, are optimized for simulation grids with N_x and N_y points as powers of 2. Due to the presence of periodic boundary conditions (PBC) in our real domain $L_x \times L_y$, any wavefunction exiting from a border of the simulation domain will re-enter inside the domain from the opposite side. Note that the presence of PBC affects the confining potential too. As a consequence, in presence of the magnetic field, the electron feels a very large confinement in the transverse directions of the device.

Additionally, due to the coupling among the axes x and k_y given by $k_y = -eBx/\hbar$ in the Landau gauge, each position x is associated to a certain wavevector, thus entailing the two following requirements.

1. For an origin at the center of the device, there is an additional maximum wavevector given by:

$$\bar{k}_y^{\max} = \frac{eBL_x}{2\hbar}. \quad (3.52)$$

In order to avoid that the wavefunction reaches a region of space in which it cannot be properly represented in terms of wavevectors, the following condition must hold:

$$\bar{k}_y^{\max} < k_y^{\max}, \quad (3.53)$$

2. Furthermore, δx and δy must be small enough with respect to the magnetic length l_m , otherwise the representation of edge states will not be accurate and they will not behave like the eigenstates of the Hamiltonian.

Regarding the convergence and the reliability of the Split-Step Fourier method:

3. δt must be smaller than any characteristic time encoded in $\hat{H}(t)$.
4. for a time-independent \hat{H} , δt must be small enough if compared to the transition times v_g of the wavepacket between two grid points, given by $\delta x/v_g$.
5. The product $\hbar^{-1}\delta t \cdot V$ at the exponent of the evolution operator $\hat{U}_V(\delta t)$ must be small enough if compared to the period of the exponential (2π), i.e.

$$\delta t \ll \frac{2\pi\hbar}{\max V}. \quad (3.54)$$

Thanks to the Virial theorem², if the previous condition is satisfied, Eq.(3.44) holds also for $\hat{U}_T(\delta t)$.

6. The spacing of the grid δx in real space must be small enough if compared to the variations of the wavefunction along x or, equivalently, the maximum wavevector k_x^{\max} in Fourier space must be large enough to describe the highest-momentum component of the wavefunction.

The discretization of the real and reciprocal space implies the discretization of the operators and the wavefunction. Indeed, the continuous wavefunction is represented by a matrix:

$$\Psi(x, y) \rightarrow \Psi_{x,y} = \Psi(x, y) \sqrt{dx} \sqrt{dy}, \quad (3.55)$$

so that the integration of the squared modulus of the wavefunction can be obtained with the *sum* function:

$$\int |\Psi(x, y)|^2 dx dy \rightarrow \sum_{x,y} |\Psi_{x,y}|^2. \quad (3.56)$$

Operators like the evolution one, $\hat{U}_V(\delta t)$, are instead 4D tensor operators. However, in our implementation of the evolution operator they always act in the space in which they are diagonal. Then, they can be replaced with 2D matrices containing the diagonal of the corresponding 4D operator:

$$(U_V)_{x,y} = (U_V)_{x,y;x,y} = e^{-\frac{i}{\hbar}\delta t \cdot V_{x,y}}. \quad (3.57)$$

The tensor product $\hat{U}_V(\delta t)\Psi(x, y, t)$ becomes then a point-to-point matrix product, which is equivalent to the product of two discretized scalar functions:

$$\Psi(x, y, t + \delta t) = \hat{U}_V(\delta t)\Psi(x, y) \rightarrow \Psi'_{x,y} = (U_V)_{x,y}\Psi_{x,y}. \quad (3.58)$$

3.3 Parallel implementation and HPC-related performances of the Split-Step Fourier method

Our numerical approach enables to explore single and two-particle dynamics in a large variety of two-dimensional devices, e.g. interferometers and quantum dots. With contrast to stationary approaches, it only requires a proper geometry of the external potential $V_{ext}(x, y)$ as input

² $\langle T \rangle = \langle \vec{r} \cdot \vec{\nabla} V \rangle \sim n \langle V \rangle$

parameter, to reproduce the effect of top metallic gates on the particle motion. It also enables the numerical simulation of time-dependent potentials, which could be used to model, e.g., the electron injection processes or the effects of AC biases on devices, or to model the dynamics of flying qubits [29]. On the other hand, the simulation of two-particle transport and correlation in a full-scale geometry involves a non negligible computational load.

The execution of our code, written in Fortran 90, is divided into an (i) initialization process, (ii) the evolution of the electron wavefunction and (iii) measurement through projection. Eventually, the system properties can also be measured dynamically during the evolution step, by directly using the 2D or 4D wavefunction of the system.

3.3.1 OpenMP parallelization of the single-particle version

In the initialization process, we set the input parameters to design the external potential $V_{ext}(x, y)$ affecting the path of edge channels inside our device. V_{ext} generally contains a translationally invariant region where the single-electron wavepacket is initialized. Here, we diagonalize the effective single-particle Hamiltonian in Eq.(1.28) by means of LAPACK routines, which provide the transverse portion of the edge states $\varphi_{n,k}(x)$. The latters are then combined in a wavepacket, according to the chosen wavevector dispersion σ_k .

The Split-Step Fourier method is performed by recursively applying the evolution operator $U(\delta t)$ for a small enough time interval δt (see Sec. 3.2.5). As detailed in previous sections, within this method the evolution operator is split into a product of evolution operators, to separate those terms in the Hamiltonian that are diagonal on different spaces. To switch from the real to the reciprocal space and vice-versa, Intel wrappers of the *Fastest Fourier Transform of the West* (FFTW) from MKL library are used.

In absence of the magnetic field, two-dimensional FFTW may be used. On the contrary, in the IQH regime the Landau Gauge couples the momentum $\hat{p}_x(\hat{p}_y)$ with the real-space coordinate on the $\hat{y}(\hat{x})$ -direction. Therefore, the Split-Step Fourier method in presence of the magnetic field entail one-dimensional FFTW related to the $\hat{x}(\hat{y})$ -direction separately.

A scheme of the algorithm is reported in Fig. 3.2(a). These one-dimensional FFTW must be performed for each point of the simulation grid on the $\hat{y}(\hat{x})$ -direction, and vice-versa. Such loop has been parallelized with OpenMP, each task performing a series of one-dimensional Fourier transform

	MareNostrum (BSC)	Marconi A2(CINECA)	Hydra (UNIMORE)
Location	Barcelona (Spain)	Bologna (Italy)	Modena (Italy) Model
	Lenovo Adam Pass	Lenovo NextScale	
Processors	Intel Xeon Platinum 8160 24C	Intel Xeon Phi 7250 CPU (KNL)	Intel Xeon CPU E5-2640 v3
Freq	2.1 GHz	1.40 GHz	2.60GHz
Nodes	3240	3600	40
Cores	48 cores/node	68 cores/node	16 cores/node
Hypertreading	NO	YES	NO
RAM	96 GB/node	96 GB/node	64-128 GB/node
Peak Performance	11 PFlop/s	11 PFlop/s	
Network	100Gb Intel Omni-Path Full-Fat Tree	Intel OmniPath Architecture 2:1	InfiniBand interconnects

Table 3.1: Technical information on the supercomputing machines and hardwares used in our computations.

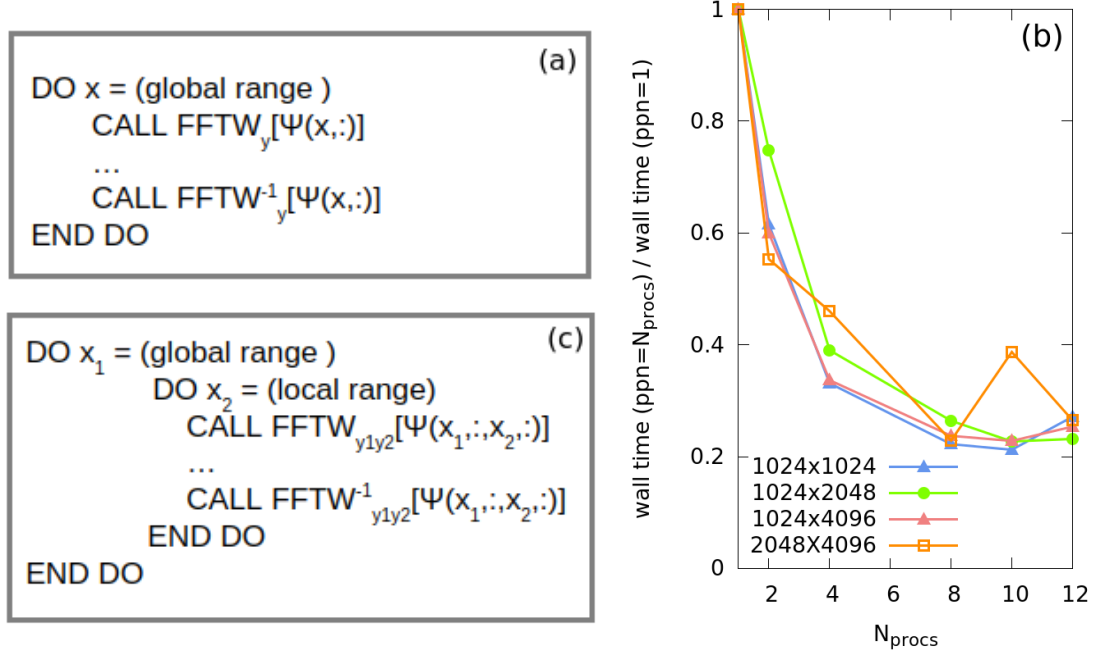


Figure 3.2: (a) Algorithm for the application of the evolution operator according to the Split-Step Fourier method to simulate single-electron transport. OpenMP tasks execute chunks of the first DO loop. (b) Numerical performances for the single-particle version of our code parallelized with OpenMP. Each task performs a chunk of the DO loops in panel (a). Relative clock times for different grid sizes are compared. (c) Algorithm for the application of the evolution operator according to the Split-Step Fourier method to simulate two-electron transport. MPI processes execute the double DO loop according to their local range. Note that FFTW calls are *blocking*, i.e. they are executed simultaneously for all the MPI processes. Consequently, all the processes execute the FFTW with regards to the same x_1 parameter.

on $\hat{x}(\hat{y})$ according to its interval of iteration on $\hat{y}(\hat{x})$. Fig. 3.2(b) shows the HPC performances for an increasing number of tasks and different grid sizes. The ratio between the clock time of a single iteration with N_{proc} tasks and the clock time of a single iteration for the serial version is here displayed: for such simulation grids, performances are significantly increased by increasing the number of OpenMP tasks involved, and saturates similarly when $N_{\text{procs}} \simeq 10$.

3.3.2 MPI parallelization of the two-particle version

If OpenMP is satisfactory to simulate also very large two-dimensional systems (up to the mesoscopic scale) in a single-particle picture, the numerical simulation of two-particle transport requires HPC resources. Indeed, the two-particle wavefunction contains four degrees of freedom, i.e. two real-space or reciprocal-space coordinates for each particle. Differently from the common approach to two-particle dynamics in the IQH regime, we prefer not to use a one-dimensional model exploiting the chiral nature of edge channels, but we consider a two-dimensional system to investigate the effect of realistic potential landscapes, whose shape determines energy-dependent effects.

In a 2D system, the two-particle wavefunction $\Psi(x_1, y_1, x_2, y_2)$ requires the allocation of an

$(N \times M)^2$ complex matrix on an $N \times M$ real-space simulation grid. Due to its large memory cost, the wavefunction must be allocated by adopting multi-node data distribution on a supercomputing machine. As an example, the two-particle wavefunction, allocated as a 4D complex array with double precision, requires about 1 TB on a 512×512 simulation grid. This amount of memory can not be provided by a single node even in supercomputing machines, as visible from Tab. 3.1.

To this end, the code has initially been parallelized with a one-dimensional distribution of Ψ in the MPI paradigm: the \hat{y}_2 index only is defined on a local range for each MPI process involved in the computation, so that each MPI process allocates in its own memory a portion of the two-particle wavefunction. The Split-Step Fourier method is so applied by each process to its own portion of the distributed wavefunction. In presence of the magnetic field, two-dimensional Fourier transforms on the $\hat{x}_1, \hat{x}_2(\hat{y}_1, \hat{y}_2)$ domain, which are not coupled by the Landau Gauge, are performed for each point of the local $\hat{y}_1, \hat{y}_2(\hat{x}_1, \hat{x}_2)$ grid (see Fig. 3.2(c)). According to the chosen Landau gauge, one loop (e.g. the one on \hat{x}_1, \hat{x}_2) can be performed serially, while the second one (e.g. the one on \hat{y}_1, \hat{y}_2) requires collective MPI communications during the execution of the FFTWs, whose number of calls depends on the grid points on the global directions.

In this algorithm, HPC performances are affected by the (i) size of the chunk of Ψ manipulated by each MPI process with total number N_{procs} , Ψ_{loc} , and (ii) the number of communications involved. By increasing N_{procs} , the size of Ψ_{loc} decreases, but the number of communications increases. In a one-dimensional distribution, however, the number of MPI cores involved in the computations can not be larger than the number of grid points in the global direction. This fixes a maximum number of MPI processes involved, that limits HPC performances for the sizes of our simulation grids.

In the second version of the software, the previous parallelization scheme has been replaced by a Cartesian topology of the MPI processes: we distribute the two-electron wavefunction with respect to both \hat{x}_2 and \hat{y}_2 coordinates. A scheme of the distribution protocol is reported in Fig. 3.3(a). A number N_{procs}^x of MPI processes are distributed on the \hat{x}_2 -direction and a number of N_{procs}^y MPI processes are distributed on the \hat{y}_2 -direction. *Per-row* and *per-column* communicators are created

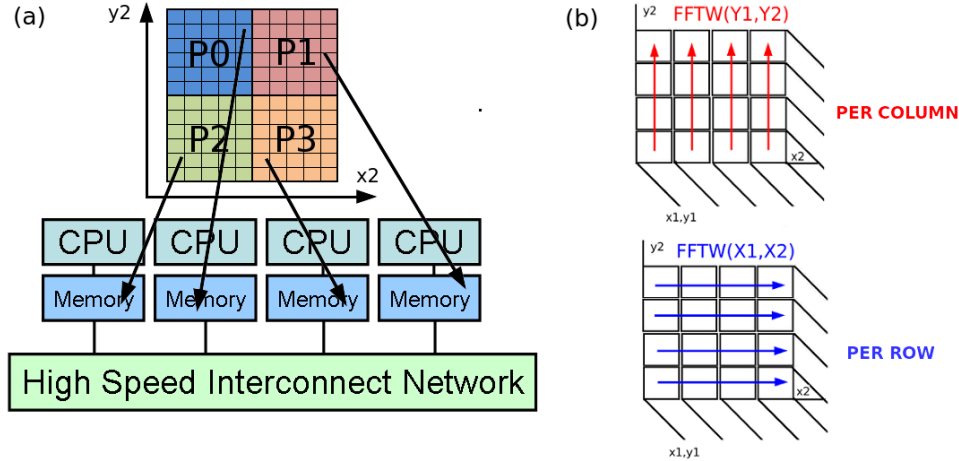


Figure 3.3: Parallelization protocol adopted to allocate and evolve the two-particle wavefunction. (a) Cartesian topology adopted for the MPI pool in a distributed-memory machine. The wavefunction is distributed among the MPI processes P_i according to the local range of $\mathbf{r}_2 = (x_2, y_2)$ (b) Communication protocol during the execution of the 2D FFTWs with per-row and per-column communicators.

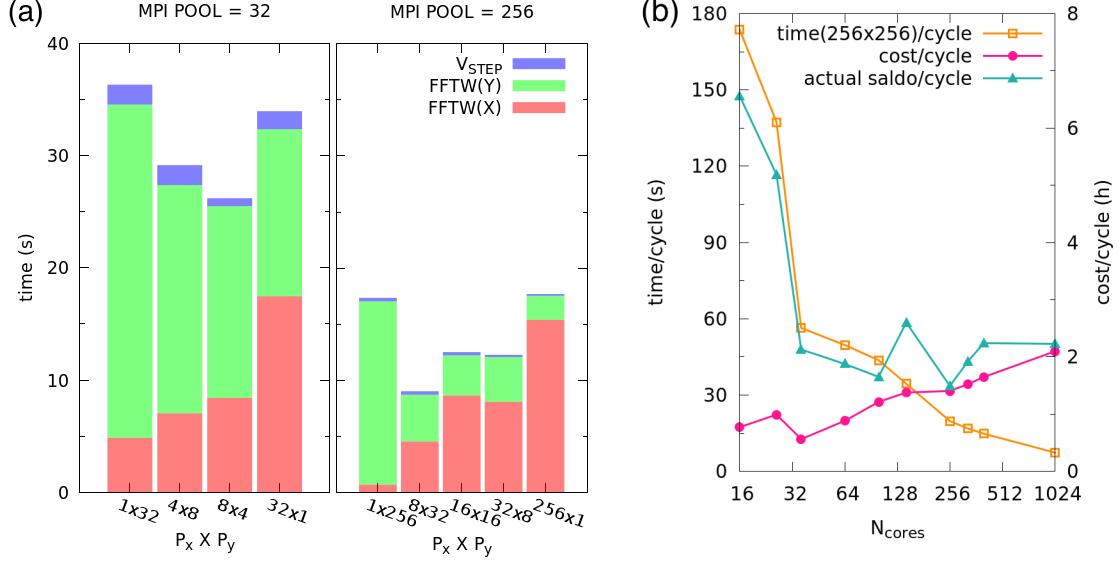


Figure 3.4: (a) Clock time to execute one step of the Split-Step Fourier method for different Cartesian topologies and MPI pools on MareNostrumIV. (b) HPC performances for the execution of one step of the Split-Step Fourier method by increasing the number of MPI processes, which are equally distributed on the \hat{x} and \hat{y} -direction of the simulation domain.

to organize MPI communications during the execution of the Fourier transforms, as depicted in Fig. 3.3(b). Therefore, both loops are performed in parallel. However, in the present scheme the number of MPI processes is not limited by the size of the simulation grid in the direction where the wavefunction is distributed. Moreover, collective communicators generally involve a smaller number of processes (only the ones on the same row or column) during the execution of FFTW.

As evident from Fig. 3.4(a), for a given value of N_{procs} , the clock time to execute a DO loop depends on the Cartesian topology adopted in the MPI paradigm. This generally differs if the FFTWs are executed on the \hat{x} or \hat{y} -directions. This follows from the different cache usage entailed by the Landau gauge, which couples the \hat{p}_y and \hat{x} operators only. Note from Fig. 3.4(a) that,

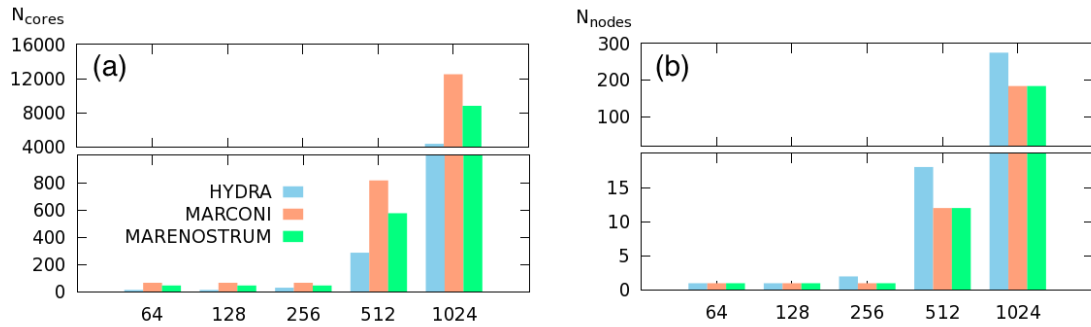


Figure 3.5: Minimum number of (a) cores and (b) nodes to allocate the 4D wavefunction on different supercomputing machines for a 2D simulation domain with N grid points per size.

indeed, the topology with the lowest computational cost does not correspond to the one with the same number of processes on the two directions, and that the computing time is higher in the one-dimensional distribution. Therefore, by adopting a Cartesian topology we can decrease the computational cost by tuning the number of MPI processes on the two directions, adequately to the hardware and network of the supercomputing machine exploited. Tab. 6.1 summarize the

technical information of the supercomputing machines we mainly exploit: the local HPC facility, named HYDRA, at the LABCSai Laboratory mostly for single-particle simulations, MARCONI A2 at CINECA (BO, Italy) and MareNostrum4 at BSC.

Regarding the two-particle simulations, memory is the main constraint in the application of our software. The number of MPI processes involved in the computations, indeed, has to scale very fast when we double the simulation mesh, to exploit the optimization of FFTW routines on domains with 2^N points per size. Fig. 3.5 provides the minimum number of (a) cores and (b) nodes to allocate the 4D wavefunction on the 3 supercomputing machines of Tab. 3.1.

Finally, Fig. 3.4(b) shows the clock time to execute a single loop of the Split-Step Fourier method as a function of the number of cores (N_{cores}) for a 2D domain with 256 points per size on Marconi A2. Note that the abscissa scales as 2^N . The clock time generally decreases with respect to N_{cores} and saturates for at $N_{cores} \simeq 1024$ (yellow line). However, the consumption in terms of CPU hours (the one accounted for the computation on supercomputing machines) takes also into account the number of cores involved (purple line) or nodes (blue line), the latter depending on the hardware itself. As an example, on Marconi A2, the best compromise between fast computations (minimum of the yellow line) and low CPU costs (maximum of the purple and blue lines) is $N_{procs} = 256$.

3.4 Kwant software for support calculations

Kwant is an open-source Python package that has been designed to simulate single-particle transport in a finite or infinite mesoscopic system described by a tight-binding model, and it allows the numerical simulation of 1D, 2D and 3D geometries. The software provides a number of subroutines to compute the properties of the system, e.g. the local density of states, the propagating wavefunctions, or dispersion relation once the tight binding model is set. Moreover, it can be exploited as building block to extract more complex physical properties as the non equilibrium Green's function.

To this aim, one has to initially define the infinite mesoscopic system, by connecting the Hamiltonian of the finite scattering region with the one of semi-infinite leads. The latters provide the incoming and outgoing plane waves inside the scattering region, in order to simulate single-particle transport in the Landauer-Buttiker formalism. A scheme of a 2D and 3D tight-binding system is displayed in Fig. 3.4.

One-particle annihilation and creation operators are used to rewrite the Hamiltonian in a time-resolved quantum representation, i.e. $H(t) = \sum_{ij} H_{ij}(t) c_i c_j$. The Hamiltonian of the infinite system is divided into sub-blocks, labeled with the index 0 for the central scattering region and with a number from 1 to M for the leads of the system. As a reference, we refer to the simple example of a one dimensional chain with two leads; the Hamiltonian has the following matricial form:

$$H = \begin{bmatrix} H_{00} & H_{01} & H_{02} \\ H_{10} & H_{11} & H_{12} \\ H_{20} & H_{21} & H_{22} \end{bmatrix}.$$

Here, each diagonal block $H_{i,i}$ contains an *onsite* energy in the leads (H_L) or in the scattering

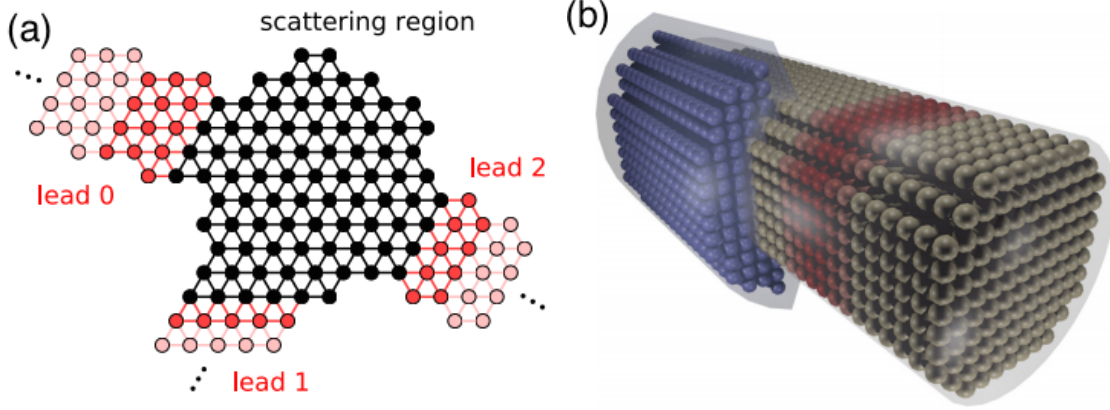


Figure 3.6: (a) Structure of an exemplary tight-binding system modeled with Kwant. Sites belonging to the scattering region are represented by black dots, sites belonging to one of the three semi-infinite leads by red dots. (b) A 3D model of a semiconducting quantum wire (gray cylinder) simulated with Kwant. The balls represent lattice sites. The red region is a tunnel barrier, used to measure tunneling conductance, and the blue region is a superconductor.

regions (H_S), an hopping term in the leads (V_L) or in the scattering region (V_S) and an hopping term between each lead and the scattering region (V_{LS}).

Due to the translational invariance of the leads where they originate, propagating waves are rewritten as a delocalized state, corresponding to the superimposition of plane waves. The Hamiltonian of the lead is then diagonalized,

$$(H_L + V_L \lambda_n^{-1} + V_L \lambda_n) \chi_n = E \chi_n, \quad (3.59)$$

to compute the eigenvalues and eigenstates of the semi-infinite system. This produces two types of eigenstates, according to the λ parameter that affects the normalization of the wavefunction.

- If $|\lambda_n| = 1$, the eigenstates define propagating modes with $\lambda_n = e^{ikn}$, which are normalized in accord to the expectation value of the particle current. In detail, $\langle I \rangle = +1$ for incoming modes and $\langle I \rangle = -1$ for outgoing ones.
- If $|\lambda_n| < 1$, the eigenstate describe evanescent modes, that do not contribute to the transport in the mesoscopic device, such that $\langle I \rangle = 0$.

Finally, to compute the scattering states the wavefunctions in the leads and the ones in the scattering region are matched through the equation $H\Psi_n = \epsilon\Psi_n$.

Kwant combines flexibility and the ease of use, together interoperability. The first peculiarity requires a high-level language, Python in particular, while the second one an universal low-level language interface and simple data structure. This is why the application of the Kwant library needs to separate the numerical simulation in two steps: first, the construction of the tight-binding Hamiltonian of the system, and then the finalization into a low-level representation. Ref. [85] proves that this results in higher performances with respect to alternative transport methods in time-independent frameworks.

Part II

Numerical simulations of Hall interferometers

Chapter 4

A multichannel geometry for the Mach-Zehnder interferometer

The electronic MZI combines two of the most basic single-qubit devices for quantum computing, the *beam splitter* and the *phase shifter*, to observe self-interference of the carrier wavefunction. In the following, we initially review the first geometries implemented in semiconductor heterostructures in the IQH regime. Then, we will present a new solid-state implementation at bulk FF 2 based on cyclotron-resolved edge states [10, 12] (see Fig. 4.1(a)), and our numerical simulations of self-electron interference in this new geometry.

In an MZI, the electron faces a self-interference between the reflected and transmitted components of its wavefunction generated by a beam splitter. A scheme of its functioning is depicted in Fig. 4.1(b). The electron state $|\psi_I\rangle$ is initialized in one of the two available channels $|0\rangle, |1\rangle$, e.g. $|\psi_I\rangle = c_0|0\rangle + c_1|1\rangle$ with $c_0 = 1$ and $c_1 = 0$, and then it is split into a coherent superposition of the *reflected* and the *transmitted* component by a first electron beam splitter, i.e. $|\psi_{II}\rangle = c'_0|0\rangle + c'_1|1\rangle$. The probability of this scattering process is related to a transmission coefficient t_{ji} from an initial channel $i = 0, 1$ to a final channel $j = 0, 1$, so that the electron wavefunction $|\psi_{II}\rangle$ is computed by applying the matrix

$$\hat{B} = \begin{pmatrix} t_{00} & t_{01} \\ t_{10} & t_{11} \end{pmatrix} \quad (4.1)$$

to the initial state: $|\psi_{II}\rangle = \hat{B}|\psi_I\rangle$. For an ideal beam splitter, $|t_{ij}|^2 = 1/2$, regardless the energy of the electron state.

Then, the phase shifter separates the paths of the two basis states, $|0\rangle$ and $|1\rangle$, in order to introduce a relative tunable phase, generally depending on the geometry of the system and on the intensity of the magnetic field. The effect of such gate on the electron state is described by the application of the following scattering matrix to $|\psi_{II}\rangle$:

$$\hat{\Phi} = \begin{pmatrix} e^{i\phi_0} & 0 \\ 0 & e^{i\phi_1} \end{pmatrix}, \quad (4.2)$$

where we assume that no additional interchannel scattering is present, as in an ideal apparatus.

The two channels are forced to follow different paths, l_0 and l_1 , so that each component of the electron state accumulates a phase

$$\phi_i = \frac{1}{\hbar} \int_i (p - qA) ds_i = \xi_i + \chi_i, \quad (4.3)$$

that depends on the line integral of the total momentum on the specific path of the channel l_i , with $i = 0, 1$. ξ_i and χ_i are called the *dynamic* and *magnetic* phase difference and depend on the linear momentum and on the vector potential respectively:

$$\xi_i = \frac{1}{\hbar} \int_{l_i} \mathbf{p} \times d\mathbf{r} \quad (4.4)$$

$$\chi_i = -\frac{1}{\hbar} \int_{l_i} q \mathbf{A} \times d\mathbf{r} \quad (4.5)$$

The dynamic phase difference between the two channels $i = 0, 1$ reads

$$\Delta\xi = \xi_1 - \xi_0 = \frac{1}{\hbar} \left(\int_{l_1} \mathbf{p} \cdot d\mathbf{r} - \int_{l_0} \mathbf{p} \cdot d\mathbf{r} \right) = -k\Delta l, \quad (4.6)$$

where $\Delta l = l_1 - l_0$ is the length difference between the two paths, while the relative magnetic phase is computed from the flux of the magnetic field through the area enclosed by the two channels (S) via the *Stoke's theorem*

$$\Delta\chi = \chi_1 - \chi_0 = \frac{e}{\hbar} \int_S \nabla \times \mathbf{A} \cdot d\mathbf{s} = \frac{e}{\hbar} BS = \pi \frac{\Phi_B}{\Phi_0}. \quad (4.7)$$

Here, $\Phi_0 = \frac{h}{2e} = 2.0678 \cdot 10^{-15} \text{Wb}$ is the magnetic flux quantum.

Finally, the two beams are recollected on a second beam splitter, where they interfere. The final wavefunction is then computed from

$$|\psi_{IV}\rangle = \hat{B}\hat{\Phi}\hat{B}|\psi_I\rangle. \quad (4.8)$$

In our numerical simulation, we further project the output state $|\psi_{IV}\rangle$ on one of the two basis states $|i\rangle$, in order to calculate the transmission probability to the i -th channel:

$$T = |\langle i|\psi_{IV}\rangle|^2. \quad (4.9)$$

As proved in the following, in absence of decoherence phenomena, the intensity of the transmission probability oscillates with the magnetic field or the geometrical parameters of the phase shifter, thus manifesting an interference pattern.

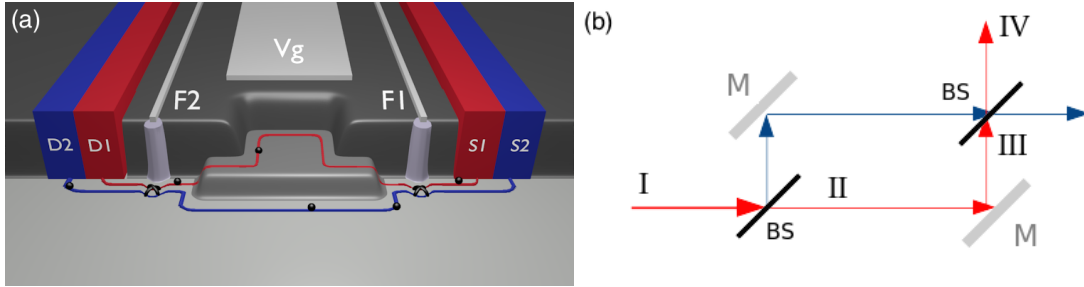


Figure 4.1: (a) The multichannel geometry of a MZI in the IQH regime [86, 13]. Electrons are injected in the first ($n = 0$) or in the second ($n = 1$) Landau level from the two sources S_1 and S_2 . F_1 and F_2 label the potential dip acting as an half-reflecting electron beam splitter. V_g is a top gate that separates the paths of the two edge channels, which are finally recollected at the second beam splitter. Two contacts D_1 and D_2 selectively absorb electrons according to their Landau index. (b) Scheme of a MZI. The red and blue solid lines represents the two paths of the electron state, which are separated by the two beam splitters (BS).

4.1 The MZI in the IQH regime

In solid-state implementations, the visibility of the oscillations in the transmission amplitude,

$$\text{vis} = \frac{\max(T) - \langle T \rangle}{\langle T \rangle}, \quad (4.10)$$

estimates the degree of decoherence induced e.g. by impurities [87, 88], phonons [89] or background charges that typically affect electron transport in semiconductor heterostructures. However, the IQH regime proved to be an ideal playground for electron interferometry, thanks to the long-coherence length of the edge states where the carrier is initialized.

In this framework, the quantum logic gates are realized by locally depleting the 2DEG, with metallic gates of top of the heterostructure that affect locally the bulk FF. The external confining potential V_{ext} felt by the electrons is locally varied, so that the path of the edge channel can be tuned according to the quantum logic operation to be performed. The specific design of the external potential $V_{ext}(x, y)$ depends on the type of edge states exploited to define the basis set. According to the bulk FF of the device, two implementations are therefore possible.

- (i) For a unitary filling, the *quantum rails* are defined by the counterpropagating edge states with opposite momentum but same Landau index, e.g. $|0\rangle = \varphi_{nk}e^{iky}$ and $|1\rangle = \varphi_{n-k}e^{-iky}$, which are located at opposite sides of the confined 2DEG.
- (ii) At FF larger than one, the two (or more) channels available at each side of the device $|i\rangle = \varphi_{n_i k}e^{iky}$ define a suitable basis set for logic gate operations. With contrast to the first scenario, these edge states propagate in the same direction of the device, but differs in the Landau index n_i .

4.1.1 The QPC at bulk FF 1

The earliest proposals of Hall MZIs are based on counterpropagating states from the same Landau level at bulk FF 1. Here, the coherent superposition of the two electron paths must be realized by a nanostructure able to scatter the electron from the edge state $\varphi_{nk}e^{iky}$ to the one with opposite chirality $\varphi_{n-k}e^{-iky}$, spatially located at the opposite border of the device. This requires the introduction on the electron path of a QPC, a narrow constriction in the 2DEG that reduces the lateral distance between the two confining barriers of the device, thus favoring the presence of interchannel tunneling. Then, when the two borders are further separated, the wavefunction splits between the two paths with an energy-dependent transmission probability given by $|t_{ji}(E)|^2$, with $i = 0, 1$ and $j = 0, 1$ labeling the input and the output channels, respectively.

If applied to electron states with an energy broadening, the energy selectivity of the QPC has a significant role on device performances. Ref. [7] provides an empirical definition of the transmission $t(k)$ and reflection $r(k)$ coefficients for the scattering of an edge state in the first channel on a full-scale QPC:

$$\begin{bmatrix} r(k) \\ t(k) \end{bmatrix} = \sqrt{\frac{1}{\exp(\pm\alpha(k - k_e) + 1)}}, \quad (4.11)$$

where k is the (gauge-dependent) wavevector of the impinging electron, k_e and α are fitting parameters depending on the design of the gate, as the opening size and the smoothness of the lateral barrier.

With the simulation in Fig. 4.2(a), we validate $t(k)$ and $r(k)$ coefficients in Eq.(4.11). Here, we simulate the scattering of a single-electron wavepacket $|\psi\rangle$ with $\sigma = 40$ nm and central energy $E^0 = 11$ meV at a QPC with an opening size of $d_x = d_y = 32.2$ nm. The transmitted $|\psi_L\rangle$

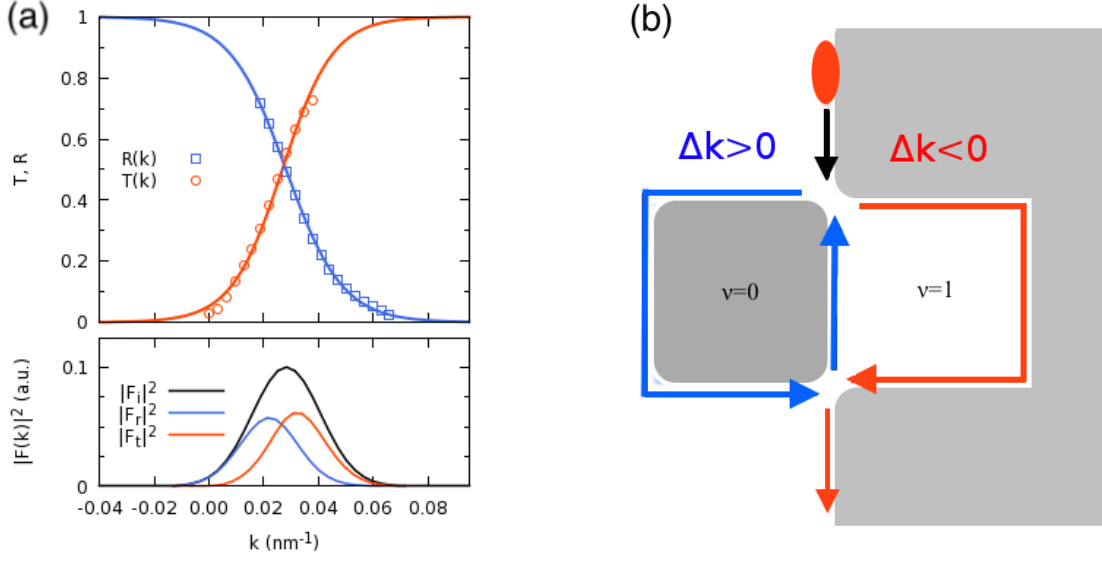


Figure 4.2: (a) The top panel displays the reflection $R(k)$ and transmission $T(k)$ coefficients of a QPC with an opening size $d = 32.2$ nm, computed by means of the wave-packet method (dot) with a single-electron wavepacket with $\sigma = 60$ nm and a central energy $E^0 = 11$ meV. Numerical data are fit by Eq.(4.11) (solid line). The bottom panel compares the probabilities that an edge state with wavevector k belongs to the the initial (black line), reflected (blue line) and transmitted (red line) wavepacket. (b) Scheme of the 2D external potential mimicking the single-channel MZI (grey area). The initial wavepacket (red shape) is partitioned between the two channels (red and blu arrows), which follow different paths. Note that the reflected channel (blue one) is not available at the output port of the device.

and reflected $|\psi_R\rangle$ components of the electron wavefunction are defined at the right $|R(k)\rangle$ or left $|L(k)\rangle$ sides of the device [7] by means of the Gaussian weight function for the initial state $F(k)$, as follows:

$$|\psi\rangle = |\psi_L\rangle + |\psi_R\rangle, \quad (4.12)$$

$$|\psi_L\rangle = \int dk F(k) r(k) |L(k)\rangle = \int dk F_L(k) |L(k)\rangle, \quad (4.13)$$

$$|\psi_R\rangle = \int dk F(k) t(k) |R(k)\rangle = \int dk F_R(k) |R(k)\rangle. \quad (4.14)$$

The *wave-packet method* provides the reflection and transmission probability for a given wavevector k by projecting the wavepacket on the local eigenstates $|L(k)\rangle$ and $|R(k)\rangle$:

$$|r(k)|^2 = \frac{|F_L(k)|^2}{|F(k)|^2} = \frac{|\langle L(k) | \Psi_L \rangle|^2}{|F(k)|^2}, \quad (4.15)$$

$$|t(k)|^2 = \frac{|F_R(k)|^2}{|F(k)|^2} = \frac{|\langle R(k) | \Psi_R \rangle|^2}{|F(k)|^2}. \quad (4.16)$$

The numerical data provided by this method (dots in top panel of Fig. 4.2(a)) are then fit by the empirical equations (solid line) for $r(k)$ and $t(k)$.

Eq.(4.11) clearly shows an energy asymmetry in the reflection and transmission probabilities. Indeed, the high-energy components in the wavepacket have an higher probability to be transmitted by the QPC, while the low-energy components are preferentially reflected. This is confirmed by the shape of the reflected (blue line) and transmitted (red line) wavepackets displayed in the bottom panel of Fig. 4.2(a). This specific design of the QPC splits the initial wavefunction into two localized states, that are characterized by identical integrated probabilities (50%), if the initial wavepacket (black line) has a central wavevector k_0 that is properly aligned with the turning point of the energy selectivity, i.e. $k_0 = k_e$. However, for a non negligible broadening of the wavepacket energy distribution, as in the present case, the reflected and transmitted components are differently distributed on the wavevector space.

Furthermore, we observe that the probabilities $R(k) = |r(k)|^2$ and $T(k) = |t(k)|^2$ on the Fourier space are properly fit by two Fermi-like distributions, so that the probability that a state with wavevector k is reflected ($|F_R(k)|^2$) or transmitted ($|F_T(k)|^2$) reads:

$$|F_R(k)|^2 = \frac{1}{\exp(\alpha_r(k - k_r) + 1)} |F(k)|^2 = F_{\alpha_t}(k - k_t) |F(k)|^2, \quad (4.17)$$

$$|F_L(k)|^2 = \frac{1}{\exp(\alpha_t(k - k_t) + 1)} |F(k)|^2 = F_{\alpha_r}(k - k_r) |F(k)|^2. \quad (4.18)$$

The optimal parameters for an half-reflecting beam splitter are therefore $k_t = k_r = k_e$ and $\alpha_t = -\alpha_r = \alpha$.

Moreover, in the case of a Gaussian weight functions $F(k)$ for the initial single-electron wavepacket, it is convenient to use a Gaussian distribution instead a Fermi-like one to compute the above probabilities. Indeed,

$$\frac{1}{\exp(\alpha(k - k_e) + 1)} \simeq \exp \left[-\frac{(\alpha(k - k_e) + \gamma)^2}{4\gamma} \right], \quad (4.19)$$

with $\gamma = 4 \ln(2)$. This approximation is appropriate for the most relevant wavevectors in the wavepacket spectrum, i.e. the components near the turning point of the energy selectivity, k_e , while those states at very high or very low energies are over- or under-estimated, respectively. However, for a large electron wavepacket centered around k_e , these contributions are in the tails of the wavepacket, and therefore they do not significantly affect the scattering process at the QPC.

Indeed, this approximation has been successfully adopted to predict analytically the visibility of a single-channel MZI [7], and the bunching probability in two-particle HOM experiments driven by exchange interaction [21] with strongly localized wavepackets, as later detailed.

4.1.2 Phase Shifter at bulk FF 1

The coherent superposition of counterpropagating edge states must be split laterally to induce a relative phase shift between the two electron paths. In the solid-state implementations under study, operating at FF 1, this is forced by the opposite sign of the effective wavevector Δk in the two edge channels of the 2DEG.

However, in order to create a loop area S at bulk FF 1, the geometry of the Hall phase shifter must force the two channels to propagate in the same direction of the device, despite their opposite group velocity. This is achieved by the external potential mapped in Fig. 4.2(b), where the phase shifter is integrated into a full MZI.

Two QPCs link a potential mesa with local FF 0 (as in the confining potential) to an indentation with local FF 1 (as in the bulk) inside the confining barrier of the 2DEG. The initial state (red wavepacket of Fig. 4.2(b)) is split by the first QPC into a reflected (blue arrow) and transmitted (red arrow) component that counterpropagate next to the lateral barriers of the mesa (for negative

Δk) and of the indentation (for positive Δk) respectively, due to the opposite slope of the potential confining barrier in the initial horizontal path. In absence of additional energy-degenerate states, the two channels follow the border of each confining potential without additional interchannel scattering.

Edge states with $\Delta k < 0$ are therefore confined at the outer edge of the indentation (see Fig. 4.3(a)), while the state with $\Delta k > 0$ originate at the edge of the potential mesa. At the bottom end of the phase shifter, where the two channels are recollected at the second QPC, the reflected component of the final state propagates back inside the indentation zone, so that it can not be reused as an input for a possible following stage of quantum processing. This is the main limitation of this solid-state implementation, and prevents the exploitation of Hall interferometers at bulk FF 1 for many-qubit architectures. Indeed, this geometry of the device requires an Ohmic contact, called *air bridge*, at the inner edge of the indentation/outer edge of the potential mesa to absorb the back-reflected channel.

To simulate the presence of the air bridge, that absorbs a wavefunction traveling along the \hat{y} -axis and limited along the \hat{x} -axis, we follow the proposal of Ref. [83], and introduce in the inner edge of the mesa, facing towards the indentation, the following potential:

$$V_{abs}(x, y) = iV_{abs}^0 \frac{\bar{\mathcal{F}}_\tau(x - x_1)\mathcal{F}_\tau(x - x_c)}{\cosh^2\left(\left(\frac{y - y_c}{d}\right)^2\right)}, \quad (4.20)$$

where d is the characteristic decay length, $\mathcal{F}_\tau(x - x_0)$ a Fermi-like function with smoothness τ and turning point x_0 , and V_{abs}^0 is the value on the top of the lead, which must be negative to absorb the wavefunction [13, 7]. By adding $V_{abs}(x, y)$ to the external potential, the reflected component of the electron state vanishes, and the final norm of the wavefunction at the end of the device provides the total transmission probability of the MZI ($|t_{00}|^2$).

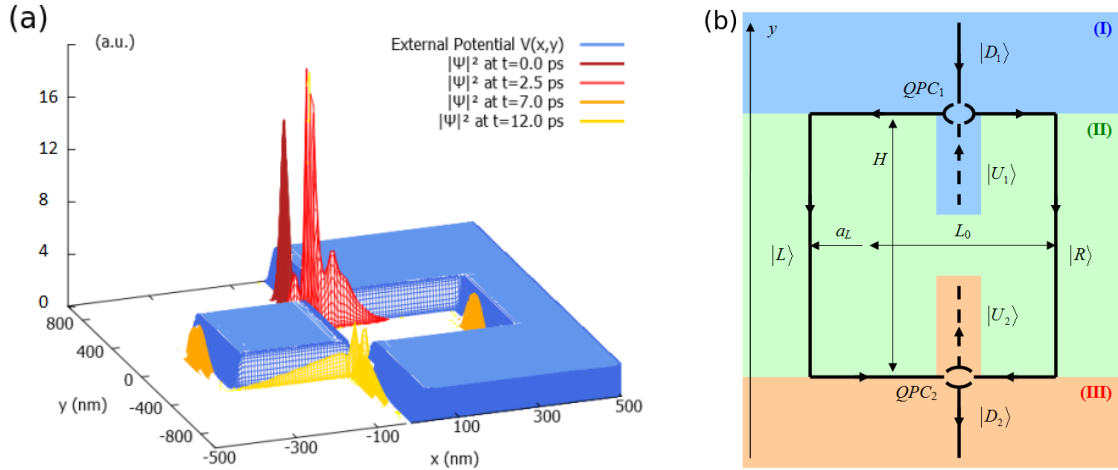


Figure 4.3: From Ref. [78]: (a) full-scale potential generated by top gates in the single-channel MZI of Ref. [7] (blue region) and dynamics of a single-electron wavepacket with $\sigma = 60$ nm; (b) scheme and geometrical parameters of the MZI to implement the 1D effective model. The device is divided into 3 sections: (I) in blue, where the channel $|D_1\rangle$ is filled, (II) in green, where two paths $|L\rangle, |R\rangle$ propagate after the first QPC, and (III) in orange, where the final channel $|D_2\rangle$ - the only one transmitted outside region II by the second QPC - is measured.

Together with preventing its scalability, the presence of the air bridge poses a technological limit to the miniaturization of the loop area, thus affecting the performances of Hall interferometers with counterpropagating channels. An efficient engineering of the MZI requires indeed a small loop area to observe the interference pattern with a large visibility [10]. Due to this topological limit, this design of the beam splitter and phase shifter have been mainly integrated into Fabry-Perot interferometers [90, 91, 92, 93, 94], while their experimental implementation in semiconductor MZIs is more recent [8, 15, 9].

4.1.3 Visibility of the MZI at bulk FF 1

In realistic implementations of Hall interferometers, where non-monochromatic beams of electrons or energy-broadened wavepackets are injected, the energy dependence of phase shifting must be also accounted for. Indeed, the line and surface integrals in Eq.(4.6) and Eq.(4.7) actually depend on the distribution of the edge states in the transverse direction of the device, due to the energy-dependence of the center $x_0^n(E)$. The interference pattern is so affected by *phase averaging* on large energy windows [95], which is detrimental for the visibility of the transmission amplitude, also in absence of decoherence induced by impurities or thermal smearing.

In the literature, the visibility of an electronic MZI is usually predicted by introducing a 1D effective model based on the analogy between edge states in 2D heterostructures and plane waves in 1D effective geometries. In Ref. [7], we study numerically a single-channel interferometer at bulk FF 1 and generalized this result for localized wavepackets of edge states, and compare the theoretical predictions to the results of full-scale numerical simulations in our time-dependent framework.

In the typical effective 1D scheme, the device is divided into three regions, as displayed in Fig. 4.3(b), containing the QPCs and the phase shifter. The initial state is a linear combination of plane waves $|D_1\rangle$ along the \hat{y} -direction, $\langle y|D_1\rangle = e^{iky}$:

$$|\psi_I\rangle = \int dk F(k) |D_1\rangle, \quad (4.21)$$

where $F(k) = N \exp(-\sigma^2(k-k_0)^2)$ is a Gaussian distribution centered at k_0 with spatial dispersion σ . By means of the scattering matrix method, the final transmission probability from channel 0 to channel 1 for a single k -component of the wavepacket at the end of the device reads[7]:

$$T(k) = |\langle D_2 | \Psi_{III} \rangle|^2 = T_0 - T_1 \cos(\Delta\chi - k_0 \Delta l), \quad (4.22)$$

where $T_0 = |r_0 r_1|^2 + |t_0 t_1|^2$ and $T_1 = 2r_0 r_1 t_0 t_1$, $\Delta\chi$ is the magnetic phase and Δl the relative length difference between the two channel paths.

We assume

- (i) energy-independent coefficients $r_i(k) = t_j(k) = \frac{1}{\sqrt{2}}$ of the half-reflecting beam splitter,
- (ii) an energy-independent phase $\Delta\chi - k_0 \Delta l$,

so that the total transmission probability for a Gaussian wavepacket can be computed analytically:

$$T = 2\pi \int dk |F(k)|^2 T(k) = T_0 - T_1 e^{-\frac{\Delta l^2}{8\sigma^2}} \cos(\Delta\chi - k_0 \Delta l). \quad (4.23)$$

The relative phase depends on the geometrical parameters of the MZI in Fig. 4.3(b):

$$\Delta\phi - k_e \Delta l = \left[\frac{e}{\hbar} H(a_L + L_0) \right] B + \varphi_0 \quad (4.24)$$

$$= \left[\frac{e}{\hbar} H B - 2k_e \right] a_L + \varphi_0, \quad (4.25)$$

and the transmission amplitude oscillates with the relative path difference a_L and with the intensity of the magnetic field B :

$$\begin{aligned} T(a_L, B) &= T_0 - T_1 e^{-\frac{(a_L - L_1)^2}{2\sigma^2}} \cos\left(\frac{e}{\hbar} B H(a_L + L_0) - 2k_e(a_L - L_1)\right) \\ &= T_0 - T_1 e^{-\frac{(a_L - L_1)^2}{2\sigma^2}} \cos(k_a a_L + \varphi_a) \end{aligned} \quad (4.26)$$

$$= T_0 - T'_1 \cos(k_B B + \phi_B), \quad T'_1 = T_1 e^{-\frac{(a_L - L_1)^2}{2\sigma^2}}. \quad (4.27)$$

This model predicts an oscillating behavior of the transmission probability as a function of the magnetic field B and geometrical parameter a_L . However, in presence of a localized wavefunction, $T(a_L)$ in Eq.(4.26) is also characterized by an exponential decrease in the visibility, which is not present in the magnetically-driven Aharonov-Bohm pattern $T(B)$ in Eq.(4.27).

Within our time-dependent approach, we explain the damping in the visibility by resorting to the dynamics of the two localized reflected and transmitted wavepackets inside the phase shifter [7, 28]. Coherently to its energy selectivity, the first QPC splits the initial wavefunction in a *reflected* and *transmitted* component that are localized in space. If the outer and inner edge of the phase shifter have the same length and smoothness, the reflected and transmitted wavepackets propagate with a very close group velocity. When $\Delta l \neq 0$ they recollect at the second beam splitter with a time delay induced by the path difference, and interfere according to their relative phase. For a larger path length difference, the two wavepackets do not overlap in space, so that the interference is suppressed. However, in contrast to the prediction of the simple theoretical model in Eq.(4.26), full-scale numerical simulations of the Aharonov-Bohm pattern in the MZI [7] show that the actual length scale for this process is larger than the spatial broadening of the wavepacket, σ . Such discrepancy is proved to decrease for $\sigma \rightarrow \infty$, that is when the electron wavepacket is well approximated by a delocalized plane-wave with a high resolution in energy. This trend is typical of scattering processes where assumption (i) is adopted, as usually done in literature.

We can increase the realism of our model by including the energy selectivity of the QPC. By resorting to the empirical coefficients $r(k)$, $t(k)$ in Eq.(4.11), we compute T_0 and T_1 as a function of the real-space broadening of the wavepacket and the geometrical parameters γ and α [20]:

$$T_0 = \frac{\sigma}{2\Sigma}, \quad T_1 = 2\frac{\sigma}{\Sigma} \exp\left(-\frac{\gamma\sigma^2}{2\Sigma^2}\right). \quad (4.28)$$

The visibility reads

$$\text{vis} = \frac{1}{4} \exp\left(-\frac{\gamma\sigma^2}{2\Sigma^2}\right). \quad (4.29)$$

$\Sigma^2 = \sigma^2 + \alpha^2/4\gamma$ represents therefore the length scale for the damping of the transmission amplitude induced by the energy selectivity of the QPC. The actual visibility is lower than the ideal value 1, which is restored only in the limit $\alpha/2\sqrt{\gamma} \ll \sigma$. This condition identifies the case with a delocalized plane wave as electron state, or a QPC with a selectivity smooth enough to neglect the energy dispersion of the wavepacket.

However, assumption (ii) is still present in this model. The validity of this approximation depends on the energy broadening of the injected wavepacket with respect to the smoothness of the energy dispersion $E_n(k)$ in the channel: for a large slope a , the states involved in the wavepacket have a dispersion that is large in energy, but small in space, so that $x_0(k)$ is expected to be almost independent from k . To reduce the impact of assumption (ii), the injection of single-electron wavepacket with a high energy resolution is clearly mandatory. However, phase averaging also depends on the miniaturization of the loop area, which is here limited by the presence of the Ohmic contact. Better performances are possibly achieved in a multichannel implementations of

the MZI, where the loop area can be decreased by almost 2 orders of magnitude with respect to the single-channel geometry [10].

4.1.4 Towards a new design: multichannel geometry at bulk FF 2

At bulk FF 2, the first two cyclotron-resolved edge states with Landau index $n = 0, 1$ and same chirality define the basis states. In this case, the implementation of the beam splitter requires elastic interchannel mixing, to be realized by a potential sharpness on the edge state path [96, 97], that extend on a scale of a few magnetic lengths [6]. For $B = 5$ T, this length is about 11 nm, which is certainly feasible with current technologies. In the present scenario, the two channels always copropagate at the same side of the confining barrier, thus solving the topological limit affecting nano-interferometers at bulk FF 1.

In the earliest experiments of electron beam splitters at bulk FF 2, abrupt potentials - called *nanofingers* - are inserted on the path of the edge states to generate interchannel scattering. However, without a fine shaping of its geometry, the potential dip acts as a beam splitter with a low transmission coefficient, far from the target of 50% for an ideal functioning of the MZI [6]. By means of arrays of nanofingers, the total transmission probability is increased in Quasi-Corbino [98, 99] and quasi-Fabry Perot interferometers [93]; however, these devices are still affected by a topological limit in scalability, as for counterpropagating edge states: the inner edge channel ($n = 1$) is confined inside the loop area, where it must be absorbed by an Ohmic contact.

Recent numerical simulations [6] show that a significant enhancement in the transmission probability can be achieved when the spatial periodicity among the nanofingers matches the *resonant condition*, as experimentally proven by using spin-resolved edge states. Here, an additional periodic in-plane magnetic field flips the edge spin to generate interchannel scattering [12].

However, due to the large dimensionality of the array, the two channels copropagate for long distances next to each other, and favor decoherence phenomena between the spin-resolved channels [100, 101], as already exposed in experiments on traditional MZIs [102, 103] and HOM geometries at bulk FF 2 [17, 104]. The injected electrons interact with the Fermi sea of the copropagating channel, and the charge is fractionalized between the two quantum rails [30]. This effect produces decoherence and significantly affects the visibility of the device [25].

4.2 Copropagating edge states for single-electron interferometry

Instead of using spin-resolved edge states, our research focuses on a multichannel MZI where the two copropagating channels belong to different Landau levels with $n = 0, 1$, as proposed by Giovannetti et al. in Ref. [10].

However, the application of the *resonant condition* for cyclotron-resolved edge states would require a much smaller spatial periodicity (few Å)[11], which is beyond the current limit of nanotechnology. The interchannel mixing is here generated by carefully designing a sharp potential dip to mimic an electron beam splitter. As a consequence, in our new geometry the length in which the two channels need to run on the same edge (i.e. the region at FF 2) is limited to the small beam splitter region, thus reducing the effect of the decoherence phenomena affecting copropagating spin-resolved edge states [25]. Furthermore, these interchannel interaction can be further quenched by introducing potential mesas to laterally separate the quantum rails [13, 31].

In the following, we will initially present our design of a steep and smaller geometry to realize coherent mixing between channel $n = 0$ and channel $n = 1$. The present electron beam splitter is devised to induce a quasi-flat energy selectivity on the energy broadening of the initial wavepacket. By adding the phase shifter and an absorbing potential, we then simulate self-electron interference in a full scale MZI with our time-dependent method [13]. Finally, we compare the numerical interference pattern in the transmission probability amplitude with the predictions of a simplified analytical model, and show that the present geometry presents higher performances with respect to the design based on a FF 1.

4.2.1 A new shape for the beam splitter: the potential dip

At bulk FF 2, the electron wavepacket is initialized in one of the two available channels with Landau index $n = 0, 1$ and scattered by a solid-state beam splitter to both Landau levels, as schematically depicted in Fig. 4.4(a).

Numerical simulations based on delocalized plane waves [96] show that a coherent edge mixing

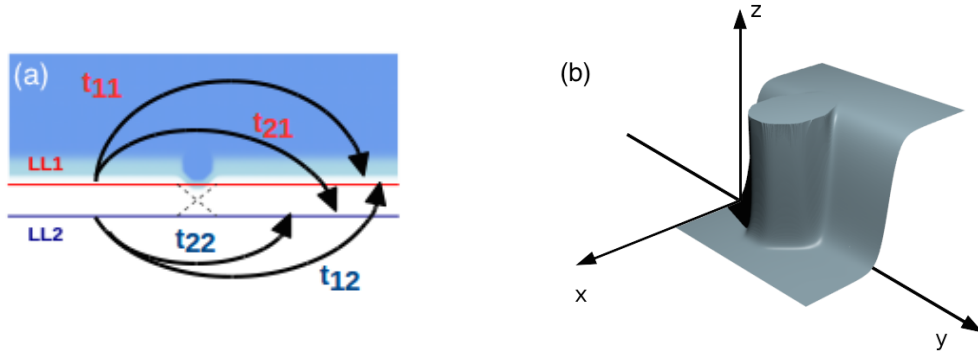


Figure 4.4: (a) Scheme of the scattering process at the beam splitter. The two horizontal lines represent the two edge channels involved in the process (red for the first Landau Level and blue for the second Landau Level), where carriers propagate from left to right. The coefficients t_{ji} label the transmission probabilities from the initial state i to the final state j . (b) Rendered picture of the potential V_{BS} profile modeling the beam splitter in Eq.(4.2.1) with $\Delta y = |y_0 - y_1| = 17.6$ nm, $\Delta x = |x_0 - x_1| = 20.0$ nm and $\tau = 0.55$ nm⁻¹.

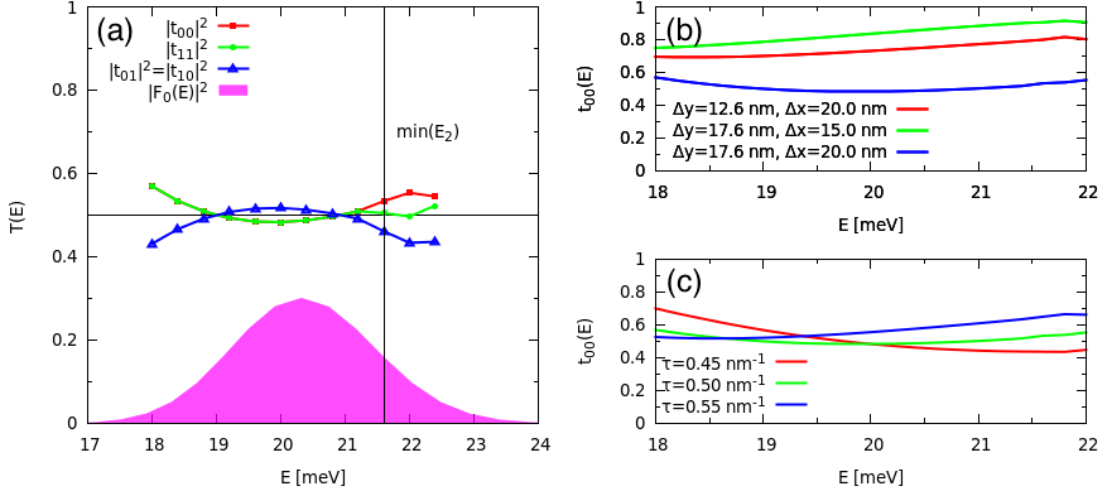


Figure 4.5: (a) Energy-dependent transmission probabilities between the two channels for the electron beam splitter modeled by Eq.(4.2.1) with $\Delta y = |y_0 - y_1| = 17.6$ nm, $\Delta x = |x_0 - x_1| = 20.0$ nm and $\tau = 0.55$ nm⁻¹. The black line identifies the minimum energy of the third Landau level ($n = 2$). (b) Energy-dependent transmission coefficient t_{00} for different sizes (Δx , Δy) and (c) smoothness τ of the potential dip in Eq.(4.2.1).

is achievable by introducing, on the path of the edge channels, spatial inhomogeneities on a scale smaller than the magnetic length l_m . Abrupt potential profiles scatter elastically an impinging plane wave with wavevector k , and redistribute the incoming wavefunction on the available states (the first two Landau Levels in the present case, with $n = 0$ and $n = 1$), with a transmission coefficient $t_{f,i}^{BS}$ from the initial $i = 0,1$ to the final $f = 0,1$ channel. This coefficient generally depends on the energy of the incoming state, on the value of the magnetic field B and on the shape of the local potential.

In presence of single-electron injection, or more generally of an energy bias, the above mechanism applies to all the states involved in the energy distribution of the injected particle. Therefore, the transmission probability of the potential profile mimicking the beam splitter must be constant, i.e. $|t_{ij}^{BS}(E)|^2 = 1/2$ with $i, j = 0,1$, for each energy component E of the electron wavepacket. By taking into account the energy dispersion of the scattered state, the sharpness must be carefully designed to maximize the overlap between the *reflected* $|\psi_R\rangle$ and *transmitted* $|\psi_T\rangle$ components of the wavepacket in the k -space. An ideal functioning of the MZI - a perfectly coherent device with an unitary visibility in the Aharonov-Bohm pattern - requires that the two contributions $|\psi_R\rangle$, $|\psi_T\rangle$ cancel each other completely, after the interference at the second beam splitter.

Fig. 4.4(b) displays our design of the potential profile $V_{ext}(x)$ at the beam splitter: this is a sharp squared potential dip smoothed at the corners with Fermi profiles, which is modeled by the following surface:

$$V_{BS}(x, y) = \frac{V_{bs}(1 + \exp[-\tau_{bs}(x - x_1)])^{-1}}{1 + \exp(\tau_{bs}(x - x_0))} \cdot \frac{(1 + \exp[-\tau_{bs}(y - y_1)])^{-1}}{1 + \exp(\tau_{bs}(y - y_0))} \quad (4.30)$$

where τ_{BS} is the smoothing parameter, and x_0, x_1 (y_0, y_1) define the position of the horizontal (vertical) edges of the beam splitter.

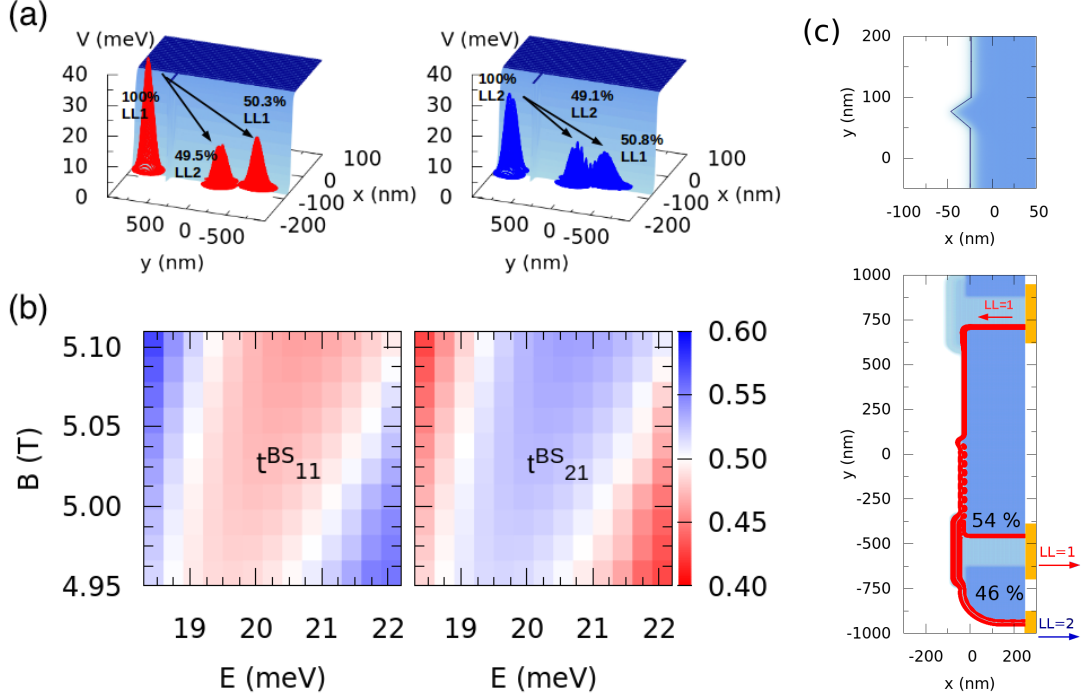


Figure 4.6: (a) Probability distribution of a single-electron wavepacket initialized in the first (red wavepacket) or second (blue wavepacket) Landau level before and after the scattering at the potential dip in Fig. 4.4(b), and corresponding integrated transmission probabilities. (b) Energy and magnetic dependence of the transmission coefficients t_{00} (left panel) and t_{10} (right panel) of the electron beam splitter in Fig. 4.4(b). Datas are computed by means of the *Kwant* software [85]. (c) Numerical simulation of the electron density probability in presence of a triangular potential dip, 40 nm long and with no extra smoothness. The beam splitter is embedded in a device with three leads, L_1 , L_2 and L_3 , that mimic the selective injection/absorption of electron current in the first or in the second Landau level [10, 12, 13]. The electron density probability after the beam splitter is a coherent superposition of the first and the second channel. In both cases, the beam is initialized in the first edge channel at $E = 20.4$ meV and it is scattered to the second channel with about $(50 \pm 4)\%$ probability.

Energy-dependence of a sharp potential dip at bulk FF 2

The energy-dependent transmission coefficient $t_{if}^{BS}(E)$ is computed by numerically simulating a single-electron scattering at the QPC, and resorting to the *wave-packet method*. We simulate the scattering of a Gaussian wavepacket of edge states ($|\psi_I\rangle$), initialized in $n = 0$ or in $n = 1$, with an energy broadening $\sigma_E \approx 1.5$ eV and central energy $E^0 = 20.4$ meV. The Fourier analysis of the scattered wavefunction after the beam splitter ($|\psi_{II}\rangle$) in the two scenarios provides the energy selectivity of the gate.

Figure 4.5(a) shows the energy dependence of the transmission probability $|t_{ji}^{BS}(E)|^2$ for $i, j = 0, 1$. Due to flux conservation, the interchannel (off-diagonal) transmission probabilities are the complementary of the interchannel ones. The transmission probabilities $|t_{ji}^{BS}(E)|^2$ are approximately constant in the energy distribution of the initial wavepacket with $n = 0$, defined by $|F(E)|^2$

in Fig. 4.5(a), thus showing its functioning as an ideal beam splitter. Fig. 4.5(b) displays the intrachannel transmission probability $|t_{11}^{BS}(E)|^2$ for different values of the geometrical parameters in Eq.(4.2.1), i.e. $\Delta x = x_0 - x_1$, $\Delta y = y_0 - y_1$ and τ ; it clarifies that $\Delta x = 20$ nm, $\Delta y = 17.6$ nm and $\tau = 0.5$ nm⁻¹ represent the best choice for our operating regime, characterized by a wavepacket initialized in $n = 0$ at $E^0 = 20.4$ meV and in presence of a perpendicular magnetic field with value $B = 5$ T.

The top panel of Fig. 4.6(a) shows the single-electron density probability before and after the scattering at the potential dip. In our operating regime, the Gaussian wavepacket initialized in the (left) $n = 0$ or (right) $n = 1$ channel is transmitted/reflected with an integrated probability about 1/2. Therefore, the scattered wavefunction after the beam splitter is well approximated by a coherent superposition of two wavepackets belonging to the first and to the second Landau level, with a probability about 0.5:

$$|\psi_{II}\rangle = c_0|\psi_0\rangle + c_1|\psi_1\rangle, \quad (4.31)$$

with $|c_0|^2 \approx 1/2$ and $|c_1|^2 \approx 1/2$ for both scenarios. Here, we observe a small discrepancy between the sum of the two scattered intensities and unity. This is due a small scattering to the edge states in the third Landau level: its minimum energy, $E_{n=2} = \frac{5}{2}\hbar\omega_c = 21.6$ meV (black line in Fig. 4.5(a)) is indeed covered by the high-energy components of our initial wavepacket.

Magnetic-field dependence

The magnetic-field dependence of the transmission coefficient t_{ji}^{BS} is instead provided by means of stationary simulations with the Kwant software [85]. This library provides the scattering matrix of an external potential V_{ext} - the sharp potential dip in the present case - for a given energy of injection through the `smatrix.transmission()` method. We compute the probability $|t_{ji}^{BS}(E, B)|^2$ in the range of values B for which Aharonov-Bohm oscillations in the transmission amplitude at the output of the MZI are expected, together with tuning the energy E according to the broadening of our initial wavepacket. A map of $|t_{f,i}^{BS}(E, B)|^2$ is displayed in Fig. 4.6(c).

The transmission probability between two different channels slowly increases with the magnetic field. We therefore expect that the visibility of Aharonov-Bohm oscillations will slightly depend on the value of B , in contrast with the prediction of stationary models for both single and multi-channel implementations of the MZI (see Eq.(4.27) and Eq.(4.55), respectively). The magnetic-field dependence of the transmission amplitude is later confirmed by our dynamical simulation of the single-electron scattering in a full-scale MZI at bulk FF 2 [13] (see Sec. 4.2.3).

Alternative shapes for the beam splitter

The realization of a coherent superposition of two localized states in the first and second Landau levels after the electron beam splitter with almost equal probabilities is possible also with alternative shapes of the potential dip. As an example, in Fig. 4.6(c), we map the density probability of a single-energy electron state in presence of a triangular potential dip. The beam splitter is inserted into a simple device with two leads for a selective injection of the first or second edge channel and its selective absorption.

The oscillations of the electron probability density between the two channels in the 2D real-space domain prove that a coherent superposition is generated from the scattering process. As for the sharp potential dip in Fig. 4.4(b), the central energy of the wavepacket is selected to induce a 50% scattering probability between the two channels. In present calculations, for both rectangular and triangular potential dips the scattering probability from the first to the second channel computed with Kwant software shows a small variation, around 5%, for an energy dispersion of 0.2 meV, which is comparable to the energy uncertainty usually obtained in experiments[17].

4.2.2 The mesa structure for phase shifting

At bulk FF 2, the output basis states copropagate at the same side of the device, where their energy dispersion $E_n(k)$, with $n = 0, 1$, depends on the local smoothness of the confining potential. At a given energy E , the two different wavevectors k^n with $n = 0, 1$ involve the localization of the edge states in the transverse direction, $\varphi_{n,k}(x)$, around separated centers x_0^n .

Then, to induce a tunable phase shift between the two paths, we further force this spatial separation by introducing an external potential that locally modifies the bandstructure, as reported in the bottom panel of Fig. 4.7(a). Here, a potential step in the transverse direction of the 2DEG shifts upwards the first Landau level, while the second one is pushed inside the bulk region. While crossing this mesa, the energies involved by the wavepacket are localized at the outer edge of the potential mesa for the second Landau level, while the first Landau level is localized at the inner edge, next to the lateral confining barrier.

From a technological perspective, this corresponds to the application of top gates that locally vary the depletion of the 2DEG, or equivalently the bulk FF, as depicted in Fig. 4.7(b). The width of the potential step controls the relative path of the two channels, Δl , together with the area enclosed by them.

We remark that this geometry solves the scalability issue of the previous phase shifter: the two channels are both available as an output of the quantum gate. However, it requires a careful engineering in order to avoid additional interchannel mixing. To this aim, we devise the phase shifter with the following smooth external potential:

$$V_G(x, y) = V_s \mathcal{F}_{\tau_s}(x - x_s) + V_b \mathcal{F}_{\tau_b}(x - x_b), \quad (4.32)$$

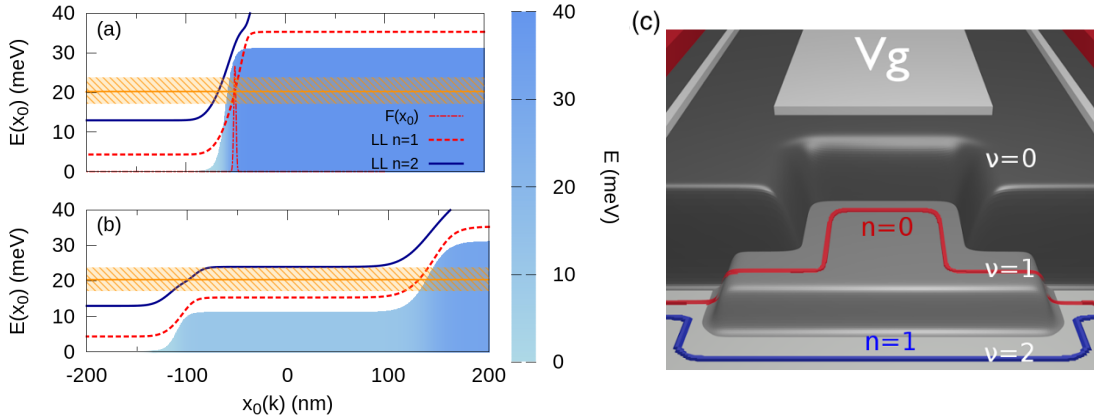


Figure 4.7: (a) Bandstructure $E_n[x_0(k)]$ of the device at $y = -800$ nm (region I) for $n = 0$ and $n = 1$ compared to the potential profile (blue shaded area). The orange striped interval defines the energy broadening of the initial wavepacket. Only the first Landau Level is filled with $F(x_0)$, as illustrated by the dotted Gaussian curve around $x_0 = -50$ nm. (b) Band structure of the device at $y = -200$ nm (region II) and potential profile of the mesa structure. The energy broadening fills the two edge channels at the two sides of the potential, inducing two different paths for $n = 0$ (red dashed line) and $n = 1$ (blue solid line), localized around $x_0 = 120$ nm and $x_0 = -100$ nm, respectively. (c) Potential profile of the confining barrier for the phase shifter based on copropagating edge states. The additional mesa with local FF 1 separates the first edge channel (red line, running along the inner edge) to the second one (blue line, running along the outer edge).

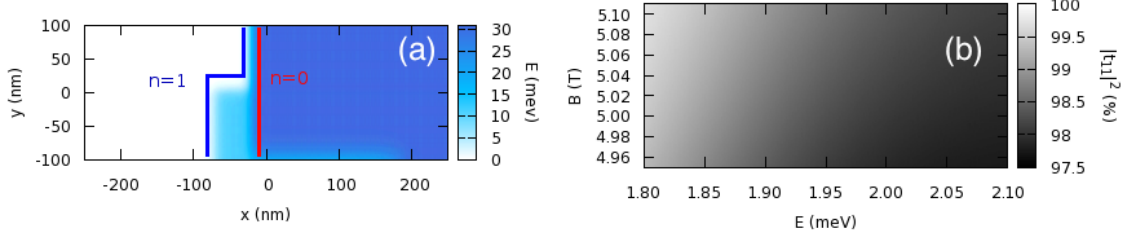


Figure 4.8: (a) 2D map of the external potential profile V_{ext} at the edge of the mesa structure. The dark blue region has bulk FF 0, the light blue region bulk FF 1 and the white region bulk FF 2, so that the two channels (solid lines) are separated and follow different paths. (a) 2D map of the transmission probability from the first to the first channel $|t_{00}(E, B)|^2$ computed with the **Kwant** software.

where the local curvature τ_s must ensure an adiabatic separation of the two edge channels [6], with a negligible mixing among them. This is achieved by selecting $V_s = 11$ meV, $V_b = 31$ meV, $\tau_b = 0.25$ nm $^{-1}$ and $\tau_s = 0.2$ nm $^{-1}$, as proved by support calculations based on the use of **Kwant** software: Fig. 4.8 shows the transmission probability $|t_{12}(E, B)|^2$, for an electron state with a well-defined energy E in the present geometry: in this operating regime, interchannel scattering from the first to the second Landau level is clearly negligible.

Finally, to design a multichannel MZI at bulk FF 2, we need to account for the different group velocities of the electrons propagating in the two cyclotron-resolved channels [13]. The bandstructures of the first and the second Landau level differ in the inner and outer edge of the mesa, where the *reflected* and *transmitted* wavepackets are localized. Even with no path difference, the two components of the wavefunction do not recollect simultaneously at the second beam splitter, thus reducing the visibility of the interference pattern. In detail, $v_g^0 > v_g^1$. Therefore, we introduce an indentation in the outer confining potential of the phase shifter (region II in Fig. 4.9), so that the larger length of the channel $n = 0$ compensate this effect. Additionally, we increase the smoothness of transverse potential profile inside the indentation, and then also the group velocity of the wavepacket in $n = 0$.

4.2.3 Electron self-interference in the multichannel MZI

The self-interference of a single-electron wavefunction has initially been observed in the double-slit experiment, and reveals the wave-particle dual nature of the electron wavefunction in quantum mechanics. Double-slit experiments have the potential to directly measure the phase of electrons, but are difficult to perform under strong magnetic fields, due to the formation of skipping orbits that breaks the symmetry of the interferometer (see Sec. 1.2). With a suitable design of a solid-state beam splitter and phase shifter, the 1D chirality of edge states provides instead the ideal playground to implement an electron MZI.

Together with unraveling the coherence of edge states in the IQH regime, self-interference in a Mach-Zehnder geometry can also be exploited to perform basic quantum operations, while the concatenation of these devices allows to generate entangled states, as in a conditional phase shifter, or to devise many-qubit architectures as the Hanbury-Brown-Twiss interferometer.

In the following, we detail the geometry adopted to simulate a full-scale MZI in the IQH regime, and prove that our scalable design of the device and fine tuning of the beam splitter ensures a large visibility of the self-interference pattern by comparing the predictions of a simplified 1D analytical model with numerical data from the Split-Step Fourier method.

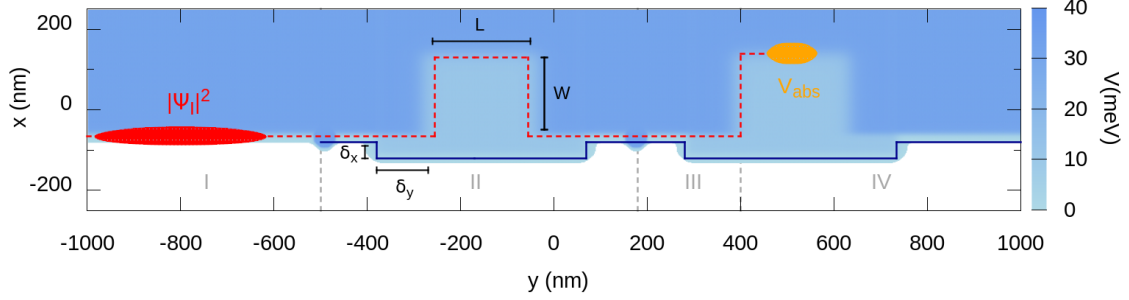


Figure 4.9: Top view of the two-channel MZI and electron probability density of the initial wavepacket $|\Psi_I|^2$ in the first edge channel with $n = 0$. The dashed red ($n = 0$) and solid blue ($n = 1$) lines describe the intended path of the two edge channels. The four regions of the device (I-IV) are indicated. Region IV contains the measurement apparatus, where the imaginary potential V_{abs} (gold shape at $y = 500$ nm) absorbs the first Landau Level. Only the electronic wavepacket in the second channel reaches the right side of the device, where the transmission measurement is performed. The central energy of the wavepacket is $E^0 = 20.4$ meV.

Full-scale numerical simulations of the 2D multichannel MZI

Figure 4.9 shows the potential profile V_{ext} (blue area) implementing the multichannel MZI in the IQH regime proposed in Ref. [10]. The device is divided into four regions, where the wavepacket, highlighted in red, propagates.

- *Region I* is the initialization region of the electron wavepacket and it is translationally invariant in the \hat{y} -direction. The exact shape of the edge states generated by our design of V_{ext} are extracted by using LAPACK routines, and then combined in a Gaussian wavepacket with $E^0 = 20.4$ meV and $\sigma = 60$ nm. As reported in the top panel of Fig. 4.7(a) the energy broadening of the simulated wavepacket presents available edge states in both channels, $n = 0, 1$. However, we initialize the electron state in $n = 0$, by selecting $F_n(k) = F_0(k)\delta_{n,0}$, so that the Gaussian wavepacket does not contain initially edge states from the second Landau level.
- *Region II* incorporates the core of the interferometer: two electron beam splitters enclose the phase shifter to realize the self-interference. The shape of the beam splitter is engineered as the sharp potential dip in Fig. 4.4(b), that produces a smooth energy selectivity around 50%. The phase shifter is a mesa in the potential landscape with local FF 1 (light blue shaded region) and a smoothness that prevents interchannel mixing. The tunable length of the two electron paths varies with the length (L) and width (W) of the mesa in Fig. 4.9.

Here, the *reflected* and *transmitted* components of the wavefunction propagate with a group velocity v_g^n , that depends on the transverse potential profile of the mesa and on the Landau index n . The overlap between the two wavepackets at the second beam splitter is therefore affected by the time difference between the propagation in the first and the second channels, inside region II: the highest overlap - and consequently visibility - is expected only when the two paths Δs_n , each one divided by the corresponding group velocity, i.e. $\Delta s_n/v_g^n$, are the same for channel 0 and channel 1. A time delay between the two components of the wavefunction is here present, and it decreases exponentially the transmission amplitude from the first to the second channel.

- Finally, *region III* and *region IV* contain an additional mesa with an imaginary potential, to mimic an absorbing lead, which is transparent to the second channel only. The density

probability of the wavefunction at the end of the device provides the final transmission probability from the first to the second channel, P_{10} . By varying the magnetic field B , or the loop area $A = W \cdot L$, Aharonov-Bohm oscillations originates in the total transmission amplitude, P_{10}^{tot} .

With regards to the full-scale numerical simulations, we assume GaAs parameter $m^* = 0.067m_e$ for the hosting material, $\sigma = 60\text{nm}$ for the initial wavepacket and $n = 0$ at initial time. The geometry of the device is characterized by $V_b = 0.031\text{ eV}$, $\tau_b = 0.25\text{ nm}^{-1}$ for the confining potential, $|x_1 - x_2| = |y_1 - y_2| = 20\text{ nm}$ and $\tau_{BS} = 0.5\text{ nm}^{-1}$ at the beam splitter, $V_s = 0.011\text{ eV}$, $\tau_s = 0.2\text{ nm}^{-1}$ for the mesa structure and $V_{abs}^0 = -100\text{ eV}$, $d = 30\text{ nm}$ for the absorbing potential. According to the discretization conditions entailed by the Split-Step Fourier method, we set $\delta x = \delta y \simeq 0.5\text{ nm}^{-1}$ and $\delta = 10^{-16}\text{ s}$.

1D analytical model based on plane wave with a pseudo-spin

We initially predict the transmission probability P_{10}^{tot} of our multi-channel MZI with a simplified analytical 1D model for single-electron interferometry. This is grounded on the description of edge channels as strictly one-dimensional systems and the application of logic gates trough scattering matrices.

In this effective 1D geometry, an edge state of the n^{th} Landau Level, $\varphi_{n,k}e^{iky}$ is mapped by a plane wave along the \hat{y} -direction, $|k, n\rangle$, with the energy dispersion of the corresponding Landau Level, $k(E, n)$:

$$\varphi_{n,k}(x)e^{iky} \rightarrow |k, n\rangle, \quad (4.33)$$

where $\langle y|k, n\rangle = e^{iky}$ is adimensional. To describe a localized wavepacket on the \hat{y} -direction, we initially compute the wavefunction by combining different edge states of the $n = 0$ level, with the Gaussian weight $F(k)$ of Eq.(3.2):

$$|\Psi_I\rangle = \int dk F(k) |k, n = 1\rangle = \int dE F(k(E, 1)) \left[\frac{dk}{dE} \right]_{n=0} |E, 0\rangle. \quad (4.34)$$

$|E, n\rangle$ denotes $|k(E, n), n\rangle$ for brevity, and $|\Psi_I\rangle$ ($|\Psi_{III}\rangle$) is the one-dimensional wavefunction in region I (III). Within this simplified model, the Landau index $n = 0, 1$ is a pseudo-spin degree of freedom.

The application of the scattering matrices for the beam splitters (\hat{B}) and the phase shifter ($\hat{\Phi}$) provides the wavepacket in region III:

$$\begin{aligned} |\Psi_{III}\rangle &= \hat{B}\hat{\Phi}\hat{B}|\Psi_I\rangle, \\ &= \int dE F(k(E, 0)) \left[\frac{dk}{dE} \right]_{n=0} \hat{B}\hat{\Phi}\hat{B}|E, 0\rangle. \end{aligned} \quad (4.35)$$

Note that in this description the energy dependence of the transmission coefficients is neglected for simplicity. In region IV an absorbing potential collects the contribution of the first Landau Level, so that at the end of the device only the component of the wavefunction in $n = 1$ survives. For a single-energy state E' :

$$P_{10}(E') = |\langle E', 1 | \Psi_{III} \rangle|^2 = \left| \int dE F(k(E, 0)) \left[\frac{dk}{dE} \right]_{n=0} \langle E', 1 | \hat{B}\hat{\Phi}\hat{B} | E, 0 \rangle \right|^2. \quad (4.36)$$

By assuming *elastic* scattering of each wavevector component,

$$\langle E', 1 | \hat{B}\hat{\Phi}\hat{B} | E, 0 \rangle = \delta(E - E') \langle E', 1 | \hat{B}\hat{\Phi}\hat{B} | E, 0 \rangle, \quad (4.37)$$

the total transmission probability is computed by integrating over the whole range of energies:

$$P_{10}^{tot} = \int dE' P_{10}(E') = \int dE' \left| F(k(E', 0)) \left[\frac{dk}{dE'} \right]_{n=0} \right|^2 |\langle E', 1 | \hat{B} \hat{\Phi} \hat{B} | E', 0 \rangle|^2. \quad (4.38)$$

In order to solve Eq.(4.38), we consider the general 2x2 matrix form of operators \hat{B} and $\hat{\Phi}$ on the pseudo-spin basis:

$$\hat{B} = \begin{pmatrix} b_{00} & b_{01} \\ b_{10} & b_{11} \end{pmatrix}, \quad \hat{\Phi} = \begin{pmatrix} e^{i\varphi_0} & 0 \\ 0 & e^{i\varphi_1} \end{pmatrix}. \quad (4.39)$$

The phase φ_i ($i = 1, 2$) includes the contributions of the magnetic (χ_i) and the dynamical (ξ_i) phases

$$\varphi_i = \frac{1}{\hbar} \int_i (p - qA) \cdot ds = \xi_i + \phi_i, \quad (4.40)$$

where the integration is performed along the path of the edge channel i on the mesa. The transmission coefficients b_{ij} are related by the probability flux conservation:

$$|b_{ii}|^2 + |b_{ij}|^2 = 1, \quad (4.41)$$

$$|b_{ij}|^2 = |b_{ji}|^2, \quad (4.42)$$

$$|b_{ii}|^2 = |b_{jj}|^2. \quad (4.43)$$

For an ideal functioning of the device, we tune the beam splitter to 50% of transmission, $|b_{ij}|^2 = 1/2$, so that the coefficients b_{ij} differ only by a phase factor φ , e.g. $b_{11} = b_{00} e^{i\varphi}$.

The wavefunction in region III for a single-energy component in the first channel, $|\psi_I\rangle = |E, 0\rangle$, is computed:

$$|\psi_{III}\rangle = \hat{B} \hat{\Phi} \hat{B} |E, 0\rangle \quad (4.44)$$

$$= (b_{00}^2 e^{i\varphi_0} + b_{01} b_{10} e^{i\varphi_1}) |E, 0\rangle + (b_{10} b_{00} e^{i\varphi_0} + b_{11} b_{10} e^{i\varphi_1}) |E, 1\rangle, \quad (4.45)$$

and then projected on a generic $|E', 1\rangle$ state to provide the single-energy probability:

$$\begin{aligned} |\langle E', 1 | \psi_{III} \rangle|^2 &= |\langle E', 1 | \hat{B} \hat{\Phi} \hat{B} | E, 0 \rangle|^2 \\ &= |b_{00} b_{10}|^2 |e^{i\varphi_0} + e^{i\varphi} e^{i\varphi_1}|^2 \\ &= 2 |b_{00} b_{10}|^2 [1 + \cos(\Phi)], \end{aligned} \quad (4.46)$$

with $\Phi = \varphi + \varphi_1 - \varphi_0$.

Finally, the *total* transmission probability

$$P_{10}^{tot} = \int dE' P_{10}(E') = 2 |b_{00} b_{10}|^2 \int dE' \left| F(k(E', 0)) \left[\frac{dk}{dE'} \right]_{n=0} \right|^2 [1 + \cos(\Phi)]. \quad (4.47)$$

is computed by integrating over the energy broadening of our operating regime.

In order to define a gauge-independent dynamical phase, we consider a quasi-linear dispersion of the two Landau Levels around the central energy of the wavepacket E^0 , and we rewrite p in terms of the constant energy E and of the group velocity v_i^{II} in region II:

$$\xi_i = \frac{1}{\hbar} \int_i p \cdot ds = \frac{1}{\hbar} \int_i \frac{E - E^0}{v_i^{\text{II}}} ds = \frac{E - E^0}{\hbar v_i^{\text{II}}} \Delta S_i, \quad (4.48)$$

where ΔS_i is the length of the path of channel i in the domain of the mesa. Note that, if a linear dispersion is appropriate for the second Landau Level, it is a stronger approximation for the first

one. Such assumption is the main source of discrepancy between our exact numerical results and the present theoretical model.

Furthermore, if we apply the Stokes theorem for the magnetic contribution χ_i of Eq.(4.40):

$$\chi_i = -\frac{1}{\hbar} \oint_i qA \cdot ds = \frac{eB}{\hbar} \int_{\S_i} (\nabla \times A) \cdot ds \quad (4.49)$$

we can rewrite the total phase as

$$\Phi = \varphi + \frac{E - E^0}{\hbar} \left(\frac{\Delta S_1}{v_1^{\text{II}}} - \frac{\Delta S_0}{v_0^{\text{II}}} \right) + \frac{eB\mathcal{A}}{\hbar}, \quad (4.50)$$

with $\mathcal{A} = L_x \cdot L_y + (2\delta_y + L_y) \cdot \delta_x$, the area enclosed by the paths of the two channels, which is tuned by changing the width W of the mesa along the \hat{x} -direction (see Fig. 4.9), $\Delta S_0 = 2\delta_y + 2L_x + L_y$, and $\Delta S_1 = 2\delta_x + 2\delta_y + L_y$. By assuming a linear dispersion $k(E)$ for the first Landau level in region I, $dk/dE = 1/v_g^{\text{I}}$, we can perform the integration over the energy in Eq.(4.38), and compute the total transmission probability from channel 1 to channel 2:

$$P_{10}^{\text{tot}} = 2|b_{00}b_{10}|^2 \int dE \frac{e^{-2\frac{\sigma^2}{(v_g^{\text{I}})^2}}}{(v_g^{\text{I}})^2} [1 + \cos(\Phi)] \quad (4.51)$$

$$= \frac{1}{2} \left(1 + \exp \left(-\frac{(\frac{\Delta S_1}{v_1^{\text{II}}} - \frac{\Delta S_0}{v_0^{\text{II}}})^2}{8\sigma^2/(v_0^{\text{I}})^2} \right) \cos(\Phi') \right), \quad (4.52)$$

where $\Phi' = \frac{eB\mathcal{A}}{\hbar} + \varphi$.

The argument of the cosine exposes the dependence of P_{10}^{tot} on the magnetic field B and on the width W of the mesa. Indeed, according to the geometry of the step potential in Fig. 4.9, the mesa has an area $\mathcal{A} = W \cdot L + (2\delta_y + L) \cdot \delta_x$, such that the two following definitions of Φ' hold:

$$\Phi' = \left(\frac{eBL}{\hbar} \right) W + \Phi_0 = k_W W + \Phi_0 \quad (4.53)$$

$$= \left(\frac{e\mathcal{A}}{\hbar} \right) B + \Phi_1 = k_B B + \Phi_1, \quad (4.54)$$

where $\Phi_0 = \varphi + \frac{eB}{\hbar}(2\delta_y + L)\delta_x$ and $\Phi_1 = \varphi$. Besides, according to Fig. 4.9, the paths of the two channels are equivalent to $\Delta S_0 = 2\delta_y + 2W + L$ and $\Delta S_1 = 2\delta_x + 2\delta_y + L$. By using an effective standard deviation $\Sigma = \sigma v_0^{\text{II}}/v_1^{\text{I}}$, the total transmission probability is

$$P_{10}^{\text{tot}} = \frac{1}{2} \left(1 + \exp \left(-\frac{(W - W_0)^2}{2\Sigma^2} \right) \cos(\Phi') \right), \quad (4.55)$$

with W_0 containing the geometrical correction to the paths of the two edge channels, and $\Phi' = \frac{eBS}{\hbar} + \varphi$ that varies with the magnetic field B or the width of the mesa W , related to the loop area \mathcal{A} .

The Aharonov-Bohm pattern

Finally, we perform the numerical simulations of single-electron interference in the full-scale MZI by means of the Split-Step Fourier method. We vary the magnetic field between 4.94 and 5.06 T at a fixed width of the mesa, $W = 200$ nm, and provide the magnetically-driven Aharonov-Bohm pattern in the transmission amplitude from the first to the second channel $P_{10}^{\text{tot}}(B)$. By tuning the

$P_{21}^{tot}(B)$			$P_{21}^{tot}(W)$		
expression	Numerical fit	Theoretical model	expression	Numerical fit	Theoretical model
A_B	0.462 ± 0.004	0.5	A_W	0.460 ± 0.002	0.5
A_B^*	0.374 ± 0.005	0.5	A_W^*	0.400 ± 0.004	0.5
k_B (T $^{-1}$)	127.4 ± 0.4	110	k_W (nm $^{-1}$)	1.750	1.9
B_1 (T)	4.982 ± 0.001	-	L_1 (nm)	192.5	-
			Σ (nm)	21.7 ± 5	18.3
			L_0	193.8 ± 0.3	-

Table 4.1: Comparison between fitting parameters for the results of exact numerical simulations and the corresponding parameters of the theoretical model of Sec. 4.2.3. The two cases of Fig. 4.10 are considered, namely with a variable magnetic field (left column) or mesa width (right column).

width of the mesa W between 50 and 350 nm at fixed magnetic-field, $B = 5$ T, we also observe the interference pattern of $P_{10}^{tot}(W)$ induced by a variation of the dynamical phase difference.

The transmission probability provided by our exact time-dependent method is finally compared to Eq.(4.55) in Fig. 4.10. The transmission probability from the first to the second channel can be generally rewritten as

$$P_{10}^{tot}(B) = A_B + A_B^* e^{-\frac{(W-W_0)^2}{2\Sigma^2}} \cos(k_B(B - B_0)) \quad (4.56)$$

for a variation of the magnetic field B [Fig. 4.10(a)], and

$$P_{10}^{tot}(W) = A_W + A_W^* e^{-\frac{(W-W_0)^2}{2\Sigma^2}} \cos(k_W(W - W_0)) \quad (4.57)$$

for a variation of the width W of the mesa region [Fig. 4.10(b)]. These equations are used as fitting functions for the numerical results provided by our time-dependent approach; a comparison between predicted and numerical values is presented in Tab. 4.1.

Consistently with the wavepacket nature of our single-electron state, a variation of the width W affects the oscillations of the transmission probability with an exponential damping, which arises when the two wavepackets in the region of the mesa reach the second potential dip with a time delay. For a width W large enough, the two wavepackets do not overlap anymore and the interference is quenched, as predicted and also in the single-channel implementation of the device where localized charges are injected[7, 20, 28].

However, the length scale Σ for the damping in the visibility in the present case is given by

$$\Sigma = \sigma \frac{v_0^{II}}{v_0^I}, \quad (4.58)$$

and it decreases with the standard deviation of the initial wavepacket σ . The length scale Σ does not directly depend on the geometrical parameters of the beam splitter, but on the dynamics of the wavepackets in the ground channel in region I and region II. In fact, a smoother slope of the indentation in region II reduces the group velocity v_0^I above the mesa with respect to same in the initialization region, v_0^I . This can be interpreted as an effective dilatation of the width W in Eq.(4.55), that determines a larger phase difference.

Furthermore, Fig. 4.10(b) shows that at the two margins of the Aharonov-Bohm pattern the amplitude oscillations are larger than the predicted ones. The analytical function $P_{10}(W)$ is a good approximation for the interference pattern in a full-scale MZI only when the asymmetry between the two electron paths in the loop area is small, as shown in the inset of Fig. 4.10(b).

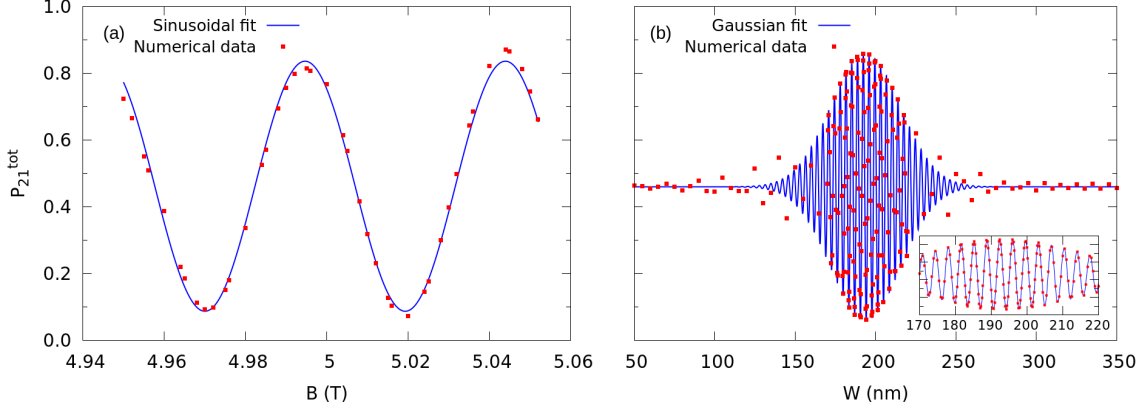


Figure 4.10: AB oscillations of the transmission amplitude at the end of the device. (a) The plot shows the behavior of P_{10}^{tot} as a function of the magnetic field for the numerical simulation (dots) and its sinusoidal fit (blue line) based on the analytical of the previous section (Eq.(4.55)). A fixed path mismatch for the two channels, $W = 200$ nm, is simulated. (b) Aharonov-Bohm oscillations as a function of the width of the mesa W at $B = 5$ T. Numerical data (dots) and the Gaussian fit (solid line) based on the theoretical model show a good agreement only in the central region (inset).

This discrepancy follows from the assumption, in our analytical model, of a linear bandstructure for $n = 0, 1$ in the loop area. This is indeed a good approximation for the second channel alone. In presence of a linear bandstructure, the derivative of $k(E, n)$ in Eq.(4.38),

$$\frac{dk(E, n)}{dE} = \frac{1}{v_g^I} \quad (4.59)$$

does not depend on the energy, and the $|F(k(E, n))|^2/v_g^I$ is a *renormalized* Gaussian weight function. Moreover, we neglect the energy dependence of the dynamical phase ΔS_i in region II, thus assuming that all the edge states in the wavepacket follow the same path, regardless their energy. The validity of these approximations clearly depend on the energy broadening of the simulated wavepacket.

Regarding the magnetically-driven Aharonov Bohm pattern in Fig. 4.10(a), we observe a slight increase in the transmission amplitude, which is not predicted by the analytical 1D model, which assumes an unitary module for the transmission coefficients in the $\hat{\Phi}$ matrix and neglects the magnetic dependence of the coefficients in the \hat{B} matrix. In a realistic scenario, a decrease of the magnetic field B reduces the energy resolution between the Landau Levels, thus enhancing additional interchannel scattering at the edges of the phase shifter, as confirmed by the stationary simulations with Kwant in Fig. 4.8 and by the numerical simulations of Ref. [96]. Region II does not act anymore as an ideal MZI, and the visibility is reduced. Moreover, this effect has an interplay with the magnetic dependence of the beam splitter coefficients b_{ij} (see Fig. 4.6(b)). A decrease in the value of the magnetic field modifies the smoothness of the quasi-flat energy selectivity, thus reducing the validity of the ideal condition $|b_{ij}| = 0.5$ for the most relevant components in our wavepacket.

In conclusion, with the geometry in Fig. 4.9 for a full-scale MZI, we measure a maximum visibility $\text{vis} = 0.87$, when injecting Gaussian wavepackets with $\sigma = 60$ nm and $E^0 = 20.4$ meV. This value is larger than the same in the single-channel geometry [7], mainly due to the weaker

energy selectivity of the present beam splitter compared to the QPC. We further stress that, in our simulations, the energy broadening of the Gaussian single-electron state is larger than its typical experimental value [17, 64], thus ensuring that the selectivity of the beam splitter is still adequate - and actually even better optimized - for larger wavepackets.

Together with increasing the visibility, the use of a simple potential dip with a small spatial extension (about 20 nm) prevents decoherence effects induced by charge fractionalization. If, according to Ref. [30], the length over which fractionalization arises depends on the emission time and group velocity of the wavepacket through $L_{frac} = v_g \cdot \tau_e$, for a Gaussian wavepacket with $\sigma = 100$ nm, an energy broadening $\Gamma = 1$ meV, velocity $v_g = 100$ nm/ps and then an emission time $\tau_e = \hbar/\Gamma$, the length of charge fractionalization results to be $L_{frac} \approx 0.07 \mu\text{m}$, which is larger than the length of the beam splitter region of our device. We expect that for larger emission times, as the ones typically exploited for experimental implementations of SESs [17], L_{frac} is even wider (typically $3 \mu\text{m}$ [30]), while the size of our beam splitter is even more optimized to produce a 50% interchannel mixing.

We also remark that, in order to reduce the length of copropagation, the two channels can be further separated by using top gates, as in Ref. [12]. This is achievable with a proper depletion of the 2DEG, to reduce locally the bulk FF to 1, as in the loop area of the full-scale MZI. In Ref. [13] we propose a protocol for the selective injection and absorption of edge channels: one lead, L_1 , has a local FF one and injects the electron in the first edge channel, while two leads, L_2 at FF 1 and L_3 at FF 2 adsorb the first and second edge channels, respectively. The introduction of top gates, together with the use of our type of beam splitter, could quench significantly the effect of interchannel interaction and avoid, or at least strongly reduce, this source of decoherence, without affecting the performances of the device.

Finally, we remark that the present geometry solves the scalability problem of the single-channel MZI, and potentially enables its concatenation in series. This property is essential to implement two-qubit interferometers and integrate this device in complex quantum computing architectures, as the solid-state implementation of the Conditional Phase Shifter that we present in Chapter 6.

Chapter 5

Two-electron bunching in the HOM interferometer

In this section we present the dynamics of two-fermion antibunching in a solid-state HOM interferometer, where the electrons are partitioned by a QPC, acting as an half-reflecting beam splitter. The two interfering charges are injected at the opposite inputs of the device, as single-charge Gaussian wave packets of edge states in the IQH regime at bulk FF 1. We compute the bunching probability P_b at the outputs and characterize the minimum of the Pauli dip in presence of exchange and/or Coulomb interaction, for a number of strongly-localized wavepackets with different values of the real-space broadening σ . By introducing the screening in electron-electron repulsion, we analyze the effect of charge localization on the non-zero bunching probability for the

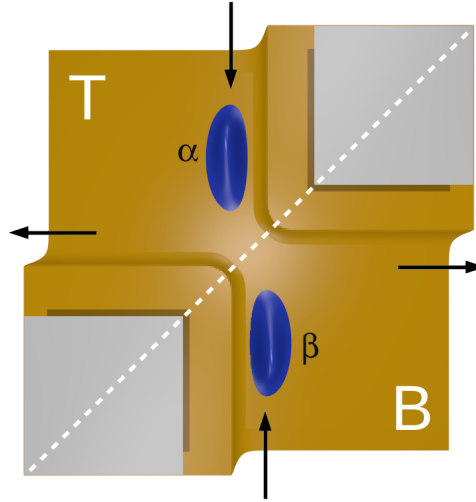


Figure 5.1: Rendered picture of HOM interferometer. The external potential (gold) reproduces the QPC in the 2DEG, and the wavepackets (blue shapes) define the unconditional density probability of particle 2 at $t = 0$. α and β are the initial counterpropagating states for $\sigma = 20$ nm, while T and B label the top and bottom regions of the HOM interferometer. Their domains are separated by the diagonal dashed line

present regime.

Indeed, experimental implementations of the device in the IQH regime are typically affected by spurious interchannel interactions, which lead to charge fractionalization and decoherence, thus preventing the observation of full antibunching. The Floquet scattering-state and capacitive models have been extensively adopted to explain the origin of such interactions. However, in these frameworks Coulomb repulsion between the two interfering charges is usually neglected. Moreover, experimental implementations are usually characterized by large wavepackets in real space, which ensure an ideal functioning of the electron beam splitter but quench the interplay between the energy broadening of the wavepacket and the energy selectivity of the QPC.

Differently, we aim to study the unexplored regime of strongly-localized single-electron excitations in presence of the exact screened and unscreened Coulomb interaction and a realistic geometry of the HOM interferometer. We then compare the bunching probabilities for a two-electron system in our time-dependent approach to the predictions of a simplified theoretical model based on the one-dimensional scattering formalism, and obtain quantitatively the entanglement-generation capabilities of the QPC by measuring the spatial entanglement between the two outputs of the device.

5.1 State of the art

The HOM experiment has been firstly implemented with photons [16]. Here, two indistinguishable particles generated from independent sources interact at a half-reflecting beam splitter and are then recollected at two detectors. The two-particle statistics is tested by measuring the coincidence counts: due to their bosonic nature, identical photons are simultaneously detected at the same output if the two sources are synchronized. The bunching probability, or equivalently the coincidence counts in an experimental implementation, then measures one. When the two sources are desynchronized by a factor Δt , the bunching probability tends to $1/2$ in the limit $\Delta t \rightarrow \infty$, as expected for distinguishable particles, which are randomly partitioned.

In the electronic counterpart of the photonic HOM experiment, the fermionic statistics is instead expected to induce a perfect antibunching of the two charges, according to the Landauer-Büttiker

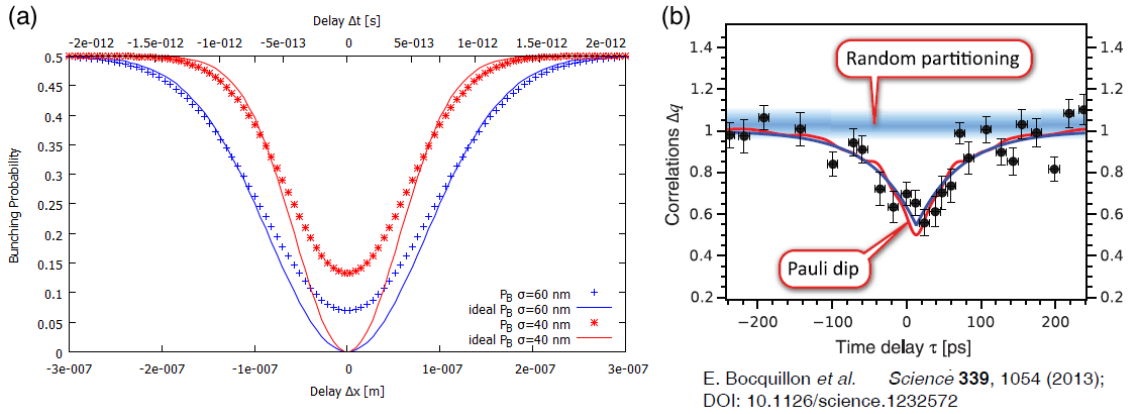


Figure 5.2: (left) Numerical simulations of the electron bunching probability in a 1D model with energy dependent effects and exchange interaction from Ref. [78], and (right) experimental results in a 2DEG from Ref. [64]. Note that the time scales are different, due to the different energies and energy spreads of the single-charge wavepackets.

theory: the simultaneous presence of two indistinguishable particles is prevented indeed by Pauli exclusion principle [105].

To measure the coincidence counts, single-shot detection of flying electrons in a semiconductor implementation is advisable. However, this is not achievable yet, and the bunching probability is typically recovered from low-frequency current noise in the output current [106].

The earliest experimental implementations of two-electron interferometry are realized by injecting a continuous stream of electrons in an HOM device [107], or in an HBT architecture [49, 15]. However, the use of electron beams prevents the interference to be directly interpreted as the overlap between single-electron wavepackets. Sources able to generate single-electron excitations have been introduced for the first time by Bocquillon et al. in 2013, to reproduce the HOM experiment in the IQH regime [64]. Two mesoscopic capacitors inject a Landau quasi-particle in edge channels with an opposite chirality. The two excitations interact at a QPC where they are partitioned. By tuning the synchronization time Δt , the excess low frequency noise is measured at one of the outputs. The excess noise as a function of Δt is characterized by a minimum, called Pauli dip, which proves the generation of coherent and indistinguishable particles from independent sources. However, its value differs from zero, differently from the theoretical predictions of stationary models (see Fig. 5.2).

This apparent violation of the Pauli exclusion principle is confirmed by experiments at bulk FF 2 [108, 65]. Refs. [30, 68] prove that this decoherence process is induced by the nature of those *Landau excitations*, that are generated by mesoscopic capacitors. These sources inject indeed linear combinations of edge-magnetoplasmons excitations, whose coherence is destroyed by Coulomb interchannel and intrachannel interactions. If copropagating channels run parallel for a long enough distance, $L_{frac} = \frac{\hbar v_g}{\sigma}$, the charge of the single-electron pulses splits between the two Landau levels. This decoherence phenomena, called *charge fractionalization*, increases the minimum of the Pauli dip for larger wavepackets [17], and it can be avoided by increasing the lateral distance between the two channels with a local variation of the FF [13], or by looping the inner one [31].

On the other side, time-dependent numerical simulations [19, 21] prove that the non-zero Pauli dip is also intrinsically related to the localized nature of the electron state, which can not be captured in a stationary picture for edge transport. By studying the two-electron tunneling at a barrier in an effective 1D scenario, Ref. [19] provides the bunching probability for an exchange and Coulomb-driven scattering of two counterpropagating Gaussian wavepackets of plane waves. In a time-dependent approach, the wavepackets contains all the energy-related information about the system, including the energy selectivity of the barrier, which is unknown a priori. The system is initialized to split each electron wavepacket with 50% of integrated transmission probability. However, this condition is not enough to generate an ideal beam splitter, as pointed out in our multichannel implementation of the MZI (see Sec. 4.1.1). Indeed, the QPC transmit mainly the highest energy components, while the lowest ones are reflected. The *reflected* and *transmitted* wavepackets after the scattering at the beam splitter are not identical, so that the exchange symmetry cancels out only those states that overlap in the Fourier space at the same output. The residual non-zero overlap between the wave-vector distribution of the *reflected* and *transmitted* wavepackets increases the bunching probability. With contrast to the bunching in presence of charge fractionalization, if the wavepacket size σ is increased, the ideal full anti-bunching is gradually restored.

5.2 Effect of QPC scattering asymmetry

Numerical simulations of electron scattering on a QPC already exhibit that the energy dependence of such gate reduces the degree of indistinguishability between its reflected and transmitted components. In the single-channel MZI, this energy selectivity decreases the visibility, as observed in Ref. [7]. This effect is present also in two-electron interferometers, as in the HOM geometry,

and produces a residual bunching probability in presence of exchange interaction only [19].

In the following, we will initially present an effective 1D geometry to compute analytically the bunching probability P_b with respect to the real-space broadening σ of a Gaussian wavepacket. Then, we use the single-particle version of our software to analyze the transmission coefficient of the QPC and properly initialize the system. Finally, we simulate two-electron dynamics in a Hall-driven HOM interferometer in presence of exchange interaction only. With contrast to the simplified analytical model in 1D, our computational approach is able to account for the interplay between the geometry of the device and the energy-broadening of the wavepackets exactly. Indeed, our method does not require the use of empiric transmission coefficients, but only a proper design of the external potential V_{ext} mimicking the HOM interferometer.

5.2.1 1D analytical model for electron bunching

In order to provide an analytical bunching probability in the electron HOM experiment, we adapt the 1D effective model in Sec. 4.1.3 to the present geometry, and introduce the empiric reflection and transmission coefficients in Eq.(4.11), we already validated to study single-qubit interferometers [13, 7]. Thanks to the chirality of edge states, the 2DEG system is modelled as a 1D rail where the QPC is replaced by a symmetric scattering barrier. Electrons are injected at opposite sides of the 1D rail, as counterpropagating states. The antibunching probability, i.e. the probability of finding the electrons in opposite outputs is evaluated by using the scattering matrix formalism [42, 109, 47].

Plane-wave model

In a steady-state scenario, the edge state $\varphi_{n=0,k}(x)e^{iky}$ is mapped by a plane-wave $\langle y|k\rangle = e^{iky}$, with an effective parabolic dispersion $E_n(k)$ characterized by a magnetic mass m_B^* . The counterpropagating state $\varphi_{n=0,-k}(x)e^{-iky}$ is then mapped by $\langle y|-k\rangle = e^{-iky}$, as reported in the scheme of Fig. 5.3(a). In the reciprocal space, the wavefunctions generated by the two sources, $|\alpha\rangle$ and $|\beta\rangle$ are defined on the pseudo-spin basis $\{|k\rangle, |-k\rangle\}$. In the following, we assume $|\alpha\rangle = |k\rangle$ and $|\beta\rangle = |-k\rangle$.

The two electrons, 1 and 2, initialized in $|\alpha\rangle$ and $|\beta\rangle$ with the exchange symmetry, impinge on a symmetric potential barrier localized in $y \in [-a, +a]$. Its effect is described by the scattering matrix \hat{S} in Eq.(5.17). For a plane wave coming from the left side of the barrier ($\Psi_+(y) = \langle y|k\rangle$), the scattering process generates:

$$\hat{S}\Psi_+(y) = ite^{iky} + re^{i\phi}e^{-iky}, \quad (5.1)$$

with a global phase factor $e^{i\phi}$ that does not get modified by the scattering process, also for a wavevector-dependent case, e.g. $\phi(k) = ky_0$ ¹.

For a couple of indistinguishable electrons, the initial state in the Dirac notation

$$|\Psi\rangle_0 = \frac{1}{\sqrt{2}}(|\alpha\rangle|\beta\rangle - |\beta\rangle|\alpha\rangle) \quad (5.2)$$

¹This is the case of desynchronized sources. This term is important when we apply the scattering operator to a wavepacket: only the wavevectors multiplying the coordinate y change their sign, while those appearing in the phase do not. Otherwise, we can change sign to any wavevector in the wavepacket, and then change sign to any k -dependent phase

is in the plane-wave description given by:

$$\Psi(0) = \Psi_+(y_1)\Psi_-(y_2) - \Psi_-(y_1)\Psi_+(y_2) \quad (5.3)$$

$$= e^{iky_1}e^{-iky_2}e^{i\phi} - e^{iky_1}e^{i\phi}e^{iky_2}. \quad (5.4)$$

After the interaction with the barrier, we apply Eq.(5.1) to the initial state Ψ_0 and compute the scattered wavefunction at *infinite* distance from the barrier:

$$\begin{aligned} \Psi(\infty) &= (ite^{iky_1} + re^{-iky_1})(ite^{-iky_2}e^{i\phi} + re^{iky_2}e^{i\phi}) - (ite^{-iky_1}e^{i\phi} + re^{iky_1}e^{i\phi})(ite^{iky_2} + re^{iky_2}) \\ &= -t^2(e^{ik(y_1-y_2)} - e^{ik(y_2-y_1)}) + r^2(e^{-ik(y_1-y_2)} - e^{ik(y_2-y_1)}). \end{aligned} \quad (5.5)$$

For any dephasing ϕ , the wavefunction has a partially destructive interference, so that both electrons are transmitted or reflected and perfect anti-bunching is observed.

Wave-packet model

In the following, we model the injection protocol of single-electron excitations by initializing the two electrons in Gaussian wavepackets of plane waves:

$$\psi_\alpha(y) = N_x e^{-\frac{(y-y_0)^2}{4\sigma^2}} e^{ik_0(y-y_0)}, \quad (5.6)$$

$$\psi_\beta(y) = N_x e^{-\frac{(y-y'_0)^2}{4\sigma^2}} e^{-ik_0(y-y'_0)}, \quad (5.7)$$

where

$$N_y = \frac{1}{\sqrt[4]{2\pi\sigma^2}}, \quad N_k = \sqrt[4]{\frac{2\sigma^2}{\pi}}. \quad (5.8)$$

are the normalization constants for the real and reciprocal space, respectively. In the Dirac notation, the initial state reads:

$$|\alpha(\beta)\rangle = \int dk F_\sigma(k, k_0^{\alpha(\beta)}, y_0^{\alpha(\beta)}) |k\rangle \quad (5.9)$$

where $F_\sigma(k, k_0, y_0)$ is the Gaussian weight function centered at y_0 in the real space and at k_0 in the reciprocal one. The wavepackets have the same energy distribution but group velocities with opposite directions. They are emitted by two sources at opposite sides with respect to origin of the 1D rail, $y = 0$, at the times t and $t + \Delta t$, respectively.

For a small Δt , the broadening of the wavepacket in σ is negligible, so that:

$$y'_0 = -(y_0 + \Delta y_0), \quad (5.10)$$

and

$$\Delta y_0 = v_{gB} \cdot \Delta t = -\frac{\hbar k_0}{m_B^*} \Delta t, \quad (5.11)$$

where m_B^* is the effective mass deriving from the curvature of the edge states band, that we assumed to be parabolic. ²

With contrast to a 2D geometry, in the 1D scenario the output channels, I and II , coincide with the input channels α and β . The corresponding stationary states, $|I\rangle$ and $|II\rangle$, outgoing from

²Previous considerations hold both for delays $\Delta t > 0$ and timing advances $\Delta t < 0$.

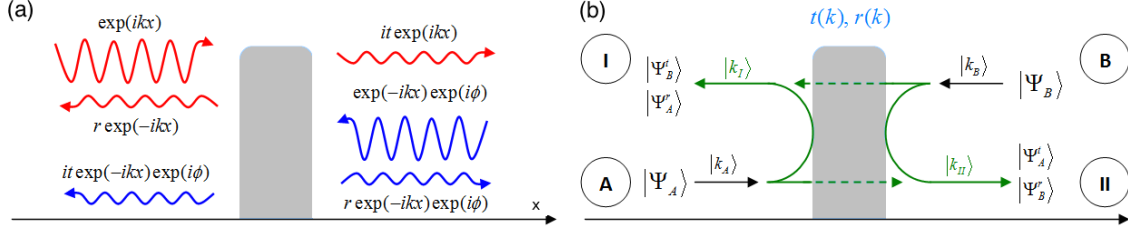


Figure 5.3: Scheme for the application of the (a) *plane-wave model* and (b) *wavepacket model* to two-electron bunching in an effective 1D geometry of the HOM interferometer.

the scattering region, differ from $|\alpha\rangle$ and $|\beta\rangle$ in the sign of the momenta only, i.e. $k_I = -k_{II} = -k_\alpha = k_\beta$.

We introduce the projections operators P_I and P_{II} :

$$P_I = \int_I dk_I \int_I dk'_I |k_I\rangle \langle k_I| \otimes |k'_I\rangle \langle k'_I| \quad (5.12)$$

$$P_{II} = \int_{II} dk_{II} \int_{II} dk'_{II} |k_{II}\rangle \langle k_{II}| \otimes |k'_{II}\rangle \langle k'_{II}|, \quad (5.13)$$

where the two terms in the projectors correspond to the contribution of the first ($|k_i\rangle \langle k_i|$ for $i = I, II$) and the second ($|k'_i\rangle \langle k'_i|$ for $i = I, II$) particle respectively. The integration is carried over the wavevectors of the scattering states that belong to region I or region II in Fig. 5.3(b); the probability of finding two particles in region $i = I, II$ is therefore given by:

$$p_i^b = \left| \lim_{t \rightarrow \infty} P_i |\psi(t)\rangle \right|^2, \quad (5.14)$$

with $|\psi(t)\rangle$ the two-particle wavefunction at time t .

According to the topology of the original 2D system, an injected plane wave $|\alpha\rangle$ impinging from the left of the QPC and $|\beta\rangle$ from the right are scattered to the output states as follows:

$$\hat{S} |k_A\rangle = r(k) |k_I\rangle + t(k) |k_{II}\rangle, \quad (5.15)$$

$$\hat{S} |k_B\rangle = t(k) |k_I\rangle + r(k) |k_{II}\rangle, \quad (5.16)$$

where \hat{S} is the single-particle operator described by the matrix:

$$\hat{S} = \begin{pmatrix} r(k) & t(k) \\ t(k) & r(k) \end{pmatrix}. \quad (5.17)$$

For a scattering state with positive k (i.e. coming from the left), the scattering amplitudes $r(k)$ and $t(k)$ are given by the empiric equations,

$$r(k) = \sqrt{\frac{1}{\exp(+\alpha(k - k_0)) + 1}} \simeq \exp \left[-\frac{(+\alpha(k - k_0) + \gamma)^2}{8\gamma} \right], \quad (5.18)$$

$$t(k) = i \sqrt{\frac{1}{\exp(-\alpha(k - k_0)) + 1}} \simeq i \exp \left[-\frac{(-\alpha(k - k_0) + \gamma)^2}{8\gamma} \right], \quad (5.19)$$

with $\gamma = 4 \ln 2$ (see Sec. 4.2.3). By adopting the Gaussian approximation, the coefficients read:

$$\begin{bmatrix} r(k) \\ t(k) \end{bmatrix} = \begin{bmatrix} 1 \\ i \end{bmatrix} \exp\left(-\frac{\alpha^2}{8\gamma}(k-k_0)^2\right) \exp\left(\mp \frac{\alpha}{4}(k-k_0)\right) \exp\left(-\frac{\gamma}{8}\right). \quad (5.20)$$

Note that for negative k (i.e. scattering states coming from the right) we substitute k with $-k$, and the central wavevector k_0 with $-k_0$.

The scattering process described by the operator $\hat{S} = \hat{R} + \hat{T}$ applies independently to each plane-wave component of our Gaussian wavepackets $|\alpha\rangle$ and $|\beta\rangle$. This produces a reflected $|\alpha(\beta), R\rangle$ and a transmitted $|\alpha(\beta), T\rangle$ state:

$$|\alpha, R\rangle = \int dk F_\sigma(k, k_0^\alpha, y_0^\alpha) r(k) |k\rangle = \int dk |k''\rangle r(k) F_\sigma(k, -k_0, -y_0), \quad (5.21)$$

$$|\alpha, T\rangle = \int dk F_\sigma(k, k_0^\alpha, y_0^\alpha) t(k) |k\rangle = \int dk |k''\rangle t(k) F_\sigma(k, +k_0, y_0), \quad (5.22)$$

$$|\beta, R\rangle = \int dk F_\sigma(k, k_0^\beta, y_0^\beta) r(k) |k\rangle = \int dk |k''\rangle r(k) F_\sigma(k, +k_0, -y'_0), \quad (5.23)$$

$$|\beta, T\rangle = \int dk F_\sigma(k, k_0^\beta, y_0^\beta) t(k) |k\rangle = \int dk |k''\rangle t(k) F_\sigma(k, -k_0, y'_0). \quad (5.24)$$

with $k_0^\alpha = k_0$, $y_0^\alpha = y_0$, $k_0^\beta = -k_0$, $y_0^\beta = -y_0$. Due to the introduction of y'_0 in the second equalities, we modify the Gaussian distribution F_σ according to the relative sign of the scattering states in the 1D geometry. This equals to a change in the central momentum of the wavepacket together with a change in the sign of the k -dependent phase in case of reflections. Indeed, in the limit $\sigma \rightarrow \infty$ the scattering state is so properly described:

$$\lim_{\sigma \rightarrow \infty} F_\sigma(k, -k_0, y'_0) = \delta(k + k_0) e^{-iky'_0} \quad (5.25)$$

$$\begin{aligned} \lim_{\sigma \rightarrow \infty} \langle y | \psi_B \rangle &= \int dk \langle y | k \rangle F_\sigma(k, -k_0, y'_0) \\ &= \int dk e^{+iky} \delta(k + k_0) e^{-iky'_0} \\ &= e^{-ik_0(y-y'_0)} \end{aligned} \quad (5.26)$$

$$\begin{aligned} \lim_{\sigma \rightarrow \infty} \langle y | \beta, R \rangle &= \int dk \langle y | k \rangle r(k) F_\sigma(k, +k_0, -y'_0) \\ &= \int dk e^{+iky} r(k) \delta(k - k_0) e^{+iky'_0} \\ &= e^{+ik_0(y+y'_0)} r(k_0) \end{aligned} \quad (5.27)$$

We then compute the stationary state

$$\begin{aligned} |\Psi(\infty)\rangle &= \frac{\hat{S} |\alpha\rangle \hat{S} |\beta\rangle - \hat{S} |\beta\rangle \hat{S} |\alpha\rangle}{\sqrt{2}} \\ &= \frac{(|\alpha, R\rangle + |\alpha, T\rangle)(|\beta, R\rangle + |\beta, T\rangle) - (|\beta, R\rangle + |\beta, T\rangle)(|\alpha, R\rangle + |\alpha, T\rangle)}{\sqrt{2}}, \end{aligned} \quad (5.28)$$

and we separate the bunching and anti-bunching contributions, corresponding to

$$|\Psi(\infty)\rangle = |\psi_{abun}\rangle + |\psi_{bun}\rangle, \quad (5.29)$$

$$|\psi_{abun}\rangle = \frac{1}{\sqrt{2}} (|\alpha, R\rangle |\beta, R\rangle + |\alpha, T\rangle |\beta, T\rangle - |\beta, R\rangle |\alpha, R\rangle - |\beta, T\rangle |\alpha, T\rangle), \quad (5.30)$$

$$|\psi_{bun}\rangle = \frac{1}{\sqrt{2}} (|\alpha, R\rangle |\beta, T\rangle + |\alpha, T\rangle |\beta, R\rangle - |\beta, R\rangle |\alpha, T\rangle - |\beta, T\rangle |\alpha, R\rangle). \quad (5.31)$$

Note that, the localization of the wavepackets ensures the orthogonality between the scattered states of $|\alpha\rangle$ and $|\beta\rangle$, i.e.

$$\langle \alpha, R | \alpha, T \rangle = 0, \quad (5.32)$$

$$\langle \beta, R | \beta, T \rangle = 0, \quad (5.33)$$

The bunching probability

$$\mathcal{P}_b = \langle \psi_{bun} | \psi_{bun} \rangle = 1 - \mathcal{P}_{ab} = 1 - \langle \psi_{abun} | \psi_{abun} \rangle \quad (5.34)$$

is computed by using the projected states

$$|\psi_{bun}^I\rangle = P_I |\psi_{bun}\rangle = \frac{1}{\sqrt{2}} (|\alpha, R\rangle |\beta, T\rangle - |\beta, T\rangle |\alpha, R\rangle) \quad (5.35)$$

$$|\psi_{bun}^{II}\rangle = P_{II} |\psi_{bun}\rangle = \frac{1}{\sqrt{2}} (|\alpha, T\rangle |\beta, R\rangle - |\beta, R\rangle |\alpha, T\rangle) \quad (5.36)$$

as follows

$$\mathcal{P}_B = \langle \psi_{bun}^I | \psi_{bun}^I \rangle + \langle \psi_{bun}^{II} | \psi_{bun}^{II} \rangle.$$

We then compute separately the two contributions:

$$\langle \psi_{bun}^I | \psi_{bun}^I \rangle = \langle \alpha, R | \alpha, R \rangle \langle \beta, T | \beta, T \rangle - |\langle \alpha, R | \beta, T \rangle|^2 \quad (5.37)$$

$$\langle \psi_{bun}^{II} | \psi_{bun}^{II} \rangle = \langle \alpha, T | \alpha, T \rangle \langle \beta, R | \beta, R \rangle - |\langle \alpha, T | \beta, R \rangle|^2 \quad (5.38)$$

with

$$\langle \alpha, R | \alpha, R \rangle = \int dk N_k^2 e^{-2\sigma^2(k+k_0)^2} |r(k)|^2, \quad (5.39)$$

$$\langle \beta, T | \beta, T \rangle = \int dk N_k^2 e^{-2\sigma^2(k+k_0)^2} |t(k)|^2, \quad (5.40)$$

$$\langle \alpha, R | \beta, T \rangle = \int dk N_k^2 e^{-2\sigma^2(k+k_0)^2} e^{-ik(y_0+y'_0)} r^*(k') t(k), \quad (5.41)$$

$$\langle \beta, R | \beta, R \rangle = \int dk N_k^2 e^{-2\sigma^2(k-k_0)^2} |t(k)|^2, \quad (5.42)$$

$$\langle \alpha, T | \beta, R \rangle = \int dk N_k^2 e^{-2\sigma^2(k-k_0)^2} |r(k)|^2, \quad (5.43)$$

$$\langle \alpha, T | \beta, R \rangle = \int dk N_k^2 e^{-2\sigma^2(k-k_0)^2} e^{+ik(y_0+y'_0)} t^*(k') r(k). \quad (5.44)$$

For an half-reflecting and half-transmitting potential barrier, i.e. $\langle \alpha, R | \alpha, R \rangle = \langle \beta, R | \beta, R \rangle = \langle \alpha, T | \alpha, T \rangle = \langle \beta, T | \beta, T \rangle = 1/2$, the interference terms are the only responsible for anti-bunching.

We finally replace $r(k)$ and $t(k)$ with their expressions in the Gaussian approximation of Eq.(5.20) and carry on the integrations analytically:

$$\begin{aligned}\langle \alpha, R | \beta, T \rangle &= (+i) \int dk N_k^2 \exp \left(-2 \left(\sigma^2 + \frac{\alpha^2}{8\gamma} \right) (k + k_0)^2 \right) e^{-ik\Delta y} \frac{1}{2} = \\ &= \frac{+i}{2} N_k^2 e^{+ik_0\Delta y} \sqrt{\frac{\pi}{2\Sigma^2}} e^{-\frac{\Delta y^2}{8\Sigma^2}}\end{aligned}\quad (5.45)$$

$$\begin{aligned}\langle \alpha, T | \beta, R \rangle &= (-i) \int dk N_k^2 \exp \left(-2 \left(\sigma^2 + \frac{\alpha^2}{8\gamma} \right) (k - k_0)^2 \right) e^{+ik\Delta y} \frac{1}{2} = \\ &= \frac{-i}{2} N_k^2 e^{+ik_0\Delta y} \sqrt{\frac{\pi}{2\Sigma^2}} e^{-\frac{\Delta y^2}{8\Sigma^2}},\end{aligned}\quad (5.46)$$

Here, we introduce a new geometrical parameter, Σ , related to the energy broadening of the wavepacket (σ) and the smoothness of the energy selectivity of the QPC (a):

$$\Sigma = \sqrt{\sigma^2 + \frac{\alpha^2}{8\gamma}}. \quad (5.47)$$

The bunching probabilities in region I and II ,

$$\langle \psi_{bun}^I | \psi_{bun}^I \rangle = \langle \psi_{bun}^{II} | \psi_{bun}^{II} \rangle = \frac{1}{4} - \frac{1}{4} \frac{\sigma^2}{\Sigma^2} e^{-\frac{\Delta y^2}{4\Sigma^2}}, \quad (5.48)$$

are finally summed up to compute the total bunching probability:

$$\mathcal{P}_b(a, \Delta y) = \langle \alpha, T | \alpha, T \rangle \langle \beta, R | \beta, R \rangle + \langle \alpha, R | \alpha, R \rangle \langle \beta, T | \beta, T \rangle - 2 |\langle \alpha, R | \beta, T \rangle|^2 \quad (5.49)$$

$$= \frac{1}{2} - \frac{1}{2} \frac{\sigma^2}{\Sigma^2} e^{-\frac{\Delta y^2}{4\Sigma^2}}. \quad (5.50)$$

An ideal beam splitter requires then a negligible energy-dependence of the transmission and reflection coefficients, i.e. $r(k) = t(k) = 1/\sqrt{2} \quad \forall k$. This condition is fulfilled for $a \rightarrow 0$ ($\Sigma = \sigma$), so that the bunching probability becomes

$$\mathcal{P}_b(0, \Delta y) = \frac{1}{2} \left(1 - e^{-\frac{\Delta y^2}{4\sigma^2}} \right), \quad (5.51)$$

as expected for a fermionic system. Pauli exclusion principle prevents indeed the wavefunction of two indistinguishable electrons to occupy the same output channel at the same time, that is when the time-delay between the emission of the two wavepacket goes to zero ($\Delta y \rightarrow 0$). For synchronized sources, indeed, the reflected and transmitted components of the two scattered wavefunctions from opposite inputs reach at the same time the two output channels, where they interfere destructively. Instead, for large time delays ($\Delta y \rightarrow \infty$), the two electrons are partitioned at the QPC independently: the two charges are equally bunched and antibunched, and $\mathcal{P}_b(0, \infty) = \frac{1}{2}$. An intermediate delay gives an outcome between the full anti-bunching and the random partitioning, i.e. $\mathcal{P}_b \in (0; \frac{1}{2})$.

Eq.(5.50) represents however a more general equation for the bunching probability able to include energy-dependent effects related to the energy broadening of the wavepacket and the energy selectivity of the QPC. The full antibunching that characterize the plane wave model is restored not only for $a \rightarrow 0$, but also if $\sigma \rightarrow \infty$. More generally, full antibunching is restored when $\sigma \gg a$ ($\Sigma = \sigma$), which correspond to the injection of very large wavepackets that can be considered as a plane wave *with respect to* the geometry of the QPC.

5.2.2 2D numerical bunching probability

In a steady-state framework, where the injection of plane waves is assumed, \mathcal{P}_b is expected to be zero for an half-reflecting beam splitter, due to the exchange symmetry of a fermionic two-particle state, even neglecting Coulomb interaction [48].

Differently, by using a time-dependent model in a 1D effective framework, as well as a wavepacket description of the electron state in a stationary model, we proved in the previous section that the energy broadening of the single-electron state affects the bunching probability. This behavior is confirmed by our full-scale time-dependent simulations of the two-electron bunching in 2D for different wavepacket sizes.

In our approach, the time-dependent wavefunction is evolved by means of a parallel implementation of the Split-Step Fourier method in a two-dimensional potential landscape, that reproduces the field generated by top gates in the typical GaAs/AlGaAs heterostructure. The energy broadening of the single-particle is directly included in the propagating state and time is an intrinsic variable of our simulations, so that we can access the dynamical properties of the two-particle system.

It should be noticed that traditional approaches in the literature bypass the huge computational load for such simulations by using scattering matrices in effective 1D schemes, which proved not to fully capture the interplay between two-electron correlations and the realistic geometry of the device, as for electron bunching. Here, we privilege the exact solution by developing a scalable parallel numerical solver of the time-dependent Schrödinger equation for two particles in a 2D realistic geometry.

In the following, we will describe the initialization of our operating regime in the HOM geometry, from the building up of the single-particle wavepackets to the exact two-particle wavefunction in 2D. Then, we analyze the transmission coefficient of the electron beam splitter by combining single-particle simulations and the wave-packet method. Finally, we present the results of our full-scale two-electron bunching in presence of exchange only.

Initialization of the device

According to our numerical modeling of electron injection in an edge channel, the particle state emitted by each source is a Gaussian combination of edge states from the first Landau Level $\varphi_{1,k}(x)e^{iky}$:

$$\psi(x, y) = \int dk F_\sigma(k, k_0, y_0) e^{iky} \varphi_{0,k}(x), \quad (5.52)$$

where $F_\sigma(k, k_0, y_0) = \sqrt[4]{\sigma^2/2\pi^3} e^{-\sigma^2(k-k_0)^2} e^{-iky_0}$ is the weight function in the k space centered at $k_0 = -\frac{eB}{\hbar}x_0$ and σ is the real-space broadening in the \hat{y} direction.

Each source S_α and S_β generates a single-charge state, $\psi_\alpha(x, y)$ and $\psi_\beta(x, y)$, that is initialized in a translationally invariant region of the HOM interferometer (region α and β in Fig. 5.1, respectively). The external potential in the two regions is a smooth confining barrier:

$$V_{ext}^\alpha(x) = \frac{V_b^\alpha}{\exp(\tau_\alpha(x - x_b^\alpha)) + 1} = V_b^\alpha \mathcal{F}_{\tau_\alpha}(x - x_b^\alpha), \quad (5.53)$$

$$V_{ext}^\beta(x) = \frac{V_b^\beta}{\exp(\tau_\beta(-x + x_b^\beta)) + 1} = V_b^\beta \mathcal{F}_{\tau_\beta}(-x + x_b^\beta), \quad (5.54)$$

with a smoothness parameter τ , height V_b and a turning point x_b , which refers to the center of the Fermi-like function $\mathcal{F}_\tau(x)$.

To implement an HOM experiment, the initial wavepackets $\psi_\alpha(x, y)$ and $\psi_\beta(x, y)$, must be (i) indistinguishable and (ii) counterpropagating. At $t = 0$, the first requirement is ensured by the

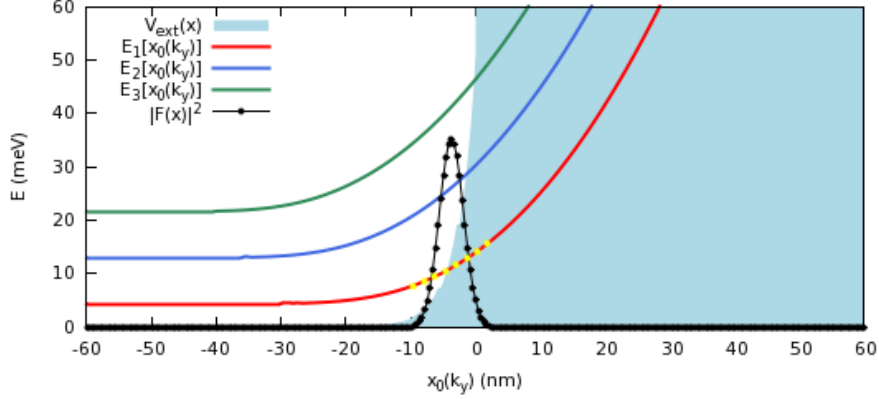


Figure 5.4: Energy bandstructure of the first 3 Landau levels $E_n[x_0(k)]$ (solid line) generated by the confining barrier $V_{ext}(x)$ with $V_b = 10$ eV and $\tau = 3$ nm in the TOP initialization region of the HOM interferometer. The dotted black line identifies the Gaussian weight function $F_0[x_0(k)]$ for the linear combination of edge states (dots on $E_0[x_0(k)]$) in the single-electron wavepacket.

identical smoothness $\tau^\alpha = \tau^\beta$ and height $V_b^\alpha = V_b^\beta$ of the confining barriers, which induces the same bending for the Landau Levels in the two regions. The opposite direction of propagation follows instead by the different chirality of the edge channels in region α and β due to the antisymmetry of the confining barrier, $V_{ext}^\alpha(x) = V_{ext}^\beta(-x)$. For synchronized sources, i.e. a zero time delay dt in the emission process, and due to $k_0^\alpha = -k_0^\beta$ and $y_0^\alpha = -y_0^\beta$, the two wavepackets are expected to impinge on the beam splitter simultaneously. Fig. 5.4 displays the transverse potential profile with $V_b = 10$ eV and $\tau = 3$ nm, together with the bandstructure $E_0[x_0(k)]$ and wavevector distribution probability $|F_0[x_0(k)]|^2$ for $\psi_\alpha(x, y)$ in our operating regime.

As visible from the energy-dependence of the distribution $|F_0[x_0(k)]|^2$, our implementation of the HOM interferometer operates at bulk FF 1. This is done to prevent the presence of those inter-channel interactions that are proved to affect the coherence of single-electron excitations traveling in an edge channel at a larger bulk FF. Ref. [30] proves this to be the main source of decoherence when cyclotron-resolved channels copropagate for large distances. As an example, at bulk FF 2, many-body Coulomb interactions generate an entanglement between the outer channel, where the single-electron is injected, and the inner channel, acting as the environment, thus bringing quantum information *away* from the wavepacket.

A unitary bulk FF ensures therefore the absence of *charge fractionalization*[65], that is not included in our numerical model. Moreover, even in absence of this coupling to environmental channels, decoherence may arise due the creation of electron/hole pairs generated by the space and time-dependent electric potential of the single-electron excitation, that is a traveling bare charge injected above the Fermi sea. However, this decoherence scenario is expected to be less stringent[30] than coupling to environmental channels and more favorable to its control.

After setting $\psi_\alpha(x, y)$ and $\psi_\beta(x, y)$ as the injected states in a full-scale HOM geometry, we observe the dynamics of the two-electron interferometer entailed by our engineering of the device. Design-related performances are estimated exactly, as well as the electron dynamics induced by the local shape of the edge states. To include two-particle correlations as the exchange interaction, we finally compute the two-electron state from the orbital states $\psi_\alpha(x, y)$ and $\psi_\beta(x, y)$ by assuming a

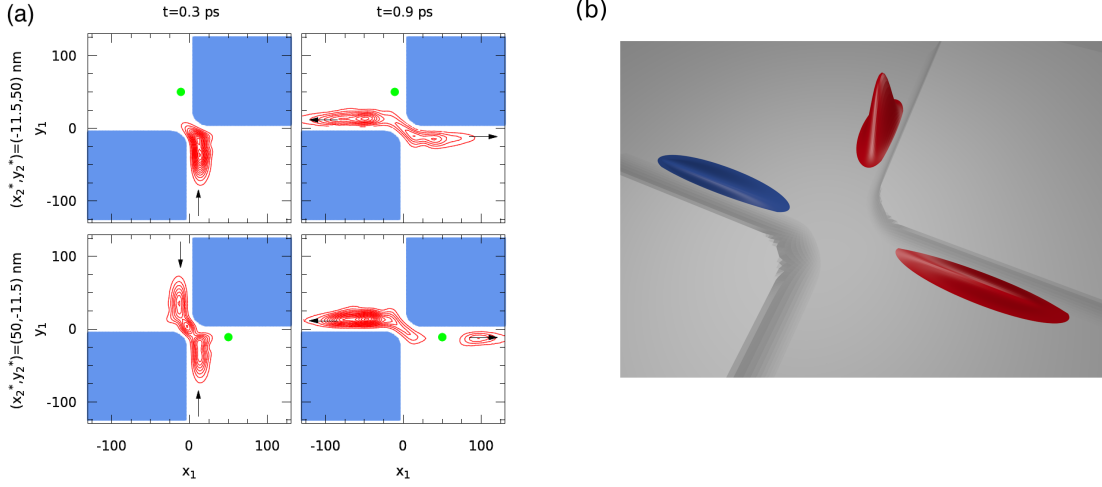


Figure 5.5: (a) Conditional probability (red contour lines) for particle 1 $P^*(x_1, y_1, x_2^*, y_2^*, t') = |\Psi(x_1, y_1, x_2^*, y_2^*, t')|^2$ at $t' = 0.3$ ps (left column) and $t = 0.9$ ps (right column) for the selected positions (green dots) of particle 2, $(x_2^*, y_2^*) = (-11.5, 50)$ nm (first row) and $(x_2^*, y_2^*) = (50, -11.5)$ nm (second row), in the potential landscape of the HOM. Note that, due to Pauli exclusion principle, the wavefunction always vanishes at $(x_1, y_1) = (x_2, y_2)$. By selecting different couples of coordinates (x_2^*, y_2^*) the conditional probability shows the evolution of one of the two or both single-particle wavepackets, as indicated by the arrows. (b) Rendered picture of the QPC. Red and blue wavepackets define the single-particle density probability before and after the scattering. The impinging wavepacket (red shape) before the QPC is partially transmitted into a channel with the same chirality (red shape) and partially reflected to the channel with opposite chirality (blue shape).

symmetric spin part of the wavefunction:

$$\Psi(x_1, y_1; x_2, y_2) = \frac{\psi_\alpha(x_1, y_1)\psi_\beta(x_2, y_2) - \psi_\alpha(x_2, y_2)\psi_\beta(x_1, y_1)}{\sqrt{2}}. \quad (5.55)$$

From a computational perspective, the allocation of the two-electron state above has a memory burden that significantly increases the numerical cost of the present simulations with respect to the previous works [13, 7]. The adopted parallelization technique and its performance on HPC facilities are detailed in Sec. 3.3. In summary, we partitioned the domain of particle 2, (x_2, y_2) , between interconnected supercomputing nodes with the MPI paradigm, and developed a parallel version of the Split-Step Fourier [27] (see Sec. 3.2) to evolve the distributed two-particle wavefunction.

The amount of information provided by the 4D wavefunction in a two-electron system becomes accessible only by reducing the number of degrees of freedom, as in the computation of the dynamical bunching probability. Additional information on the two-electron system in the HOM interferometer could be extracted from the *conditional probability*, which is the probability of finding particle i at (x_i, y_i) by selecting the coordinates of particle j ($i \neq j$). An example is displayed in Fig. 5.5(a), at two different times in two different positions. Note that, coherently with the Pauli exclusion principle for a fermionic system, this probability is always zero when $(x_1, y_1) = (x_2, y_2)$. Moreover, the dynamics of the single-electron wavepacket can also be observed via the *unconditional probability* of one particle, which measures the probability of finding particle i at (x_i, y_i) , regardless the position of particle j , with $i \neq j$.

Electron beam splitter

The present solid-state implementation of the HOM device requires a proper design of the QPC, to partially scatter the impinging electron wavefunction into the two counterpropagating edge channels. This effect is produced by the following external potential,

$$\begin{aligned} V_{ext}^{BS}(x, y) = & V_b \mathcal{F}(-x - \infty) \mathcal{F}(x - x_L) \mathcal{F}(-y - \infty) \mathcal{F}(y - y_B) \\ & + V_b \mathcal{F}(-x + x_R) \mathcal{F}(x - \infty) \mathcal{F}(-y + y_T) \mathcal{F}(y - \infty) \end{aligned} \quad (5.56)$$

The parameters x_L and x_R define the left and right side of the barrier along the \hat{x} -direction, and y_T and y_B the top and bottom side of the barrier along the \hat{y} -direction, respectively. Note that in the present geometry $x_b = x_R = -x_L$ and $y_T = -y_B$.

An ideal QPC working as an half-reflecting electron beam splitter in the HOM interferometer scatters an impinging wavepacket to the opposite channel with an energy-independent probability [7]. A rendered picture of scattering process at the QPC is displayed in Fig. 5.5(b). By fixing the injection energy of our initial wavepacket, which is conserved during the two-particle interferometry in absence of inelastic scattering, we are also fixing the central position of the wavepacket with respect to the confining barrier at the QPC. The smoothness, height and QPC opening size must be chosen accordingly, and require a study of the energy selectivity entailed by our specific design of the beam splitter.

The coefficients of the energy-dependent scattering matrix in Eq.(5.17) can be computed by applying the *wave-packet method*, described in Sec. 3.1.3. According to this method, the single-electron wavefunction $|\psi\rangle$ after the scattering at the logic gate must be Fourier transformed in the \hat{y} -direction only. By projecting the Fourier-transformed wavefunction on the edge states at the output of the device, we calculate the weight function $F(k)$ of the electron state. At bulk FF 1, due to the opposite chirality of the two channels, the wave-packet method requires to numerically simulate the scattering process in the geometry of Fig. 5.6(a).

After the partition at the QPC, the wavefunction is split into a *reflected* $|\psi_r\rangle$ and a *transmitted* $|\psi_t\rangle$ component characterized by an opposite direction of propagation. As already pointed out in the single-channel MZI of Sec. 4.2.3, at bulk FF 1, the two counterpropagating wavepackets $|\psi_r\rangle$ and $|\psi_t\rangle$ can be forced to propagate in the same direction by introducing a region with local FF 0 between them. $|\psi_r\rangle$ runs along the outer edge, while $|\psi_t\rangle$ propagate at the inner edge of the confining potential. The bandstructure of $|\psi_r\rangle$ and $|\psi_t\rangle$, $E(k_t)$ and $E(k_r)$ present then the same chirality, but are shifted by a geometry/gauge-dependent parameter related to the distance between the turning points of each barrier. The origin of the two bandstructures and the corresponding weight functions $F_r(k)$, $F_t(k)$ must therefore be aligned to the turning points of the barrier in the initialization region. Finally, the ratios between the properly-shifted weight functions in the Fourier spaces, $F(k_r)$, $F(k_t)$ and $F(k_i)$ provide the transmission and reflection coefficients $r(k)$ and $t(k)$ of the QPC.

By means of the empiric formula for the reflection and transmission coefficients

$$\begin{bmatrix} r(k) \\ t(k) \end{bmatrix} = \begin{bmatrix} 1 \\ i \end{bmatrix} \exp\left(-\frac{(\mp a(k - k_t) + \gamma)^2}{8\gamma}\right), \quad (5.57)$$

the numerical data are fit to compute a and k_0 , as done in Ref. [7], with $\gamma = 4 \ln(2)$. As visible from Eq.(5.57), in order to scatter the single-electron wavepacket at the QPC with a 1/2 transmission probability, the central wavevector k_0 must coincide with the center of the energy selectivity of the QPC, i.e. $k_0 = k_t$. This choice fixes the group velocity v_g of the wavepacket, as well as its distance from the confining barrier.

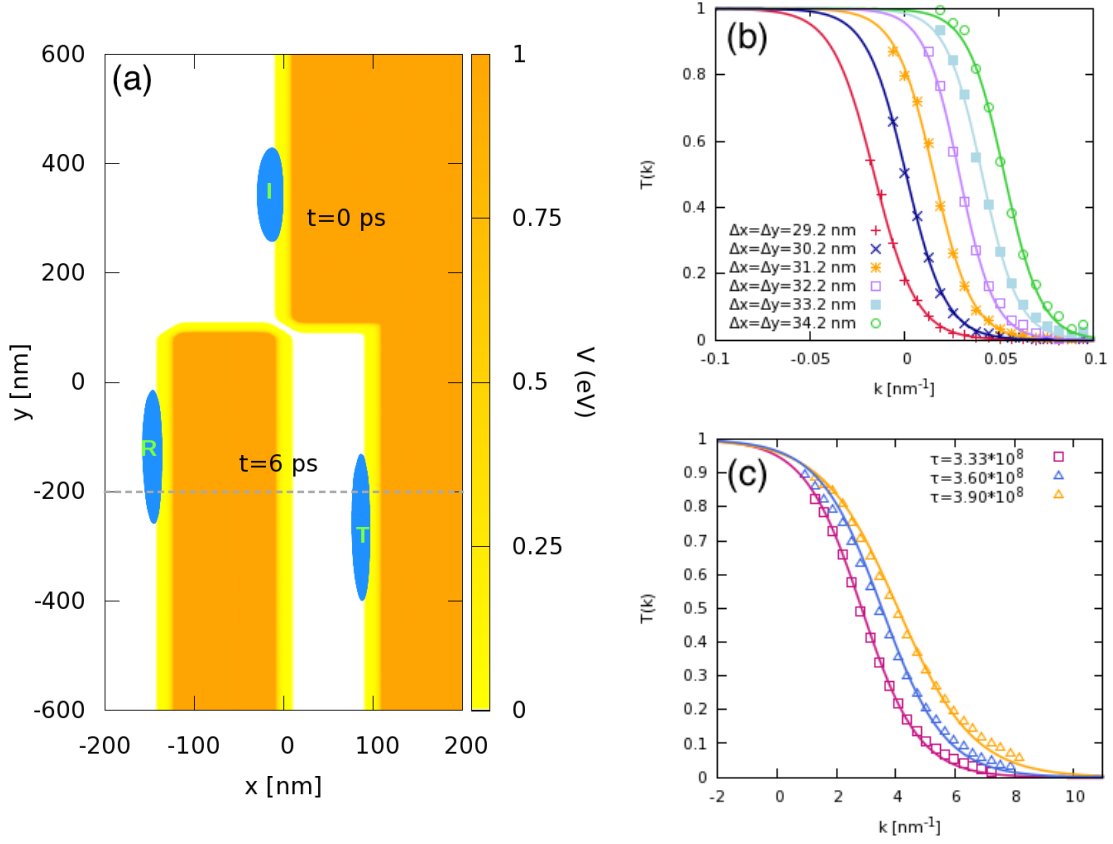


Figure 5.6: (a) External potential profile V_{ext} for the application of the wave-packet method to compute the transmission coefficient of the QPC (orange area) and probability distribution of a single-electro Gaussian wavepacket of edge states (blue shapes) before (I) and after (R,T) the scattering at the QPC with $\sigma = 60$ nm. (b) Transmission coefficients of a QPC computed by means of the wave-packet method (dots) and numerical fit with Eq.(5.57) (solid line) for different symmetric opening sizes. (c) Transmission coefficients of a QPC computed by means of the wave-packet method (dots) and numerical fit with Eq.(5.57) (solid line) for different values of the smoothness τ .

Moreover, we observe that the exact relation between the empiric parameter a and k_t and the geometrical ones, τ , d_x and d_y is generally unknown. Indeed, in a two-dimensional QPC, a change in one of the geometrical parameters of the device modifies both the smoothness a and the center k_t of the energy selectivity in a non-trivial way. For example, in order to modify the smoothness of the energy selectivity a , we need to tune the geometrical smoothness τ , thus also affecting the group velocity. In order to change v_g alone, the center x_0 of the wavepacket must be further distanced from the turning point of the lateral barrier. However, this would also modify the central energy/wavevector of the wavepacket. The single-electron state is no more equally reflected and transmitted by the QPC, which does not act as an ideal beam splitter anymore.

A relevant merit of our numerical method is indeed that we only need to define the geometry of the two-dimensional QPC as an input of our simulations, without providing any guess on the energy selectivity, as in a real experiment. Then, thanks to the application of the Split-Step Fourier

method, the energy selectivity is exactly accounted for during the evolution of the two-particle wavefunction in the external potential $V_{ext}(x, y)$ we designed.

In our software, in order to avoid asymmetry effects in the observation of electron antibunching, we need a proper choice of the initial position x_0 of the wavepacket with respect to the confining barrier, to be performed according to the design of the QPC, i.e. its smoothness τ and the QPC opening with an area $d_x \cdot d_y$. The transmission probability $T(k) = |F_t(k)|^2 / |F(k_i)|^2$ is computed by means of the wave-packet method previously described and displayed in Fig. 5.6(b) for different opening sizes of a symmetric QPC, with $\tau = 3$ nm. Due to the symmetry in the geometry of the QPC, $T(k)$ is sensitive to the area, rather than a length of the QPC. This is equivalent to a tuning of the k_t parameter in the empiric $t(k)$ coefficient, and, in an equivalent 1D scattering at a simple quadratic barrier, to a variation of the barrier height V_b .

Fig. 5.6(c) displays instead how the energy selectivity is affected by a tuning of the smoothness τ at constant QPC size $d_x = d_y = 32.2$ nm. With contrast to the previous case, this variation modifies both k_t and α_t parameters in Eq.(5.57). Due to the relation $x_0(k)$, an increase in the smoothness of the lateral edge reduces indeed the sharpness of the LLs and the energy dispersion $E(k)$ at the confining barrier. This affects not only the central wavevector k_0 but also the group velocity v_g of the Gaussian wavepacket that is half-transmitted.

Measurement: the bunching probability

In a realistic experiment the measurement of the coincidence counts for single-electron wavepackets would require single-shot detection of flying electrons in a semiconductor device. Though robust protocols have been proposed theoretically [56], this is beyond the current technology. Consequently, one has to resort to ensemble measurements on a stream of single-electron wavepackets, as done when probing electron interference with DC currents (e.g. in Ref. [49]).

Differently, in our numerical simulations we directly compute 4D time-dependent wavefunction for a two-particle system in a 2D geometry. From an experimental perspective, the access to the dynamics of the full two-particle wavefunction and its dependence on several parameters, as the spatial dispersion of the carriers, represents a formidable ingredient to assess the origin of low-frequency fluctuations in the electrical current. In fact, the low-frequency noise is proportional to the overlap between the two electron states, and provides the degree of indistinguishability of the two electrons impinging on the beam splitter. By introducing desynchronization between the two

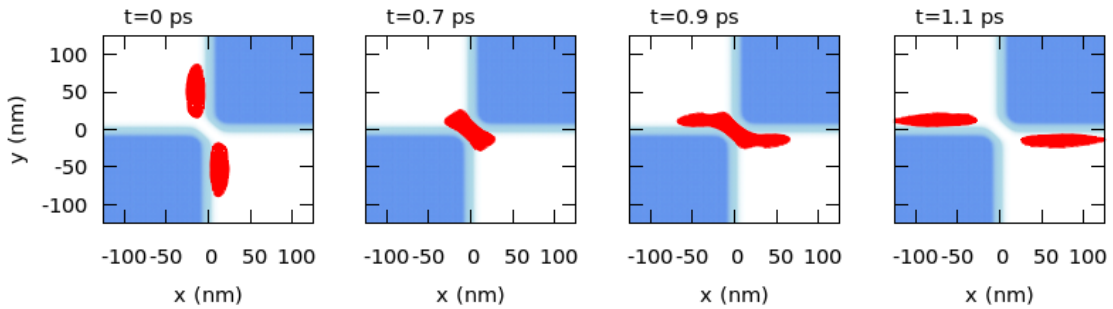


Figure 5.7: Unconditional probability of particle 1 $P(x_1, y_1, t') = \int \int dx_2 dy_2 |\Psi(x_1, y_1, x_2, y_2, t')|^2$ at different time steps t' in the potential landscape of the HOM. The snapshots show that the stationary regime is achieved between 0.9 ps and 1.2 ps. Note that due to exchange correlation, the unconditional probability of particle 1 shows the evolution of both wavepackets.

sources the full minimum of the Pauli dip can be characterized without resorting to a challenging detection of coincidence counts.

Essentially, low-frequency fluctuations in the electrical current is usually computed, as in the first HOM experiment with single electrons injected from two mesoscopic capacitors at opposite arms of the device [64]. Ref. [70] proves that the low frequency current noise at one of the outputs is proportional to $[1 - |\langle \phi_1 | \phi_2 \rangle|^2]$, where $\langle \phi_1 | \phi_2 \rangle$ is the overlap between the two electron states, and provides the degree of indistinguishability of the two electrons impinging on the beam splitter. By introducing desynchronization between the two sources the full minimum of the Pauli dip can be characterized, as with coincidence counts in photonic HOM experiments or by computing the exact two particle wavefunction in our simulations.

By computing the exact two-particle wavefunction in 2D, we can directly measure the bunching (antibunching) probability \mathcal{P}_b (\mathcal{P}_{ab}) from its definition, i.e. the probability that the two electrons are detected at the same output (opposite outputs) at the same time. In our device (Fig. 5.1) the outputs are labelled as region T and region B . The 4D domain $(r_1, r_2) = (x_1, y_1; x_2, y_2)$ is therefore partitioned into 4 distinguishable regions labeled $S_{i,j}$, where the indexes $i = T, B$ refers to particle 1, while $j = T, B$ to particle 2. The joint probability of detection at the same side of the device is computed by integrating the two-particle state as follows:

$$\mathcal{P}_b = \int_{S_{TT}} |\Psi(r_1, r_2)|^2 dx_1 dy_1 dx_2 dy_2 + \int_{S_{BB}} |\Psi(r_1, r_2)|^2 dx_1 dy_1 dx_2 dy_2. \quad (5.58)$$

The antibunching probability is similarly computed by integrating over S_{TB} and S_{BT} ; bunching and antibunching probability are related by $\mathcal{P}_{ab} = 1 - \mathcal{P}_b$. Thanks to the use of the Split-Step Fourier method, our numerical simulations provide the dynamical bunching probability $P_b(t)$ from the time-dependent 4D wavefunction $\Psi(r_1, r_2, t)$.

5.2.3 Two-electron detection driven by exchange

In the following, we present the numerical results for a series of HOM experiments in the IQH regime with $B = 5$ T. By considering GaAs ($m^* = 0.067m_e$) as the hosting material, we vary the spatial broadening σ of the two indistinguishable electron wavepackets ($\sigma = 10, 12.5, 15, 17.5, 20$ nm), to observe the interplay between the HOM geometry and two-electron exchange correlations in different scenarios.

Fig. 5.7 displays the dynamics of the unconditional probability of particle 2. When the two wavepackets interact at the QPC ($t = 0.7$ ps), the bunching probability in Fig. 5.8(a) reaches its maximum. Then, when the two wavepackets leave the QPC, it decreases without vanishing, even in the stationary regime achieved at $t \simeq 1.0$ ps. An increase of σ decreases the final bunching probability linearly, so that we expect the full antibunching to be restored in the plane wave limit ($\sigma \rightarrow \infty$).

Moreover, we compare the outcomes of our time-dependent numerical solver with the predictions of the simplified analytical model described in Sec. 5.2.1. In the inset of Fig. 5.8(a), the stationary values ($t = 1.2$ ps) of the bunching probability $\mathcal{P}_b(\sigma)$ are fit by Eq.(5.51) with $\Delta y = 0$, i.e.:

$$\mathcal{P}_b(\sigma) = \frac{1}{2} - \frac{1}{2} \frac{\sigma^2}{\Sigma^2}, \quad (5.59)$$

with $\Sigma^2 = \sigma^2 + a^2/8\gamma$. The fit shows a linear trend in the bunching probability with respect to the wavepacket size σ , with $a = (60 \pm 1)$ nm. Indeed, our strongly-localized wavepackets present a spatial broadening that is comparable to the opening size of the QPC, i.e. $d_x = d_y = 32.2$ nm. By choosing this operating regime, we characterize the interplay between the transmission coefficient $T(k)$ of the electron beam splitter and the exchange interaction between the two electrons, to

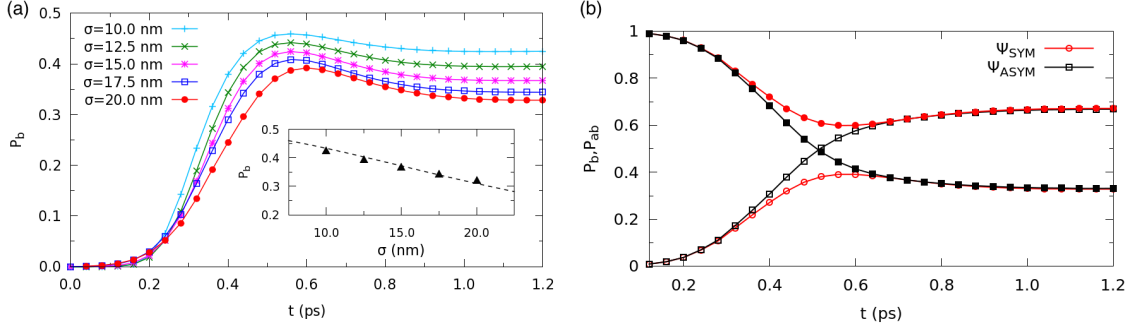


Figure 5.8: Numerical simulations of the exchange-symmetry driven HOM interferometer. (a) Bunching probability of the two-fermion state in absence of Coulomb interaction for different spatial dispersions σ . (inset) Numerical fit of Eq.(5.50) (black dashed line) with the stationary bunching probabilities in panel (a) at $t = 1.2$ ps. This provides the geometrical parameter in Eq.(5.57) for our QPC, $a = 60 \pm 1$ nm. (c) Bunching (empty dots) and antibunching (full dots) probabilities for an antisymmetric (red) and symmetric (black) two-particle wavefunction with $\sigma = 20$ nm. Only exchange symmetry is present.

explain how the energy broadening affects the Pauli dip. Alternative regimes, as the one in Ref. [64], would not provide this amount of information: there, the energy distribution of the single-electron wavepackets is very narrow (of the order of 10^{-2} meV) and the QPC transmission amplitude vs. energy curve is essentially flat on that scale.

If $\Delta y \neq 0$, the generalized formula of the bunching probability

$$P_b(\sigma) = \frac{1}{2} - \frac{1}{2} \frac{\sigma^2}{\Sigma^2} e^{-\Delta y^2 / \sigma^2}, \quad (5.60)$$

clearly depends on the overlap between the reflected and transmitted single-electron wavepackets generated after the QPC, $-2\langle\alpha T|\beta R\rangle$. The amplitude of this overlap depends on the smoothness of the transmission probability on the wavevector space, which affects the shape and energy distribution of the reflected and transmitted wavepackets. Indeed, the bunching probability vanishes for a very narrow broadening in space, i.e. in the plane-wave limit with $\sigma \rightarrow \infty$, or for a very smooth energy selectivity of the QPC, $a \rightarrow 0$. The latter case requires the use of a very sharp potential dip, that could be implemented with the multichannel beam splitter at bulk FF 2 in Ref. [13]. Within this condition, the overlap on the k -space between the *reflected* and *transmitted* wavepackets increases, thus inducing a destructive interference in the two-particle process. By decreasing the sharpness in real space of the beam splitter, the reflected and transmitted components becomes distinguishable, so that a non zero electron bunching probability is restored

Instead, for a symmetric wavefunction, this overlap provides a positive contribution to the bunching probability, i.e. $+2\langle\alpha T|\beta R\rangle$. This case is displayed in Fig. 5.8(b). Here, we compare the dynamical bunching and antibunching probabilities of a two-particle wavefunction with $\sigma = 20$ nm in presence of exchange symmetry only: in the stationary regime, the two configurations are characterized by exchanged values of \mathcal{P}_b and \mathcal{P}_{ab} .

Finally, Fig. 5.9(a) displays \mathcal{P}_b for desynchronized sources ($\Delta y \neq 0$) in presence of exchange interaction only (blue dots, $V_{12} = 0$). With contrast the the regime of synchronized sources, $\Delta y = 0$, the stationary bunching probability does not depend on the exchange statistics for $\Delta y \rightarrow \infty$, where the *random partition limit* is achieved (see Eq.(5.50)). In a time-dependent scenario, by increasing Δy , the two electrons impinge on the beam splitter with a growing time delay,

so that the overlap between the two wavepackets decreases. This reduces the relevance of their relative exchange symmetry, and gradually restores the classical probability of joint detection for two distinguishable particles. By fitting the numerical data with Eq.(5.50), we compute the characteristic length for this transition, that is $\lambda = 2\sqrt{\sigma^2 + \frac{a^2}{8\gamma}} \approx 30$ nm at $\sigma = 15$ nm, (blue solid line in Fig. 5.9(a)).

5.3 The role of Coulomb repulsion

Thanks to the use of a 4D domain for the system wavefunction, we can simulated the scattering of two electrons in 2D in presence of the exact Coulomb repulsion between the two charges. We initially introduce the long-range potential:

$$V_{12}(x_1, y_1, x_2, y_2) = \frac{e^2}{4\pi\epsilon\sqrt{(x_1 - x_2)^2 + (y_1 - y_2)^2 + d_z^2}}, \quad (5.61)$$

in the two-electron Hamiltonian of the system. ϵ is the medium permittivity and d_z accounts for the finite thickness of the 2D heterostructure in the divergence at $x_1 = x_2$ and $y_1 = y_2$.

5.3.1 Coulomb-driven antibunching

Initially we simulate bunching in the HOM interferometer for two distinguishable particles, so that the scattering process is exclusively driven by electron-electron repulsion, together with the effect of the QPC. The wavefunction at initial time is represented by the product state:

$$\Psi_C(x_1, y_1, x_2, y_2; t = 0) = \psi_\alpha(x_1, y_1)\psi_\beta(x_2, y_2). \quad (5.62)$$

Fig. 5.9(b) displays the stationary value ($t = 1.2$ ps) of the bunching probability for a range of d_z parameters and $\sigma = 20$ nm. Antibunching clearly increases with the Coulomb repulsive interaction. For a large enough d_z parameter ($d_z = 100$ nm), the *random partition limit* for distinguishable particles is restored. The two wavepackets evolve indeed independently without interacting significantly at the QPC. The overlap term in Eq.(5.49) vanishes:

$$\langle \alpha T | \beta R \rangle \simeq 0 \quad (5.63)$$

so that the bunching probability reaches 50% only if

$$\langle \alpha(\beta) T | \alpha(\beta) T \rangle = \langle \alpha(\beta) R | \alpha(\beta) R \rangle = 1/2. \quad (5.64)$$

The fulfillment of this condition shows that in the present regime the two wavepackets ψ_α and ψ_β are properly initialized, to be identical and both half-transmitted by the QPC.

Additionally, for $d_z \rightarrow 0$, the bunching probability exhibit the difference between a 1D electron-electron repulsion and the same interaction in a 2D geometry. In the first scenario, the two electrons, being confined on the same rail, are forced to get across the same coordinate, e.g. $x_1 = x_2$, with Coulomb repulsion acting as an infinite barrier for $d = 0$. On the contrary, the two-dimensional geometry presents alternative paths with a finite barrier, where the electron charge is only partially reflected by the Coulomb potential. This allows partial bunching, as displayed in Fig. 5.9(b), where \mathcal{P}_b saturates instead of vanishing by decreasing the d_z parameter.

5.3.2 Interplay between Coulomb repulsion and exchange interaction

Exchange symmetry is then added to the interacting system, to compute the dynamical bunching probability in Fig. 5.10(a), while Fig. 5.10(b) compares the stationary values of P_b in presence of electron-electron repulsion and/or exchange interaction. As visible by comparing the two frameworks, in our operating regime Coulomb repulsion dominates on the exchange interaction: by adding the indistinguishability in the two-electron wavefunction, indeed, the bunching probability is equally lowered for all the broadenings σ with respect to the separable case. Furthermore we show, in Fig. 5.9(a), the stationary bunching probability of indistinguishable and interacting electrons ($V_{12} \neq 0$) for different initial displacements Δy and $\sigma = 15$ nm: numerical data (green squares) are fit by

$$g(x) = \frac{1}{2} \cdot \left[1 - \frac{\sigma_{eff}^2}{\sigma_{eff}^2 + \alpha_{eff}^2/8\gamma} \exp\left(-\frac{x^2}{4(\sigma_{eff}^2 + \alpha_{eff}^2/8\gamma)}\right) \right] \quad (5.65)$$

(green dashed line), which corresponds to Eq.(5.51) with an effective σ_{eff} and

$$\alpha_{eff} = 2\sqrt{2\gamma}\sqrt{\Sigma_{eff}^2 - \sigma_{eff}^2}, \quad (5.66)$$

that are used as fitting parameters. The fit provides $\sigma_{eff} \simeq 21$ nm and $\alpha_{eff} \simeq 86$ nm, which are larger than the counterparts in the non interacting scenario (inset of Fig. 5.8).

As visible in both separable and non separable interacting framework (Fig. 5.10(a)), the effect of long-range Coulomb interaction turns out to depend on the spatial broadening of the wavepacket σ . The stationary bunching probabilities of the separable and non-separable cases are compared in Fig. 5.10(b). In presence of long-range Coulomb interaction, $\mathcal{P}_b(\sigma)$ differs from the quasi-linear trend in the inset of Fig. 5.8(a), where the antibunching is exclusively driven by the exchange interaction.

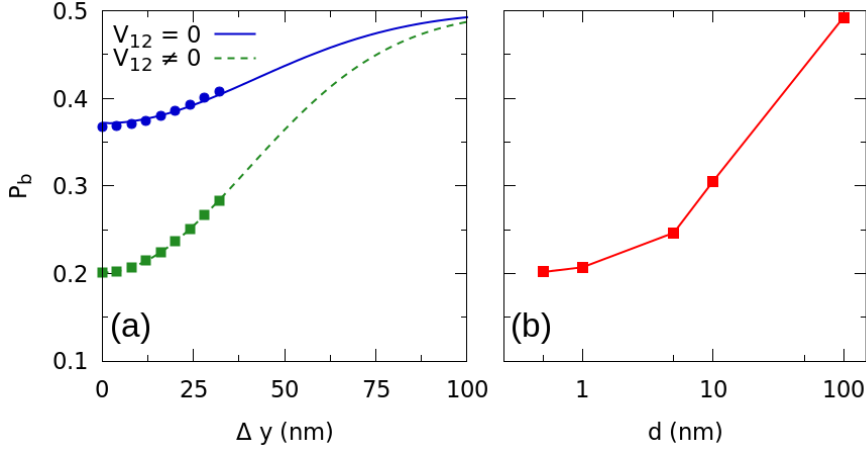


Figure 5.9: (a) Bunching probability as a function of the initial displacement Δy between two indistinguishable wavepackets ($\sigma = 15$ nm) with zero (blue) and non zero (green) Coulomb interaction V_{12} with $d = 1$ nm. For $V_{12} = 0$ the numerical data (blue dots) are compared to Eq.(5.50) (blue line) with $\alpha = 60$ nm, while for $V_{12} \neq 0$ numerical data (green dots) are fit by the equation $g(x)$ (green dashed line) as explained in the main text. The fit provides an effective broadening $\sigma_{eff} = 21.75 \pm 0.03$ nm and an effective geometrical parameter $\alpha_{eff} = 84.0 \pm 0.1$ nm. (b) Stationary bunching probability ($t = 1.2$ ps) in presence of long-range Coulomb interaction without exchange symmetry for different d parameters in Eq.(5.61) and $\sigma = 20$ nm .

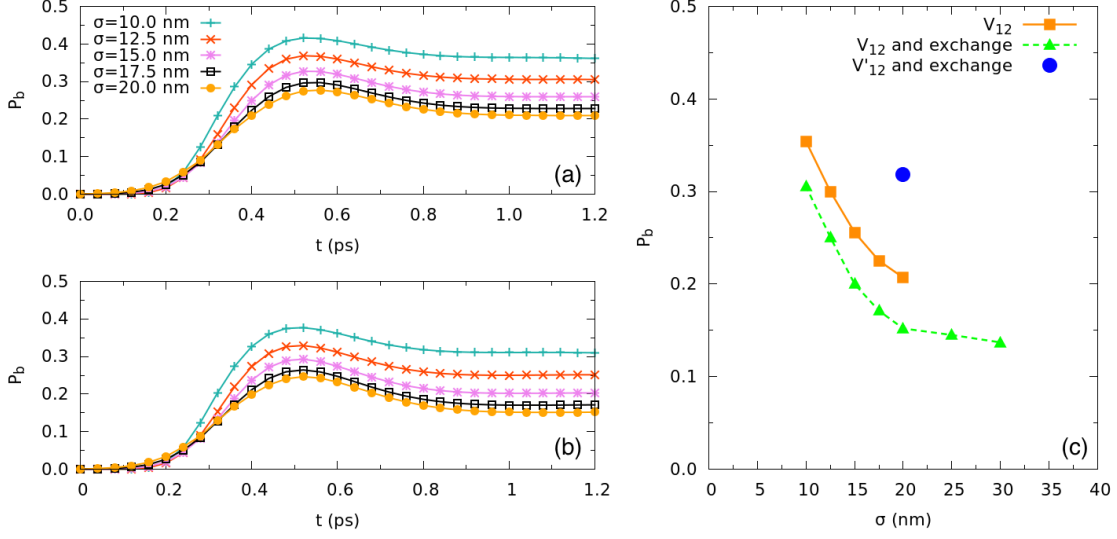


Figure 5.10: (a) Bunching probability in presence of long-range Coulomb interaction without exchange symmetry and (b) with exchange symmetry for different σ and $d = 1$ nm. (c) Comparison between the stationary bunching probability of two distinguishable electrons (yellow dotted line) and indistinguishable electrons (green dotted line) with long-range Coulomb interaction. We also report the stationary bunching probability of two indistinguishable electrons in presence of screened Coulomb interaction for $\sigma = 20$ nm and a cutoff length $\sigma_c = 5$ nm (blue circle).

5.3.3 Effects of screening

Finally, we add the effect of screening on two-electron bunching for the largest wavepacket, i.e. $\sigma = 20$ nm. To this aim, we include an exponential damping to Coulomb repulsion, so that the range of interaction is reduced:

$$V'_{12}(x_1, y_1, x_2, y_2) = \frac{Ce^2}{4\pi\epsilon} \frac{e^{-\frac{\sqrt{(x_1-x_2)^2+(y_1-y_2)^2}}{\sigma_c}}}{\sqrt{(x_1-x_2)^2+(y_1-y_2)^2+d_z^2}}, \quad (5.67)$$

as done in Ref. [18] for two wavepackets that scatter at a 1D double barrier. Here, the parameter C is a global constant that quantifies the interaction, while σ_c determines its spatial range. The stationary bunching probability is reported in Fig. 5.10(b) for $\sigma = 20$ nm, $\sigma_c = 5$ nm and $C = 1$ (blue dot) and compared to the unscreened simulations. The value of the bunching probability in the screened scenario is very near to the one of the exchange-driven scattering process, reported in the inset of Fig. 5.8(a). This suggests that, for the present damping parameters, exchange-driven bunching is restored, and the dominance of the Coulomb interaction is gradually suppressed in the intermediate regimes.

We further stress that our operating regime differs from the one adopted in traditional HOM experiments, where SESs do not generate strongly-localized excitations, but rather wavepackets with an emission time of the order of tens of picoseconds (two orders of magnitude larger than in our geometry)[64]. The simulation of larger wavepackets is beyond the current limit of our computing capabilities, already involving massive parallelization and costly intra-node data communication protocols on top-level European supercomputing hardware. In order to fulfill a number of boundaries entailed by the Split-Step Fourier Method, as avoiding aliasing or the underestimation of the wave-packet dynamics, a significantly larger number of grid points would be required.

However, we can propose some predictions by considering our numerical results and the analytical model we implemented to support our findings.

- (i) Regarding the non-interacting case, Eq.(5.58) can be used to estimate the bunching probability for wavepackets with a sigma of the order of micrometers in the present geometry. Our QPC is characterized by a smoothness in the k -space given by $a = 60$ nm, so that if $\sigma = 10^{-6}$ m, then $\Sigma \simeq \sigma$ and the bunching probability is approximately zero.
- (ii) In presence of long-range interaction, we do not observe a full antibunching by increasing the wavepacket size. In the range of energies we are considering, the long-range Coulomb repulsion produces a saturation of the bunching probabilities by increasing sigma. In Fig. 5.10(c) we introduce the stationary values of \mathcal{P}_b for two additional numerical simulations of indistinguishable electrons with $\sigma = 25$ and 30 nm. The green dashed curve confirms that, in our operating regime, the bunching probability saturates to a non zero value for larger wavepackets.

Such predictions apply to the present scenario, where the bunching is sensitive to the energy selectivity of the QPC and the long-range Coulomb interaction is considered. Indeed, the bunching probability in presence of screening suggests that the dominance of the Coulomb interaction is suppressed. Therefore, for a proper choice of σ_c , the bunching probability eventually decreases to zero for larger wavepackets, as experimentally observed.

5.4 Von Neumann entropy for the spatial entanglement

Finally, we measure the dynamical *Von Neumann entropy* of the antibunched configuration in the two-electron system, which represents the degree of non-separability of the spatial representation of the two-particle wavefunction.

We partition the Hilbert space into two separate subsystems, the *top* (T) and the *bottom* (B) region in the inset of Fig. 5.11(a), so that $H = H_T \otimes H_B$. Due to the indistinguishability of the two electrons, we fix the position of particle 1 in the top region ($(x_1, y_1) \in T$), and particle 2 in the bottom one ($(x_2, y_2) \in B$); we expect the opposite configuration to be equally entangled due to the symmetry of the two single-electron wavepackets at $t = 0$.

The exact computation of the density matrix for two particles in a 2D real space requires the allocation of a density matrix with a large memory cost, together with challenging communications between the MPI processes involved in our parallelization scheme. Thanks to the chirality of the edge states, we can reduce the computational burden and compute the von Neumann entropy by projecting the two-particle wavefunction on the 1D path of edge channels at the outputs of the device. We therefore fix the \hat{y} -coordinate of the two rails, with correspondence to the expected maximum of the density probability distribution, namely $y_1 = y_1^* \in T$ and $y_2 = y_2^* \in B$. To provide y_1^* and y_2^* , we identify the maximum of the two single-electron wavepackets at $t = 0$, in the \hat{x} direction. Note indeed that the initial distance between the 1D rail of the edge channel and the turning point of the confining barrier must coincide before and after the scattering with the QPC. The process is indeed energy conserving, and the bandstructure has the same bending before and after the opening of the beam splitter. Then, in the present case, $y_1^* = 11.5$ nm and $y_2^* = -11.5$ nm (black dashed lines in the inset of Fig. 5.11(a)).

The conditional two-particle wavefunction,

$$\phi(x_1, x_2) = \Psi(x_1, y_1^*, x_2, y_2^*) \quad (5.68)$$

is then renormalized, so that the density matrix reads:

$$\rho_{TB}(x_1, x_2; x'_1, x'_2) = \phi(x_1, x_2) \phi^*(x'_1, x'_2). \quad (5.69)$$

Note that the von Neumann entropy generally does not depend on the subspace chosen to be traced out. However, in our parallelization scheme the real-space domain of the second particle is distributed among the MPI processes in a Cartesian topology. Therefore, the following definition of the reduced density matrix has the lowest computational cost:

$$\rho_T(x_1, x'_1) = \int_{x_2 \in B} dx_2 \phi(x_1, x_2) \phi^*(x_2, x'_1). \quad (5.70)$$

Each MPI process can indeed allocate its contribution to the global reduced density matrix $\rho_T(x_1, x'_1)$, by summing over its local domain $\hat{r}_2 = (x_2, y_2)$. Then, MPI processes gather their local reduced density matrix to a master process. The latter finally calculates the spatial entanglement by means of the von Neumann entropy:

$$S = \text{Tr}[\rho_T \ln(\rho_T)]. \quad (5.71)$$

Fig. 5.11(a) shows the dynamics of the von Neumann entropy S , with exchange symmetry only. An increase of the spatial distribution σ of the wavepacket quenches the entanglement, so that we expect it to vanish in the plane-wave limit. In Fig. 5.11(b) we compare the stationary von Neumann entropy in presence of: (i) exchange symmetry alone (red solid line), (ii) a separable wavefunction with Coulomb interaction (green dashed line), (iii) Coulomb interaction and a symmetric wavefunction (blue dotted line). In the latter case, the Coulomb repulsion, which acts as an additional barrier, further prevents the two particles to reach the opposite regions, so that entanglement is reduced. The von Neumann entropy in the interacting scenario with exchange interaction does not differ from the one in the distinguishable case: the two electrons are already prevented to occupy the same coordinates due to the infinite barrier represented by V_{12} at $(x_1, y_1) = (x_2, y_2)$.

5.5 Bunching probability for alternative single-electron excitations

As detailed in Sec. 3.1, the use of Gaussian wavepacket of edge states in our discussion is aided by their higher numerical control during time evolution, with respect to alternative shapes for an

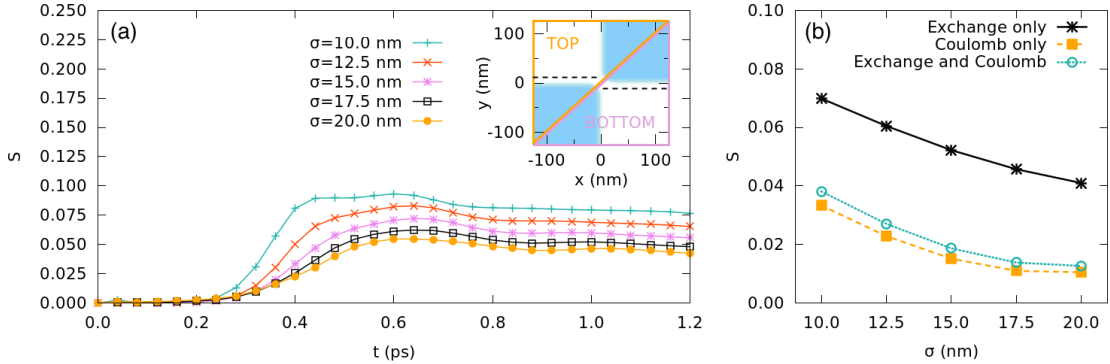


Figure 5.11: Entanglement between T and B regions in the antibunched configuration. (a) Von Neumann entropy for different σ and $d = 1$ nm in presence of exchange symmetry only; the dotted black lines in the inset show where the full scale wavefunction is projected with respect to the top-view of the potential profile. (b) Comparison between the stationary Von Neumann entropy in the different scenarios.

electron wavepacket, together with the recent interest towards the generation of single-electron excitations with a Gaussian shape [72] by means of quantum dot pumps.

However, experimental works on two-electron bunching mainly exploit alternative SES to study two-electron bunching in the HOM interferometer. By neglecting Coulomb interaction between the two charges, we adopt a semi-analytical approach to predict the bunching probability for alternative shapes of the localized electron wavefunction.

In Sec. 5.2.1, we calculate the bunching probability for two indistinguishable electrons in an effective 1D model:

$$\mathcal{P}_b(\Delta y) = \langle \psi_\alpha^r | \psi_\alpha^r \rangle \langle \psi_\beta^t | \psi_\beta^t \rangle + \langle \psi_\alpha^t | \psi_\alpha^t \rangle \langle \psi_\beta^r | \psi_\beta^r \rangle - 2 |\langle \psi_\alpha^t | \psi_\beta^r \rangle|^2, \quad (5.72)$$

where α and β is the wavepacket index, while t and r label the transmitted and reflected component of the single-electron wavepacket, respectively.

The scalar products in Eq.(5.72) are here computed by means of the weight functions $F(k)$, $F_r(k)$ and $F_t(k)$ in the Fourier space, for a single-electron wavepacket that scatters at a QPC. After simulating the dynamics of the single-electron excitation in the full-scale geometry of the HOM interferometer, we apply the *wave-packet method* to compute the above weight functions.

By accounting for the presence of a discrete simulation grid, so that $\Psi(x, y) \rightarrow \Psi_{x,y} = \Psi(x, y) \sqrt{dx} \sqrt{dy}$, we rewrite the scalar products in Eq.(5.72) as follows:

$$\langle \psi_A^t | \psi_A^t \rangle = \langle \psi_B^t | \psi_B^t \rangle = \sum_k |F_t(k)|^2, \quad (5.73)$$

$$\langle \psi_A^r | \psi_A^r \rangle = \langle \psi_B^r | \psi_B^r \rangle = \sum_k |F_r(k)|^2, \quad (5.74)$$

$$\langle \psi_A^t | \psi_B^r \rangle = -i \sum_k F_t^*(k) F_r(k) e^{ik\Delta y}, \quad (5.75)$$

where the phase factor $e^{ik\Delta y}$ has been introduced *a posteriori* to simulate the time delay induced by desynchronized sources.

5.5.1 Lorentzian wavepackets in the energy domain

A large number of electronic HOM experiments have been realized by using *mesoscopic capacitors*, to alternatively inject electrons and holes. These single-charge excitations are called *Landau quasiparticles* and are characterized by a Lorentzian distribution in energy (see Sec. 2.1 for details). By neglecting many-body effects arising from the nature of this quantum excitation, we exploit our time-dependent numerical method to simulate the injection of a "Landau quasi-particle", by assuming that this is only defined by the shape of its energy distribution. The single-electron wavefunction reads:

$$\Psi(\epsilon, t_0) = \frac{N e^{\frac{i\epsilon t_0}{\hbar}}}{\epsilon - \epsilon_0 + i\frac{\Gamma}{2}} = F_{ini}(E(k, n=0)) \quad (5.76)$$

where t_0 is the injection time, ϵ_0 the injection energy and $\gamma = \frac{1}{v\tau_e}$ is the FWHM.

The electron wavefunction in the energy domain is therefore weighted by $F[E(k, n=0)] = \Psi(\epsilon, t_0)$, while in the wavevector space it depends on the specific bandstructure $E = E(k(x_0))$. For a linear $E(k)$, $F(k)$ can be approximated by a Lorentzian shape, so that in the real space it has an exponential decay on the direction of propagation, the \hat{y} direction. The actual shape, however, depends on the specific bending of the Landau levels at the injection coordinate, y_0 .

In Fig. 5.12 we show our numerical simulation of an HOM experiment with Lorentzian wavepackets. Panel (a) displays the energy bandstructure $k = k(E)$ for the first Landau level in our operating

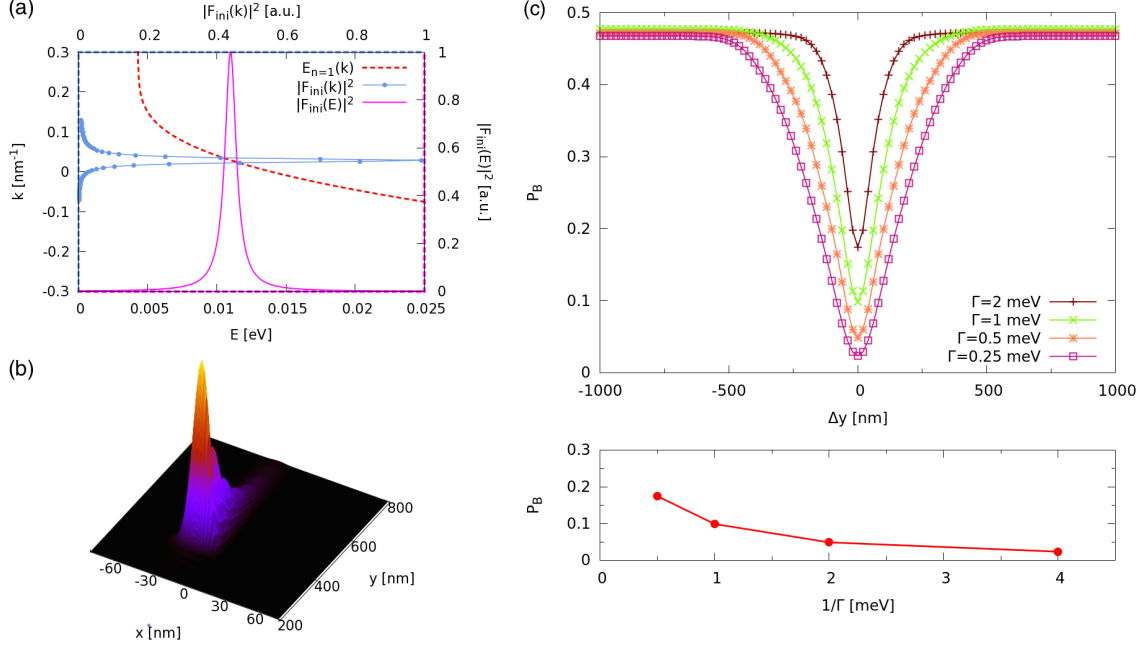


Figure 5.12: (a) Energy distribution of the Lorentzian wavepacket at $t = 0$ ps with $\Gamma = 1$ meV (purple line) and corresponding distribution on the wavevector space k (light blue line). The red dashed line identifies the bandstructure of the first Landau level, which relates energies and wavevectors. (b) Electronic density probability at $t = 0$ ps for the Lorentzian wavepacket with $\Gamma = 1$ meV. (c) Two-electron bunching probability for desynchronized sources computed by means of our semi-analytical method in presence of single-electron wavepackets with a Lorentzian distribution in energy. The minimum of the Pauli dip for different values of Γ are compared in the bottom panel.

regime, as well as the energy-dependent and wave-vector dependent weight function, $F_1(E)$ and $F_1(k)$ respectively. Both are characterized by a Lorentzian shape, due to the quasi-linearity of $E = E(k)$ in the range of energies we are simulating, together with the use of a small enough Γ parameter. The central energy is indeed large enough to lie far from the bottom part of the first Landau level, where the bending is mostly quasi-parabolic, and small enough to reduce the effect of scattering-induced filling of the second Landau Level. Indeed, in case of energy-conserving scattering processes, only those states with a flat dispersion, i.e. not contributing to electron transport, can be significantly filled. The central energy is $\epsilon_0 = 20$ meV and $\Gamma = 2, 1, 0.5, 0.25$ meV. The real-space profile is displayed in panel (b). The exponential damping in the \hat{y} -direction is here clearly visible.

By means of the Split-Step Fourier method, we evolve the single-electron wavefunction in the HOM geometry and provide the weight functions for the initial, reflected and transmitted wavepackets; with Eq.(5.72) we finally compute the purely exchange-driven bunching probability. Fig. 5.12(c) displays the Pauli dip for a set of Γ parameters, while in panel (d) we show $P_b(\Gamma)$ for synchronized sources.

Here, the minimum bunching probability has a lower value, with respect to a Gaussian wavepackets. This follows from the higher localization in the energy domain of a Lorentzian distribution of states with respect to a Gaussian one. Indeed, due to the presence of larger tails in the first

case, the number of states that contribute significantly to the two-electron destructive interference is smaller. The narrower peak induces therefore to a larger overlap between the reflected and transmitted components of the two wavepackets.

By increasing the time delay between the injection from the two sources, we observe that the bunching probability saturates for values smaller than $1/2$, regardless the value of Γ . Note indeed that, due to its smaller energy dispersion, it is numerically more difficult to identify the central coordinate $x_0(k_0)$ of the electron wavepacket that realizes the ideal condition for the QPC, i.e. $T(k_0) = 0.5$.

In summary, in this chapter, we contribute to shed light on the apparent violation of Pauli exclusion principle in two-electron bunching by presenting the numerical results of our full-scale modeling of a solid-state electron beam splitter at bulk FF 1 and the time-dependent simulation of two-electron bunching in a Hall HOM interferometer.

Our numerical method includes exactly the interplay between a realistic geometry of the QPC in 2D and correlation in the two-particle wavefunction, so that we can relate the non-zero bunching probability to the exact energy selectivity of the electron beam splitter, according to its specific design. A full understanding of this interplay is important for the integration of the HOM interferometer into sophisticated computing architectures as the Hanbury-Brown-Twiss interferometer. Moreover, it can also be exploited to measure the degree of indistinguishability of electrons generated from different sources [110], or to study the statistics of exotic particles as anyons in the fractional quantum Hall regime [111]. Furthermore, the electron HOM experiment in the IQH regime has been recently applied to study the decoherence phenomena affecting quasi-particles emitted from SESs [65].

The decrease in the bunching probability by increasing the spatial localization confirms, for a full scale 2D spatial geometry, the findings of Ref. [19], where this effect is explained with a 1D time-dependent model as a signature of the non-orthogonality between the states scattered by the potential barrier.

By means of a simplified analytical model in 1D, we relate the stationary bunching probability to the non-perfect overlap between the transmitted and reflected wave-packets generated from the single-electron scattering at the QPC. This model clarifies the interplay between the spatial dispersion of the wavepacket σ and the geometry of the QPC, which is encoded in the single-particle parameter Σ of Eq.(5.50).

By comparing the predictions of the analytical model and the results of the full-scale numerical simulations, we also validate the empiric equations for the reflection and transmission coefficients of a QPC in Eq.(4.11), which is used to predict analytically the bunching probability in the HOM interferometer and the transmission amplitude in the multichannel MZI. Moreover, By using a semi-analytical model based on the wavepacket approach and the full-scale numerical simulation of single-electron scattering at the beam splitter, we also estimate the electron bunching probability for wavepackets with a Lorentzian distribution in energy, as the Landau quasi-particles emitted from mesoscopic capacitors. Thus, we demonstrate that our findings do not depend qualitatively on the shape of the excitation.

We show how the perfect antibunching is recovered in the plane-wave limit and point out the role of exchange symmetry by simulating the HOM experiment both for a symmetric and an antisymmetric wavefunction. As an additional advantage in treating exactly the two-particle scattering, we include electron-electron repulsion in the Hamiltonian to evaluate the interplay with the fermionic statistics. We observe that in a 2D real-space geometry, differently from the typical 1D scenario adopted in literature, the bunching probability does not vanish for an infinite repulsive Coulomb interaction. Additionally, for unscreened interacting particles, we find that $\mathcal{P}_b(\sigma)$ saturates to non zero values. Our conclusions do not contradict the results obtained in Ref. [64], as in the experiment the device does not generate strongly-localized excitations, but

rather wavepackets with an emission time of the order of picoseconds, i.e. 2 orders of magnitude larger than in our geometry. Furthermore, by including an exponentially-decaying screening in our interacting regime, we show how the effect of Coulomb repulsion can be suppressed with a proper choice of the damping length, so that the limit of exchange-driven bunching is restored, also for interacting particles.

Finally, a dynamical measurement of the spatial von Neumann entropy between the top and bottom regions of the device allows us to assess the spatial entanglement between the two anti-bunched carriers; we found that long-range Coulomb interaction quenches the entanglement by enhancing the Pauli dip with respect to the antisymmetry alone.

Chapter 6

Conditional phase shifter for entanglement generation

A universal set of logic gates for quantum computing requires a two-qubit device able to generate entanglement from a product state, in addition to arbitrary single-qubit operations, as the ones implemented with the beam splitter and the phase shifter in Sec. 4.2.1 and Sec. 4.2.2 respectively. Entanglement can be realized by means of the *conditional phase shifter*, that generates non-separable two-qubit states, by selectively adding a phase γ to a specific configuration of the two-qubit state.

In a two-level system with states $|0\rangle$ and $|1\rangle$, the two-qubit transformation performed by the conditional phase shifter is described, on the ordered basis $\{|00\rangle, |01\rangle, |10\rangle, |11\rangle\}$, by the following matrix:

$$\mathbf{T}(\gamma) = \begin{pmatrix} 1 & 0 & 0 & 0 \\ 0 & 1 & 0 & 0 \\ 0 & 0 & 1 & 0 \\ 0 & 0 & 0 & e^{i\gamma} \end{pmatrix}, \quad (6.1)$$

which selectively rotates the $|11\rangle$ component of the two-qubit wavefunction by a phase factor γ , without affecting the relative weight of the four states. Thus, the detection of quantum entanglement requires a composite transformation able to alter the detection probability of the states and to create maximally entangled Bell's states[112].

Differently from early solid-state proposals based on quantum wires [22], we propose and study its realization in the IQH regime with the geometry reported in Fig. 6.1. Here, two of our multi-channel MZIs [13] are concatenated in parallel to generate a two-qubit gate. Due to a bulk FF 2, two cyclotron-resolved Landau Levels ($n = 0$ and $n = 1$) run at each side of the confining lateral potential. By varying the width of the mesa with local FF 1 (W), the lateral distance between the two counterpropagating channels with $n = 1$ is increased or reduced, while the two channels with $n = 0$ can be further spaced by increasing the indentation where they propagate.

Single-electron sources (labeled with S_0 and S_1 in the figure) inject identical electrons, e.g. in the ground state ($n = 0$), at each side of the device. Each single charge is partitioned between the two copropagating edge channels by the electron beam splitter, that is here the sharp potential dip studied in Sec. 4.2.1. In the central area of the device, the strength of Coulomb interaction between the two counterpropagating carriers depends on their Landau indexes. To induce a selective coupling, we properly tune W and limit the active region (zoomed area in Fig. 6.1) to the outer edges of the area at bulk FF 1, which is accessible only by the edge channels with $n = 1$.

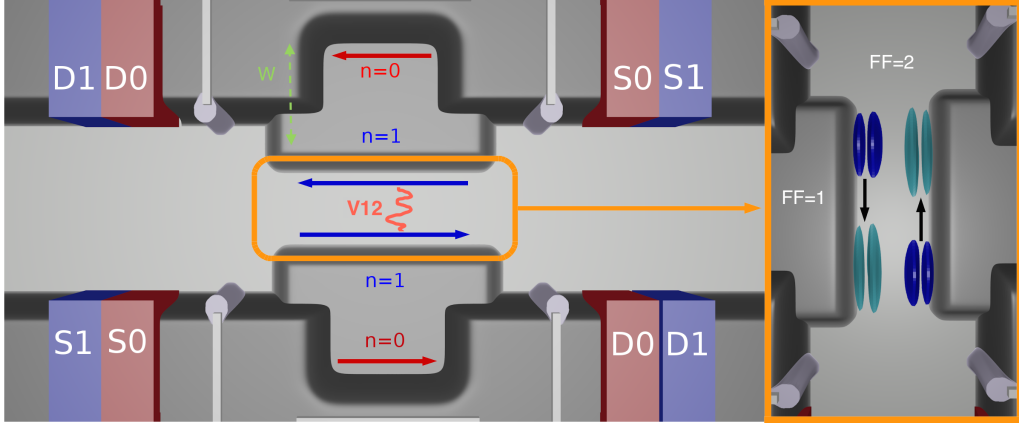


Figure 6.1: Rendered picture of our proposal for a solid-state implementation of the conditional phase shifter [23]. Two multichannel MZIs of Ref. [13] are concatenated in parallel at each side of the device. The two channels with Landau index $n = 1$ interact in the active region (squared yellow box), while the channels with $n = 0$ are further separated by increasing the width W of the region at FF 1. The inset displays the initial and final single-electron density probability of the two particles in the $n = 1$ channels.

Here, Coulomb repulsion is the coupling force that induces the \mathbf{T} transformation. When two electrons in $n = 1$ approach each other, electron-electron repulsion transforms part of their kinetic energy into a repulsive coupling potential, so that the velocity along their path is reduced. The relative distance returns then to the original value, and the potential energy is transformed back into kinetic energy when the initial velocity is restored. This turns into a delay in the propagation of the two electrons compared to the non-interacting case, that corresponds to a phase factor in front of the $|11\rangle$ component of the two-qubit wavefunction.

By resorting to our numerical solver for two-electron transport in a 2D topology, we simulate the Coulomb-driven scattering between two single-electron wavepackets in the active region of the conditional phase shifter, and prove that Coulomb interaction can act as a selective entangler in this geometry. In Sec. 4.2.3 we showed that our time-dependent numerical method is able to reliably analyze the geometry-dependent properties of the MZI. With contrast to effective 1D models, it requires indeed the design of the full-scale potential profile V_{ext} affecting electron transport in the device and so that no guessing on the energy dependence of the transmission coefficients is needed. Moreover, in the HOM experiment presented in Sec. 5.3.2, we observed that the manipulations of the 4D wavefunction for two electrons in 2D ensures the exact inclusion of bare or screened Coulomb interaction. Our full-scale approach is then even more suitable in the present device, where the geometrical parameters of the system, e.g. the length of the coupling region and the distance between the channels, affect the strength of Coulomb repulsion and the corresponding γ factor.

The system is initialized with two counterpropagating states $\psi_{\alpha,i}(x,y)$ and $\psi_{\beta,j}(x,y)$ localized at each side of the confined 2DEG. The two wavepackets are characterized by wavevectors k_{α} and k_{β} that are identical in module but opposite in sign. The Landau index of the two states depends on the system under study: we generally define the (n,m) configuration as the two-electron state generated by fixing $\psi_{\alpha,i=n}(x,y)$ and $\psi_{\beta,j=m}(x,y)$. Exchange interaction is then eventually added by computing the Slater determinant, as in the HOM interferometer of Sec. 5.3.2.

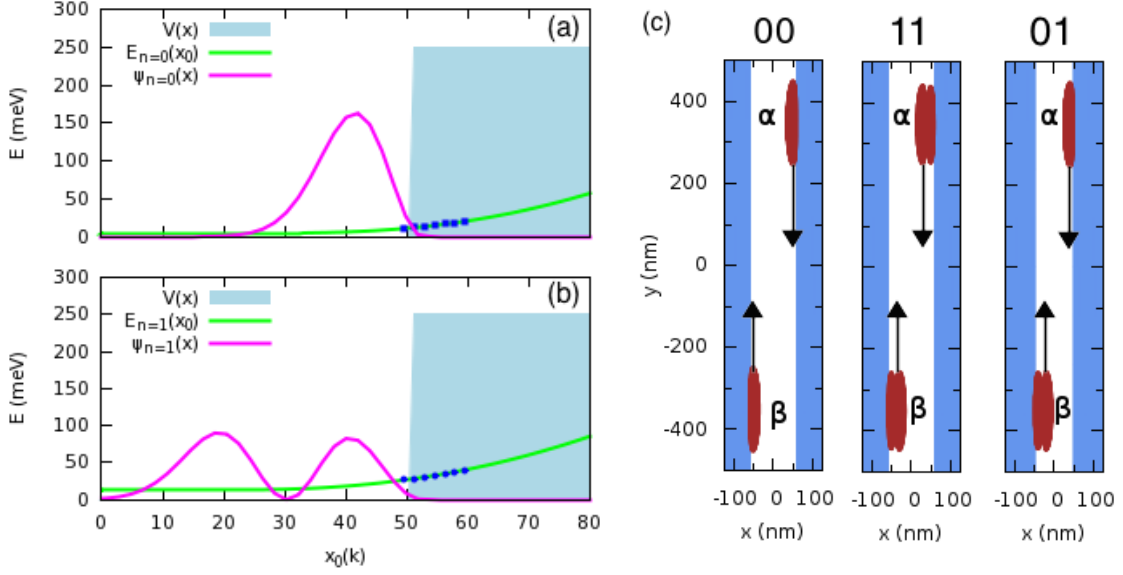


Figure 6.2: Bandstructure of the active region induced by the sharp potential profile (blue shaded area) for the (a) first and (b) second Landau level (green lines) at $B = 5$ T. The blue dots define the centers of the edge states contained in the wavepackets. The purple line define the transverse profile of the probability density for a wavepacket injected with a central energy $E^0 \simeq 15$ meV and $\sigma = 40$ nm. (c) Map of the active region of the device (blue) and initial density probability distributions of two single-electron wavepackets (red) in the three configurations under study: (00) both electrons in channel 1, (01) one electron in channel 1 and one electron in channel 0, (11) both electrons in channel 1. Black arrows define the direction of propagation of the wavepackets.

6.1 A toy model with sharp barriers

The active region of the conditional phase shifter is here modeled by a translationally invariant external potential that defines two confining barriers with distance d .

We initially adopt a toy model where we assume the active region to be described by sharp square walls, as displayed in Fig. 6.2 (blue shaded area). The transverse profile of the external potential $V_{ext}(x)$ is described by a combination of Heaviside functions in the \hat{x} -direction, as follows:

$$V_{ext}(x) = V_b[\theta_H(x - x_R) + \theta_H(x_L - x)], \quad (6.2)$$

with $V_b = 250$ meV and $|x_R - x_L| = d$.

As in the multichannel MZI, we operate with two cyclotron-resolved channels at each side, and simulate the injection of electron wavepackets in the available channels. Tab. 6.1 reports the central energies and group velocities for the set of wavepackets with $\sigma = 40$ nm and $n = 0$ or $n = 1$. In our operating regime, single-charge wavepackets with a Gaussian shape are injected with the same central energy $E_0^0 = E_1^0 = 15$ meV, while, due to the different smoothness of the corresponding Landau levels, the group velocities differ significantly: $v_g^0 = 2 \cdot 10^5$ m/s and $v_g^1 = 0.7 \cdot 10^5$ m/s. The distance between the two confining transverse barriers runs from $d = 100$ nm to $d = 200$ nm. Moreover, we investigate Coulomb-driven scattering at smaller distances, in order to prove that tunneling is negligible for $d > 40$ nm.

Fig. 6.2 shows the transverse profile of the probability density for a single-electron wavepacket with $\sigma = 40$ nm (purple solid line) in the (a) first and in the (b) second Landau Level. The picture

displays only the positive domain of the device in the \hat{x} direction, while the negative counterpart of the transverse density probability is symmetric by construction. The single-electron density probability at initial time vanishes at the origin, so that we expect that the two counterpropagating wavepackets do not overlap significantly in the transverse direction. This suppresses elastic tunneling between the two channels and ensures that the scattering is purely driven by Coulomb repulsion.

To discuss the selective coupling in the conditional phase shifter, we analyze two-electron dynamics and correlations in the three different initial configurations reported in Fig. 6.2(c), named (00), (01) and (11).

6.1.1 Coulomb-driven scattering in the (00) configuration

The effect of Coulomb interaction is here encoded in the difference between the final density probability of the second particle in the interacting case and in the non-interacting scenario. Due to the presence of exchange, we expect that at final time ($V_c \simeq 0$) the probability of one of the two particles, e.g. particle 2, integrated on the other one, shows the real-space configuration of both single-electron wavepackets in the two outputs. An example is presented in Fig. 6.3 for two indistinguishable electrons in the (a) 0 channel and (b) 1 channel.

The difference between the maxima of the two distributions at the outputs of the device in the interacting and non-interacting scenario, namely δy depends on the geometry of the active region. In detail, it can be strongly affected by the distance between the two lateral edges, the wavepacket size and the smoothness of the confining barriers. With regards to the last parameter, a proper design of $V(x)$ with sharp lateral barriers is necessary to induce a quasi-parabolic dispersion of the second or first Landau Level, rather than a linear one. This ensures indeed a larger δy : in the presence of linear dispersion, the kinetic energies of the two wavepackets are initially decreased and finally increased by the same amount, so that the effect of electron-electron repulsion would not be equally detectable.

Two-electron scattering is initially driven by a long-range Coulomb interaction

$$V_{12} = \frac{e^2}{4\pi\epsilon_r \sqrt{(x_1 - x_2)^2 + (y_1 - y_2)^2 + d_z^2}}, \quad (6.3)$$

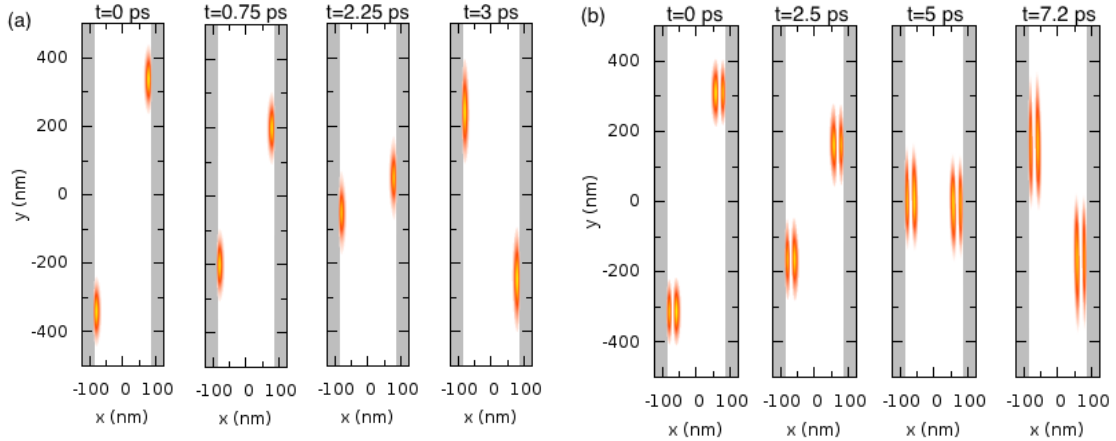


Figure 6.3: Density probability of particle 2 in the (a)(00) and (b)(11) configuration at different iteration times in the geometry of the toy model with $d = 180\text{nm}$, $\sigma = 40\text{nm}$ and $E^0 \simeq 15\text{ meV}$.

while screening effects, e.g. induced by metallic gates or background electrons, are later accounted for by means of an exponential damping in the Coulomb potential, i.e.

$$V_{12} = \frac{Ce^2 \exp(-\sqrt{(x_1 - x_2)^2 + (y_1 - y_2)^2}/\sigma_c)}{4\pi\epsilon_r \sqrt{(x_1 - x_2)^2 + (y_1 - y_2)^2 + d_z^2}}, \quad (6.4)$$

where σ_c describes the effective interaction length, C the amplitude of the screening and d_z avoids the divergence at $\mathbf{r}_1 = \mathbf{r}_2$.

First, we simulate Coulomb-driven scattering of two indistinguishable electrons both in channel $n = 0$, i.e. in the (00) configuration, for a number of wavepacket sizes $\sigma = 20, 30, 40, 50, 60$ nm and $d_z = 1$ nm. In presence of exchange interaction, the antisymmetric wavefunction $\Psi(x_1, y_1, x_2, y_2)$ is initialized with the two electrons in both wavepackets. The two-particle probability,

$$\mathcal{P}(x_2, y_2) = \int dx_1 \int dy_1 |\Psi(x_1, y_1, x_2, y_2)|^2 \quad (6.5)$$

shows therefore the dynamics of both single-electron wavepackets in the 0 channel.

To define the quantum rails where the two electrons propagate, we select the two maxima of $\mathcal{P}(x_2, y_2)$ in the transverse direction at initial time $t = 0$, i.e. $x_1 = x_1^M$ and $x_2 = x_2^M$. Then, we calculate the maxima in the \hat{y} -direction of the above probability projected on x_2^M , $\mathcal{P}(x_2^M, y_2)$, at the end of the Coulomb-driven scattering for the interacting ($y_2 = Y_2^I$) and non interacting ($y_2 = Y_2^{NI}$) simulation. The spatial shift induced by Coulomb interaction is finally computed as $\delta y = |Y_2^I - Y_2^{NI}|$.

Effects of the bandstructure on the spatial shift δy

Fig. 6.4 displays δy as a function of the distance between the two barriers, d , for different values of σ . Our numerical simulations show a decrease in δy by increasing the lateral distance between the two edges, which slightly depends on the wavepacket size. In particular, δy is generally enhanced for smaller wavepackets, when $d > 120$ nm, since the stronger localization of the electron charge increases the electron-electron repulsion. For smaller values of the parameter d , the spatial shift δy starts to invert its trend.

We relate this behavior to the bending of the Landau levels in the present operating regime. In addition to depending on the transverse shape of the external potential $V_{ext}(x)$, the smoothness of the Landau levels is affected by the finite size of the simulation box. This follows from the use of periodic boundary conditions to compute the edge states. In the effective 1D Hamiltonian $H_{eff}(x)$, the parabolic magnetic potential $V_B(x)$ centered at $x_0(k)$ adds to the designed potential profile $V_{ext}(x)$. When the center of the right barrier, x_R , approaches the positive boundary of the simulation box, L_x , the magnetic confinement $V_B(x)$ at the negative boundary of the device, $x \rightarrow -L_x$, is very large. An electron wavepacket initialized at $x_0 \rightarrow x_R$ experiences therefore a large magnetic barrier in addition to $V_{ext}(x)$.

When $x_0(k)$ is distant from the edge, the finite-size of the simulation box becomes less effective. Finally, when $x_0(k) \rightarrow 0$, the quasi-parabolic dispersion at the right and left borders of $V_{ext}(x)$ overlap, so that the minimum of the Landau levels increases; this is depicted in Fig. 6.5, which shows the bandstructure of the (a) first and (b) second Landau Levels for different values of the parameter d , together with the energy broadening we use to compute the Gaussian wavepackets. Here, we initialize the center of the wavepacket $x_0(k_0)$ at a fixed distance from the turning points of the confining barrier, x_L or x_R . Therefore, the central energy E_n^0 and the energy broadening σ_E^n of the wavepacket slightly decreases by reducing d , as reported in Tab. 6.1.

Additionally, Fig. 6.5(b) shows that the bandstructure of the second Landau level is generally characterized by a smoother bending, thus inducing a smaller energy broadening for $n = 1$ with

respect to a wavepacket initialized in $n = 0$. We further observe that in our operating regime the energies are well below the third Landau level, whose minimum is represented by the grey dashed line at $E_{min}^3 \simeq 21$ meV.

Coulomb energy exchanged during the two-electron scattering

To estimate the amount of Coulomb energy exchanged during the scattering in the (00) configuration, we initially map the Coulomb potential $V_{12}(x_1, y_1, x_2, y_2)$ by fixing the x_1 and x_2 coordinates to the maxima of the single-electron wavepackets, namely $x_1 = x_1^M$ (right channel) and $x_2 = x_2^M$ (left channel):

$$V(x_1^M, y_1; x_2^M, y_2) = \frac{e^2}{4\pi\epsilon_r \sqrt{(x_1^M - x_2^M)^2 + (y_1 - y_2)^2 + d^2}} \quad (6.6)$$

The Coulomb potential energy $V(x_1^M, y_1, x_2^M, y_2)$ is then averaged over the discrete set of \hat{y} -coordinates that define the path of each edge channels, i.e. $y_1 = -y_2 = Y$ with $Y \in [-L_y, L_y]$, where L_y is the positive coordinate of the boundary in the \hat{y} -direction.

By accounting for the spatial distribution of the wavepackets, we average the Coulomb potential $V(x_1^*, Y; x_2^*, -Y)$, on a 2D Gaussian distribution $F(x, x^*, y, y^*)$ centered in $x^* = x^M$ and $y^* = Y$,

$$F(x, x^M, y, Y) = a_x e^{-(x-x^M)^2/2\sigma_x^2} a_y e^{-(y-Y)^2/2\sigma_y^2}, \quad (6.7)$$

with σ_x and σ_y real-space broadening of the distribution in the transverse and longitudinal direction, respectively. The integrated Coulomb energy exchanged during the scattering per length size reads:

$$\mathcal{E}_c = \frac{1}{L_y} \int dY dx_1 dx_2 dy_1 dy_2 F(x_1, x_1^M, y_1, Y) V(x_1^M, Y, x_2^M, -Y) F(x_2, x_2^M, y_2, -Y). \quad (6.8)$$

\mathcal{E}_c is displayed in Fig. 6.4(b) as a function of the distance d for different values of σ . Here, we approximate the spatial distribution of a single-electron wavepacket with $n = 0$ by means of the above Gaussian distribution $F(x, x^M, y, Y)$ with $\sigma_x = 5$ nm and $\sigma_y = \sigma$.

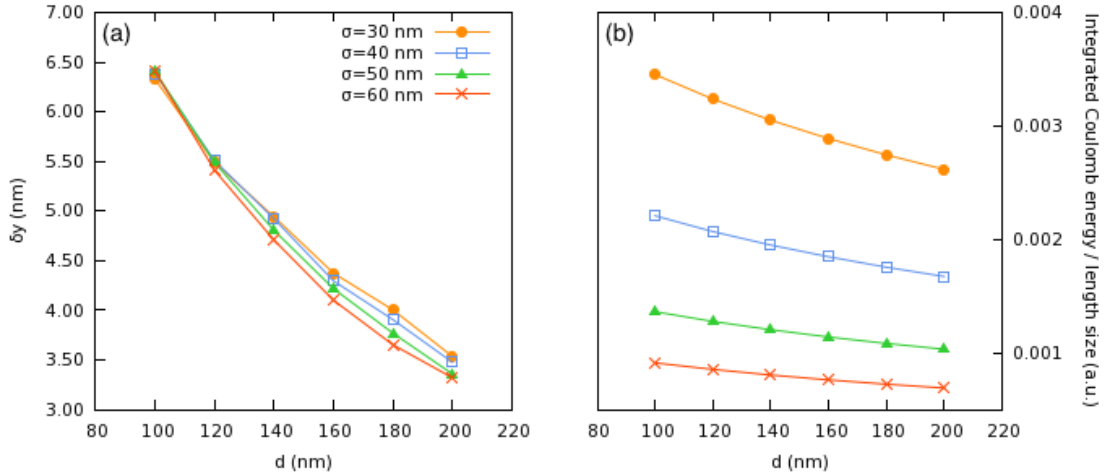


Figure 6.4: (a) Spatial shift δy and (b) integrated Coulomb energy per length size \mathcal{E}_c (Eq.(6.8)) exchanged during the scattering of two indistinguishable electrons in the (00) configuration as a function of the distance between the edges of the confining potential d , and for different wavepacket sizes σ .

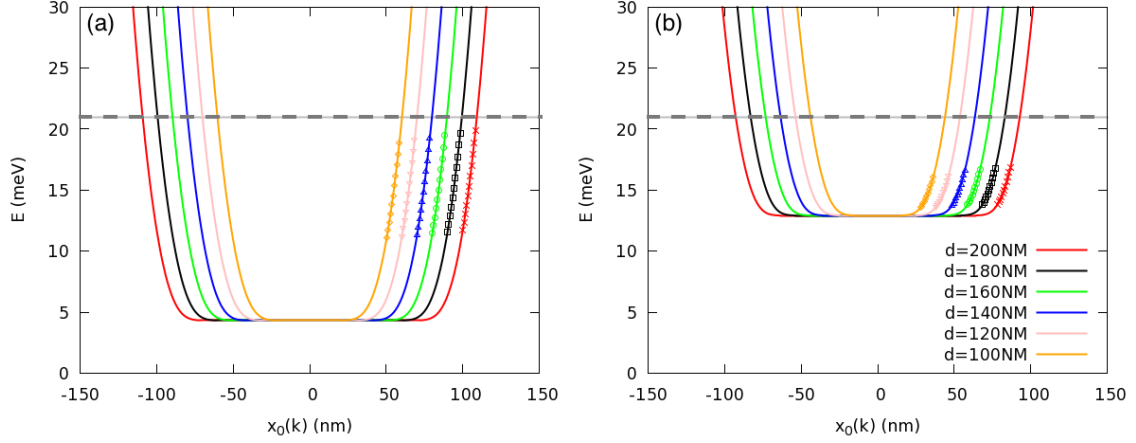


Figure 6.5: Bandstructure $E^n[x_0(k)]$ of the (a) first and (b) second Landau levels for different values of the distance between the two edges of the device, d . The gray line identifies the minimum energy of the third Landau level; The selected energies (dots) for the electron wavepackets in (a) and (b) are both centered at $E^0 \simeq 15$ meV and $\sigma = 40$ nm. Note that the energy broadenings of the electron wavepackets do not fill the third Landau level in neither cases.

The integrated Coulomb energy in Fig. 6.4(b) confirms that for smaller wavepackets Coulomb repulsion is higher, as a result of the increase in charge localization. This difference decreases with the distance d , coherently to the fact that Coulomb repulsion becomes less effective when the electrons are further separated.

However, this simple model does not take into account the real shape of the edge states and their corresponding bandstructure. Electrons with higher energies, or equivalently an higher group velocity, feel a smaller Coulomb barrier with respect to slower ones. By reducing the distance, as displayed in Fig. 6.5, the energy broadening of the wavepackets at $\sigma = 40$ nm moves towards lower energies, that is the wavepacket decreases its velocity. This effect is stronger for smaller wavepackets with respect to larger ones, so that at short distances ($d < 120$ nm) δy increases with σ .

dist(nm)	E_0^0	σ_E^1	E_1^0	σ_E^1
100	14.83	1.56	14.61	0.50
120	14.99	1.57	14.67	0.49
140	15.14	1.59	15.00	0.55
160	15.30	1.60	15.05	0.57
180	15.45	1.61	15.11	0.58
200	15.61	1.63	15.16	0.59

Table 6.1: Fit parameters of the weight function $F(E(k))$ for a single-electron wavepacket in the first ($n = 0$) or second ($n = 1$) channels in presence of the confining potential of Eq.(6.2) with $V_b = 250$ meV and $|x_R - x_L| = d$. The energy-dependent weight function is approximated by the Gaussian distribution $F_n(E) = \exp(-(E - E_n^0)^2/2\sigma_E^2)$, with E_n^0 the central energy of the wavepacket and σ_E^n the energy broadening.

dist(nm)	$ F_{00} ^2$	$ F_{01} ^2$	$ F_{02} ^2$
10	0.94001700	0.48252783E-05	0.26253228E-03
20	0.75805192	0.22146294E-03	0.24468394E-04
30	0.69461795	0.23929992E-01	0.11382228E-03
40	0.91427170	0.27233537E-01	0.33283118E-03

Table 6.2: Squared modulus $|F_{n_1 n_2}|^2$ defining the probability that electron 1 with $n = 0$ in the right channel and electron 2 with $n = 0$ in the left channel at initial time are promoted to n_1 and n_2 at the same side of the device respectively. Note that $|F_{00}|^2$ generally differs from unity because of the distinguishability of the two electrons; the complementary amount of probability refers indeed to the probability that electron 1 is scattered to n_1 and electron 2 is scattered to n_2 at the opposite side of the device.

6.1.2 Two-electron tunneling, bunching and entanglement in the (00) configuration

In the following, we use the *wave-packet method* (see Sec. 3.1.3) to compute the weight functions $F_{n_1 n_2}(k_1, k_2)$ of the two-electron wavefunction and prove that interchannel tunneling is absent for $d > 40$ nm. For distinguishable electrons, the squared modulus $|F_{ij}(k_1, k_2)|^2$ (with $i, j = 0, 1$) defines the probability of finding the two-particle state Ψ in a configuration with particle 1 in the edge state with $k = k_1$ and $n = i$ and particle 2 in the edge state with $k = k_2$ and $n = j$. By summing over the wavevectors k , we compute $|F_{ij}|^2 = |\sum_{k_1} \sum_{k_2} F_{ij}(k_1, k_2)|^2$, which is the probability of finding the two particles in the configuration $n_1 = i, n_2 = j$, regardless their wavevector.

Let us consider two distinguishable electrons, that are initialized in the two counterpropagating states of Fig. 6.2(c), case (00). Particle 1 is in a state centered at k_1 and particle 2 in a state centered

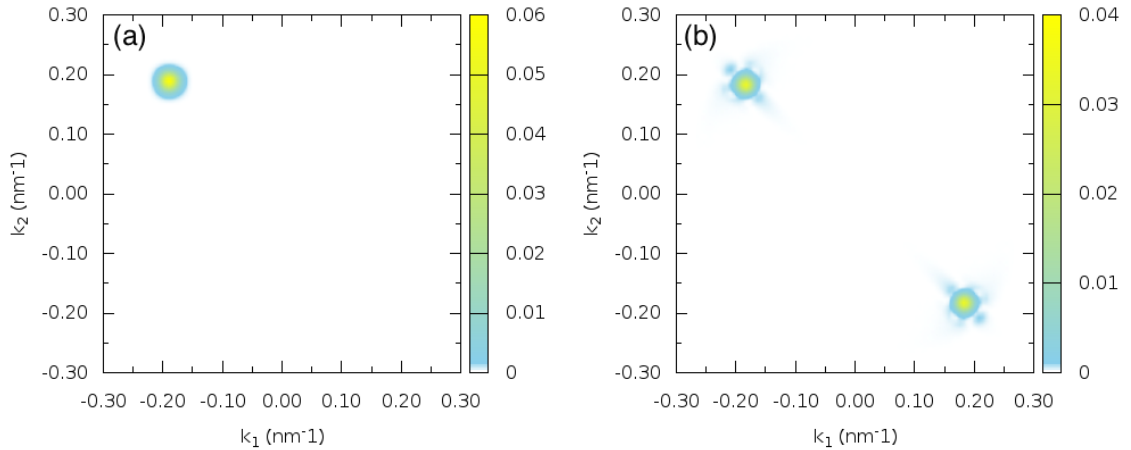


Figure 6.6: Squared modulus of the weight functions $F_{n_1, n_2}(k_1, k_2)$ presented in Sec. 3.1.3 with $n_1 = 0$ and $n_2 = 0$ (a) at initial time for distinguishable electrons and (b) at final time for indistinguishable electrons in presence of a geometry with $d = 40$ nm.

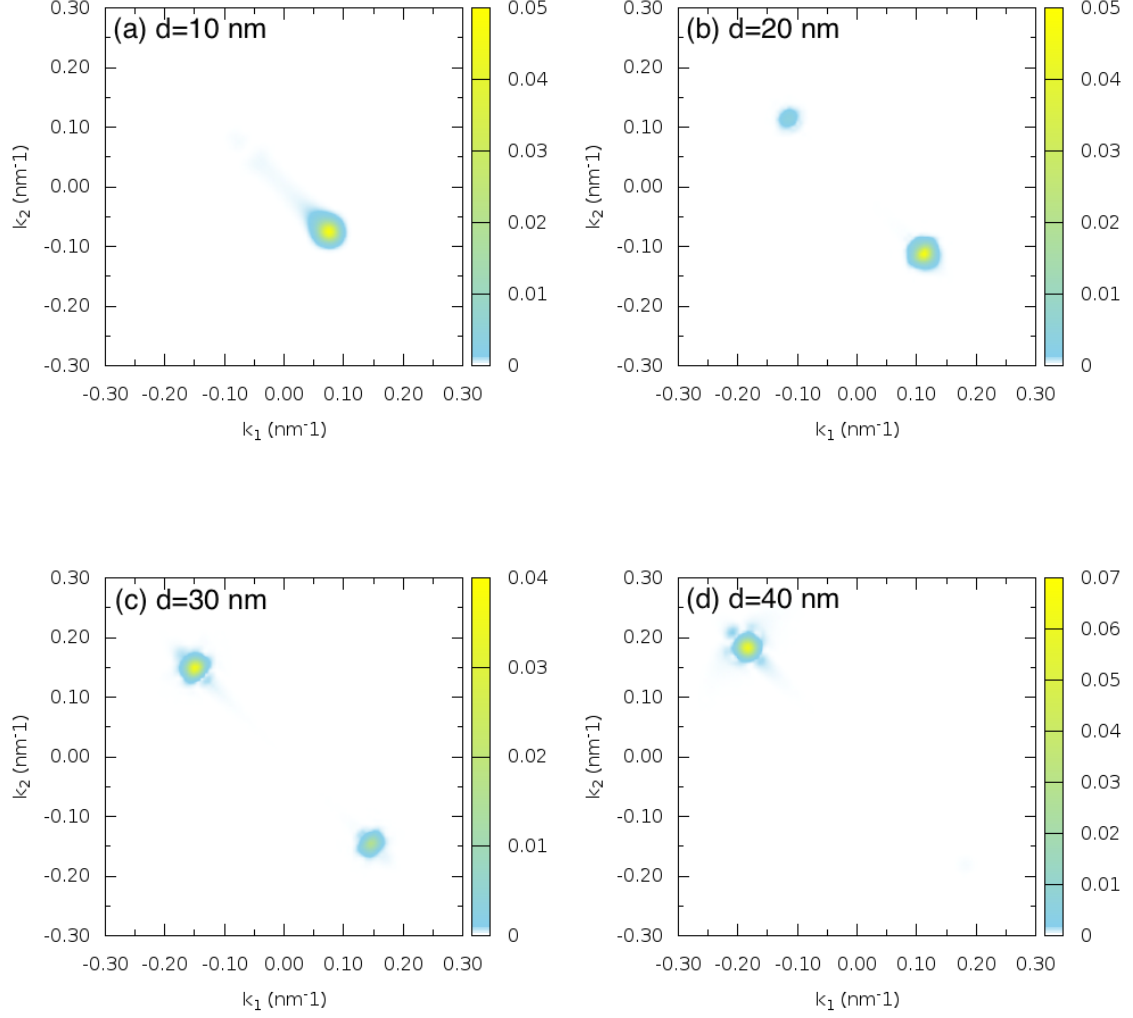


Figure 6.7: Squared modulus of the weight functions $F_{n_1, n_2}(k_1, k_2)$ presented in Sec. 3.1.3 at final time for distinguishable electrons with $\sigma = 40$ nm and $n = 0$ in a geometry with different values of the parameter d .

at k_2 , so that $k_1 = -k_2 = k$. At $t = 0$ the weight function $F_{00}(k_1, k_2)$ is a 2D Gaussian distribution centered at $k_1 = k$ and $k_2 = -k$, as visible in Fig. 6.6(a). In presence of exchange symmetry, the squared modulus of the weight function is instead characterized by a 2D Gaussian distribution peaked at $k_1 = -k$ and $k_2 = +k$. As visible from Fig. 6.6(b), which displays $|F_{00}(k_1, k_2)|^2$ at the end of the Coulomb-driven scattering process, the presence of exchange symmetry in the two-particle wavefunction prevents the observation of new states arising from interchannel tunneling. The promotion of an electron to an higher cyclotron resolved channel is instead detected by a non zero probability $|F_{ij}|^2$, with i or j different from zero. Tab. 6.2 shows that for distinguishable

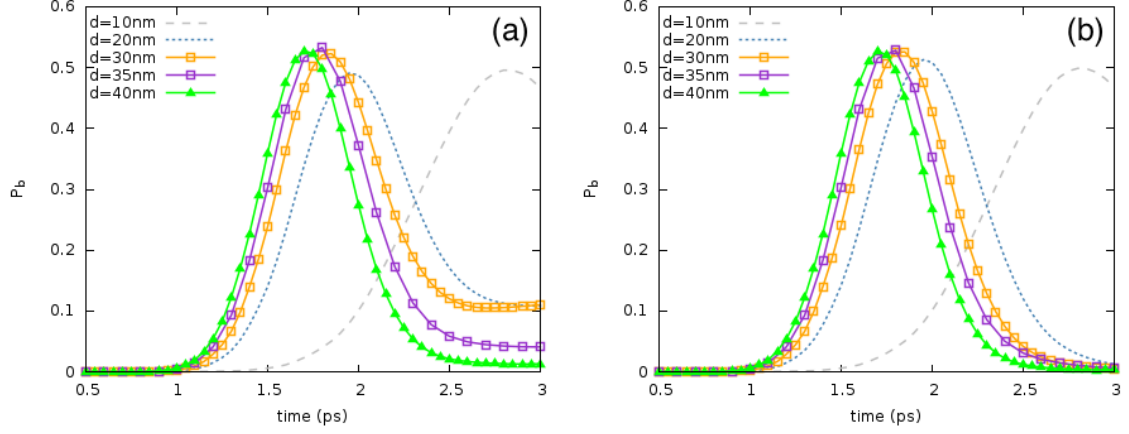


Figure 6.8: Bunching probability $P_b(t)$ during the Coulomb-driven scattering for two (a) distinguishable and (b) indistinguishable electrons initialized in Gaussian wavepackets with $\sigma = 40$ nm in the (00) configuration for different values of the parameter d . Note that tunneling is present in this regime.

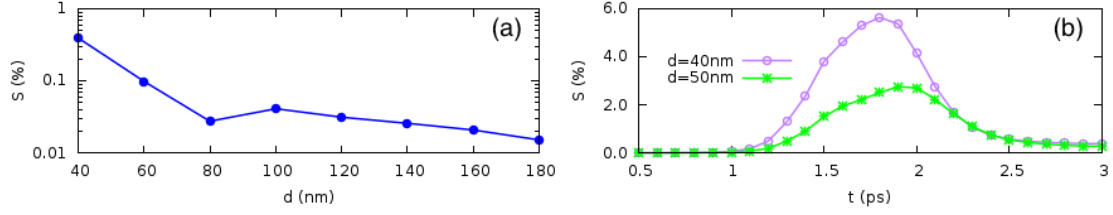


Figure 6.9: Von Neumann entropy of two indistinguishable electrons in the (00) configuration with $\sigma = 40$ nm as a function of (a) the distance between the two confining barriers d at final time and (b) the time for $d = 40, 50$ nm.

electrons and small d parameters this probability is always below 2%; this proves the absence of tunnel coupling between cyclotron-resolved channels due to Coulomb interaction in the stationary regime.

In Fig. 6.7 we map the probability distribution $|F_{ij}(k_1, k_2)|^2$ at the end of the scattering process for distinguishable electrons, with $d = 10, 20, 30, 40$ nm. By starting from the configuration in Fig. 6.6(a), we observe that the two electron states in the Fourier space (k_1, k_2) are fully reflected for $d < 10$ nm, while full transmission arise when $d > 40$ nm. Interchannel tunneling between the two counterpropagating states characterize therefore the intermediate regime ($10 < d < 40$ nm), with Coulomb interaction acting as a partitioner.

The bunching probability of the two electrons is then investigated. We partition the 2D real-space domain in a *TOP* ($y > 0$) and a *BOTTOM* ($y < 0$) region, and calculate such probability with

$$P_b = \int_{S_{TT}} dr_1 dr_2 |\Psi(r_1, r_2)|^2 + \int_{S_{BB}} dr_1 dr_2 |\Psi(r_1, r_2)|^2, \quad (6.9)$$

where S_{TT} and S_{BB} correspond to the 4D domain in the configuration space with $y_1, y_2 > 0$ and $y_1, y_2 < 0$ respectively.

Fig. 6.8 displays P_b for a (a) separable and (b) antisymmetric wavefunction. By selecting a

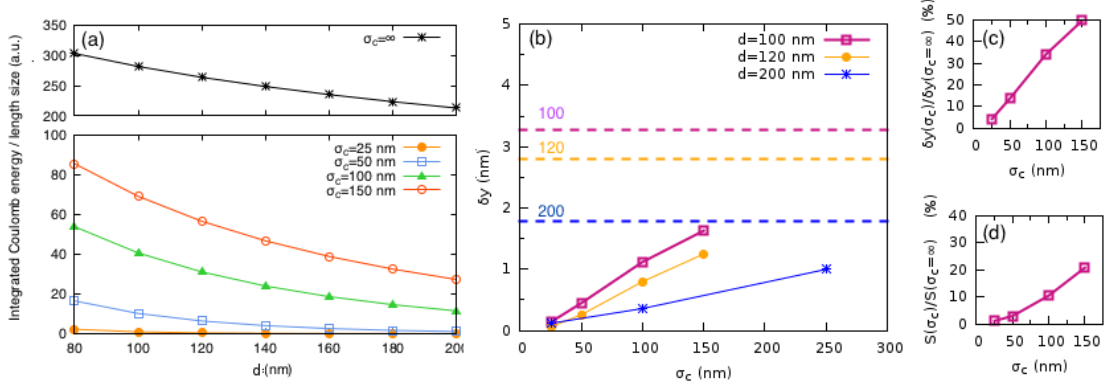


Figure 6.10: (a) Integrated Coulomb energy per length size \mathcal{E}_C as a function of d in the (00) configuration and in presence of screening with different values of the parameter σ_c . The top panel shows \mathcal{E}_C in presence of long-range Coulomb interaction. (b) Spatial shift δy in presence of screening for two indistinguishable electrons initialized in wavepackets with $\sigma = 40$ nm in the (00) configuration. The dashed horizontal lines correspond to the unscreened value of δy in presence of long-range interaction. (c) Ratio between the spatial shifts δy with an effective screening σ_c and with a long-range Coulomb interaction ($\sigma_c = \infty$). (d) Ratio between the von Neumann entropies S at $d = 100$ nm with an effective screening σ_c and with a long-range Coulomb interaction ($\sigma_c = \infty$).

small value for d_z , we ensure that the two electrons experience a very large Coulomb interaction with respect to their energies. For the simulated values of d , we measure a non-zero bunching probability that raises by reducing the distance. As in the HOM geometry, this proves that - for our operating regime - Coulomb repulsion in 2D does not prevent the two electrons to be transmitted; this differs from the expected bunching probability in an equivalent 1D scenario, where the two electrons are forced to propagate on the same rail, and experience an infinite barrier at $x_1 = x_2$. With contrast to the case of the HOM interferometer, this bunching is fully quenched by the exchange interaction, regardless the distance between the two rails.

As in the HOM interferometer, we then compute the *von Neumann Entropy* S of the system and measure the spatial entanglement between the two rails where electrons counterpropagate. In this scenario, the *RIGHT* ($x < 0$) and *LEFT* ($x > 0$) region of the device define separate subspaces of the 2D Hilbert space, respectively H_L and H_R , so that $\hat{H} = \hat{H}_L \oplus \hat{H}_R$.

To reduce the numerical cost, we select the configuration with particle 1 in the right channel and particle 2 in the left one, and project the two-electron wavefunction on the rails at $x_1 = x_r^*$ and $x_2 = x_l^*$, where the density probability of the single-electron wavepackets at $t = 0$ is peaked. Fig. 6.9(a) displays the von Neumann entropy as a function of the parameter d in the stationary regime, while panel (b) displays the dynamical evolution $S(t)$ for $d = 40$ nm and $d = 50$ nm. S shows a logarithmic increase of the spatial entanglement, which is generated by Coulomb interaction only, due to the absence of tunneling for $d > 40$ nm.

6.1.3 Screened Coulomb coupling in the (00) configuration

In this subsection, we analyze the effect of screening by introducing an exponential damping in the Coulomb repulsive potential, Eq.(6.4), between two indistinguishable electrons in the (00) configuration and with $\sigma = 40$ nm.

Fig. 6.10(a) displays the energy exchanged during the Coulomb scattering for a range of d

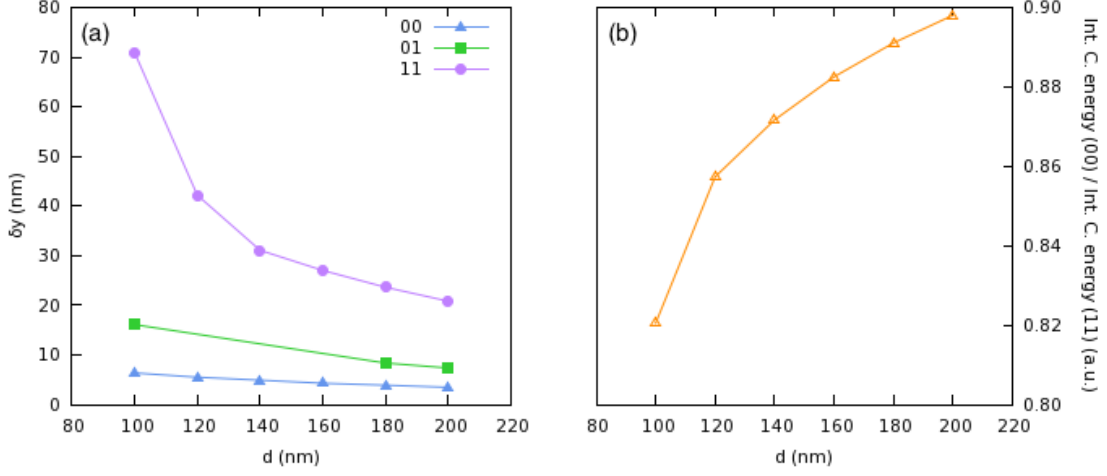


Figure 6.11: (a) Spatial shift δy for two indistinguishable electrons in the 3 different configurations with $\sigma = 40$ nm and in the presence of long-range unscreened Coulomb interaction. (b) Ratio between the integrated Coulomb energy per length size \mathcal{E}_C in the (00) configuration and in the (11) configuration.

values between 100 and 200 nm, with $C = 1$ and $\sigma_c = 25, 50, 100, 150$ nm. The energy exchanged during the scattering is significantly different in presence of screening (bottom panel) and in the unscreened case (top panel); the discrepancy visibly increases with the value of d due to the exponential damping in the Coulomb repulsion.

In Fig. 6.10(b), we provide the spatial shift δy for the (00) configuration, in the additional presence of screening. By choosing $d = 100, 120, 200$ nm, we ensure that no tunneling is present. The ratios between the values of the parameter δy in the screened scenario and in the long-range case reported in Fig. 6.10(c) show that the screening reduces the effect of the Coulomb interaction of a factor $1/2$. As illustrated by Fig. 6.10(d), the reduction of the *von Neumann entropy* is even stronger.

6.1.4 Coulomb-driven scattering in the (11) and (01) configurations

To demonstrate the selectivity of the two-electron coupling induced by Coulomb interaction, we compare the value δy generated in the previous scenario to the one in the (11) configuration. Note that the probability distribution of a single electron wavepacket with $n = 1$ is characterized by a double peak in the transverse direction, as previously observed in e.g. Fig. 6.5(b). The presence of a larger density probability in the bulk for the (11) configuration increases the strength of Coulomb interaction in the middle of the active region with respect to the (00) case.

This is confirmed by Fig. 6.11(a), where we compare the spatial shifts δy as a function of the distance d in the 3 configurations, (00), (01) and (11): Coulomb repulsion affects more strongly two electrons with $n = 1$. The discrepancy between the values of δy in the three cases increases significantly when the distance between the two charges is reduced.

However, the different strength of Coulomb interaction in the different configurations is not sufficient to explain this discrepancy. Fig. 6.11(b) displays the ratio between the integrated energy exchanged during the scattering in the (00) configuration and in the (11) configuration, which is - in our operating regime - between 80% and 90%. We also need to account for the bandstructure of the second Landau level, which has a smoother dispersion with respect to first one, thus reducing

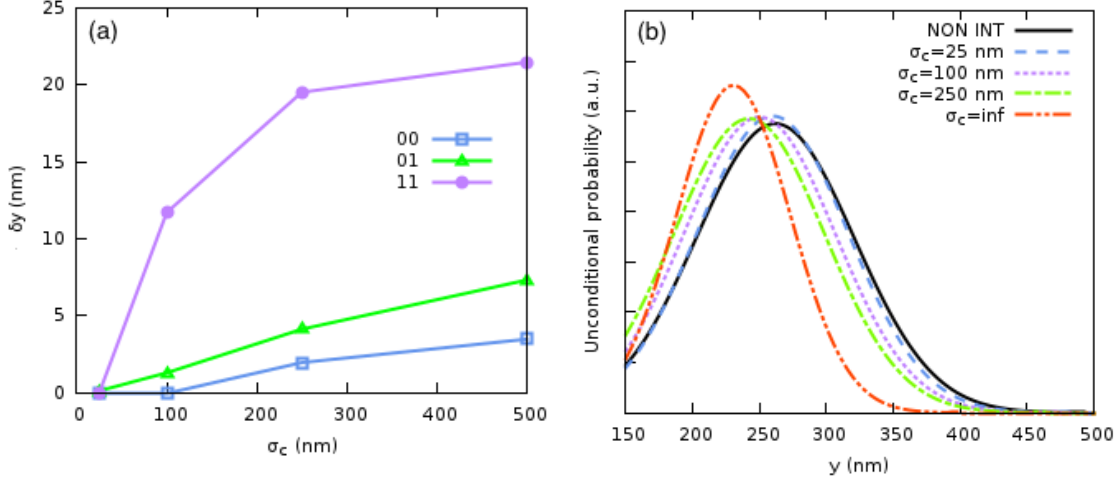


Figure 6.12: (a) Comparison between the spatial shifts δy for two indistinguishable electrons with $\sigma = 40$ nm in the three different configurations and $d = 200$ nm. (b) Longitudinal profile of the probability density of particle 2 in the positive domain of the device (TOP region) for different values of the σ_c parameter.

the group velocity and increasing δy .

Finally, Fig. 6.12(a) compares the spatial shifts in presence of screening for the three scenarios with $\sigma = 40$ nm, and a distance between the edges of the confining barrier $d = 200$ nm. If the screening is included with σ_c comparable to the width of the active region, the spatial shift δy in the (00) or (01) configuration approaches the precision of our simulation grid. This is not the case for the (11) configuration, which is instead characterized by a spatial shift δy that is still visible in our numerical simulations. An example is reported in Fig. 6.12(b), which shows the longitudinal profile of the density probability of particle 2 in the TOP region of the device for different values of σ_c at the end of the scattering.

Our numerical simulations then predict that by properly tuning the geometrical parameters of the active region with modulation gates, or by varying the effective length for the screening, e.g. by modifying the electron density of the 2DEG, it is possible to quench the effect of Coulomb repulsion for all configurations except the (11) one, so that electron-electron repulsion acts a selective entangler also for this simple geometry, whose length size can be clearly engineered state of the art nanotechnology.

In the next section we further simulate Coulomb-driven scattering between two indistinguishable electrons in a more realistic geometry of the active region, and predict the phase shift γ that rotates the (11) component of the two-electron wavefunction of the full-scale conditional phase shifter.

6.2 Towards a realistic conditional phase shifter

Here, the confining barrier is modeled with a smoothed profile in the \hat{x} -direction:

$$V_{ext}(x) = V_b \left(\frac{1}{1 + e^{\frac{x-x_b}{\lambda}}} + \frac{1}{1 + e^{\frac{-x+x_b}{\lambda}}} \right), \quad (6.10)$$

with $V_b = 0.31$ eV, $\lambda = 3$ nm and $x_b = 55$ nm. Fig. 6.13 shows the potential profile in the transverse direction (blue shaded area), together with the bandstructure of the second Landau level (orange

dashed line) and the density probability of a single electron wavepacket with $n = 1$, $\sigma = 40\text{nm}$, and an injection energy of $E^0 = 20.4\text{ meV}$ (black dashed line). Note that this regime reproduces the geometry and the injection protocol of the multichannel MZI described in Chapter 4, which is the building block of our proposal for a solid-state implementation of the full-scale conditional phase shifter.

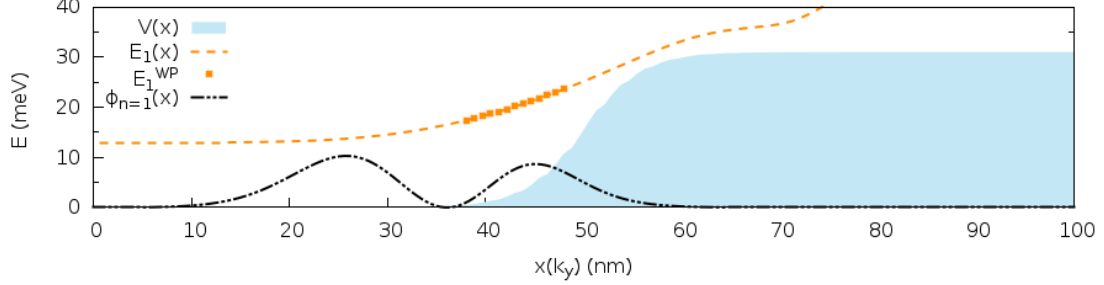


Figure 6.13: Energy band structure (orange dashed line) of the second Landau level $E_1(x)$ in the presence of the confining barrier V_{ext} defined in Eq.(6.10) with $V_b = 0.31\text{ eV}$, $\lambda = 3\text{ nm}$ and $x_b = 55\text{ nm}$ (blue shaded area). The black dashed line displays the transverse probability distribution of the electron wavepacket in the second edge channel at the initial coordinate $y_0 = 350\text{ nm}$ and $E^0 = 20.4\text{ meV}$ in arbitrary units.

Consistently to our previous study of an ideal geometry with two square potential steps, we expect a stronger Coulomb interaction between the counterpropagating electrons with $n = 1$. The sharper bending of the first Landau level determines a smaller magnetic mass m_B^* with respect to a wavepacket with the same energy distribution but higher cyclotron index, n . The smaller group velocity for $n = 1$ induces a larger shift in the real-space δy . Moreover, for a fixed injection energy $E^0(k)$, the center $x_0^n(k)$ of a set of edge states with $n = 0$ is closer to the profile of the confining barrier with respect to the same parameter with $n = 1$. Then, the transverse probability distribution of two wavepackets in the second Landau level is higher in the bulk with respect to the case of two wavepackets initialized in the ground state. This further increases the effect of Coulomb interaction in a symmetric geometry of the active region.

6.2.1 Self-electron interference for the phase factor

The relation between the spatial shift δy and the γ factor in the \mathbf{T} matrix can not be trivially determined by the wavevector k alone, due to its gauge dependence. We resort indeed to the longitudinal separation L_{eff} , that is necessary to produce a 2π rotation in each single-electron MZI at the edge of the device.

By means of our single-particle solver, we simulate the dynamics of the single-electron interference in the potential of Fig. 6.13. At initial time, the single-electron wavefunction is a coherent superposition of two wavepackets in $n = 0$ and $n = 1$ with the same energy distribution centered at $E^0(k) = 20.4\text{ meV}$, that corresponds to the output state of the half-reflecting potential dip designed in Sec. 4.2.1. The wavefunction scatters then on a second beam splitter, so that the integrated density probability at the end of the device in $n = 0$ is expected to present the interference pattern of a full-scale MZI with a zero loop area.

Differently from Ref. [13], in the present geometry we artificially introduce a relative shift in the \hat{y} -direction between the two components of the initial wavefunction, ΔY . This spatial shift corresponds to a relative phase factor in the single-electron wavefunction between the wavepackets in $n = 0$ and $n = 1$, and mimic the effect of Coulomb repulsion on the second edge channel in

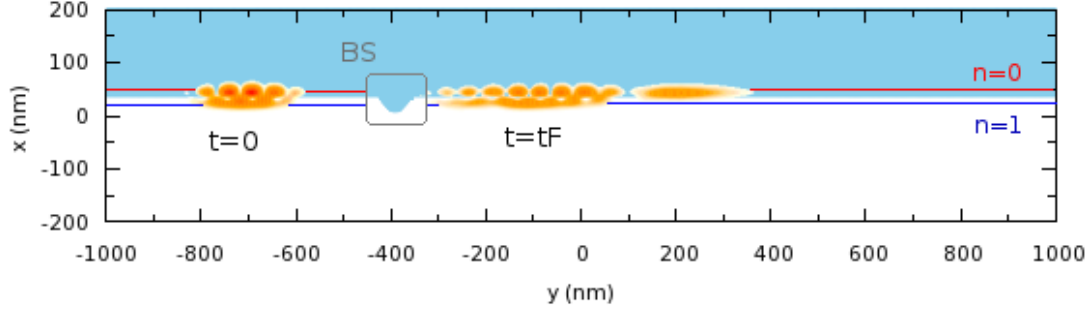


Figure 6.14: Evolution of the single-electron probability distribution (orange) in the effective geometry of a multichannel MZI (light blue shaded area), with two translationally invariant regions before and after the electron beam splitter of Sec. 4.2.1. The wavefunction is initialized at $t = 0$ in a coherent superposition of two wavepackets of edge states with $\sigma = 40\text{nm}$, same central energy $E^0 = 20.4\text{ meV}$ and different cyclotron indexes $n = 0, 1$.

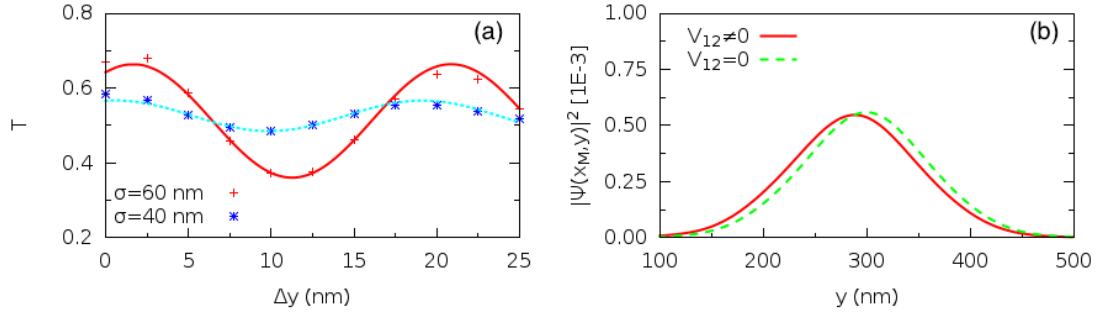


Figure 6.15: (a) Interference pattern of the effective geometry for the MZI as a function of the longitudinal distance Δy between the two wavepackets of the initial state in Fig. 6.14. T measures the probability that the electron state is transmitted to the output channel 0, for different spatial broadenings of the wavepacket $\sigma = 60, 40\text{ nm}$. (b) Comparison between the longitudinal profile of the probability distribution of particle 2 at final time in the positive domain of the active region with (red solid line) and without (green dashed line) electron-electron interaction. x_M is the maximum of the probability distribution in the \hat{x} direction.

presence of a counterpropagating state. In the single-electron simulation, ΔY rotates the final state at the output of the MZI. The spatial periodicity L_{eff} of the interference pattern in the transmission amplitude for the 0 channel, $T(\Delta y)$, has to be related with γ : if L_{eff} corresponds to a 2π rotation in the output state of single-electron Mach-Zehnder experiment, the same rotation, $\gamma = 2\pi$, is obtained by introducing a selective Coulomb repulsion that shifts the final position of the two wavepackets in $n = 1$ by a factor $\delta y = L_{eff}$.

6.2.2 The γ factor in the full-scale device

The interference pattern of the single-electron simulation is displayed in Fig. 6.15(b). The effective length L_{eff} depends slightly on the wavepacket size σ , which instead affects more strongly

the visibility of the oscillations in the transmission amplitude. The two component of the single-electron wavefunction are indeed characterized by a different group velocity v_g^n in the two channels, which does not depend significantly on the wavepacket size. However, this prevents the two components to impinge on the beam splitter simultaneously, so that for smaller wavepackets their overlap is reduced. Within the present regime, we measure an effective length $L_{eff} = 20$ nm.

The dynamical simulation of the Coulomb-driven scattering of two indistinguishable electrons in the second edge channel provides instead the shift δy in this geometry. Fig. 6.15(b) shows the two peaks of the probability distribution for particle 2 at the top of the device. The red solid line reproduces this probability in the non-interacting scenario, and the green dashed line the same parameter in presence of electron-electron repulsion. The difference between the coordinates of the maxima in the two distributions is $\delta y = 11$ nm.

We finally relate the shift δy to the corresponding γ in the \hat{T} transformation by using L_{eff} as a reference in the following equation,

$$\gamma = 2\pi \frac{\delta y}{L_{eff}}, \quad (6.11)$$

which provides $\gamma = \pi$ in the full-scale conditional phase shifter. This proves the feasibility of a selective phase shifter with a factor π in our geometry, where the smoothed barriers are characterized by a relative distance $W = 110$ nm at $B = 5$ T. A proper increase of the distance between the outer edges of the two mesas at the nanometer scale is expected to induce a rotation that ranges from $\pi/2$ to 2π , thus making this device a viable approach for conditional phase shifting driven by Coulomb interaction.

Part III

Alternative frameworks for electron transport

Chapter 7

On the incompatibility between Frensley's inflow boundary conditions and stationary Wigner distribution functions

The numerical simulation of a quantum electron device requires a partition between an active region and the reservoirs. Instead of simulating a close system, one has to deal with an open quantum system. The Wigner distribution function [113], dealing with the phase-space of open quantum systems, has a large tradition in the simulation of quantum electron devices, but it requires reasonable physical arguments to fix the properties of electrons at the spatial borders of the active region. To guarantee irreversibility, Frensley suggested the reasonable assumption of treating the reservoir as a blackbody; he assumes that the energy (or momenta) distribution of electron emitted into the device is described by the thermal equilibrium distribution function of the reservoir, while the outflowing electrons are absorbed without reflection [41]

From an intuitive point of view, Frensley boundary conditions are very reasonable. However, its practical application in simulations can lead to unphysical results. The problem discussed in this chapter appears because the definition of the momentum of the Wigner distribution function - through a Wigner-Weyl transformation - is not the same as the orthodox one. Although its marginal probability coincides, the former momentum depends on position, while the latter does not. We show that this mathematical incompatibility can have dramatic consequences in time-independent scenarios, as for scattering states in a single/double potential barrier.

The situation is even more dramatic when dealing with a resonant state, where an electron with positive orthodox momentum at the left, induces unexpected inflowing negative Wigner-Weyl momenta at the right. In the literature, the solutions to this incompatibility is either criticizing the Frensley's boundary conditions [114] or looking for a new phase-space distribution[115]. On the contrary, we show that this apparent incompatibility is simply solved by using time-dependent approaches, where electrons are defined as wave-packets with a spatially limited quantum non-locality.

This discussion has been presented at the *International Wigner Workshop* during the **IWCN2019 - International Workshop on Computational Nanoelectronics** in Evanston, Illinois (USA), by L. Bellentani, E. Colomés, Z. Zhan, P. Bordone, A. Bertoni, and X. Oriols.

7.1 Boundary conditions on a joint momentum-position space

7.1.1 Properties of the Wigner distribution function

Despite in quantum mechanics the probability distribution of a dynamic variable, as the momentum or the position, has an appropriate classical limit, classical mechanics provides also the description of correlations between such variable dynamics by means of a joint probability distribution, $\rho_c(x, k)$.

For a quantum system with state ρ on the phase space, the quantum distribution $\rho_Q(x, k)$ with $\rho_c(x, k)$ as its classical limit should fulfill the probability axioms:

$$(i) \int \int dx dk \rho_Q(x, k) = 1,$$

$$(ii) \rho_Q(x, k) \geq 0,$$

and the marginal distribution should provide the usual position and momentum probability distributions, i.e.:

$$\int dx \rho(x, k) = \langle k | \rho | k \rangle, \quad (7.1)$$

$$\int dk \rho(x, k) = \langle x | \rho | x \rangle. \quad (7.2)$$

Several attempts have been done to provide a quantum distribution on a joint momentum-position space, as with the Wigner distribution function, $f_W(x, k)$. This is defined as the Weyl-Wigner transform of the density matrix:

$$f_W(k, x) = \frac{1}{\pi \hbar} \int \rho(x + s, x - s) e^{-2iks} ds. \quad (7.3)$$

If the system is described by a pure state, the density matrix reads $\rho = |\psi\rangle\langle\psi|$ and the Wigner distribution is:

$$f_W(k, x) = \frac{1}{\pi \hbar} \int \psi(x + s) e^{-2iks} \psi^*(x - s) ds, \quad (7.4)$$

while for a mixed state $|\psi\rangle = \sum_i p_i |\psi_i\rangle\langle\psi_i|$ on the basis $\{|\psi_i\rangle\}$, it is defined as follows:

$$f_W(k, x) = \frac{1}{\pi \hbar} \sum_i p_i \int \psi_i(x + s) e^{-2iks} \psi_i^*(x - s) ds. \quad (7.5)$$

It is proved that the requirement of non negativity is not always covered [116], so that $f_W(x, k)$ can not be directly interpreted as a probability distribution. By integrating over the space and momentum coordinates, the trace of the state ρ is restored, i.e. $\int \int dk dx f_W(k, x) = \text{Tr}[\rho] = 1$. Moreover, the property $\rho = \rho^\dagger$ ensures that $f_W(k, x)$ is real.

The Wigner distribution function is usually integrated to compute the expectation value of an operator \hat{A} ,

$$\langle A \rangle = \sum_i \rho_i \langle \psi_i | A | \psi_i \rangle = \text{Tr}[\rho A], \quad (7.6)$$

according to the following relation:

$$\langle A \rangle = \frac{1}{\pi \hbar} \int \int f_W(k, x) A(x) dk dx. \quad (7.7)$$

Similarly, for a momentum-dependent operator $B(k)$, the expectation value reads:

$$\langle B \rangle = \frac{1}{\pi\hbar} \int \int f_W(k, x) B(k) dk dx. \quad (7.8)$$

The extension to a two particle system follows then straightforwardly:

$$f_W(x_1, x_2, k_1, k_2) = \frac{1}{(\pi\hbar)^2} \int ds_1 \int ds_2 \Psi(x_1 + s_1, x_2 + s_2) \Psi^*(x_1 - s_1, x_2 - s_2) e^{-2ig_1 s_1} e^{-2ig_2 s_2} ds_1 ds_2, \quad (7.9)$$

which is clearly separable if the two particles are distinguishable and not interacting, so that, if $\Psi(x_1, x_2) = \phi_1(x_1)\phi_2(x_2)$, then

$$f_W(x_1, x_2, k_1, k_2) = f_W^1(x_1, k_1) f_W^2(x_2, k_2). \quad (7.10)$$

7.1.2 Frensky's inflow boundary conditions

Despite the Wigner function cannot be directly interpreted as a probability distribution, it represents a powerful tool to study a nanodevice integrated in an electron circuit as a confined quantum systems connected to semiclassical leads [117, 118, 119, 120]. Thanks to its definition on the (x, k) space, it provides indeed simultaneous information about the position and the momentum of the particle.

The use of the density matrix in presence of open boundaries provides an ideal framework to describe both phase coherent phenomena and dephasing effects in nanostructured devices [121, 122], where it is not possible to adopt a periodic description of the system. For a finite quantum core, as the one depicted in Fig. 7.1(a), boundary conditions are mandatory to take into account the finite size of the scattering region connected to external charge reservoirs by electric contacts.

In 1987 Frensky proposed the *inflow boundary conditions* [41] to ensure the absence of reflection for the electron wavefunction coming from the semi-infinite contact toward the scattering region. For a simplified 1D geometry, we adopt the *U boundary condition scheme* displayed in Fig. 7.1(b): this translates into fixing entirely the Wigner distribution function for all positive (negative) momenta at the left (right) border of the active region. These boundaries fix the inflowing semi-classical, i.e. positive-definite, carrier distributions $f_L^b(k)$ and $f_R^b(k)$ at the left and right interfaces located at x_L and x_R , respectively:

$$f_W(x = x_L, k > 0) = f_L^b(k), \quad (7.11)$$

$$f_W(x = x_R, k < 0) = f_R^b(k). \quad (7.12)$$

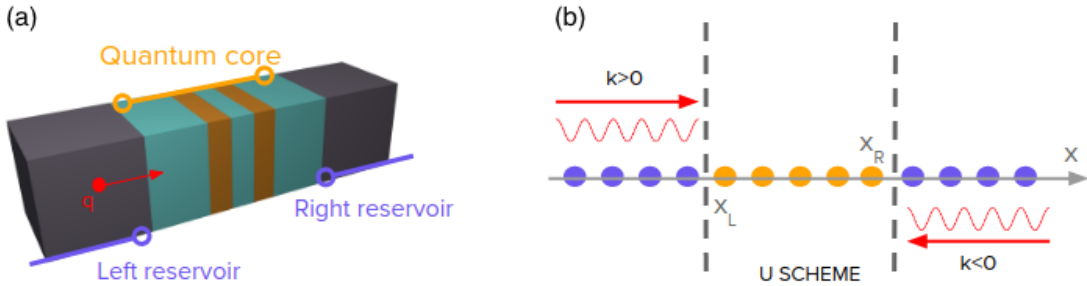


Figure 7.1: (a) Rendered scheme of an electron nanodevice. (b) The "U" scheme adopted in a 1D geometry to model electron transport from the reservoir to the active region of the device.

The carrier distributions $f_L^b(k)$ and $f_R^b(k)$ are typically the Fermi-Dirac distributions in the momentum, and depend on the Fermi level of each contact.

The problem we are discussing arise in the above equations. The Frensey's inflow boundary condition impose the localization of the momentum in the Wigner description of a confined nanostructure. Indeed, to fulfill Eq.(7.11) and Eq.(7.12), the momentum in the Weyl-Wigner transform of the density matrix must be explicitly referred to the position of the right or the left interface. On the contrary, in the orthodox theory the momentum of a particle is non-local, and indeed it is represented trough a plane wave in the real space: $\langle x|k \rangle = 1/\sqrt{2\pi}e^{ikx}$. The effects of this inconsistency are illustrated in the next section.

7.2 Inconsistencies for a stationary picture

The inflow boundary conditions on the Wigner distribution function have been applied firstly by Frensey in 1987 to simulate electron transport in a Resonant Tunneling Diode, where the negative differential resistance has been successfully reproduced [41].

However, recent numerical simulations [114, 123] highlight that the electron current computed from the Wigner distribution function is generally higher than the one provided by alternative numerical tools, e.g. by the Non-Equilibrium Green function. In detail, Ref. [114] analyzes the interplay between the size of the contact region in the RTD and the accuracy of the Frensey inflow boundary conditions on the Wigner distribution function. Jiang et al. observe that the I-V curves provided by the Wigner function method are similar to those simulated by the NEGF method for low bias potentials as the length of the contacts increases. This shows that, in order to provide exact results, the interface for the inflow boundary condition should be located at infinite distance from the active region. The application of the inflow boundary condition to the Wigner distribution function is therefore always affected by a numerical error related to the finite size of

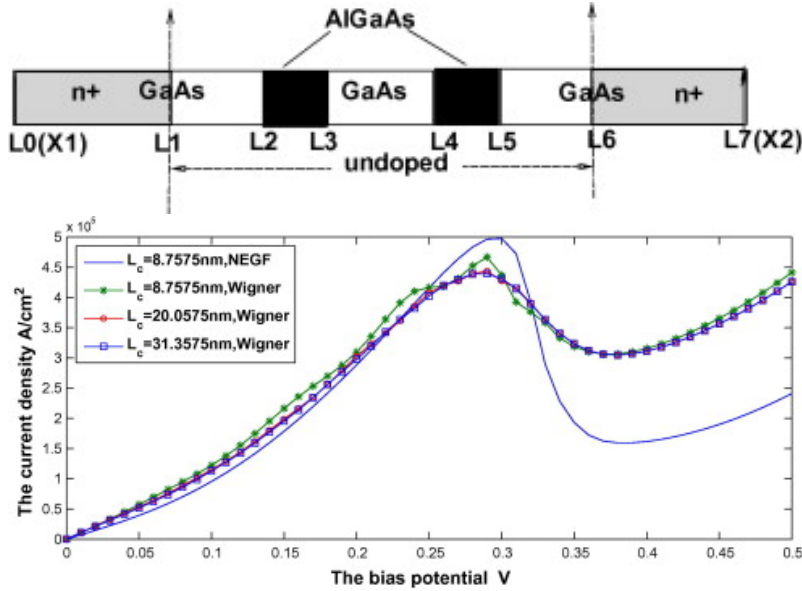


Figure 7.2: (Top) Scheme of the GaAs/AlGaAs heterostructure simulated with the Wigner method and NEGF method in Ref. [114], with a resonant tunneling diode in the active region and (Bottom) convergence of the I-V current computed with the Wigner function and NEGF method.

the simulation region.

Moreover, it is proved that a probability distribution of states $f^b(k)$ injected at a boundary according to Frensey's inflow condition does not always provide a Wigner distribution function in the active region of the device, or, in the coherent limit, the solution is not unique [124]. To solve this, Ref. [115] proposes an alternative definition of the Wigner distribution function, based on a generalized Weyl-Wigner transform of the density matrix. Instead of using a basis set of plane waves, the transform of ρ is applied on a basis composed by the scattering states of the active region. The Weyl-Wigner transform of the density matrix on the $\{|k\rangle\}$ basis set,

$$u_{\alpha_1\alpha_2}(x, k) = \frac{1}{\pi\hbar} \int ds \psi_{\alpha_1}(x+s) e^{-\frac{ik(x+s)}{\hbar}} e^{+\frac{ik(x-s)}{\hbar}} \psi_{\alpha_2}^*(x-s), \quad (7.13)$$

is so generalized on the basis $\{|\beta\rangle\}$ as follows:

$$u'_{\alpha_1\alpha_2}{}^{\beta_1\beta_2}(x) = \Omega \int ds \psi_{\alpha_1}(x+s) \chi_{\beta_1}^*(x+s) \chi_{\beta_2}(x-s) \psi_{\alpha_2}^*(x-s), \quad (7.14)$$

where Ω is the volume of the simulated region. By using as generalized basis states $\{|\beta\rangle\}$ the scattering states of the quantum core, the unphysical features usually arising from the use of the conventional Wigner distribution function are removed.

Both approaches expose the incompatibility between Frensey's boundary condition and the Wigner distribution function. In the first case, Jiang et al. conclude that a reasonably valid solution requires contact lengths large *enough*, according to the size of the scattering potential inside the nanostructured core. The second approach proposed by Zaccaria et al. provides instead an alternative definition of the Wigner distribution function based on the scattering states, to match with Frensey's inflow boundary conditions.

However, both solutions imply a dependence between the distribution of the inflowing states and the scattering process in the active region. We aim instead at identifying a framework for the Wigner distribution function that preserves the independence of electron injection from the scattering inside the nanostructured core. Despite it is not possible to provide the exact shape of the electron wavepacket injected from an Ohmic contact, we expect indeed that a description by a scattering state (extended everywhere) is not physical. We expect that an electron inflowing from the reservoir at the interface should not be described by a state accounting for the scattering process before the event itself. As we prove in the next sections, this contradiction is naturally overcome in a time-dependent picture, where electrons are encoded in spatially localized wavepackets.

7.2.1 Inconsistencies for a monoenergetic injection of plane waves

In the following, we will firstly expose the origin of this inconsistency by analyzing the Wigner distribution function for a monoenergetic electron state that propagates in the active region of the device. We initially compute the Wigner distribution function $f_W(x, k)$ in a stationary scenario where electrons are injected as monoenergetic plane waves with wavevector k_0 inside the scattering region from the left boundary of the system:

$$f_L^b(k) \propto \delta(k - k_0). \quad (7.15)$$

No electrons are instead injected from the right reservoir, where we expect to have only outflowing states, i.e.

$$f_R^b(k) = 0. \quad (7.16)$$

The nanostructured core is designed with two different potential profiles: a (i) simple and a (ii) double potential barrier, as displayed in the (top) and (bottom) panels of Fig. 7.3, respectively.

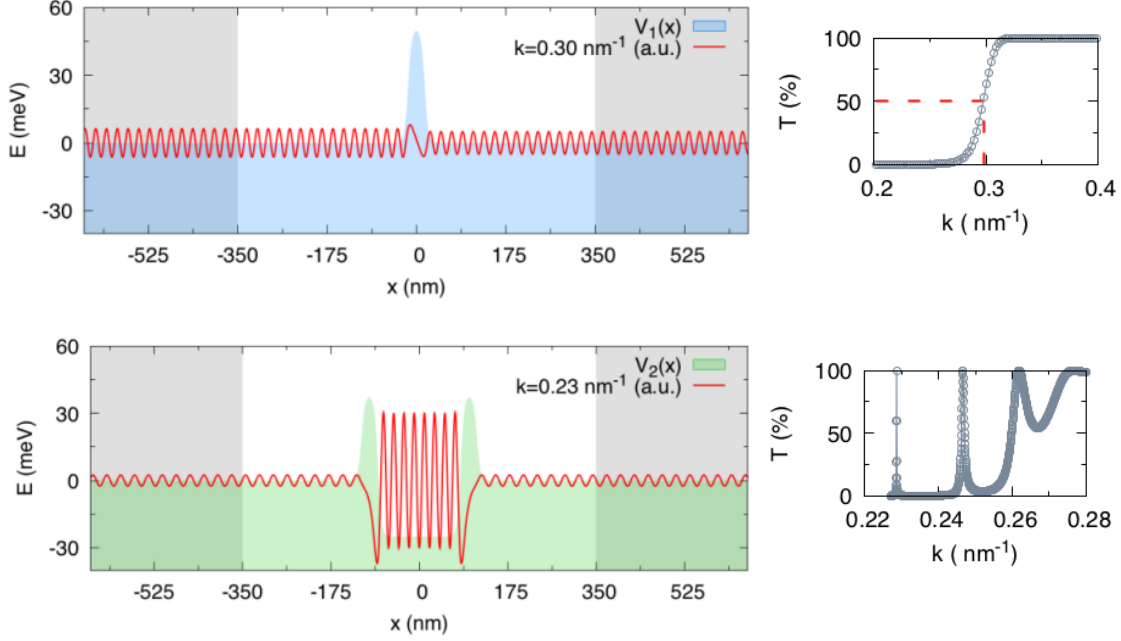


Figure 7.3: 1D scheme of the simulated nanodevices and corresponding transmission probability in the wavevector space. (Top) Single potential barrier (blue shaded area) and squared modulus of the propagating wavefunction computed by **Kwant** at $k_0 = 0.30 \text{ nm}^{-1}$. The arrow in the transmission probability at the right side of the panel shows that the selected state is half-reflected. Gray areas identify the position of the contacts, i.e. $x_L = -350 \text{ nm}$ and $x_R = 350 \text{ nm}$. (Bottom) Equivalent scheme for the double barrier scenario with the resonant state $k_0 = 0.23 \text{ nm}^{-1}$.

On the right side of each panel we show the transmission probability for the scattering potential on the left. The arrows highlight the selected wavevectors, which are an half-reflected state for case (i), and a resonant one for case (ii). The scattering state $\psi_{k_0}(x)$ is provided by the **Kwant** software, by simulating a one-dimensional system large enough to contain the active region of the device, plus the contacts from where electrons are injected. The grey areas define the interface with the reservoir: we select a right, x_R and a left x_L interface far enough from $V(x) \neq 0$ to ensure that the electron wavefunction inside the contacts is properly described by a linear combination of plane waves with wavevectors $\pm k_0$.

Then, we apply the definition of the Wigner distribution function as the Weyl-Wigner transform of the density matrix for the state $\psi_{k_0}(x)$,

$$f_W(x, k) = \frac{1}{2\pi\hbar} \int \psi_{k_0}(x+s) \psi_{k_0}^*(x-s) e^{-2iks} ds, \quad (7.17)$$

which is displayed in Fig. 7.4 for a selected set of x values. The green triangle locates the injected wavevector k_0 , while the gray areas define the location of the reservoir according to our modeling of the nanodevice. By adopting the U scheme described in Fig. 7.1(b), we assume that the left reservoir injects electrons with $k > 0$, and the right reservoir electrons with $k < 0$. Therefore, the

following boundary conditions apply:

$$f_W(x_L, k > 0) \propto \delta(k - k_0), \quad (7.18)$$

$$f_W(x_R, k < 0) = 0. \quad (7.19)$$

The Wigner distribution functions computed from the Weyl-Wigner transform at the interfaces, i.e. $f_W(x_L, k)$ and $f_W(x_R, k)$, are highlighted in red in Fig. 7.4.

(i) The simple potential barrier

For the single barrier case in Fig. 7.4(a), the Wigner distribution function presents more features than the simple delta at the left interface, which is expected from the Frensey's inflow boundary condition in Eq.(7.18) at positive values of k . In detail, it is characterized by the expected peaks at $k = \pm k_0$, that corresponds to the injected (positive) and reflected (negative) states due to the scattering at the potential barrier. The height of such peaks is large but finite, due to the finite size of the domain to numerically compute the Weyl-Wigner transform of the density matrix.

Moreover, $f_W(x_L, k)$ shows an additional peak at $k = 0$ and additional oscillations for all positive values of the wavevector $0 < k < k_0$. These features are not included in the inflow condition at the interface, and are related to the specific shape of the scattering potential $V(x)$ in the nanostructured core. Furthermore, these oscillations do not disappear by moving the interfaces far away from the active region: the Wigner distribution function is indeed stationary for $x < x_L$ or $x > x_R$.

(ii) The resonant double barrier

These inconsistencies becomes more visible in the presence of a double barrier. The map of the Wigner distribution is displayed in Fig. 7.4(b). Similarly to the previous scenario, the Wigner distribution function shows a peak at $\pm k_0$, while the negative counterpart at the left interface is here absent due to the unitary transmission probability of the injected state.

However, in the present configuration, stronger oscillations characterize a range of wavevectors $k > k_0$, as well as the negative wavevector range $0 < k < k_0$ at both interfaces. Therefore, due to the presence of strong oscillations at $k < 0$ for $x = x_R$, in the double barrier case the Wigner distribution function $f_W(x, k)$ violates not only Eq.(7.18), but also Eq.(7.19).

The origin of spurious oscillations

The presence of spurious oscillations at $0 < k < k_0$ is clearly related to the shape of the propagating wavefunction in proximity to the potential barrier.

Indeed, at the left interface ($x = x_L$), if s is not too large, $\psi_{k_0} \simeq e^{ik_0(x+s)} + re^{-ik_0(x+s)}$, so that the integrand for the Wigner distribution function reads:

$$\begin{aligned} \psi_{k_0}(x+s)\psi_{k_0}^*(x-s)e^{-2iks} &= (e^{ik_0(x+s)} + re^{-ik_0(x+s)})(e^{-ik_0(x-s)} + r^*e^{ik_0(x-s)})e^{-2iks} \\ &= e^{-ik_0(x+s)}e^{+ik_0(x-s)}e^{-2iks} + re^{-ik_0(x+s)}e^{-ik_0(x-s)}e^{-2iks} \\ &\quad + e^{ik_0(x+s)}r^*e^{ik_0(x-s)}e^{-2iks} + re^{-ik_0(x+s)}r^*e^{ik_0(x-s)}e^{-2iks} \\ &= e^{-2i(k-k_0)s} + re^{-2i(k_0x+ks)} + r^*e^{2i(k_0x+ks)} + |r|^2e^{-2i(k_0+k)s}. \end{aligned} \quad (7.20)$$

Note that generally $r = |r|e^{i\phi}$. By integrating over a large enough space in the s coordinate, and assuming that the contribution near to the scattering potential is negligible, the $f_W(x_L, k)$ can be approximated by:

$$f_W(x_L, k) = \delta(k - k_0) + |r|^2\delta(k + k_0) + |r|e^{i\phi}e^{-2ik_0x}\delta(k) + |r|e^{-i\phi}e^{+2ik_0x}\delta(-k) \quad (7.21)$$

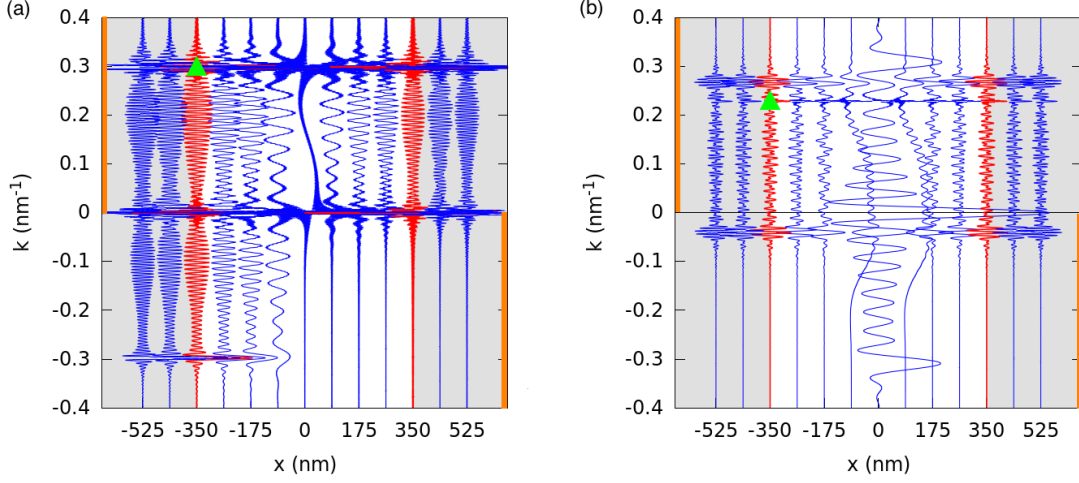


Figure 7.4: Wigner distribution function $f_W(x, k)$ projected on a set of x values for the (a) simple potential barrier and (b) double potential barrier. The green triangle locates the wavevector of the electron state injected from the reservoir. Gray areas define the reservoir and the yellow line identifies the range of inflowing states where the Frensky's boundary conditions apply. The Wigner distribution function at the interface is highlighted in red.

The first two delta functions correspond to the peak observed in the Wigner distribution function at the wavevector of injection k_0 and at the opposite value, $-k_0$. These identify the outflowing states. The last two contributions correspond instead to an oscillating term localized at $k = 0$, which then arises from the interference between the injected plane-wave and the reflected one at infinite distance from the scattering region.

However, for a value of s large enough, the scattering state has a shape that can not be described simply as the sum of two plane wave, i.e. the injected and reflected ones. Here, $\psi_{k_0}(x)$ is a linear combination of plane waves with a generic wavevector k' . By adopting a time-dependent picture for electron transport, we show in the next section that the oscillations arising at $0 < k < k_0$ are related to the specific shape of the wavefunction in proximity to the potential barrier.

7.3 Charge localization in a time-dependent picture

As a solution to the incompatibility between the Frensky's inflow boundary condition and the Wigner distribution function, we propose the modeling of electron transport in a time-dependent picture, where charges are injected as wavepackets rather than using stationary states.

We stress that by introducing the time-dependence in electron transport, both Wigner distribution function and charge distribution at the interface become time-dependent in principle. The introduction of time as a degree of freedom in the distributions at the interface could naturally solve the inconsistency, by arguing that the boundary on the inflowing states relates to the initial time only. At $t = 0$, the Wigner distribution function is computed from a state that is an injected wavepacket. At later times, the electron state is affected by scattering and therefore the Wigner distribution function can eventually be modified at the interface. For $t > 0$ the charge distribution at the interface is not bound to the Frensky's inflow condition anymore. In the following we show that our findings are not related to the time dependence of the inflow distribution at the boundaries

Fig. 7.5(a) shows the wavepacket dynamics in the potential landscape of a single barrier. We

assume the injection of a Gaussian wavepacket $\psi_{k_0}(x,0)$, centered at k_0 at the interface:

$$\psi(x,0) = \frac{1}{\sqrt[4]{\sigma^2 2\pi}} e^{-\frac{(x-x_0)^2}{4\sigma^2}} e^{ik_0(x-x_0)} \quad (7.22)$$

and evolve the localized wavefunction by means of a on-dimensional implementation of the Split-Step Fourier method. After the interaction at the barrier, the reflected and transmitted wavepackets reach the two interfaces and are absorbed by the contacts. We then compute the Weyl-Wigner transform of the density matrix for the time evolved state $\psi(x,t)$. Fig. 7.5(b) compares the initial Wigner distribution function ($t = 0$) to the final one, which is composed by the 3 contributions signed as R , T , INT .

Initially, $f_W(x,k)$ is non zero in correspondence to a Gaussian distribution of states centered at k_0 . This is clearly not a delta function, as for the monoenergetic state, but correspond to a very narrow distribution in the wavevector space, whose broadening depends on the size of the injected wavepacket. In the present scenario, an analytical form of the Wigner distribution function can be provided:

$$f_W(x,t=0) = \frac{1}{\pi\hbar} e^{-\frac{(x-x_0)^2}{2(\sigma)^2}} e^{-\frac{(k-k_0)^2}{2(\sigma_k)^2}}, \quad (7.23)$$

which is the product of two Gaussian distributions centered at x_0 and k_0 with a real-space broadening σ and a size $\sigma_k = 1/2\sigma$ in the wavevector space.

At the end of the scattering, when the reflected and transmitted wavepackets reach the two interfaces, the Wigner distribution function is characterized by two Gaussian distributions centered at k_0 and $-k_0$, plus an oscillating contribution centered at $k = 0$. By assuming that the final state is properly described by the sum of two counterpropagating Gaussian wavepackets centered at k_0 and $-k_0$:

$$\psi(x,t=t_F) = \frac{1}{\sqrt{2(1+e^{x_0^2/2\sigma^2})} \sqrt{2\pi\sigma^2}} (e^{-\frac{(k-k_0)^2}{4\sigma^2}} + e^{-\frac{(k+k_0)^2}{4\sigma^2}}), \quad (7.24)$$

the Wigner distribution function is approximated by:

$$f_W(x,k,t=t_F) = \frac{N^2}{2\pi\hbar} (e^{-\frac{(x-x_0)^2}{2\sigma^2}} + e^{-\frac{(x+x_0)^2}{2\sigma^2}} \cos(\frac{2kx_0}{\hbar})). \quad (7.25)$$

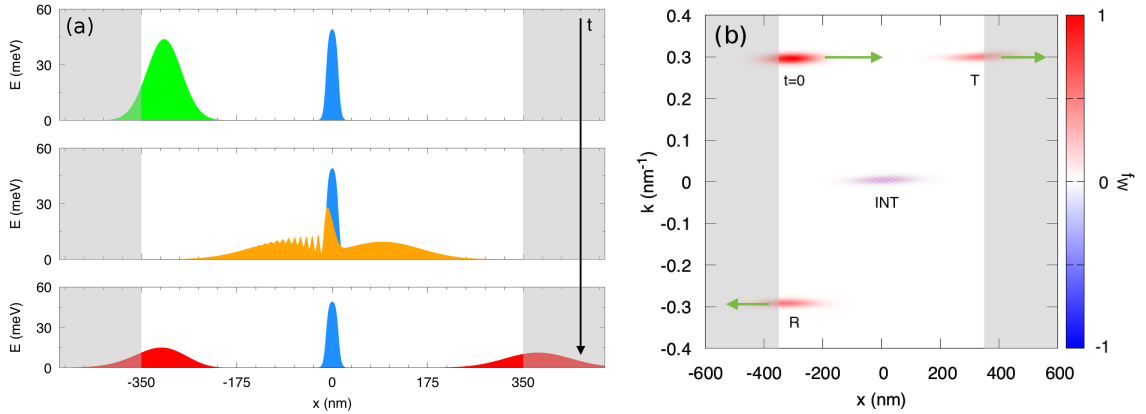


Figure 7.5: (a) Evolution of a Gaussian wavepacket in the active region containing a simple potential barrier. (b) Wigner distribution function $f_W(x,k,t)$ at initial ($t = 0$) and final time, where the wavepacket is split into 3 contributions: R , T and INT . Green arrows define the direction of propagation for each wavepacket.

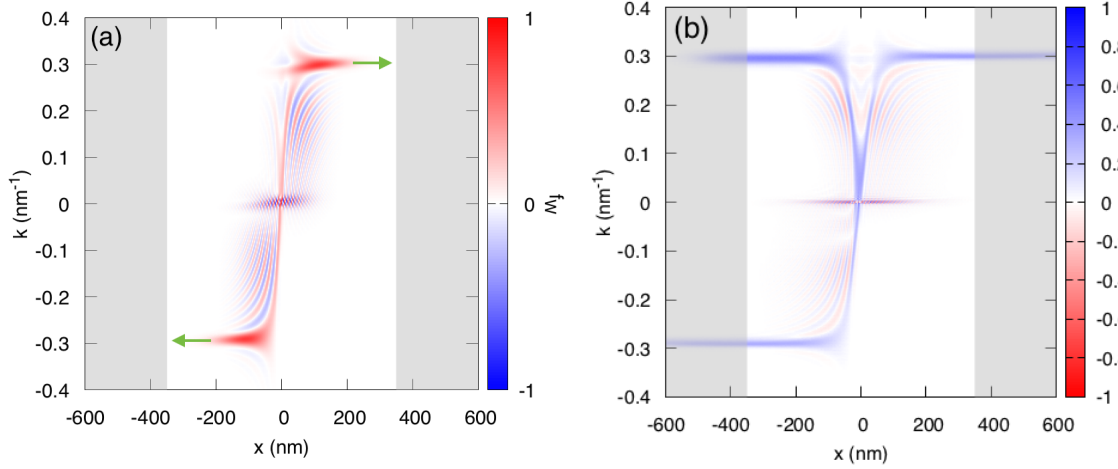


Figure 7.6: (a) Wigner distribution function $f_W(x, k, t)$ at intermediate time $t = t_M$ for the Gaussian wavepacket of plane waves that propagates in presence of the simple potential barrier. (b) Stationary Wigner distribution function computed by integrating over time the time-dependent Wigner distribution. Here, we assume each electron to be injected as an independent wavepacket.

The cosine clearly shows that the oscillatory term at $k = 0$ originates from the interference between the transmitted and the reflected wavepackets. With contrast to the stationary picture, this term does not reach the interfaces, but it is quenched by the spatial localization of the electron wavefunction due to the presence of the damping exponential term depending on σ .

In order to observe the additional oscillations for $0 < k < k_0$, we select an intermediate simulation time $t = t_M$, and compute the Wigner distribution function for the corresponding time-evolved electron state. As depicted in Fig. 7.6(a), oscillations arise when the density probability of the electron wavefunction is non zero in proximity to the scattering potential. These oscillations spread along the whole k -space during the time evolution, but do not reach the two interfaces due to the spatial localization of the electron wavepacket.

Finally, we observe that the stationary picture can be recovered from our time-dependent modeling of electron transport. Here, due to the charge localization, we expect that this procedure does not provide those spurious oscillations affecting the Wigner distribution function in the stationary scenario, so that the Frensey's inflow boundary conditions can be applied. In detail, we assume the continuous injection of single-electron wavepackets in time centered at k_0 . In presence of non-interacting electrons, that are separately injected one at a time within the approximations of Ref. [86], the stationary Wigner distribution function for the injection of a stream of electrons is well approximated by integrating the time-dependent Wigner distribution function over time. The result is mapped in Fig. 7.6(b): if the two interfaces are well separated from the scattering region as in the present case, the Wigner distribution function at the boundaries fulfills Eq.(7.18) and Eq.(7.19). The inflowing states determine indeed a non-zero $f_W(x, k)$ only at left interface for $k = k_0$, while all additional oscillations are quenched.

Finally, in Fig. 7.7 we show the time-dependent Wigner distribution function for a Gaussian wavepacket that interacts with the double potential barrier at 4 different iteration times. In the present regime, we select a central wavevector k_0 that corresponds to the resonant state in the stationary picture. However, due to the presence of an energy broadening which is larger than the resonant peak, we expect to observe a reflected component of the Gaussian wavepacket that outflows from the scattering region. As visible in Fig. 7.7, the distribution $f_W(x, k, t)$ for the present

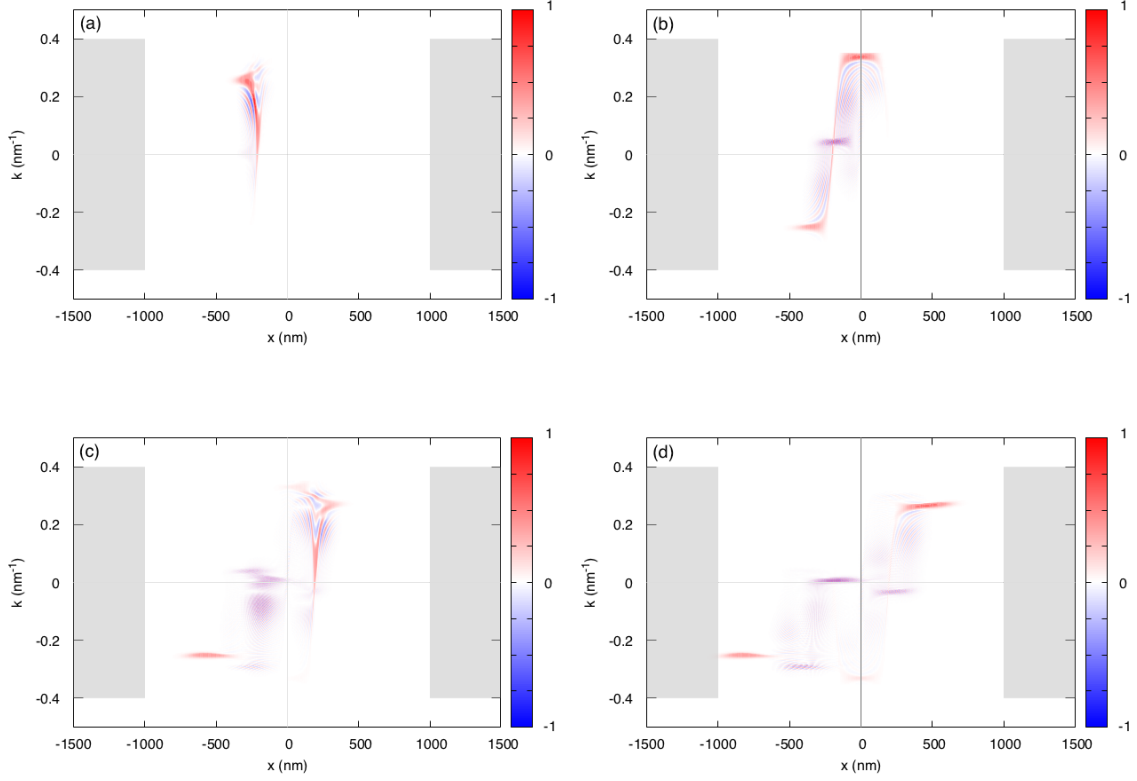


Figure 7.7: Map of the time-dependent Wigner distribution function $f_W(x, k, t)$ at different iteration times in presence of the double potential barrier. The central wavevector of the Gaussian wavepacket is the resonant state of the scattering potential, $k_0 = 0.23 \text{ nm}^{-1}$.

system is characterized by the interference pattern we already observed in the simple barrier case. However, for a proper choice of the interfaces as well as of the wavepacket size, these oscillations are localized inside the scattering region. Only the reflected and transmitted wavepackets (red shapes) reach the two interfaces, thus affecting the boundary condition.

7.4 Non-locality of the orthodox momentum

In the previous sections we highlight the inconsistencies that arise when matching the Wigner distribution function to the Frensel's inflow boundary condition. We also observed that the additional oscillations of the Wigner distribution $f_W(x, k)$ at the interfaces are not related to the position of the boundary, namely x_L and x_R for the left and right side of the active region respectively.

These spurious features arise indeed due to non-local nature of the orthodox momentum \hat{p} . In a stationary framework, the scattering state $\psi_{k_0}(x)$ that describes the electron state in presence of a potential barrier is described - at an appropriate distance from the potential itself - as a linear combination of plane waves with wavevector $\pm k_0$, which are non-local by definition. In proximity to the potential barrier, the electron state is actually a linear combination of plane

waves with different momenta $-k_0 < k' < k_0$, depending on the scattering process. Then, the Wigner distribution function $f_W(x, k)$ for such state involves an integral on the whole domain that correlates, at any position x in the simulation box, a *local* momentum k that contains information regarding all the momenta in the electron state $\psi_{k_0}(x)$, i.e. $-k_0 \leq k' \leq k_0$.

Differently, the Frensky's inflow boundary condition refers to a local momentum, i.e. the one at the boundaries x_L or x_R , which in principle should not be related to any other event affecting the electron state elsewhere in the device, except electron injection from the reservoir. The Wigner distribution function provides a simultaneous description of the position and momentum of the particle through its definition on the (x, k) domain, thus enabling - from a mathematical point of view - the application of boundaries for the momenta at the interface.

However, as explained above, if the Wigner distribution function is computed with the scattering states in a stationary picture, the momentum k at a given position x contains information on the events affecting the electrons in the whole device, due to the non locality of the orthodox momentum. This incompatibility manifests when applying these spatially-dependent boundary condition to the Wigner distribution function, which can be interpreted as a *projection* of a non-local information (the orthodox momentum in the scattering states) on a local one (the momentum at the interface). For infinite extended states the difference between the non-local orthodox momentum and the local momentum in Frensky's approach prevent to fulfill the boundary conditions.

The most natural solution to this inconsistency is to "force" a local description to the wavefunction by encoding the electron state in a wavepacket. This is a local wavefunction that correlates a given position of the one-dimensional domain x to a set of wave-vectors k with a probability distribution that depends on the position itself. For an adequate distance from the scattering potential and a small enough broadening of the wavepacket in real space, the electron state is composed by a narrow set of wavevectors centered at k_0 that define the injection process (the density matrix is zero anywhere else). When approaching the scattering potential, new states contributes to the electron wavefunction. When the wavefunction splits at the potential barrier, two contributions propagate in the opposite direction. The new states arising from the scattering process are correlated to the center of the active region only, and still do not contribute to the Wigner distribution at the interface, so that the injection is not affected by scattering process.

We further observe that, in an orthodox picture, the momentum at the end of the scattering process of a single-electron wavepacket impinging on a potential barrier is oriented in the two opposite direction of propagation for the reflected and transmitted wavepackets. This does not represent an issue for the Frensky's boundary conditions, which fixes the distribution of the inflowing states at the interfaces only. However, this is still a signature of the non locality of the orthodox momentum: indeed, the Wigner distribution in the middle of the active region is characterized by an oscillating interference term, whose spatial extension depends on the wavepacket size. The orthodox quantum mechanics solves this non locality with the collapse theory: when the outflowing electron is thermalized, the interference term vanishes. An alternative solution is represented by the use of the conditional wavefunction in the Bohmian distribution, which always allows a simultaneous definition of position and momentum for a wavepacket description of the electron state [116, 125].

Article

A Proposal for Evading the Measurement Uncertainty in Classical and Quantum Computing: Application to a Resonant Tunneling Diode and a Mach-Zehnder Interferometer

Devashish Pandey ^{1*}, Laura Bellentani ², Matteo Villani ¹, Guillermo Albareda ³, Paolo Bordone ^{2,4}, Andrea Bertoni ⁴ and Xavier Oriols ¹

¹ Departament d'Enginyeria Electrònica, Universitat Autònoma de Barcelona, 08193-Bellaterra (Barcelona), Spain; devashish.pandey@uab.cat (D.P.); matteo.villani@uab.cat (M.V.); xavier.oriols@uab.cat (X.O.)

² Dipartimento di Scienze Fisiche, Informatiche e Matematiche, Università degli Studi di Modena e Reggio Emilia, Via Campi 213/A, I-41125 Modena, Italy; laura.bellentani@unimore.it (L.B.); paolo.bordone@unimore.it (P.B.)

³ Max Planck Institute for the Structure and Dynamics of Matter and Center for Free-Electron Laser Science, Luruper Chaussee 149, 22761 Hamburg, Germany; guillermo.albareda@mpsd.mpg.de (G.A.)

⁴ S3, Istituto Nanoscienze-CNR, Via Campi 213/A, 41125 Modena, Italy; andrea.bertoni@unimore.it (A.B.)

* Correspondence: devashish.pandey@uab.cat

Received: 8 April 2019; Accepted: 29 May 2019; Published: 4 June 2019



Abstract: Measuring properties of quantum systems is governed by a stochastic (collapse or state-reduction) law that unavoidably yields an uncertainty (variance) associated with the corresponding mean values. This non-classical source of uncertainty is known to be manifested as noise in the electrical current of nanoscale electron devices, and hence it can flaw the good performance of more complex quantum gates. We propose a protocol to alleviate this quantum uncertainty that consists of (i) redesigning the device to accommodate a large number of electrons inside the active region, either by enlarging the lateral or longitudinal areas of the device and (ii) re-normalizing the total current to the number of electrons. How the above two steps can be accommodated using the present semiconductor technology has been discussed and numerically studied for a resonant tunneling diode and a Mach-Zehnder interferometer, for classical and quantum computations, respectively. It is shown that the resulting protocol formally resembles the so-called collective measurements, although, its practical implementation is substantially different.

Keywords: quantum computing; classical computing; Mach-Zehnder Interferometer; resonant tunneling diode; quantum uncertainty; measurement

1. Introduction

Assessing the future of emergent technologies is not an easy task. Today there is a lively debate in the scientific community about whether classical or quantum computing will offer better performance in the coming future. At present, the field effect transistor is still the most efficient device to perform classical computations. The electronic industry is able to fit 10^{10} transistors all together in a single chip, working at frequencies of a few GHz [1]. State-of-the-art transistors, with nanoscale dimensions, are quantum devices in the sense that their ability to convert the input into output information is based on quantum laws governing electron transport [2]. In digital binary classical computing, the logical state '1' is encoded into a value of a well-defined measurable physical property of the transistor, while the logic state '0' corresponds to a different value of such property. Usually the physical properties used in

electron devices for classical computing are the electrical current or the voltage in different (input and output) terminals. It is important to notice that although the transistor is a quantum device whose performance is determined by the evolution of quantum states, these quantum states are not directly used to encode information in classical computing.

In quantum computing [3], contrarily, the logical state '1' is directly encoded in a quantum state of the physical system, namely $|1\rangle \rightarrow \psi_1(\vec{r}, t)$ where \vec{r} represents the degrees of freedom of the system. Similarly, the logical state '0' corresponds to another quantum state $|0\rangle \rightarrow \psi_0(\vec{r}, t)$. Because of the quantum superposition principle, a sum of the two physical states, $a|1\rangle + b|0\rangle$ where a and b are complex numbers, is also a valid physical state of the system. As a consequence, quantum mechanics offers the possibility of operating simultaneously on the logical states '1' and '0'. This opens classically inaccessible computing possibilities.

Many companies and researchers are advocating for quantum computing. Among many others, for example, Google has said that its state-of-the-art quantum chip will be the first to perform calculations beyond the best existing classical supercomputers [4]. Other companies and researchers, on the contrary, understand quantum computing as an exciting discipline, with an unquestionable scientific interest, but argue that quantum technologies will not substitute our classical computing machines at home (because quantum computers are complex, expensive and built using a more immature technology) [5,6]. In any case, without making any risky prediction, what seems clear today is that classical and quantum computing are both valuable research avenues.

Any classical or quantum computation using quantum devices is implemented following three main steps: (i) initial preparation of the quantum state, (ii) unitary evolution of the state and (iii) the final measurement of the state. In this paper, we will focus on the last step for both classical and quantum computations. The measurement step is linked to the quantum uncertainty [7] that implies a practical inconvenience since it gives rise to quantum noise at the output of the device (The reader can argue that the uncertainty disappears when the quantum state is prepared as an eigenstate of the projective (measuring) operator. However, typically, the *preparation* of the state of an electron being injected into the active device region from the contact (reservoir) is done by the contacts itself, which do not provide such eigenstates). Solid-state quantum electron devices are unquestionably the best technology to implement classical computing. It is, however, not clear today which will be the best technology for quantum computing. In any case, it seems clear that the possibility of implementing quantum computing algorithms with solid-state devices would benefit from the maturity of the existing technology and offers the possibility of making quantum computing platforms compatible with classical ones.

The paper is structured as follows. In Section 2, we will propose a simple protocol that allows evading the quantum uncertainty associated with the measurement process in quantum electron devices, for either classical or quantum computing applications. This is the main result of this work. In Section 3, we will first investigate the measurement of the electrical current under this protocol for a resonant tunneling diode (RTD) understood as a quantum electron device useful for classical computing. Later, in Section 4, we will analyze the measurement of the electrical current in a Mach-Zehnder interferometer (MZI) which is tailored to design the logic gates suitable for implementing quantum computing. We will conclude in Section 5. More technical details are presented in the appendices.

2. Quantum Uncertainty: The Problem and the Solution

In this section, in order to simplify the discussion and better understand the problem and the solution explained here, we made the following simplifying assumptions. First, we will focus on a quantum electron device with just one degree of freedom indicated by \vec{r} . The consideration of more realistic situations, with many degrees of freedom in a quantum device, would not modify the conclusions drawn here and would only complicate the notations and understanding of the results.

See Appendix A for the straightforward generalization of the present results to an unmodified (original) quantum device with many degrees of freedom in the active region.

Second, we will assume that the measurement of the electrical current of the quantum electron device is done through a projective (strong) operator and that the state of the system after the measurement is just an eigenstate of this operator. In other words, we will assume that the measurement process is done with a projective value measure (PVM), while it has been argued that the realistic type of measurement of the electrical current is better described by a positive operator valued measure (POVM) [8,9]. In any case, the explicit consideration of a POVM to describe the measurement process will not add any relevant point in the discussion. In Appendix C, we explain with more detail the measurement of the electrical current in a realistic quantum electron device as a POVM.

2.1. The Problem

The first step to implement a classical or quantum computing algorithm using quantum devices is the initial preparation of the quantum state associated with the quantum electron device $\psi_{in}(\vec{r}, 0)$. In quantum computing, the initial state is directly linked to a combination of two states, $\psi_1(\vec{r}, 0)$ and $\psi_0(\vec{r}, 0)$, respectively associated with the logical values '1' and '0', whereas in classical computing, the link between logical information and initial quantum state is not direct. Typically, a quantum device for classical computation is connected to the external world through the contacts (also known as reservoirs) that determine the electron wave function depending on temperature and doping conditions. The input logical information is then linked to a value of an observable I , not directly to the quantum state. We have used the symbol I to remind readers that hereafter, we will consider the electrical current as the physical magnitude where information is encoded.

The second step is the manipulation of the initial quantum state through the quantum electron device (also known as gate in the literature). Typically, such manipulation, whether in classical or quantum computing is done through a (usually unitary) operator $\hat{U}(t, 0)$. In quantum computing, the final state $\psi_{out}(\vec{r}, t) = \hat{U}(t, 0)\psi_{in}(\vec{r}, 0)$ is directly linked to the output logical information, while in classical computing the output logical information is linked to an observable I associated with this final state through a measurement process that we describe below. See Figure 1a where different gates of an RTD which are connected to exemplify a classical computation gate connected through output values of the electrical current (or voltage), while the connection among different gates of the quantum computing device is done through the wave function itself as depicted in Figure 1b.

The third and last step, both in classical or quantum computing algorithms, is the measurement step. To get the final observable value I in classical computing, the quantum electron device has to be measured through a (non-unitary) process. Such non-unitary process is depicted as an ammeter in Figure 1. The evolution from the final state to the measured state, $\psi_{out}(\vec{r}, t) \rightarrow \psi_I(\vec{r}, t)$, is called collapse or reduction of the wave function. The subindex I here refers to the measured state of the current which corresponds to an eigenvalue I of the eigenfunction $\psi_I(\vec{r}, t)$ associated with the operator \hat{I} . In quantum computing, the final wave function $\psi_{out}(\vec{r}, t)$ is not directly measurable in a single shot measurement. Instead, the logical information assigned to this final quantum state has to be indirectly deduced from the measurement of an observable assigned to such final state. See Figure 1b. Notice that the measurement in quantum computing has to be done only once, at the end of the gate, because each measurement collapses the wave function, destroying the required superpositions of different states in the quantum computing algorithms.

The process of measurement involves a quantum uncertainty which is a consequence of the fact that each time a quantum measurement is done, the wave function collapses into an eigenstate of the operator \hat{I} associated with the measuring apparatus. The observable output I_{out} is a random value equal to the eigenvalue associated with the mentioned eigenstate. In general, and this is true for the measurement of the electrical current, the final state before measurement $\psi_{out}(\vec{r}, t)$ is not an eigenstate of the current $\psi_I(\vec{r}, t) \neq \psi_{out}(\vec{r}, t)$. In fact, the final state can be written as a superposition of many different current eigenstates. Thus, each time we repeat an experiment to obtain information about

the output current, we get different values. This randomness in the output values can be quantified through the probability distribution $P(I) = |\langle \psi_I(\vec{r}) | \psi_{out}(\vec{r}, t) \rangle|^2$ given by Born's law. From a quantum engineering point of view, this quantum uncertainty (seen as noise in the current) is inconvenient for efficiently processing logical (either classical or quantum) information.

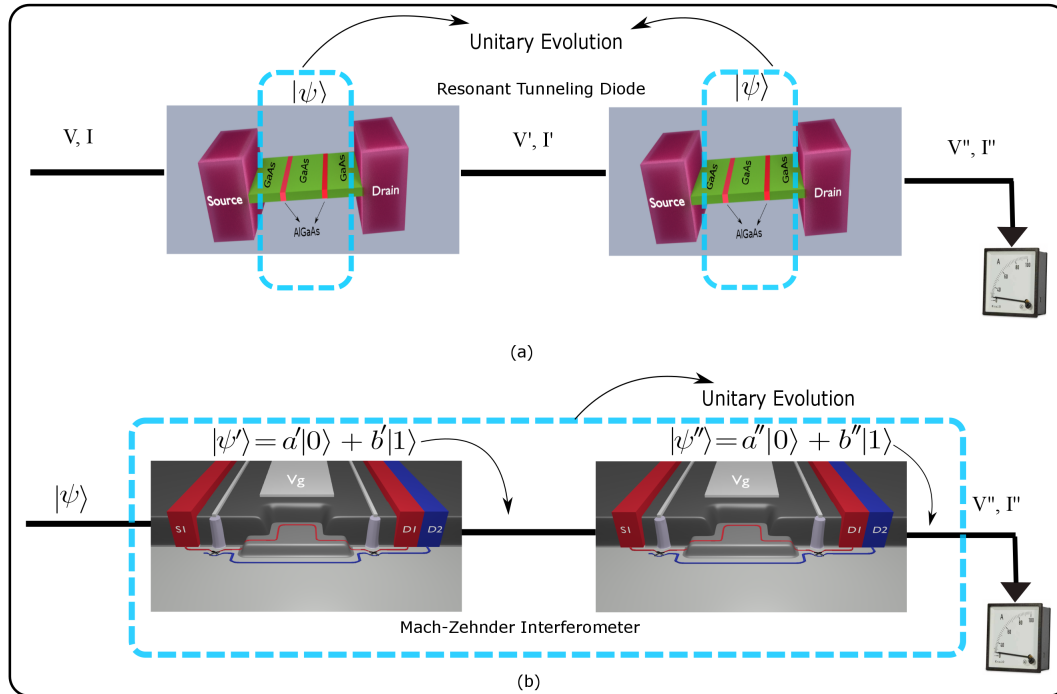


Figure 1. (a) Schematic of classical computing exemplified with RTD where only the active device is governed by unitary quantum evolutions (enclosed in the cyan color dashed line), while the contacts and the cable leads to quantum decoherence which provides a fixed value of the current obtained in the measuring apparatus (shown at the right end). (b) Schematic of quantum computing exemplified with an MZI where the quantum wholeness requires that a coherent unitary evolution appears in all the gates (enclosed in the cyan color dashed line). Only at the end, when the wave function is measured, decoherence can be accepted.

In classical computations, the uncertainty on the electrical current can be eliminated by using the ensemble value of the current $\langle I \rangle$ computed from a large number of identical experiments, each one giving I^i , with the subindex i identifying the experiment. The ensemble value is defined as $\langle I \rangle = (\sum_{i=1}^{N_{exp}} I^i) / N_{exp}$, where $N_{exp} \rightarrow \infty$ is the number of experiments. In principle, this ensemble value would require repeating the same experiment for a large set of N_{exp} identical quantum electron devices. In practice, by invoking ergodic arguments, the repetition of the experiment is substituted by measuring at different times in the same quantum electron device. Thus, instead of defining the signal of the output logical value as the instantaneous current I^1 (which has noise) one defines it as the DC value of the electrical current $\langle I \rangle$ computed during a large time interval (which has no noise). This solution is efficient for reducing the noise, but it requires a large measuring time. (In our simulation example with an RTD with a device active region length of 10 nm, the injection time of 0.05 ps and the velocity of electrons as 10^4 m/s, the time after which we get the non-fluctuating value of the current is around 50 ps. In any case, the measuring time is again a parameter that depends on many factors, like injection time, velocity of electrons, electron density, level of tolerable uncertainty, etc., and that can be enlarged or reduced as desired by manipulating these parameters.)

The quantum uncertainty described above represents also a problem for quantum computing. In fact, although the logical output information in quantum computing is encoded in the final wave function $\psi_{out}(\vec{r}, t)$ (not in an observable I^i), the quantum state $\psi_{out}(\vec{r}, t)$ is not itself an observable

(i.e., it cannot be measured in a single shot measurement). Thus, the quantum state of the system needs to be deduced from the expectation value $\langle I \rangle$. Again, the measurement process of such observable $\langle I \rangle$ has the same inconveniences mentioned above for classical computing, due to the quantum uncertainty. We notice that in a quantum computing algorithm, with many interconnected quantum gates, the measurement of the observable is done only at the last gate. In fact, trying to measure at an intermediate gate would be understood as a type of decoherent phenomena that would dramatically perturb the unitary evolution required in typical quantum algorithms. In Figure 1 we encircle the regions of the connected gates where the dynamics of electrons are supposed to be governed by unitary quantum evolutions. From Figure 1, one can understand why decoherence is a serious problem for quantum computing, but not for classical computing. In an array of interconnected classical computing devices, the decoherence that can appear at the output of each particular device due to the measurement does not affect the performance of the algorithm because the interconnection between devices is done in terms of observables (not in terms of wave functions).

In summary, the electrical current in nanoscale devices, for classical or quantum computing, has an inherent quantum uncertainty, seen as noise in the measured value of the electrical current. Since the information is usually encoded in the average value $\langle I \rangle$ of the electrical current, we require an effort to wash out the noise from the measured current to get valid information. The typical solution in the literature to wash out the noise is repeating the experiment many times (or using the ergodic theorem to get $\langle I \rangle$ after a large time).

2.2. The Solution

In this work, we explain a novel solution to the problem discussed above about reducing the quantum noise induced by the measurement process. We argue in this paper that such noise can be eliminated by modifying the quantum device to accommodate $N \rightarrow \infty$ electrons, simultaneously. We will show that the dispersion of a random distribution of the (normalized) electrical current of $N \rightarrow \infty$ electrons tends to zero, which implies eliminating the quantum noise.

Let us consider an original or unmodified quantum electron device (before applying our protocol) that has only one transport electron, at each time, responsible for the measured current. Such electron at time t_{in} is described by a single particle quantum state $|\psi^1(t_{in})\rangle$ where the superindex 1 refers to this first electron. We are measuring the current through a single particle operator \hat{I}^1 . If the state $|\psi^1(t_{in})\rangle$ is not an eigenstate of the operator \hat{I} , then, the measurement of the I gives rise to the quantum noise discussed in the previous subsection (we notice again that the generalization to more electrons is done in Appendix A).

The solution that we propose to minimize the quantum noise requires designing a new quantum device (that we will refer to as the modified quantum device or just the quantum device) so that this new device satisfies the following two conditions:

- **Condition 1:** We enlarge the original quantum electron device in order to accommodate a large number of electrons $N \rightarrow \infty$ simultaneously. Then, the many-particle wave function $\Psi_T(t_{in})$ that defines this N electrons at time t_{in} is:

$$|\Psi_T(t_{in})\rangle = |\psi^1(t_{in})\rangle \otimes |\psi^2(t_{in})\rangle \otimes \dots \otimes |\psi^N(t_{in})\rangle, \quad (1)$$

where the wave function $|\psi^i(t_{in})\rangle$ is the single electron wave function that corresponds to the i -th electron prepared under the same conditions that we have used to prepare the wave function $|\psi^1(t_{in})\rangle$ in the original quantum electron device.

Strictly speaking, the condition $N \rightarrow \infty$ is inaccessible in a practical scenario. We will see numerically in the following sections that a finite number of electrons is enough to drastically reduce the quantum noise. Identically, if the number of transport electrons in the original (unmodified) quantum electron device is already larger than one, the solution proposed here is still perfectly valid. See Appendix A for a generalization of the present protocol to more than one

electron in the unmodified electron device. Finally, as can be seen in Equation (1), we assume a many-particle wave function of non-interacting electrons. This is obviously an approximation in realistic quantum devices since these electrons will suffer exchange and Coulomb interactions. These issues will be further elaborated in the practical implementation of this protocol in next two section.

We mention that some (small) variation in the preparation of the state $|\psi^1(t_{in})\rangle, |\psi^2(t_{in})\rangle, \dots$ forming $\Psi_T(t_{in})$ is allowed. For example, the time delay between the injection of different single electron wave packets can vary. Also the central position of the wave packets along the lateral dimension of the device can be different. Similarities between different wave packets have to be enough to justify that the probability distribution of the values of the current is identical for all single electron wave packets.

- **Condition 2:** We substitute the measuring apparatus associated with the single particle operator \hat{I}^1 with a new measuring apparatus whose associated many-body operator \hat{I}_T is:

$$\hat{I}_T = \frac{\hat{I}^1 + \hat{I}^2 + \dots + \hat{I}^N}{N}, \quad (2)$$

where $\hat{I}^i = \hat{\mathbb{I}} \otimes \dots \otimes \hat{I}^i \otimes \dots \otimes \hat{\mathbb{I}}$ acts only on the quantum state $|\psi^i(t_{in})\rangle$ and $\hat{\mathbb{I}}$ is the identity operator in the small Hilbert space of each degree of freedom. Notice the presence of the factor $N \rightarrow \infty$ in the denominator of the operator \hat{I}_T .

In next section, we will show the physical soundness of the many-particle operator in Equation (2) for typical semiconductor electron device technology.

Now let us formally demonstrate that the dispersion of the electrical current of the modified quantum device (satisfying **condition 1** and **condition 2**) is zero. For the operator \hat{I}_T defined in Equation (2), we calculate the variance of the $\langle \hat{I}_T^2 \rangle$ as the mean square value of the operator \hat{I}_T as:

$$\langle \Psi_T | (\hat{I}_T)^2 | \Psi_T \rangle = \frac{1}{N^2} \sum_i \langle \psi^i | \hat{I}^i \hat{I}^i | \psi^i \rangle + \sum_{i,j \neq i} \frac{1}{N^2} \langle \psi^i | \hat{I}^i | \psi^i \rangle \langle \psi^j | \hat{I}^j | \psi^j \rangle. \quad (3)$$

By construction of the wave function in Equation (1), we know that the mean values $\langle \psi^j | \hat{I}^j | \psi^j \rangle$ are all identical for any j . Therefore, we can consider $\langle \psi^j | \hat{I}^j | \psi^j \rangle = \langle \psi^1 | \hat{I}^1 | \psi^1 \rangle$ because all electrons are described by the same wave function and we can rewrite Equation (3) as follows,

$$\langle \Psi_T | (\hat{I}_T)^2 | \Psi_T \rangle = \frac{N}{N^2} \langle \psi^1 | (\hat{I}^1)^2 | \psi^1 \rangle + \frac{N(N-1)}{N^2} \langle \psi^1 | \hat{I}^1 | \psi^1 \rangle \langle \psi^1 | \hat{I}^1 | \psi^1 \rangle. \quad (4)$$

Therefore, when $N \rightarrow \infty$, we get:

$$\langle \hat{I}_T^2 \rangle = \langle \Psi_T | (\hat{I}_T)^2 | \Psi_T \rangle = \langle \psi^1 | \hat{I}^1 | \psi^1 \rangle \langle \psi^1 | \hat{I}^1 | \psi^1 \rangle = \langle \hat{I}^1 \rangle^2. \quad (5)$$

Now, we have to demonstrate that the logical information provided by the modified quantum device dealing with I_T is the same as the one that one gets from the original quantum device. As we discussed, the logical information of the original quantum device was represented by the mean value of the current $\langle \hat{I}^1 \rangle$ and not by the instantaneous value I^1 (which was too noisy due to quantum uncertainty). It is quite simple to demonstrate that $I_T = \langle \hat{I}^1 \rangle$ for $N \rightarrow \infty$. By construction, we know $\langle \hat{I}^1 \rangle = \langle \hat{I}^j \rangle$, from Equation (2) we get $\langle \hat{I}_T \rangle = N \langle \hat{I}^1 \rangle / N = \langle \hat{I}^1 \rangle$ and with Equation (5), we conclude that the dispersion σ_{I_T} of the distribution of the total current I_T is zero:

$$\sigma_{I_T}^2 = \langle \hat{I}_T^2 \rangle - \langle \hat{I}_T \rangle^2 = 0. \quad (6)$$

The result $\sigma_{I_T} = 0$ in Equation (6) implies that the distribution of I_T is a delta function around $\langle \hat{I}^1 \rangle$. This implies that in every measurement one gets the mean value of the single particle average current $I_T = \langle I^1 \rangle$.

It can be easily checked that the state in Equation (1) in the limit $N \rightarrow \infty$ is, in fact, an eigenstate of any operator of the type of Equation (2) at any time. This state, with this unusual property, has been used by one of the co-authors to study the quantum-to-classical transition [10]. In addition, a similar state and operator as the ones invoked in our **condition 1** and **condition 2** has been used to develop the new concept of collective measurements [11,12]. Such collective measurements do really invoke multiple physical repetitions of the quantum system, while in our paper we make use of this idea in the same many-particle state and operator and in a single (modified) quantum device. In other words, the demonstration provided above is mathematically equivalent to the one that appears in the theory of collective measurements, but their physical implementation in the laboratory is radically different. In the rest of the paper, we will show how these two conditions can be effectively implemented with the semiconductor electron device technology in a single device for classical and quantum computing.

3. Application to Classical Computing Device: Resonant Tunneling Diode

As an example for the application of the discussed protocol in a classical computing device, we consider the computation of the electrical current in an RTD. This type of electron device is a pure quantum device, whose performance is based on tunneling, and has been successfully implemented in some particular high frequency applications particularly to explore the missing THz gap for various analog and digital applications [13–16]. The main element that defines an RTD is a double barrier potential created, for example, by alternating Gallium Arsenide (GaAs) and Aluminum Gallium Arsenide (AlGaAs) III-V semiconductors with different energy gaps, as shown in Figure 2. The combination of low band gap and high band gap semiconductors leads to the formation of a well in the potential energy profile, which gives rise to discrete set of energies inside, known as resonant energies.

As depicted in Figure 2, two reservoirs or contacts emit or collect the electrons through the RTD structure. We name the left contact as source (also known as emitter in the literature) and the right contact as drain (also known as collector in the literature). These contacts are responsible for the first step of classical computing algorithm: the preparation of the initial quantum states. The energy of the injected electrons is determined by the Fermi-Dirac statistics (depending on the doping conditions of the contacts). A regular injection of electrons is assumed according to the discussion of the Appendix B. The second step of the classical computing algorithm is carried out by the barrier structure that determines whether the injected electrons are effectively transmitted or not. An electron incident on the double barrier with an energy equal to one of the resonant energies tunnels through the barrier, being transmitted with a transmission coefficient T close to one, while electrons with other energies have a transmission coefficient close to zero. An external potential between the drain and source potentials, modifies the double barrier potential energy profile, controlling the ON and OFF currents. One value of the current can be assigned to the logical output information '1' and the other to the '0'.

The last step of the classical computing algorithm is the measurement of the ON or OFF current which implies the measurements (collapse) of the quantum wave function assigned to electrons inside the RTD, which provides the undesired quantum uncertainty in the output values of the current. We discuss next how the conditions of Section 2.2 can be implemented.

3.1. Implementation of Condition 1 and Condition 2

We consider that the RTD depicted in Figure 2 corresponds to the modified design of the device that accommodates a large number of N electrons simultaneously inside. In this particular device, enlarging the lateral area A is enough to enlarge the number of electrons inside the RTD. We can reasonable assume that the contact *prepares* the wave packets of each electron in a similar way so that the **condition 1** of our protocol in Equation (1) is easily satisfied. Certainly, a point that requires

further discussion is how to ensure that the many-body wave function of electrons in the active region of this modified device can be approximated by the non-interacting wave function in Equation (1). In the Appendices A and B some qualitative indications are mentioned. A different solution for minimizing the undesired Coulomb and exchange interactions will be discussed in next section, for quantum computing.

To satisfy the second condition we have to ensure that all electrons inside the device contribute equivalently to the measured value of the electrical current. A detailed discussion of the conditions that have to be satisfied by the quantum device to ensure this point is provided in the Appendix C. We anticipate here that such discussion is greatly simplified by associating to each electrons a quantum (Bohmian) trajectories, whose positions and velocities are well-defined even in absence of a measurement, in addition to the orthodox wave function. Then, the electrical current due to the simultaneous contribution of all electron leads to the following expression,

$$I_{exp}(t) = \sum_{i=1}^{N(t)} I^i(t) = \sum_{i=1}^{N(t)} q \frac{v_x^i(t)}{L}, \quad (7)$$

As discussed in the Appendix C the above expression assumes that the lateral dimensions of the (two terminal) electron device are much larger than the longitudinal one, and that the contacts are formed by metals with a fast screening time in comparison with that on the active region. The **condition 2** of our protocol to define the current operator as in Equation (2), requires to define the output instantaneous value of the current as,

$$I_T(t) = \frac{I_{exp}(t)}{N(t)}, \quad (8)$$

The value of $N(t) \approx N$ can be assumed to be proportional to the enlarged lateral area, and the value $I_T(t)$ computed from $I_{exp}(t)$ after knowing the ratio of the modified/unmodified areas. The detailed discussion on the definition of the current and the implications of **condition 2** is given in Appendix C.

3.2. Numerical Results

In this subsection, to show how the quantum uncertainty of the values of the measured electrical currents can be controlled, we compute the autocorrelation function of the current I_T defined as:

$$\langle I_T(t_2) I_T(t_1) \rangle = \int dI_T^k \int dI_T^\omega I_T^k I_T^\omega P(I_T^k, I_T^\omega), \quad (9)$$

where $P(I_T^k, I_T^\omega)$ is the probability associated with the subsequent measurement of the multiparticle state $|\Psi_T\rangle$ at two times t_1 and $t_2 > t_1$, with I_T^ω and I_T^k defined as the output values of the current at times t_1 and t_2 , respectively.

As indicated in the previous section, for practical reasons in the computation of the particle and displacement components of the current, we will use a wave function plus a Bohmian trajectory for each electron in the computation of the dispersion of I_T in the modified quantum device through expressions in Equations (7) and (8). The measurement of the current in an electrical device is a weak measurement process [8] in the sense that the perturbation of the wave function due to the measurement process is not very dramatic. This type of measurement is mathematically represented by three subsystems: the quantum system, the measuring apparatus plus an intermediate system or *ancilla*. In fact, the system interacts with the *ancilla* during the measurement (not with the apparatus) and the apparatus measures the *ancilla* (not the system). This indirect way of getting information of the system by measuring the *ancilla* implying that the output value of the total current has the quantum noise of the system plus the quantum noise of the *ancilla*. In our particular example, the *ancilla* is just the cable (in fact there are a very large number of electrons) connecting the RTD with the ammeter [8]. As indicated in the previous section, for practical reasons in the computation of the particle and

displacement components, in addition to the wave function, each electron will be described by a Bohmian trajectory.

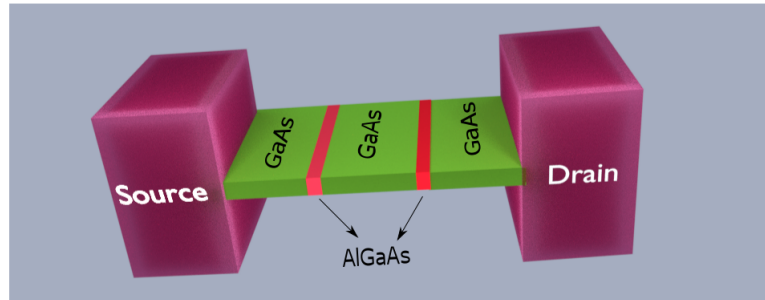


Figure 2. A 3D schematic of the RTD where the green material represents GaAs while the red represents AlGaAs. The alternating AlGaAs-GaAs-AlGaAs structure results in a potential well with discrete resonant energies.

As we have mentioned, the elimination of the quantum uncertainty in the measured current implies that the total wave function in Equation (1) is an eigenstate of the many-particle operator in Equation (2). Then, the first measured value of the current $I_T(t_1)$ at time t_1 has no influence on the output of a second measurement $I_T(t_2)$ at time t_2 , and it can be shown [17] that the two time probability of the autocorrelation given in Equation (9) can be written as the product of two independent probabilities, which leads to the following expression of the two time correlation in Equation (9),

$$\begin{aligned} \langle I_T(t_2) I_T(t_1) \rangle &= \int dI_T^k \int dI_T^\omega I_T^k I_T^\omega P(I_T^k) P(I_T^\omega) \\ &= \int dI_T^k I_T^k P(I_T^k) \int dI_T^\omega I_T^\omega P(I_T^\omega) \end{aligned} \quad (10)$$

$$= \langle I_T(t_2) \rangle \langle I_T(t_1) \rangle \quad (11)$$

The condition in Equation (11) is a test of the fact that the quantum uncertainty has disappeared in the measurement process of the modified device. Please note that from a pure engineering point of view, the autocorrelation mentioned above contains rich information on the high frequency response of the quantum device. In order to get the frequency response of the device we compute the power spectral density which is just the Fourier transform of the autocorrelation function (since the current signal has a constant mean, it is in a wide sense a stationary process, hence the auto-correlation depends only on the time difference $t = t_2 - t_1$. Therefore the auto-correlation function and the PSD form a Fourier transform pair). We therefore define the power spectral density due to the unmodified system, i.e., the system where the protocol is not applied, as $\mathbb{P}_{unmodified} = \mathcal{F}\{\langle I_T(t_2) I_T(t_1) \rangle\}$ while $\mathbb{P}_{modified} = \mathcal{F}\{\langle I_T(t_2) \rangle \langle I_T(t_1) \rangle\}$ for the modified system where the protocol is implemented. Here \mathcal{F} represents the Fourier transform operator. Finally we can define the relative error (RE) as:

$$RE = \frac{\mathbb{P}_{modified} - \mathbb{P}_{unmodified}}{\mathbb{P}_{modified}}, \quad (12)$$

which is plotted in Figure 3. The RE in Equation (12) contains quantum noise at all frequencies. Since all electrical devices are, in fact, a low pass filter, it is interesting for engineering purposes to quantify the error as a function of the frequency. A value of the RE equal to zero indicates that the quantum uncertainty (of the system and *ancilla*) has been eliminated which has a direct correspondence with the increase in the transport electrons in the device that can be further attributed to a large transmission or a large average current. Besides this it is also easy to see that to arrive at a zero quantum uncertainty we do not need an infinite number of electrons.

In our simulation the total number of electrons injected is given by $N = t/\tau_{in}$ where t is the total simulation time (the time after which the mean current reaches a constant value) and τ_{in} is the injection time of electrons. Now we know that $\langle I_T \rangle = \frac{qTf_e}{\tau_{in}}$ where T is the transmission coefficient and f_e is the Fermi function which we assume to be unity. So it is straightforward to see that $N = \frac{t\langle I_T \rangle}{qTf_e}$. We used the total time of simulation as 50 ps, $T = 0.7$, $f_e = 1$ and $\langle I_T \rangle = 5 \mu\text{A}$. These values correspond to a point in graph where the uncertainty starts to disappear which gives us the value of $N \approx 2232$. Which is a large value but not infinite.

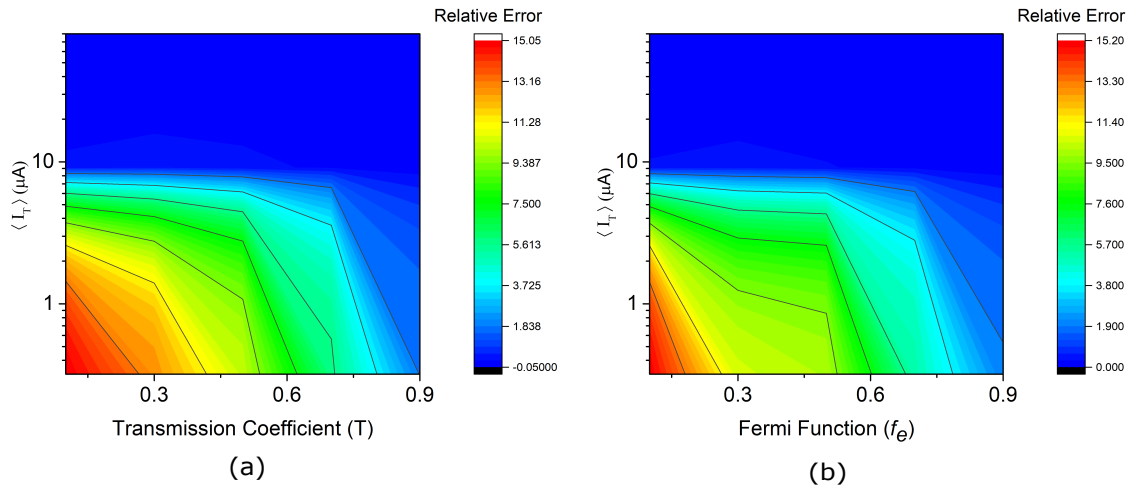


Figure 3. (a) Plot between the relative error, the transmission coefficient and the average current with the Fermi function fixed to unity. The relative error which is an indicator of quantum randomness, goes to zero, when the number of electrons in the device quantified by transmission coefficient and the mean current becomes very large (blue shaded region) while the relative probability of error is greater (in the red region) when the number of particles in the device is very small. In the green region the uncertainty already starts to disappear. (b) The same plot but with a constant transmission probability as unity and varying Fermi function also demonstrate the same outcome.

4. Application to Quantum Computing Devices: Mach-Zehnder Interferometer

We provide now an example of our protocol for reducing the quantum uncertainty in a quantum computing device. Quantum computing algorithms require a suitable set of quantum gates to reproduce logical operations [18–20]. With respect to most recent implementations, mainly based on superconducting [21] or single-ion qubits [22], solid-state devices are promising candidates because of their scalability and potential to be integrated into classical circuitry. In this section we will study how the quantum uncertainty can be eliminated in a solid-state MZI acting as quantum gate.

It is important to notice that any practical implementation of a quantum gate tends to have a non-negligible interaction between the quantum system and the environment (in terms of scattering with photons, background charges, impurities etc.) even when no measurement is designed. This interaction affects the expected unitary evolution of the state of the quantum system and produces loss of the logical information encoded in the state (decoherence). In solid-state MZI proposal, decoherence can be successfully minimized by injected electrons in *edge states*, chiral conductive channels generated in the Integer Quantum Hall regime [23]. Then, a strong enough magnetic field B is applied perpendicularly to a 2DEG, so that the band structure is discretized into Landau levels. In proximity to the confining potential of the device, the system eigenstates form chiral channels where an electron propagates coherently for large distances [24]. The chirality of such *edge states* prevents the electron to be back-reflected by eventual impurities on its path, unless it is scattered to the counterpropagating edge channel by a narrow quantum point contact [25,26]. Coherent transport

of electrons in *edge states* has been tested in a large variety of semiconductor devices, as Fabry-Perot interferometers [27], Hanbury-Brown-Twiss [28] and Hong-Ou-Mandel interferometers [29], thus validating the Integer Quantum Hall regime as an ideal framework to implement solid-state quantum logic gates [30].

Our MZI is schematically depicted in Figure 4. To simplify the discussion, as done along the whole paper, only one degree of freedom (one qubit) is considered for the unmodified quantum device. The generalization of the present protocol to a realistic quantum computing gate with more qubits, is explained in Appendix A. We consider that a contact or reservoir (as elaborated in Appendix B) is connected to the source contact (S1) in Figure 4a filling only one Landau level and all injected electrons have the same wave function $|0\rangle$, but displaced in time by the distance $\tau_{in}v_x$, as depicted in Figure 4b. At this point, we have not yet constructed the superposition of states to get our initial qubit. In our device setup, a potential dip or a quantum point contact acts as a half-reflecting beam splitter by randomly scattering the electron in one of the two available edge channels [31–33] so that the description of the quantum electron in the central region of our MZI is given by the quantum bit $a|0\rangle + b|1\rangle$. This conclude the first step of the preparation of the quantum state. Then, a tunable potential mesa generated by top gates further separates the two quantum rails, so that the traveling electron accumulates a different phase according to its path [34] as shown in Figure 4a. The two electron beams are then recollected at the second beam splitter to produce the electron interference which is the second step in a quantum device for the (unitary) manipulation of our initial quantum logical information. The final step is the measuring of the observable associated with the final qubit $a'|0\rangle + b'|1\rangle$ by the detectors D1 and D2 in Figure 4. As in the case of the RTD, typically the electrical current (which is proportional to the transmission probability from source $i = 1$ to detector $j = 1, 2$) is used to indirectly identify the final qubit [35].

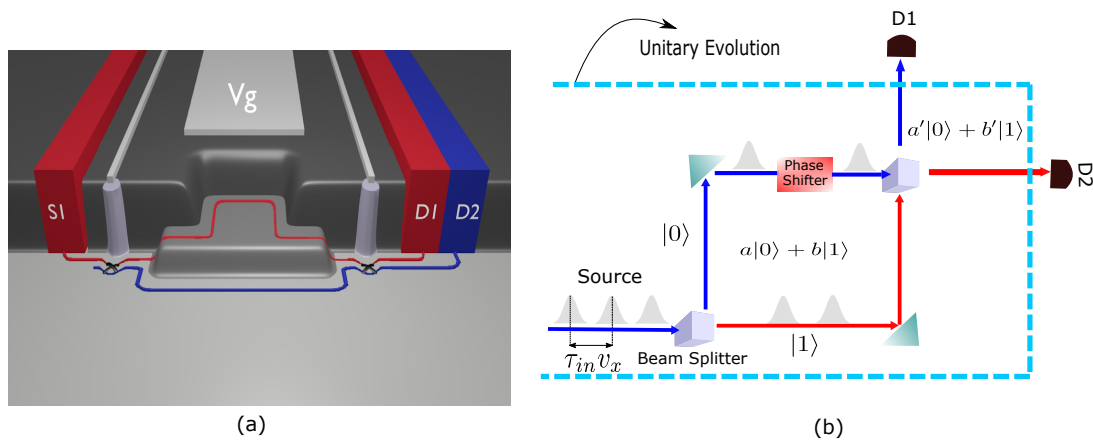


Figure 4. (a) 3D view of the potential landscape felt by the electrons in the MZI at bulk filling factor 2 in the Integer Quantum Hall regime, in presence of a perpendicular magnetic field [34]. Electrons are injected in the first edge channel by the source S_1 , and collected at the end of the device by the drain D_1 (D_2). The paths of the electrons in the interferometer is defined by the red (blue) line for the first (second) Landau level. (b) Schematic diagram and functioning of the MZI. Electron injection with non-interacting and non-overlapping wavepackets is shown in gray, while the region encapsulated by the cyan color dashed line box defines the region where the unitary evolution of the quantum states is preserved.

The magnetically dependent transmission probability $T_{21}(B)$ for an electron in the input channel S1 to be detected at D2 can be analytically computed by means of a simplified 1D model based on the scattering matrix approach, as in Ref. [34] and reads:

$$T_{21}(B) = 2T(1 - T)(1 + \cos(\Phi)), \quad (13)$$

where T is the transmission coefficient of the single beam splitter and Φ is the total phase difference accumulated in the MZI:

$$\Phi = \frac{qB\mathcal{A}}{\hbar} + \varphi. \quad (14)$$

Aharonov-Bohm oscillations in the transmission amplitude [36] are then driven by a variation of the magnetic field B or the loop area \mathcal{A} , affecting the phase Φ . This platform can be used to implement other electron interferometry schemes for single electrons, e.g., Fabry-Perot geometries [27], or two interacting electrons [31,37,38]. Let us notice that the consideration of more qubits in the unmodified quantum device will just require occupying different Landau levels, but the basic understanding of how the uncertainty in the measurement can be controlled will not be modified by the presence of more qubits.

4.1. Implementation of Condition 1 and Condition 2

As with Section 3, here too we ensure that our modified quantum device satisfies the conditions mentioned in Section 2.2. Here **condition 1** can be obtained with a different strategy than the one used for the RTD since electrons are entering in the MZI one by one (as in a quantum wire). The strategy is enlarging the length L of the arms of the active region of the device (between $S1$ and $D1, D2$) to increase the number of simultaneous single particle wave packets that fit inside the device. We argue in the Appendix B that a *natural* way in the injection of electrons from the contacts in the device is at time intervals τ_{in} , as defined in Equation (A8) in Appendix B. Neglecting the thermal noise of the contacts the spatial separation between electrons is therefore given by $\tau_{in}v_x$ as plotted in Figure 4. Notice that such spatial separation ensures that the consideration of non-interacting electrons required in Equation (1) is more accurate for our modified MZI than for the RTD mentioned before.

As indicated in Appendix C, the consideration of metallic contacts with a lateral area A satisfying $\sqrt{A} \gg L$ is necessary condition to be able to successfully use Equation (7) in the computation of the experimental current. Notice that enlarging the lateral area A does not imply an increment of the number N of electrons here since electrons can only enter inside the device, one by one, in the 1D edge channels. Besides this **condition 2** can again be obtained by post-processing the experimental current I_{exp} as indicated in Section 3, by fixing the total time T that we allow the electrons to enter inside the enlarged active device region, $N = T/\tau_{in}$.

4.2. Numerical Results

To prove the discussions in the previous sections numerically we implemented the Mach-Zehnder like behaviour in the simulations. We were able to attain the Aharonov-Bohm oscillations where the maximum and the minimum value of the current obtained in one of the drains of the MZI oscillates with the change in the magnetic field (see Figure 5a). These oscillations are a signature of the correct working of our simulations. As expected, we observe that the instantaneous current $I_T(t)$ computed in the quantum device with a large number of electrons is much less noisy than the ones with fewer electrons, as plotted in Figure 5b. The noise in the current value due to fewer electrons results in very high fluctuations in the instantaneous value (black line in Figure 5b) which forces the experimenter to record the values in several experiments to finally get an ensemble value which is non-fluctuating. However, with the successful application of our protocol the fluctuation of the instantaneous value of the current almost disappears (cyan line in Figure 5b) as a result one needs to make just one measurement to get the correct value of the current. The final step of this protocol is determining the value of N which as discussed above can be given by $N = T/\tau_{in}$.

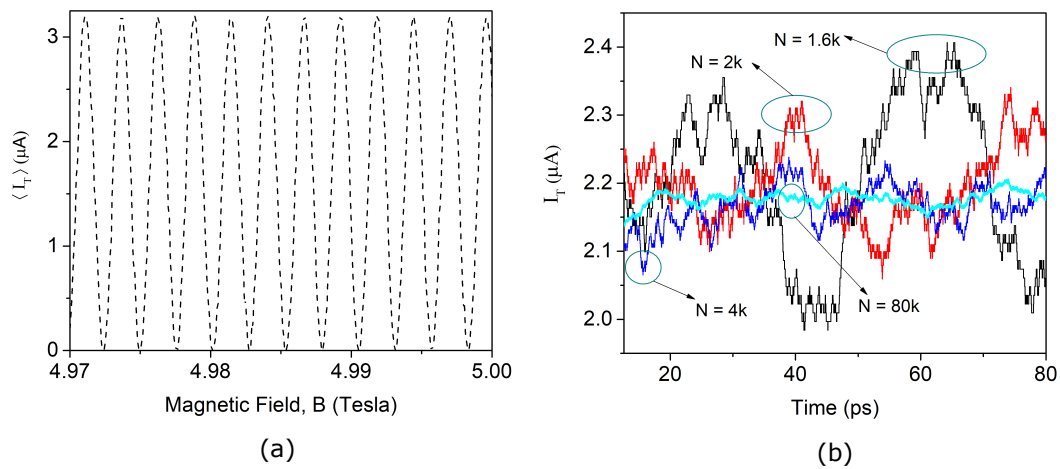


Figure 5. (a) The Aharonov-Bohm oscillations of the mean current resulting due to the interference of the wavepackets at the output of the Detector 2 oscillating between the maximum and minimum limit of the mean current. (b) The instantaneous current normalized to the number of particles is plotted at the output of the detector 2 of the MZI with respect to the simulation time, for different number of electrons N . As expected, the noise in the current reduces with the increase in the number of transport electrons due to the elimination of quantum uncertainty demonstrating the successful implementation of the protocol discussed in the text.

5. Conclusions

The measured current associated with a quantum device with few electrons has a quantum uncertainty due to the intrinsic stochastic process of the quantum measurement of the electrical current. From an engineering point of view, this quantum uncertainty becomes an undesired quantum noise that makes the discrimination of the final state in classical or quantum gates more difficult. To avoid the quantum uncertainty in the evaluation of the output value, one usually repeats the measurement at different time (using ergodic arguments) to compute a time-averaged value free from uncertainties. We have presented in this paper a new protocol that modifies the original quantum electron device to accommodate a larger number of electrons inside, so that the total electrical current of the modified device (when normalized to the number of electrons inside) gives the value of the output current without quantum uncertainty. We provide numerical examples for classical and quantum computing, with an RTD and MZI, respectively. We demonstrate that the many-particle wave function associated with the modified device is, in fact, an eigenstate of the many-particle electrical current operator. The similitude and differences of our protocol with the collective measurements is mentioned in the text. The results of our protocol can be alternatively understood as a consequence of the central limit theorem (see Appendix E). Although the assumption of non-interacting quasi-particles can seem reasonable in nanoscale electron devices, further work is needed to check whether or not the presence of strong Coulomb and exchange correlations among electrons located inside the device can affect the present predictions. In addition, the discussion on the advantages of the protocol presented here needs to be explored for the quantum measurements of transient currents and delay time of classical and quantum gates.

Author Contributions: Conceptualization, D.P., L.B., M.V., G.A., P.B., A.B. and X.O.; Formal analysis, D.P., L.B., M.V., G.A., P.B., A.B. and X.O.; Investigation, D.P., L.B., M.V., G.A., P.B., A.B. and X.O.; Methodology, D.P., L.B., G.A., P.B., A.B. and X.O.; Software, D.P., L.B., M.V., G.A., P.B., A.B. and X.O.; Supervision, G.A. and X.O.; Validation, D.P., L.B., M.V., G.A., P.B., A.B. and X.O.; Visualization, D.P., L.B., M.V. and X.O.; Writing—original draft, D.P., L.B., M.V., G.A., P.B., A.B. and X.O.; Writing—review and editing, D.P., L.B., M.V., G.A., P.B., A.B. and X.O.

Acknowledgments: The authors acknowledge funding from Fondo Europeo de Desarrollo Regional (FEDER), the “Ministerio de Ciencia e Innovación” through the Spanish Project TEC2015-67462-C2-1-R, the European Union’s Horizon 2020 research and innovation programme under grant agreement No Graphene Core2 785219 and under the Marie Skłodowska-Curie grant agreement No 765426 (TeraApps), and the EC Research Innovation Action under the H2020 for the Project HPC-EUROPA3 (INFRAIA-2016-1-730897), together with the support provided by Barcelona Supercomputing Center (project HPC17D8XLY).

Conflicts of Interest: The authors declare no conflict of interest. The funders had no role in the design of the study; in the collection, analyses, or interpretation of data; in the writing of the manuscript, or in the decision to publish the results’.

Appendix A. Generalization to an Unmodified Quantum Device with Many Electrons

In the text, to simplify the notation and the discussion of our protocol, we have assumed that the unmodified (original) quantum device has only one electron in the active region. This assumption is obviously unrealistic in many scenarios for either classical or quantum computing. For example, in quantum computing, we need a nanoscale devices with, at least, the number of electrons equal to the number of qubits we want to deal with. We show in this appendix that the very same protocol described in the text for one electron can be straightforwardly generalized to deal with an unmodified (original) quantum device with many electrons present in the active region of the nanoscale device.

We consider an unmodified (original) quantum device with M electrons in the active region. To simplify the discussion, we will write the quantum state in the position representation. Then, each electron is described by the degree of freedom x_j with $j = 1, 2, \dots, M$. Such quantum system is described by the M -particle wave function:

$$\psi(x_1, x_2, \dots, x_M, t_{in}) \quad (A1)$$

Notice that we do not assume any particular shape of this M -particle wave function so that exchange and Coulomb interaction among the M electrons is taken into account in the definition of this M -particle system (without any restriction).

Now, we consider N set of M electrons which are prepared under the same conditions as the ones in Equation (A1). In other words, the quantum dynamics of each set of these M electrons can be described by the same wave function in Equation (A1). Thus, we define $N \times M$ degrees of freedom for the modified quantum device as x_j^i with $i = 1, 2, \dots, N$ counting the repetitions and $j = 1, 2, \dots, M$ counting the number of electrons in each repetition. We define N wave function identical to Equation (A1), but with a superindex $i = 1, 2, \dots, N$ indicating which is the repetition we are dealing with:

$$\psi^i(x_1^i, x_2^i, \dots, x_M^i, t_{in}) \quad (A2)$$

Introducing the wave function in Equation (A2) into the quantum state of the modified quantum device written in Equation (1), in the position representation, we have:

$$\Psi_T(x_1^1, \dots, x_M^N, t_{in}) = \psi^1(x_1^1, \dots, x_M^1, t_{in}) \cdot \psi^2(x_1^2, \dots, x_M^2, t_{in}) \cdot \dots \cdot \psi^N(x_1^N, \dots, x_M^N, t_{in}) \quad (A3)$$

Clearly, we have assumed in our definition of $\Psi_T(x_1^1, \dots, x_M^N, t_{in})$ in Equation (A3) that there is no Coulomb or exchange interaction between the subset of electrons $\{x_1^k, \dots, x_M^k\}$ and the subset of electrons $\{x_1^l, \dots, x_M^l\}$ for any $j \neq k$, but no restriction is imposed on the interaction among the M electrons of each subset. The rest of the demonstration till the final result in Equation (6) with $\sigma_{I_T}^2 = 0$ are basically the same that we wrote in Equations (3)–(5) for the evaluation of mean values.

A relevant point in our discussion is that even with our best technological means to exactly reproduce the same wave function in Equation (A1) with another set of M electrons, the quantum dynamics of these new set of electrons is not exactly identical to the previous one because of the inherent quantum uncertainty. The key element in our demonstration is that all these N different uncertainties of the set of M electrons have to follow an identical probability distribution given by the same wave function ψ in Equation (A1).

We notice that we have discussed in this appendix that if a system of $N \times M$ electrons are described by Equation (A3) (what we call **condition 1** in the text) and if we use a (center-of-mass-type) operator in Equation (2) (what we called **condition 2** in the text), then, the uncertainty in the measurement disappears in the $\lim N \rightarrow \infty$. A different question is how to ensure that a modified quantum device is effectively described by Equation (A3) and the measurement by the operator in Equation (2). This last point is what we discussed in detail in the implementations of our protocol with a RTD and a MZI in the text.

Finally, let us notice that the results in this appendix can be understood in a quite different way. It can be used to justify that some amount of Coulomb interaction (between nearest neighbors) can be accepted between the different N subsets. Let us consider again an unmodified system with only one electron described by the wave function $\psi(x_1, t_{in})$. Let us consider that some of the electrons of the N subsets (not all) do have interaction among them. We define M as the number of electrons that have interaction among them (for example we can consider two-electron interaction, but neglect three-electron interaction). Then, the wave function that define these interacting electrons is $\psi^i(x_1^i, x_2^i, \dots, x_M^i, t_{in})$. If we assume that the (normalized to the number of electrons) probability distribution of the electrical current assigned to $\psi^i(x_1^i, x_2^i, \dots, x_M^i, t_{in})$ is not much different than the probability distribution of the electrical current assigned to $\psi(x_1, t_{in})$, then, the demonstration in this appendix can be used to justify that our protocol can be reasonably valid when some interaction is accepted between nearest neighbors $\{x_1^k, \dots, x_M^k\}$ and $\{x_1^l, \dots, x_M^l\}$.

Appendix B. The Injection Time

The phase space density of electrons in a reservoir can be anticipated by assuming that each degree of freedom of an electron needs a phase space area equal to 2π , which is usually derived by using the single particle wavefunction of electrons as the Bloch states and then introducing the Born-von Karman boundary conditions. The interpretation of this result for two wave packets with spatial dispersion σ_x and wave vector dispersion $\sigma_k = 1/\sigma_x$, center positions x_{01} and x_{02} , and center wave packets k_{01} and k_{02} is simple. When they are far away from each other in the phase space, i.e., $|x_{01} - x_{02}| \gg \sigma_x$ or $|k_{01} - k_{02}| \gg \sigma_k$, the norm of the two-electron wave function is equal to the unity. However, when the wave packets are approaching each other, the probability decreases. In particular, for $x_{01} = x_{02}$ and $k_{01} = k_{02}$, we get $\psi_1(x) = \psi_2(x)$ and $\Phi(x_1, x_2) = \psi_1(x_1)\psi_1(x_2) - \psi_1(x_2)\psi_1(x_1) = 0$. This is the time-dependent wave packet version of the Pauli exclusion principle (or exchange interaction) mentioned for time-independent Hamiltonian eigenstates.

For example, for electrons in a 2D space (with the position $\vec{r} = \{x, y\}$ and wave vector $\vec{k} = \{k_x, k_y\}$), we consider a volume of the phase space equal to $\Delta x \Delta z \Delta k_x \Delta k_z$, with the degrees of freedom $\{x_0, z_0, k_x, k_z\}$ satisfying $x_0 < x < x_0 + \Delta x$, $z_0 < z < z_0 + \Delta z$, $k_{x0} < k_x < k_{x0} + \Delta k_x$ and $k_{z0} < k_z < k_{z0} + \Delta k_z$. The total number of electrons in this phase space cell taking into account the properties of a fermion are,

$$n_p = \frac{\Delta x \Delta z \Delta k_x \Delta k_z}{(2\pi)^2}, \quad (\text{A4})$$

where $(2\pi)^2$ is the volume occupied by a single electron in the 2D phase space. Then, the time of injection of an electrons in the x direction from this volume of the phase space will be given by:

$$\tau_{in} = \frac{\Delta x}{v_x n_p} = (2\pi)^2 \frac{1}{v_x \Delta z \Delta k_x \Delta k_z}, \quad (\text{A5})$$

where v_x is the electron velocity in the phase space volume. It can be demonstrated [39] that interpretation of Δx and Δk_x in terms of the wave packets mentioned above implies:

$$\Delta x = \sigma_x \sqrt{2\pi}, \quad (\text{A6})$$

$$\Delta k_x = \sigma_k \sqrt{2\pi}. \quad (\text{A7})$$

We notice that the condition $\sigma_x \cdot \sigma_k = 1$ implies the desired condition $\Delta x \cdot \Delta k_x = 2\pi$. Then, the injection time in Equation (A5) is just:

$$\tau_{in} = \frac{\sigma_x}{v_x}, \quad (\text{A8})$$

which only depends on the properties of the reservoir.

Appendix C. Description of the Current Signal and Condition 2

We discuss here which are the necessary considerations to design the modified (new) quantum device that allows us to assume that all electrons inside it have identical simultaneous contribution to the total current I_T .

The first step is identifying the proper single particle operator \hat{I}^1 . Then, once we identify \hat{I}^1 , we can compute the eigenstates $|\psi^1(t_{in})\rangle$ and the eigenvalues I^1 that will correspond to the measured output results. However, identifying the electrical current operator is not so simple for several reasons. First, the measured current in an ammeter at time t_{in} is not just the particle current, defined as the number of particles crossing a particular surface of the device, but it also includes the displacement current. The latter component of the electrical current is proportional to the time-dependent variations of the electric field on a particular surface of the device. Typically, such component is not relevant at low frequencies, but at larger frequencies no instantaneous current conservation at time t_{in} can be guaranteed without it. What is the operator associated with the measurement of the total, particle plus displacement, current? The answer is not trivial at all. In fact, the measurement of the electrical current in quantum electron devices has an additional difficulty. The measurement of the electrical current corresponds to a generalized or weak measurement, which are mathematically described by a POVM. So, the proper question is even more complicated now: What is the POVM associated with the measurement of the total, particle plus displacement, current?

Fortunately, we can describe the measurement of the total electrical current in a quantum electron device without having to anticipate the POVM. We will use in this appendix an explanation of the measurement process of the total electrical current using the Bohmian quantum theory. Such theory is formally equivalent to the orthodox quantum theory, it gives the same empirical results, but it does not require to identify *a priori* the measurement operator. Such theory defines a quantum system assigned to one electron by the orthodox wave function $\psi^1(\vec{r}, t)$ plus a quantum trajectory $\vec{r}^1(t) = \{x^1(t), y^1(t), z^1(t)\}$ constructed from a velocity field given by the wave function itself. Such trajectory allows the definition of the properties of a quantum system, like the instantaneous electrical current $I^1(t)$, independently of the fact of being measured or not. An identically prepared state for a second experiment will be described by the same wave function $\psi^2(\vec{r}, t) = \psi^1(\vec{r}, t)$, but with a different trajectory $\vec{r}^2(t) = \{x^2(t), y^2(t), z^2(t)\}$. The quantum uncertainty in the output value of the electrical current is due to the different initial positions of the trajectories, which describe an ensemble of identical experiments. The selection of the initial positions of the i -th trajectories is selected according to the quantum equilibrium [40].

According to the Bohmian theory, for the electron with trajectory $\vec{r}^1(t) = \{x^1(t), y^1(t), z^1(t)\}$ and velocity $\vec{v}^1(t) = \{v_x^1(t), v_y^1(t), v_z^1(t)\}$, the electrical (particle plus displacement) current $I^1(t)$ generated in a surface of the quantum device is given by the Ramo-Shockley-Pellegrini theorem [41]. If we assume that each dimension of the lateral contact area A of the quantum device is much larger than the length L between contacts (from source to drain), i.e., $\sqrt{A} \gg L$, and this contacts are ideal metals (with an instantaneous screening time), then the total current generated by an electron crossing the device between the metals is given by the expression:

$$I^1(t) = q \frac{v_x^1(t)}{L} [\Theta(t - t_{in}^1) \Theta(t_{out}^1 - t)], \quad (\text{A9})$$

where $\Theta(t)$ is the Heaviside function representing the time dependence of the single electron current pulse with t_{in}^1 and $t_{out}^1 = t_{in}^1 + t_r$ being the entering and leaving times, respectively, and t_r is the

electron transit time. The pulse starts when the electron enters the device and ends when the electron leaves it. We notice that the integration in time of Equation (A9), during the time interval L/v_x , gives the fundamental electron charge $\int_{t_{in}^1}^{t_{out}^1} I(t)dt = q$.

As discussed in the Appendix B, we do not have a perfect control on the preparation of the electrons leaving the contacts and entering inside the device but, assuming the contact to be in (quasi) thermodynamic equilibrium we can anticipate the energy distribution of the injected electrons (Fermi-Dirac distribution) and the interval time between consecutive injection of electrons. The total (particle plus displacement) instantaneous current I_{exp} of the device is then given by:

$$I_{exp}(t) = \sum_{i=1}^{N(t)} I^i(t) = \sum_{i=1}^{N(t)} q \frac{v_x^i(t)}{L}, \quad (A10)$$

where $N(t)$ is the number of electrons inside the device at time t . Expression (A10) has the desired property that the current due to all electrons inside the device is just the sum of currents due to individual electrons. Notice, however, that I_{exp} in terms of Bohmian currents is not exactly equal to the I_T defined in Equation (2) reinterpreted in terms of Bohmian currents, because a factor N in the denominator of Equation (2) is missing in Equation (A10).

Finally, we emphasize that the Bohmian trajectories have been introduced in this last part just to simplify our practical discussion about the measurement of the total (particle plus displacement) current in quantum electron devices, but it has no fundamental role in the demonstration of the proposed protocol. In other words, the validity of the main result in Equation (6) can be equivalently demonstrated with orthodox quantum mechanics (as we have done) or with Bohmian quantum mechanics. The knowledge that we gain from the Bohmian development done here is that the total (particle plus displacement) current measured in experiments do satisfy the required superposition of currents associated with individual electrons and that a factor $N(t)$ has to be added into the experimentally measured current of the modified quantum device I_{exp} to properly define I_T as $I_T(t) = \frac{I_{exp}(t)}{N(t)}$ where two proper ways of computing $N(t)$ are explained in the RTD and MZI applications mentioned in the text.

Appendix C.1. On the Assumption of a Large Lateral Area in the Active Region

The size of the lateral area A is a very important point in our protocol since we want that each electron inside the device active region contribute to the measured electrical current. If the electrical current were only due to the particle (conduction) current component, then, only the electrons crossing the drain (or source) surface, would have contributed to the current. However, it is well known that the electrical current is due to both particle and displacement currents. In fact, an electron far from the drain surface can still affect the current if its dynamics generates a significant perturbation in the electric field. If the lateral area is large compared to the longitudinal ones i.e., $\sqrt{A} \gg L$, then, effectively all electrons inside the active device region can contribute to the measured current, as required by the operator in Equation (2). The formal derivation of this issue is presented in Ref. [8]. Thus, the large lateral area is an important point of our protocol.

Only when $L \ll W, H$, then, one can ensure that all electrons are equally contributing (through the displacement current) to the total current and hence condition 2 in the main text is satisfied.

Appendix C.2. On the Assumption of an Instantaneous Screening Time in the Metallic Contacts

Next we discuss the motivation behind approximating the screening time in the metallic contacts to be instantaneous. The fact that we assume a screening time in the contacts (metals) much smaller than in the active region is something usual in electron semiconductor devices. Typically, the screening time in metals is considered to be negligible in comparison with the screening time in a semiconductor. The implications of this condition is that we do not need to simulate the electrons deep inside

the source/drain contact (without entering in the device) generating displacement current in the drain (or source) contact. This is possible only if we assume the screening time in the metals to be (almost) instantaneous.

Appendix D. Effects of Exchange Symmetry on the Total Current Many Body Operator

In the text, we have assumed that the many-particle wave function in Equation (1) has no exchange symmetry. Here, we discuss the physical soundness of such approximation. Let us evaluate the effects of exchange symmetry on the squared total current of Equation (2) for two particle case, which can be rewritten as:

$$\langle \hat{I}_T^2 \rangle = \frac{1}{4} \sum_{i=1}^2 \langle I_i I_i \rangle + \frac{1}{4} \sum_{i=1, j \neq i}^2 \langle I_i I_j \rangle, \quad (\text{A11})$$

where indexes i, j refers to the particle with coordinate x^i in the phase space. We assume the system wave function described by the two-fermion state with exchange symmetry

$$\Psi(x_1, x_2) = \frac{1}{\sqrt{2}} (\psi^1(x^1) \psi^2(x^2) - \psi^2(x^1) \psi^1(x^2)), \quad (\text{A12})$$

where the superindex k of the state ψ^k refers to the injection time (e.g., ψ^1 is injected at t_{in} , while ψ^2 is injected at $t_{in} + \tau_{in}$). Within this definition of the state, the diagonal average values of the first value in Equation (A11) read:

$$\begin{aligned} \langle I^1 I^1 \rangle &= \frac{1}{4} (\langle \psi^1 | (I^1)^2 | \psi^1 \rangle \langle \psi^2 | \psi^2 \rangle + \langle \psi^2 | \psi^2 \rangle \langle \psi^1 | (I^1)^2 | \psi^1 \rangle \\ &- \langle \psi^1 | (I^1)^2 | \psi^2 \rangle \langle \psi^2 | \psi^1 \rangle - \langle \psi^2 | (I^1)^2 | \psi^1 \rangle \langle \psi^1 | \psi^2 \rangle), \end{aligned} \quad (\text{A13})$$

for $i = 1, 2$. We reasonably assume an initial negligible overlap of the wave packets,

$$\langle \psi^\alpha | \psi^\beta \rangle \approx \delta_{\alpha, \beta}, \quad (\text{A14})$$

which is conserved during the evolution of the two electrons, carrying out the same procedure for the second diagonal element we get:

$$\langle I^1 I^1 \rangle + \langle I^2 I^2 \rangle = \frac{1}{2} (\langle \psi^1 | (I^1)^2 | \psi^1 \rangle + \langle \psi^2 | (I^2)^2 | \psi^1 \rangle), \quad (\text{A15})$$

as for distinguishable particles. Similarly, the first non-diagonal term of Equation (A11) is computed:

$$\begin{aligned} \langle I^1 I^2 \rangle &= \frac{1}{4} (\langle \psi^1 | I^1 | \psi^1 \rangle \langle \psi^2 | I^2 | \psi^2 \rangle + \langle \psi^2 | I^1 | \psi^2 \rangle \langle \psi^1 | I^2 | \psi^1 \rangle \\ &- \langle \psi^1 | I^1 | \psi^2 \rangle \langle \psi^2 | I^2 | \psi^1 \rangle - \langle \psi^2 | I^1 | \psi^1 \rangle \langle \psi^1 | I^2 | \psi^2 \rangle), \end{aligned} \quad (\text{A16})$$

Computing the same for the second non-diagonal element we get,

$$\langle I^1 I^2 \rangle + \langle I^2 I^1 \rangle = \frac{1}{2} \langle \psi^1 | I^1 | \psi^1 \rangle \langle \psi^2 | I^2 | \psi^2 \rangle. \quad (\text{A17})$$

So using Equations (A15) and (A17) in Equation (A11) we get,

$$\begin{aligned} \langle \hat{I}_T^2 \rangle &= \frac{1}{4} \sum_{i=1}^2 \langle I_i I_i \rangle + \frac{1}{4} \sum_{i=1, j \neq i}^2 \langle I_i I_j \rangle \\ &= \frac{1}{4} \sum_{i=1}^2 (\langle \psi^i | (I^i)^2 | \psi^i \rangle) + \frac{1}{4} \sum_{i=1, j \neq i}^2 \langle \psi^i | I^i | \psi^i \rangle \langle \psi^j | I^j | \psi^j \rangle, \end{aligned} \quad (\text{A18})$$

The mean value of the squared of the total current for distinguishable particles is therefore recovered by assuming $\langle \psi^i | I | \psi^j \rangle \approx \delta_{i,j}$. This constraint is fulfilled by Equation (A14), together with the definition of the current operator, which is related to momentum (proportional to a spatial derivative in the real space) and position operators. Indeed, we expect that for a weak measurement of the current discussed in the text, the state $|\psi^i\rangle'$ produced by its application to a wave packet ($|\psi^i\rangle' = I|\psi^i\rangle$) is characterized by a spatial localization that does not significantly differ from the unperturbed state $|\psi^i\rangle$, so that $\langle \psi^i | I | \psi^j \rangle \approx 0$ is valid.

Appendix E. The Ontological Meaning of the Total Measured Current \hat{I}_T and the Classical Central Limit Theorem

We discuss here a simple interpretation of the main result given in Section 2.2. The ammeter mentioned in the text does only measure the value of the total current \hat{I}_T . Therefore, strictly speaking, the currents \hat{I}^1, \hat{I}^2 , etc. contributed by the single electrons, have not been measured, so the electrons have no (orthodox) definite value of their current. We are invoking here the well known eigenvalue-eigenstate link. The i -th electron has a well-defined value of the current when its wavefunction is an eigenstate of the single particle current operator \hat{I}^i . However as explained in Section 2.1, the single particle state describing the i -th electron is not a current eigenstate. Therefore there is no orthodox value for the current assigned to the i -th electron.

In any case, let us assume that we can assign (unmeasured) values of the current of each electron (for $i = 1, \dots, N$) at any time (The physical correctness of this assumption will be provided below). Thus, the definition of the total current in Equation (2) in terms of operators can be translated into an expression in terms of variables which takes well-defined values:

$$I_T = \frac{\mathcal{I}^1 + \mathcal{I}^2 + \dots + \mathcal{I}^N}{N}, \quad (\text{A19})$$

We eliminate the “hat” in Equation (A19) to clarify that now \mathcal{I}^i is not an operator, but a variable. Then, assuming again the independence among the variables \mathcal{I}^i and that the total current can be given by the above sum, the simple application of the classical central limit theorem will be enough to certify that the variance of I_T goes to zero when N is large enough.

However, the reader can argue that such simple understanding is not appropriate because, as we emphasized at the beginning of this appendix, the current of each electron has no well-defined value. Such values are not measured by the ammeter and, strictly speaking, the values associated with the current operators \hat{I}^1, \hat{I}^2 are undefined in the orthodox theory.

In any case, the simple understanding based on the central limit theorem, can be invoked by using a quantum theory with a definition of the reality of the properties of electrons independent of the measurement process. This understanding is supported for example from modal interpretation of the quantum world where the reality of some properties of electrons (like its electrical current) has a well-defined value independently of the fact that they are measured or not. This understanding is consistent with our paper where the Bohmian theory [40], which is the most famous modal interpretation today, is invoked for the computation of the currents. At the end of the day, the discussion about the (hidden) reality of the values of the current of each electron are not relevant for the empirical results presented along the work. Bohmian and orthodox theories are empirically equivalent for all known experiments. The above discussion provides a simple and intuitive understanding of the physical soundness of providing a many-body quantum state in Equation (1) with no quantum uncertainty.

References

1. Le, H. Q.; Van Norstrand, J. A.; Thompto, B. W.; Moreira, J. E.; Nguyen, D. Q.; Hrusecky, D.; Kroener, M. IBM POWER9 processor core. *IBM J. Res. Dev.* **2018**, *62*, 2:1–2:12.
2. Cory, C.D.; Datta, S. Nanoscale transistors—Just around the gate? *Science* **2013**, *341*, 140–141.

3. Nielsen, M.A.; Chuang, I.L. Quantum computation. In *Quantum Information*; Cambridge University Press: Cambridge, UK, 2000.
4. Boixo, S.; Isakov, S.V.; Smelyanskiy, V.N.; Babbush, R.; Ding, N.; Jiang, Z.; Neven, H. Characterizing quantum supremacy in near-term devices. *Nat. Phys.* **2018**, *14*, 595.
5. Classical and quantum computers are vying for superiority. *Nature* **2018**, *564*, 302.
6. Tang, A.E. Quantum-inspired classical algorithm for recommendation systems. *arXiv Preprint* **2018**, arXiv:1807.04271.
7. Deutsch, D. Uncertainty in quantum measurements. *Phys. Rev. Lett.* **1983**, *50*, 631.
8. Marian, D.; Zanghi, N.; Oriols, X. Weak values from displacement currents in multiterminal electron devices. *Phys. Rev. Lett.* **2016**, *116*, 110404.
9. Zhan, Z.; Kuang, X.; Colomés, E.; Pandey, D.; Yuam, S.; Oriols, X. Time-dependent quantum Monte Carlo simulation of electron devices with two-dimensional Dirac materials: A genuine terahertz signature for graphene. *Phys. Rev. B* **2019**, *99*, 155412.
10. Oriols, X.; Benseny, A. Conditions for the classicality of the center of mass of many-particle quantum states. *New J. Phys.* **2017**, *19*(6), 063031.
11. Lloyd, S.; Slotine, J. J. E. Quantum feedback with weak measurements. *Phys. Rev. A* **2000**, *62*, 012307.
12. Hou, Z.; Tang, J.F.; Shang, J.; Zhu, H.; Li, J.; Yuan, Y.; Wu, K.D.; Xiang, G.Y.; Li, C.F.; Guo, G.C. Deterministic realization of collective measurements via photonic quantum walks. *Nat. Commun.* **2018**, *9*, 1414.
13. Encomendero, J.; Faria, F. A.; Islam, S. M.; Protasenko, V.; Rouvimov, S.; Sensale-Rodriguez, B.; Xing, H. G. New tunneling features in polar III-nitride resonant tunneling diodes. *Phys. Rev. X* **2017**, *7*, 041017.
14. Gaskell, J.; Eaves, L.; Novoselov, K.S.; Mishchenko, A.; Geim, A.K.; Fromhold, T.M.; Greenaway, M.T. Graphene-hexagonal boron nitride resonant tunneling diodes as high-frequency oscillators. *Appl. Phys. Lett.* **2015**, *107*, 103105.
15. Avedillo, M.J.; Quintana, J.M.; Roldán, H.P. Increased Logic Functionality of Clocked Series-Connected RTDS. *IEEE Trans. Nanotechnol.* **2006**, *5*, 606–611.
16. Park, J.; Lee, J.; Yang, K. A 24-GHz Low-Power RTD-Based ON-OFF Keying Oscillator with an RTD Pair Configuration. *IEEE Microwave Wirel. Comp. Lett.* **2018**, *28*, 521–523.
17. Pandey, D.; Albareda, G.; Oriols, X. Measured and unmeasured properties of quantum systems. *arXiv Preprint* **2018**, arXiv:1812.10257.
18. Bertoni, A.; Bordone, P.; Brunetti, R.; Jacoboni, C.; Reggiani, S. Quantum Logic Gates based on Coherent Electron Transport in Quantum Wires. *Phys. Rev. Lett.* **2000**, *84*, 5912, doi:10.1103/PhysRevLett.84.5912.
19. Buscemi, F.; Bordone, P.; Bertoni, A. Carrier-carrier entanglement and transport resonances in semiconductor quantum dots. *Phys. Rev. B* **2007**, *76*, 195317.
20. Buscemi, F.; Bordone, P.; Bertoni, A. Quantum teleportation of electrons in quantum wires with surface acoustic waves. *Phys. Rev. B* **2010**, *81*, 045312.
21. Lanting, T.; Przybysz, A. J.; Smirnov, A. Y.; Spedalieri, F. M.; Amin, M. H.; Berkley, A. J.; Dickson, N. Entanglement in a Quantum Annealing Processor. *Phys. Rev. X* **2014**, *4*, 021041, doi:10.1103/PhysRevX.4.021041.
22. Debnath, S.; Linke, N.M.; Figgatt, C.; Landsman, K.A.; Wright, K.; Monroe, C. Demonstration of a small programmable quantum computer with atomic qubits. *Nature* **2016**, *536*, 63–66, doi:10.1038/nature18648.
23. Büttiker, M. Absence of backscattering in the quantum Hall effect in multiprobe conductors. *Phys. Rev. B* **1988**, *38*, 9375, doi:10.1103/PhysRevB.38.9375.
24. Roulleau, P.; Portier, F.; Roche, P.; Cavanna, A.; Faini, G.; Gennser, U.; Mailly, D. Direct Measurement of the Coherence Length of Edge States in the Integer Quantum Hall Regime. *Phys. Rev. Lett.* **2008**, *100*, 126802, doi:10.1103/PhysRevLett.100.126802.
25. Venturelli, D.; Giovannetti, V.; Taddei, F.; Fazio, R.; Feinberg, D.; Usaj, G.; Balseiro, C. A. Edge channel mixing induced by potential steps in an integer quantum Hall system. *Phys. Rev. B* **2011**, *83*, 075315, doi:10.1103/PhysRevB.83.075315.
26. Beggi, A.; Bordone, P.; Buscemi, F.; Bertoni, A. Time-dependent simulation and analytical modelling of electronic Mach–Zehnder interferometry with edge-states wave packets. *J. Phys.: Condens. Matter* **2015**, *27*, 475301.
27. Deviatov, E. V.; Lorke, A. Experimental realization of a Fabry-Perot-type interferometer by copropagating edge states in the quantum Hall regime. *Phys. Rev. B* **2008**, *77*, 161302, doi:10.1103/PhysRevB.77.161302.

28. Neder, I.; Ofek, N.; Chung, Y.; Heiblum, M.; Mahalu, D.; Umansky, V. Interference between two indistinguishable electrons from independent sources. *Nature* **2007**, *448*, 333–337, doi:10.1038/nature05955.
29. Bocquillon, E.; Freulon, V.; Berroir, J.M.; Degiovanni, P.; Plaçais, B.; Cavanna, A.; Jin, Y.; Fève, G. Coherence and Indistinguishability of Single Electrons Emitted by Independent Sources. *Science* **2013**, *339*, 1054–1057, doi:10.1126/science.1232572.
30. Weisz, E.; Choi, H.K.; Sivan, I.; Heiblum, M.; Gefen, Y.; Mahalu, D.; Umansky, V. An electronic quantum eraser. *Science* **2014**, *3444*, 1363–1366, 10.1126/science.1248459.
31. Giovannetti, V.; Taddei, F.; Frustaglia, D.; Fazio, R. Multichannel architecture for electronic quantum Hall interferometry. *Phys. Rev. B* **2008**, *77*, 155320, doi:10.1103/PhysRevB.77.155320.
32. Karmakar, B.; Venturelli, D.; Chirolli, L.; Giovannetti, V.; Fazio, R.; Roddaro, S.; Pellegrini, V. Nanoscale Mach-Zehnder interferometer with spin-resolved quantum Hall edge states. *Phys. Rev. B* **2015**, *92*, 195303, doi:10.1103/PhysRevB.92.195303.
33. Bellentani, L.; Beggi, A.; Bordone, P.; Bertoni, A. Dynamics of copropagating edge states in a multichannel Mach-Zehnder interferometer. *J. Phys.: Conf. Ser.* **2017**, *906*, 012027.
34. Bellentani, L.; Beggi, A.; Bordone, P.; Bertoni, A. Dynamics and Hall-edge-state mixing of localized electrons in a two-channel Mach-Zehnder interferometer. *Phys. Rev. B* **2018**, *97*, 205419, doi:10.1103/PhysRevB.97.205419.
35. Ji, Y.; Chung, Y.; Sprinzak, D.; Heiblum, M.; Mahalu, D.; Shtrikman, H. An electronic Mach-Zehnder interferometer. *Nature* **2003**, *422*, 415, doi:10.1038/nature01503.
36. Bird, J. P.; Ishibashi, K.; Stopa, M.; Aoyagi, Y.; Sugano, T. Coulomb blockade of the Aharonov-Bohm effect in GaAs/Al_xGa_{1-x}As quantum dots. *Phys. Rev. B* **1994**, *50*, 14983–14990, 10.1103/PhysRevB.50.14983.
37. Marian, D.; Colomés, E.; Oriols, X. Time-dependent exchange and tunneling: Detection at the same place of two electrons emitted simultaneously from different sources. *J. Phys.: Condens. Matter* **2015**, *27*, 245302.
38. Bellentani, L.; Bordone, P.; Oriols, X.; Bertoni, A. **2019**, arXiv:1903.02581.
39. Oriols, X. Non-universal conductance quantization for long quantum wires: The role of the exchange interaction. *Nanotechnology* **2004**, *15*, S167.
40. Oriols, X.; Mompert, J. *Applied Bohmian Mechanics: From Nanoscale Systems to Cosmology*; CRC Press: 2012.
41. Albareda, G.; Traversa, F.L.; Benali, A.; Oriols, X. Computation of quantum electrical currents through the Ramo-Shockley-Pellegrini theorem with trajectories. *Fluctuat. Noise Lett.* **2012**, *11*, 1242008



© 2019 by the authors. Licensee MDPI, Basel, Switzerland. This article is an open access article distributed under the terms and conditions of the Creative Commons Attribution (CC BY) license (<http://creativecommons.org/licenses/by/4.0/>).

Part IV

Conclusions

Conclusions

By resorting to coherent carrier transport in Hall edge states, the numerical simulation presented in this thesis show the viability of semiconductor-based quantum gates to process quantum information. Indeed, carriers propagating in edge channels are topologically protected from decoherence phenomena, so that, as long as the coherent dynamics of carriers is preserved, serial operations of quantum gates can be realized. The search for quantum computing devices is nowadays a prominent research effort, specially in the field of semiconductor nanoelectronics; furthermore, quantum information processing framework and entanglement theory have an important role also in the assessment of coherent dynamics beyond computer science and physics [126].

By solving exactly the Schrödinger equation for a single- or two-particle system in an arbitrary 2D external potential, we successfully reproduced coherent electron transport in the IQH regime. We observed that the interplay between an orthogonal magnetic field and the confining potential of a 2DEG generates specific paths of quasi-1D edge channels. Moreover, we demonstrate that the peculiarities of transport in edge channels, as chirality and immunity to backscattering, are generally preserved also for localized wavepackets that are linear combination of edge states. With our numerical modeling, we can therefore propose unexplored flying-qubit implementations of quantum computing architectures, as for the multichannel MZI in Chapter 4 or the solid-state Conditional Phase Shifter in Chapter 6. Furthermore, the numerical modeling of single-electron wavepackets mimics the injection of localized quasi-particles with a single charge performed by single-electron sources. This injection protocol is usually adopted in the most recent experiments on electron interferometry, where the qubit state is described by the spin degree of freedom, the Landau index or the spatial localization of the carrier. In our framework, we showed that by encoding the qubit on the which-path localization at bulk FF 1 or on the index of the Landau level at bulk FF 2, it is possible to realize electron interferometry in solid-state devices for a universal set of quantum gates.

Among the possible protocols for the injection of single carriers in edge states, we adopted the recent proposal of Ref. [72] and simulated a minimum uncertainty wavepacket of edge states. This injection protocol is based on the use of quantum dot pumps to generate and detect almost identical Gaussian wavepackets from non-identical sources. Furthermore, the evolution of a localized charge in the IQH regime with a Gaussian real-space broadening is easier to control numerically with respect to alternative shapes of the energy distribution. We proved indeed analytically and numerically that a Gaussian wavepacket of edge states preserves its shape during the evolution in time on a 2D real-space domain. We stress however that the method adopted in our works for the numerical propagation of the wavepacket does not rely on a specific form of the initial state. In fact, various modelings of the single-electron excitation at initial time can be implemented to evaluate how the energy broadening affects the operating regime of the device. As an example, by using the Split-Step Fourier method in a single-particle description, in Ref. [13] we reproduce the dynamics of a single-electron wavepacket with a Lorentzian distribution in the energy domain, and in Chapter 5 we analyze the scattering of a Leviton-like wavepacket with a QPC to compute the two-electron bunching probability.

Furthermore, we proved that the use of strongly-localized wavepackets with a tunable energy distribution is a more reliable tool to study energy-dependent phenomena in solid-state interferometers with respect to the use of stationary states and the scattering matrix method. The latter approach, which is usually adopted in the literature, exploits the chirality of edge states to analyze the single or two-electron interferometry in an effective 1D geometry. On the contrary, here, we have addressed the problem in a full-scale 2D geometry, through the definition of an external potential mimicking the effect of gates on top of the heterostructure. We then did not need to define arbitrarily the energy-dependence of the scattering matrices involved; our dynamical approach requires instead the design of the external potential at initial time, as in a real experiment. The Split-Step Fourier method applies indeed to all the energies involved in the initial wavepacket, so that, while propagating the localized charge in a realistic potential landscape, it exactly accounts for the energy selectivity of the quantum gates.

Moreover, the application of the *wave-packet method* to the evolved wavefunction provides the energy dependence of the transmission probability for an arbitrary design of the 2D quantum gate. In Chapter 4, we exploited this procedure to devise a realistic solid-state electron beam splitter, whose geometry ensures an ideal transmission probability ($T = 1/2$) of the impinging wavepacket. We proved that a sharp enough potential dip at bulk FF 2 scatters a localized wavepacket initialized in the ground channel in a coherent superposition of two states localized in the two available channels. We observed that its geometry can be tuned to generate a quasi-flat energy selectivity, so that the overlap between the *reflected* and *transmitted* wavepackets is increased with contrast to a traditional QPC. By numerically simulating its functioning in a full-scale MZI at bulk FF 2, we measured a larger visibility of the interference pattern with respect to alternative geometries at bulk FF 1, and showed that the scalability issue affecting previous implementations at bulk FF 1 can be solved by using copropagating edge channels. We also proved that the small spatial extension of the potential dip, together with the use of tunable potential mesa at bulk FF 1, is expected to reduce the decoherence induced by charge fractionalization between copropagating channels. Furthermore, thanks to the numerical engineering of the transverse confining potential in the 2DEG, we were able to directly relate the smoothness of the external potential to the exact bending of the Landau levels at the edges of the device. For example, we exploited this relation in the multichannel MZI to engineer single-electron wavepackets with a quasi-linear energy bandstructure and a reduced spreading in the real space at the end of evolution in time, or to locally modify the group velocity in the indentation region.

In addition to improve the design-related performances of our gates, by implementing the Split-Step Fourier method for a two-particle system in 2D, we included the exact screened or unscreened long-range Coulomb repulsion between the propagating charges in a full-scale geometry. In the HOM interferometer, the method enabled to study the exact interplay between exchange interaction and electron-electron repulsion, which is usually neglected in alternative numerical approaches [17]. By simulating strongly-localized wavepacket with an energy broadening comparable to the energy selectivity of the beam splitter, we observed how the bunching probability is affected by the non orthogonality of the two wavepackets generated by a QPC. Thanks to the introduction of screening effects, we further analyzed the transition from a Coulomb-driven to an exchange-driven two-electron bunching, and observed that the saturation of the bunching probability with the wavepacket size, which is in contrast to the plane-wave limit predicted by stationary models, is a signature of the dominance of Coulomb interaction in our operating regime.

The potentiality of our numerical approach manifests also in the Conditional Phase Shifter. Here, the exact simulation of electron-electron interaction in a realistic geometry is desirable to analyze the effects of the Coulomb potential acting as a selective coupler. In the manuscript, we proposed a solid-state implementation of the Conditional Phase Shifter based on the above scalable architecture of the MZI and tested the functioning of its active region. By simulating two-electron scattering between counterpropagating channels at bulk FF 2, we proved that the confining

potential of the 2DEG can be designed to differently affect the final electron state according to its Landau index, so that this device operates as a selective entangling two-qubit gate. We also predicted the two-qubit rotation induced by Coulomb interaction in a realistic geometry of the potential landscape, whose realization is feasible with the current nanotechnology.

Finally, our numerical simulations of electron interferometry in edge channels expose the potentialities of a time-dependent description based on strongly-localized wavepackets. In Chapter 7 we also illustrate that, together with being the most intuitive way to describe electron transport, the use of a dynamical approach for electron transport allows to overcome the inconsistencies arising when matching the stationary Wigner distribution function of a quantum device to the Frensky's boundary conditions, and ascribe the origin of this incompatibility to the non-locality of momentum in orthodox quantum mechanics.

In summary, with our time-dependent solver it is easy to include electron-electron interaction in the system, and to assess the dynamical properties of one or two-particle wavepackets in Hall interferometers. However, the two-particle version of our software requires the allocation and evolution of a time-dependent 4D wavefunction and then the use of supercomputing machines. We showed that, for its allocation, the 4D wavefunction has to be distributed among different computing nodes, thus entailing costly MPI communications during the execution of the Fourier transforms involved by the Split-Step Fourier method. To improve the numerical performances of our software, we identified a parallelization protocol based on a Cartesian topology of the MPI processes, where data distribution can be arranged according to the hardware of the supercomputing machine; this indeed enabled us to successfully reproduce two-electron interferometry in full-scale geometries of a confined 2DEG in the IQH regime. Possible perspectives for further research are then the numerical simulation of unexplored solid-state two-qubit gates as the Hanbury-Brown-Twiss interferometer at bulk FF 2 [10] to test Bell's inequality, or the study of electron-hole collisions in a Hall HOM interferometer [70]. Moreover, with our method it is easy to include time-dependent potentials. These finds an important application in the numerical simulation of electron-transport sustained by surface acoustic waves (SAW) [127, 128, 129, 130, 131], or in the numerical simulation of the emission process from single-electron sources, as mesoscopic capacitors [37] or quantum dot pumps [72].

Acknowledgements

Firstly, I wish to address to Prof. Paolo Bordone and Dr. Andrea Bertoni my gratitude for their scientific guidance and invaluable humanity. I sincerely thank my advisor, Prof. Paolo Bordone, for giving me the opportunity to do research under his leadership. With his knowledge and *expertise*, he guided my work in challenging directions helping me to achieve worthwhile targets from a scientific and personal perspective. In addition to his professional support, I wish to express my gratitude for his kindness and cordiality, which have been essential for me in order to address the professional challenges with determination and a growing confidence. I extend my warmest thanks also to Dr. Andrea Bertoni, who supervised this thesis and supported the computational side of the project. Thanks to its teachings and suggestions, I approached the field of high-performance computing, which impassions me today and which I aspire to further study in the next years.

I am grateful to Prof. Xavier Oriols Pladevall for kindly hosting me at the Departament d'Enginyeria Electrónica of the Universidad Autònoma de Barcelona. His passionate attitude has been inspiring and further motivated me in pursuing the path of scientific research. I am thankful for the time invested in the stimulating discussions on our shared projects, and for introducing me to the fascinating Bohmian interpretation of quantum mechanics. I am thankful to my colleagues in Barcelona, in particular Enrique, Matteo and Devashish, for sharing their knowledge with me and for enriching my visit in Barcelona with their friendship. I also thank Samira, with whom I had the pleasure to share everyday life at Cerdanyola del Valles.

I wish to thank my colleagues at the University of Modena and Reggio Emilia for their support. In particular, I am grateful to Andrea for introducing me to the field of quantum transport based on edge states at the beginning of my PhD, and Dhawal for his careful friendship.

With the deepest affection, I express my gratitude also to Maria Letizia Barigazzi and Paolo Bellentani, whose love and example provided me a precious determination to follow my ambitions also when I feel a *polpetta in gymshoes*. I warmly thank Francesco and Cecilia for their loving support against the tortuosity of the path. I am deeply grateful to my relatives for their kind love and closeness, and to my sincere friends, for being a firm anchor all these years.

Bibliography

- [1] <https://quantumexperience.ng.bluemix.net/qx/experience>.
- [2] I. M. Georgescu, S. Ashhab, and Franco Nori. “Quantum simulation”. In: *Rev. Mod. Phys.* 86 (1 2014), pp. 153–185. DOI: [10.1103/RevModPhys.86.153](https://doi.org/10.1103/RevModPhys.86.153). URL: <https://link.aps.org/doi/10.1103/RevModPhys.86.153>.
- [3] Floris A. Zwanenburg et al. “Silicon quantum electronics”. In: *Rev. Mod. Phys.* 85 (3 2013), pp. 961–1019. DOI: [10.1103/RevModPhys.85.961](https://doi.org/10.1103/RevModPhys.85.961). URL: <https://link.aps.org/doi/10.1103/RevModPhys.85.961>.
- [4] Erwann Bocquillon et al. “Electron quantum optics in ballistic chiral conductors”. In: *Annalen der Physik* 526.1-2 (2014), pp. 1–30.
- [5] Preden Roulleau et al. “Direct Measurement of the Coherence Length of Edge States in the Integer Quantum Hall Regime”. In: *Phys. Rev. Lett.* 100 (12 2008), p. 126802. DOI: [10.1103/PhysRevLett.100.126802](https://doi.org/10.1103/PhysRevLett.100.126802). URL: <https://link.aps.org/doi/10.1103/PhysRevLett.100.126802>.
- [6] D. Venturelli et al. “Edge channel mixing induced by potential steps in an integer quantum Hall system”. In: *Phys. Rev. B* 83 (7 2011), p. 075315. DOI: [10.1103/PhysRevB.83.075315](https://doi.org/10.1103/PhysRevB.83.075315). URL: <https://link.aps.org/doi/10.1103/PhysRevB.83.075315>.
- [7] Andrea Beggi et al. “Time-dependent simulation and analytical modelling of electronic Mach–Zehnder interferometry with edge-states wave packets”. In: *Journal of Physics: Condensed Matter* 27.47 (2015), p. 475301. DOI: [10.1088/0953-8984/27/47/475301](https://doi.org/10.1088/0953-8984/27/47/475301). URL: <https://doi.org/10.1088/0953-8984/27/47/475301>.
- [8] Y. Ji et al. “An electronic Mach–Zehnder interferometer”. In: *Nature* 422 (2003), p. 415. DOI: [10.1038/nature01503](https://doi.org/10.1038/nature01503).
- [9] E. V. Deviatov et al. “Quantum Hall Mach-Zehnder interferometer far beyond equilibrium”. In: *Phys. Rev. B* 84 (23 2011), p. 235313. DOI: [10.1103/PhysRevB.84.235313](https://doi.org/10.1103/PhysRevB.84.235313). URL: <https://link.aps.org/doi/10.1103/PhysRevB.84.235313>.
- [10] Vittorio Giovannetti et al. “Multichannel architecture for electronic quantum Hall interferometry”. In: *Phys. Rev. B* 77 (15 2008), p. 155320. DOI: [10.1103/PhysRevB.77.155320](https://doi.org/10.1103/PhysRevB.77.155320). URL: <https://link.aps.org/doi/10.1103/PhysRevB.77.155320>.
- [11] Biswajit Karmakar et al. “Controlled Coupling of Spin-Resolved Quantum Hall Edge States”. In: *Phys. Rev. Lett.* 107 (23 2011), p. 236804. DOI: [10.1103/PhysRevLett.107.236804](https://doi.org/10.1103/PhysRevLett.107.236804). URL: <https://link.aps.org/doi/10.1103/PhysRevLett.107.236804>.
- [12] Biswajit Karmakar et al. “Nanoscale Mach-Zehnder interferometer with spin-resolved quantum Hall edge states”. In: *Phys. Rev. B* 92 (19 2015), p. 195303. DOI: [10.1103/PhysRevB.92.195303](https://doi.org/10.1103/PhysRevB.92.195303). URL: <https://link.aps.org/doi/10.1103/PhysRevB.92.195303>.

- [13] Laura Bellentani et al. “Dynamics and Hall-edge-state mixing of localized electrons in a two-channel Mach-Zehnder interferometer”. In: *Phys. Rev. B* 97 (20 2018), p. 205419. DOI: [10.1103/PhysRevB.97.205419](https://doi.org/10.1103/PhysRevB.97.205419). URL: <https://link.aps.org/doi/10.1103/PhysRevB.97.205419>.
- [14] P. Samuelsson, E. V. Sukhorukov, and M. Büttiker. “Two-Particle Aharonov-Bohm Effect and Entanglement in the Electronic Hanbury Brown–Twiss Setup”. In: *Phys. Rev. Lett.* 92 (2 2004), p. 026805. DOI: [10.1103/PhysRevLett.92.026805](https://doi.org/10.1103/PhysRevLett.92.026805). URL: <https://link.aps.org/doi/10.1103/PhysRevLett.92.026805>.
- [15] I. Neder et al. “Interference between two indistinguishable electrons from independent sources”. In: *Nature* 448 (2007), p. 333. DOI: [10.1038/nature05955](https://doi.org/10.1038/nature05955).
- [16] C. K. Hong, Z. Y. Ou, and L. Mandel. “Measurement of subpicosecond time intervals between two photons by interference”. In: *Phys. Rev. Lett.* 59 (18 1987), pp. 2044–2046. DOI: [10.1103/PhysRevLett.59.2044](https://doi.org/10.1103/PhysRevLett.59.2044). URL: <https://link.aps.org/doi/10.1103/PhysRevLett.59.2044>.
- [17] A. Marguerite et al. “Decoherence and relaxation of a single electron in a one-dimensional conductor”. In: *Phys. Rev. B* 94 (11 2016), p. 115311. DOI: [10.1103/PhysRevB.94.115311](https://doi.org/10.1103/PhysRevB.94.115311). URL: <https://link.aps.org/doi/10.1103/PhysRevB.94.115311>.
- [18] D Marian, E Colomès, and X Oriols. “Time-dependent exchange and tunneling: detection at the same place of two electrons emitted simultaneously from different sources”. In: *Journal of Physics: Condensed Matter* 27.24 (2015), p. 245302.
- [19] D Marian, E Colomès, and X Oriols. “Time-dependent exchange and tunneling: detection at the same place of two electrons emitted simultaneously from different sources”. In: *Journal of Physics: Condensed Matter* 27.24 (2015), p. 245302. DOI: [10.1088/0953-8984/27/24/245302](https://doi.org/10.1088/0953-8984/27/24/245302). URL: <https://doi.org/10.1088/0953-8984/27/24/245302>.
- [20] A Beggi, A Bertoni, and P Bordone. “Time-Dependent Modelling of Single-Electron Interferometry with Edge-States”. In: *Journal of Physics: Conference Series* 647.1 (2015), p. 012023. URL: <http://stacks.iop.org/1742-6596/647/i=1/a=012023>.
- [21] L. Bellentani et al. “Coulomb and exchange interaction effects on the exact two-electron dynamics in the Hong-Ou-Mandel interferometer based on Hall edge states”. In: *Phys. Rev. B* 99 (24 2019), p. 245415. DOI: [10.1103/PhysRevB.99.245415](https://doi.org/10.1103/PhysRevB.99.245415). URL: <https://link.aps.org/doi/10.1103/PhysRevB.99.245415>.
- [22] A. Bertoni et al. “Numerical simulation of coherent transport in quantum wires for quantum computing”. In: *Journal of Modern Optics* 49 (Aug. 2002), pp. 1219–1234. DOI: [10.1080/09500340110105948](https://doi.org/10.1080/09500340110105948).
- [23] Paolo Bordone, Laura Bellentani, and Andrea Bertoni. “Quantum computing with quantum-Hall edge state interferometry”. In: *Semiconductor Science and Technology* 34.10 (2019), p. 103001. DOI: [10.1088/1361-6641/ab3be6](https://doi.org/10.1088/1361-6641/ab3be6). URL: <https://doi.org/10.1088/1361-6641/ab3be6>.
- [24] Kicheon Kang. “Electronic Mach-Zehnder quantum eraser”. In: *Phys. Rev. B* 75 (12 2007), p. 125326. DOI: [10.1103/PhysRevB.75.125326](https://doi.org/10.1103/PhysRevB.75.125326). URL: <https://link.aps.org/doi/10.1103/PhysRevB.75.125326>.
- [25] Luca Chirolli et al. “Interactions in Electronic Mach-Zehnder Interferometers with Copropagating Edge Channels”. In: *Phys. Rev. Lett.* 111 (3 2013), p. 036801. DOI: [10.1103/PhysRevLett.111.036801](https://doi.org/10.1103/PhysRevLett.111.036801). URL: <https://link.aps.org/doi/10.1103/PhysRevLett.111.036801>.

- [26] F. Buscemi, P. Bordone, and A. Bertoni. “Electron interference and entanglement in coupled 1D systems with noise”. In: *The European Physical Journal D* 66.12 (2012), p. 312. ISSN: 1434-6079. DOI: [10.1140/epjd/e2012-30469-5](https://doi.org/10.1140/epjd/e2012-30469-5). URL: <https://doi.org/10.1140/epjd/e2012-30469-5>.
- [27] Tobias Kramer, Christoph Kreisbeck, and Viktor Krueckl. “Wave packet approach to transport in mesoscopic systems”. In: *Physica Scripta* 82.3 (2010), p. 038101. URL: <http://stacks.iop.org/1402-4896/82/i=3/a=038101>.
- [28] Géraldine Haack et al. “Coherence of single-electron sources from Mach-Zehnder interferometry”. In: *Phys. Rev. B* 84 (8 2011), p. 081303. DOI: [10.1103/PhysRevB.84.081303](https://doi.org/10.1103/PhysRevB.84.081303). URL: <https://link.aps.org/doi/10.1103/PhysRevB.84.081303>.
- [29] Benoit Gaury, Joseph Weston, and Xavier Waintal. “Stopping electrons with radio-frequency pulses in the quantum Hall regime”. In: *Phys. Rev. B* 90 (16 2014), p. 161305. DOI: [10.1103/PhysRevB.90.161305](https://doi.org/10.1103/PhysRevB.90.161305). URL: <https://link.aps.org/doi/10.1103/PhysRevB.90.161305>.
- [30] D. Ferraro et al. “Real-Time Decoherence of Landau and Levitov Quasiparticles in Quantum Hall Edge Channels”. In: *Phys. Rev. Lett.* 113 (16 2014), p. 166403. DOI: [10.1103/PhysRevLett.113.166403](https://doi.org/10.1103/PhysRevLett.113.166403). URL: <https://link.aps.org/doi/10.1103/PhysRevLett.113.166403>.
- [31] C. Cabart et al. “Taming electronic decoherence in one-dimensional chiral ballistic quantum conductors”. In: *Phys. Rev. B* 98 (15 2018), p. 155302. DOI: [10.1103/PhysRevB.98.155302](https://doi.org/10.1103/PhysRevB.98.155302). URL: <https://link.aps.org/doi/10.1103/PhysRevB.98.155302>.
- [32] Nastaran Dashti et al. “Minimal excitation single-particle emitters: Comparison of charge-transport and energy-transport properties”. In: *Phys. Rev. B* 100 (3 2019), p. 035405. DOI: [10.1103/PhysRevB.100.035405](https://doi.org/10.1103/PhysRevB.100.035405). URL: <https://link.aps.org/doi/10.1103/PhysRevB.100.035405>.
- [33] <http://www.hpc.cineca.it/hardware/marconi>.
- [34] <https://www.bsc.es/marenostrum/marenostrum>.
- [35] T. Jullien et al. “Quantum tomography of an electron”. In: *Nature* 514 (Oct. 2014), pp. 603–607. DOI: [10.1038/nature13821](https://doi.org/10.1038/nature13821).
- [36] J. Dubois et al. “Minimal-excitation states for electron quantum optics using levitons”. In: *Nature* 502 (2013), p. 659. DOI: [10.1038/nature12713](https://doi.org/10.1038/nature12713). URL: <https://doi.org/10.1038/nature12713>.
- [37] J. Keeling, I. Klich, and L. S. Levitov. “Minimal Excitation States of Electrons in One-Dimensional Wires”. In: *Phys. Rev. Lett.* 97 (11 2006), p. 116403. DOI: [10.1103/PhysRevLett.97.116403](https://doi.org/10.1103/PhysRevLett.97.116403). URL: <https://link.aps.org/doi/10.1103/PhysRevLett.97.116403>.
- [38] G. Fève et al. “An On-Demand Coherent Single-Electron Source”. In: *Science* 316.5828 (2007), pp. 1169–1172. DOI: [10.1126/science.1141243](https://doi.org/10.1126/science.1141243). eprint: <http://science.sciencemag.org/content/316/5828/1169.full.pdf>. URL: <http://science.sciencemag.org/content/316/5828/1169>.
- [39] J. D. Fletcher et al. “Stabilization of single-electron pumps by high magnetic fields”. In: *Phys. Rev. B* 86 (15 2012), p. 155311. DOI: [10.1103/PhysRevB.86.155311](https://doi.org/10.1103/PhysRevB.86.155311). URL: <https://link.aps.org/doi/10.1103/PhysRevB.86.155311>.
- [40] Christopher Bauerle et al. “Coherent control of single electrons: a review of current progress”. In: *Reports on Progress in Physics* 81.5 (2018), p. 056503. URL: <http://stacks.iop.org/0034-4885/81/i=5/a=056503>.

- [41] William R. Frensley. “Wigner-function model of a resonant-tunneling semiconductor device”. In: *Phys. Rev. B* 36 (3 1987), pp. 1570–1580. DOI: [10.1103/PhysRevB.36.1570](https://doi.org/10.1103/PhysRevB.36.1570). URL: <https://link.aps.org/doi/10.1103/PhysRevB.36.1570>.
- [42] David K Ferry, Stephen M Goodnick, and Jonathan Bird. *Transport in nanostructures*. 2nd. Vol. 6. Cambridge University Press, 2009.
- [43] Frank WJ Olver. *NIST Handbook of Mathematical Functions Hardback and CD-ROM*. Cambridge University Press, 2010.
- [44] Hitoshi Murayama. “Landau Levels, 221A Lecture Notes (Quantum Mechanics I)”. Lecture notes. University of California, Berkeley, 2015-2016. URL: <http://hitoshi.berkeley.edu/221A/landau.pdf>.
- [45] Gilles Montambaux. “Semiclassical quantization of skipping orbits”. In: *The European Physical Journal B* 79.2 (2011), pp. 215–224.
- [46] K. v. Klitzing, G. Dorda, and M. Pepper. “New Method for High-Accuracy Determination of the Fine-Structure Constant Based on Quantized Hall Resistance”. In: *Phys. Rev. Lett.* 45 (6 1980), pp. 494–497. DOI: [10.1103/PhysRevLett.45.494](https://doi.org/10.1103/PhysRevLett.45.494). URL: <https://link.aps.org/doi/10.1103/PhysRevLett.45.494>.
- [47] Michael V Moskalets. *Scattering matrix approach to non-stationary quantum transport*. World Scientific, 2011.
- [48] M. Büttiker. “Absence of backscattering in the quantum Hall effect in multiprobe conductors”. In: *Phys. Rev. B* 38 (14 1988), pp. 9375–9389. DOI: [10.1103/PhysRevB.38.9375](https://doi.org/10.1103/PhysRevB.38.9375). URL: <https://link.aps.org/doi/10.1103/PhysRevB.38.9375>.
- [49] William D. Oliver et al. “Hanbury Brown and Twiss-Type Experiment with Electrons”. In: *Science* 284.5412 (1999), pp. 299–301. DOI: [10.1126/science.284.5412.299](https://doi.org/10.1126/science.284.5412.299). eprint: <http://science.sciencemag.org/content/284/5412/299.full.pdf>. URL: <http://science.sciencemag.org/content/284/5412/299>.
- [50] M. Henny et al. “The Fermionic Hanbury Brown and Twiss Experiment”. In: *Science* 284.5412 (1999), pp. 296–298. DOI: [10.1126/science.284.5412.296](https://doi.org/10.1126/science.284.5412.296). eprint: <http://science.sciencemag.org/content/284/5412/296.full.pdf>. URL: <http://science.sciencemag.org/content/284/5412/296>.
- [51] E. V. Devyatov. “Electronic interferometers in the quantum Hall effect regime”. In: *Low Temperature Physics* 39.1 (2013), pp. 7–17. DOI: [10.1063/1.4775355](https://doi.org/10.1063/1.4775355). eprint: <https://doi.org/10.1063/1.4775355>. URL: <https://doi.org/10.1063/1.4775355>.
- [52] A. Radu, S. Iftimie, and D. Dragoman. “Ballistic 3-port interferometric logic gates in the quantum Hall regime”. In: *Physica E: Low-dimensional Systems and Nanostructures* 109 (2019), pp. 144–151. ISSN: 1386-9477. DOI: <https://doi.org/10.1016/j.physe.2019.01.016>. URL: <http://www.sciencedirect.com/science/article/pii/S1386947718316497>.
- [53] B. Kaestner et al. “Single-parameter nonadiabatic quantized charge pumping”. In: *Phys. Rev. B* 77 (15 2008), p. 153301. DOI: [10.1103/PhysRevB.77.153301](https://doi.org/10.1103/PhysRevB.77.153301). URL: <https://link.aps.org/doi/10.1103/PhysRevB.77.153301>.
- [54] J. Keeling, A. V. Shytov, and L. S. Levitov. “Coherent Particle Transfer in an On-Demand Single-Electron Source”. In: *Phys. Rev. Lett.* 101 (19 2008), p. 196404. DOI: [10.1103/PhysRevLett.101.196404](https://doi.org/10.1103/PhysRevLett.101.196404). URL: <https://link.aps.org/doi/10.1103/PhysRevLett.101.196404>.

- [55] L. Bellentani et al. “Dynamics of copropagating edge states in a multichannel Mach-Zender interferometer”. In: *Journal of Physics: Conference Series* 906 (2017), p. 012027. DOI: [10.1088/1742-6596/906/1/012027](https://doi.org/10.1088/1742-6596/906/1/012027). URL: <https://doi.org/10.1088/1742-6596/906/1/012027>.
- [56] Masaya Kataoka, Jonathan D. Fletcher, and Nathan Johnson. “Time-resolved single-electron wave-packet detection”. In: *physica status solidi (b)* 254.3 (2017), p. 1600547. DOI: [10.1002/pssb.201600547](https://onlinelibrary.wiley.com/doi/pdf/10.1002/pssb.201600547). eprint: <https://onlinelibrary.wiley.com/doi/pdf/10.1002/pssb.201600547>. URL: <https://onlinelibrary.wiley.com/doi/abs/10.1002/pssb.201600547>.
- [57] Leonid S. Levitov, Hyunwoo Lee, and Gordey B. Lesovik. “Electron counting statistics and coherent states of electric current”. In: *Journal of Mathematical Physics* 37.10 (1996), pp. 4845–4866. DOI: [10.1063/1.531672](https://doi.org/10.1063/1.531672). eprint: <https://doi.org/10.1063/1.531672>. URL: <https://doi.org/10.1063/1.531672>.
- [58] D. A. Ivanov, H. W. Lee, and L. S. Levitov. “Coherent states of alternating current”. In: *Physical Review B* 56 (11 1997), pp. 6839–6850. ISSN: 1098-0121,1550-235X. DOI: [10.1103/PhysRevB.56.6839](https://doi.org/10.1103/PhysRevB.56.6839).
- [59] D. C. Glatthli and P. Roulleau. “Pseudorandom binary injection of levitons for electron quantum optics”. In: *Phys. Rev. B* 97 (12 2018), p. 125407. DOI: [10.1103/PhysRevB.97.125407](https://doi.org/10.1103/PhysRevB.97.125407). URL: <https://link.aps.org/doi/10.1103/PhysRevB.97.125407>.
- [60] D.C. Glatthli and P. Roulleau. “Hanbury-Brown Twiss noise correlation with time controlled quasi-particles in ballistic quantum conductors”. In: *Physica E: Low-dimensional Systems and Nanostructures* 76 (2016), pp. 216 –222. ISSN: 1386-9477. DOI: <https://doi.org/10.1016/j.physe.2015.10.034>. URL: <http://www.sciencedirect.com/science/article/pii/S1386947715302617>.
- [61] J. Gabelli et al. “Violation of Kirchhoff’s Laws for a Coherent RC Circuit”. In: *Science* 313.5786 (2006), pp. 499–502. ISSN: 0036-8075. DOI: [10.1126/science.1126940](https://doi.org/10.1126/science.1126940). eprint: <http://science.sciencemag.org/content/313/5786/499.full.pdf>. URL: <http://science.sciencemag.org/content/313/5786/499>.
- [62] M. Büttiker, H. Thomas, and A. Prêtre. “Mesoscopic capacitors”. In: *Physics Letters A* 180.4 (1993), pp. 364 –369. ISSN: 0375-9601. DOI: [https://doi.org/10.1016/0375-9601\(93\)91193-9](https://doi.org/10.1016/0375-9601(93)91193-9). URL: <http://www.sciencedirect.com/science/article/pii/0375960193911939>.
- [63] A. Mahé et al. “Current correlations of an on-demand single-electron emitter”. In: *Phys. Rev. B* 82 (20 2010), p. 201309. DOI: [10.1103/PhysRevB.82.201309](https://doi.org/10.1103/PhysRevB.82.201309). URL: <https://link.aps.org/doi/10.1103/PhysRevB.82.201309>.
- [64] E. Bocquillon et al. “Coherence and Indistinguishability of Single Electrons Emitted by Independent Sources”. In: *Science* 339.6123 (2013), pp. 1054–1057. ISSN: 0036-8075. DOI: [10.1126/science.1232572](https://doi.org/10.1126/science.1232572). eprint: <http://science.sciencemag.org/content/339/6123/1054.full.pdf>. URL: <http://science.sciencemag.org/content/339/6123/1054>.
- [65] V. Freulon et al. “Hong-Ou-Mandel experiment for temporal investigation of single-electron fractionalization”. In: *Nat. Comm.* 6 (2015), p. 6854. DOI: [10.1038/ncomms7854](https://doi.org/10.1038/ncomms7854).
- [66] J. Rech et al. “Minimal Excitations in the Fractional Quantum Hall Regime”. In: *Phys. Rev. Lett.* 118 (7 2017), p. 076801. DOI: [10.1103/PhysRevLett.118.076801](https://doi.org/10.1103/PhysRevLett.118.076801). URL: <https://link.aps.org/doi/10.1103/PhysRevLett.118.076801>.
- [67] Flavio Ronetti et al. “Crystallization of levitons in the fractional quantum Hall regime”. In: *Phys. Rev. B* 98 (7 2018), p. 075401. DOI: [10.1103/PhysRevB.98.075401](https://doi.org/10.1103/PhysRevB.98.075401). URL: <https://link.aps.org/doi/10.1103/PhysRevB.98.075401>.

- [68] Claire Wahl et al. “Interactions and Charge Fractionalization in an Electronic Hong-Ou-Mandel Interferometer”. In: *Phys. Rev. Lett.* 112 (4 2014), p. 046802. DOI: [10.1103/PhysRevLett.112.046802](https://doi.org/10.1103/PhysRevLett.112.046802). URL: <https://link.aps.org/doi/10.1103/PhysRevLett.112.046802>.
- [69] Dario Ferraro et al. “Hong-Ou-Mandel characterization of multiply charged Levitons”. In: *The European Physical Journal Special Topics* 227.12 (2018), pp. 1345–1359. DOI: [10.1140/epjst/e2018-800074-1](https://doi.org/10.1140/epjst/e2018-800074-1). URL: <https://doi.org/10.1140/epjst/e2018-800074-1>.
- [70] T. Jonckheere et al. “Electron and hole Hong-Ou-Mandel interferometry”. In: *Phys. Rev. B* 86 (12 2012), p. 125425. DOI: [10.1103/PhysRevB.86.125425](https://doi.org/10.1103/PhysRevB.86.125425). URL: <https://link.aps.org/doi/10.1103/PhysRevB.86.125425>.
- [71] Ch Grenier et al. “Single-electron quantum tomography in quantum Hall edge channels”. In: *New Journal of Physics* 13.9 (2011), p. 093007. DOI: [10.1088/1367-2630/13/9/093007](https://doi.org/10.1088/1367-2630/13/9/093007). URL: <https://doi.org/10.1088/1367-2630/13/9/093007>.
- [72] Sungguen Ryu, M. Kataoka, and H.-S. Sim. “Ultrafast Emission and Detection of a Single-Electron Gaussian Wave Packet: A Theoretical Study”. In: *Phys. Rev. Lett.* 117 (14 2016), p. 146802. DOI: [10.1103/PhysRevLett.117.146802](https://doi.org/10.1103/PhysRevLett.117.146802). URL: <https://link.aps.org/doi/10.1103/PhysRevLett.117.146802>.
- [73] M. D. Blumenthal et al. “Gigahertz quantized charge pumping”. In: *Nature Physics* 3393.343 (2007). DOI: [10.1038/nphys58](https://doi.org/10.1038/nphys58).
- [74] Bernd Kaestner and Vyacheslavs Kashcheyevs. “Non-adiabatic quantized charge pumping with tunable-barrier quantum dots: a review of current progress”. In: *Reports on Progress in Physics* 78.10 (2015), p. 103901. URL: <http://stacks.iop.org/0034-4885/78/i=10/a=103901>.
- [75] C. Emary et al. “Energy relaxation in hot electron quantum optics via acoustic and optical phonon emission”. In: *Phys. Rev. B* 99 (4 2019), p. 045306. DOI: [10.1103/PhysRevB.99.045306](https://doi.org/10.1103/PhysRevB.99.045306). URL: <https://link.aps.org/doi/10.1103/PhysRevB.99.045306>.
- [76] Y Yin. “On-demand electron source with tunable energy distribution”. In: *Journal of Physics: Condensed Matter* 30.28 (2018), p. 285301. DOI: [10.1088/1361-648x/aac843](https://doi.org/10.1088/1361-648x/aac843). URL: <https://doi.org/10.1088/1361-648x/aac843>.
- [77] Y Yin. “Quasiparticle states of on-demand coherent electron sources”. In: *Journal of Physics: Condensed Matter* 31.24 (2019), p. 245301. DOI: [10.1088/1361-648x/ab0fc4](https://doi.org/10.1088/1361-648x/ab0fc4). URL: <https://doi.org/10.1088/1361-648x/ab0fc4>.
- [78] Andrea Beggi. *Quantum entanglement and electron interference in nanostructures: Analytical and numerical study of quantum correlations and transport in Edge channels and Quantum Walks*. PhD Thesis, 2017.
- [79] Albert Messiah. “Quantum mechanics”. In: *North Holland Publishing Company, Amsterdam* 1 and 2 (1961).
- [80] DJ Tannor. *Introduction to Quantum Dynamics: A Time-Dependent Perspective*. 2007.
- [81] David Jeffery Griffiths. *Introduction to quantum mechanics*. Pearson Education India, 2005.
- [82] Jun John Sakurai and Jim Napolitano. *Modern quantum mechanics*. Addison-Wesley, 2011.
- [83] T Kramer, E J Heller, and R E Parrott. “An efficient and accurate method to obtain the energy-dependent Green function for general potentials”. In: *Journal of Physics: Conference Series* 99 (2008), p. 012010. DOI: [10.1088/1742-6596/99/1/012010](https://doi.org/10.1088/1742-6596/99/1/012010). URL: <https://doi.org/10.1088/1742-6596/99/1/012010>.

- [84] Tobias Kramer. “Time-dependent approach to transport and scattering in atomic and mesoscopic physics”. In: *AIP Conference Proceedings* 1334.1 (2011), pp. 142–165. DOI: <http://dx.doi.org/10.1063/1.3555481>. URL: <http://scitation.aip.org/content/aip/proceeding/aipcp/10.1063/1.3555481>.
- [85] Christoph W Groth et al. “Kwant: a software package for quantum transport”. In: *New Journal of Physics* 16.6 (2014), p. 063065. DOI: [10.1088/1367-2630/16/6/063065](https://doi.org/10.1088/1367-2630/16/6/063065). URL: <https://doi.org/10.1088/1367-2630/16/6/063065>.
- [86] Devashish Pandey et al. “A Proposal for Evading the Measurement Uncertainty in Classical and Quantum Computing: Application to a Resonant Tunneling Diode and a Mach-Zehnder Interferometer”. In: *Applied Sciences* 9.11 (2019). ISSN: 2076-3417. DOI: [10.3390/app9112300](https://www.mdpi.com/2076-3417/9/11/2300). URL: <https://www.mdpi.com/2076-3417/9/11/2300>.
- [87] Alexandros Metavitsiadis, Raoul Dillenschneider, and Sebastian Eggert. “Impurity entanglement through electron scattering in a magnetic field”. In: *Phys. Rev. B* 89 (15 2014), p. 155406. DOI: [10.1103/PhysRevB.89.155406](https://link.aps.org/doi/10.1103/PhysRevB.89.155406). URL: <https://link.aps.org/doi/10.1103/PhysRevB.89.155406>.
- [88] Mauro Ballicchia, Josef Weinbub, and Mihail Nedjalkov. “Electron evolution around a repulsive dopant in a quantum wire: coherence effects”. In: *Nanoscale* 10 (48 2018), pp. 23037–23049. DOI: [10.1039/C8NR06933F](http://dx.doi.org/10.1039/C8NR06933F). URL: <http://dx.doi.org/10.1039/C8NR06933F>.
- [89] Fabrizio Buscemi et al. “Electron decoherence in a semiconductor due to electron-phonon scattering”. In: *physica status solidi c* 5.1 (), p. 52. DOI: [10.1002/pssc.200776541](https://onlinelibrary.wiley.com/doi/abs/10.1002/pssc.200776541). URL: <https://onlinelibrary.wiley.com/doi/abs/10.1002/pssc.200776541>.
- [90] B. J. van Wees et al. “Observation of zero-dimensional states in a one-dimensional electron interferometer”. In: *Phys. Rev. Lett.* 62 (21 1989), pp. 2523–2526. DOI: [10.1103/PhysRevLett.62.2523](https://link.aps.org/doi/10.1103/PhysRevLett.62.2523). URL: <https://link.aps.org/doi/10.1103/PhysRevLett.62.2523>.
- [91] J. P. Bird et al. “Coulomb blockade of the Aharonov-Bohm effect in GaAs/Al_xGa_{1-x}As quantum dots”. In: *Phys. Rev. B* 50 (20 1994), pp. 14983–14990. DOI: [10.1103/PhysRevB.50.14983](https://link.aps.org/doi/10.1103/PhysRevB.50.14983). URL: <https://link.aps.org/doi/10.1103/PhysRevB.50.14983>.
- [92] F. E. Camino, Wei Zhou, and V. J. Goldman. “Aharonov-Bohm Superperiod in a Laughlin Quasiparticle Interferometer”. In: *Phys. Rev. Lett.* 95 (24 2005), p. 246802. DOI: [10.1103/PhysRevLett.95.246802](https://link.aps.org/doi/10.1103/PhysRevLett.95.246802). URL: <https://link.aps.org/doi/10.1103/PhysRevLett.95.246802>.
- [93] E. V. Deviatov and A. Lorke. “Experimental realization of a Fabry-Perot-type interferometer by copropagating edge states in the quantum Hall regime”. In: *Phys. Rev. B* 77 (16 2008), p. 161302. DOI: [10.1103/PhysRevB.77.161302](https://link.aps.org/doi/10.1103/PhysRevB.77.161302). URL: <https://link.aps.org/doi/10.1103/PhysRevB.77.161302>.
- [94] E. V. Deviatov et al. “Interference effects in transport across a single incompressible strip at the edge of the fractional quantum Hall system”. In: *Phys. Rev. B* 79 (12 2009), p. 125312. DOI: [10.1103/PhysRevB.79.125312](https://link.aps.org/doi/10.1103/PhysRevB.79.125312). URL: <https://link.aps.org/doi/10.1103/PhysRevB.79.125312>.
- [95] V. S.-W. Chung, P. Samuelsson, and M. Büttiker. “Visibility of current and shot noise in electrical Mach-Zehnder and Hanbury Brown Twiss interferometers”. In: *Phys. Rev. B* 72 (12 2005), p. 125320. DOI: [10.1103/PhysRevB.72.125320](https://link.aps.org/doi/10.1103/PhysRevB.72.125320). URL: <https://link.aps.org/doi/10.1103/PhysRevB.72.125320>.

-
- [96] J. J. Palacios and C. Tejedor. “Effects of geometry on edge states in magnetic fields: Adiabatic and nonadiabatic behavior”. In: *Phys. Rev. B* 45 (16 1992), pp. 9059–9064. DOI: [10.1103/PhysRevB.45.9059](https://doi.org/10.1103/PhysRevB.45.9059). URL: <https://link.aps.org/doi/10.1103/PhysRevB.45.9059>.
 - [97] E. V. Deviatov, V. T. Dolgoplov, and A. Würtz. “Charge redistribution between cyclotron-resolved edge states at high imbalance”. In: *Journal of Experimental and Theoretical Physics Letters* 79.10 (2004), pp. 504–509. ISSN: 1090-6487. DOI: [10.1134/1.1780561](https://doi.org/10.1134/1.1780561). URL: <https://doi.org/10.1134/1.1780561>.
 - [98] A. Würtz et al. “Separately contacted edge states: A spectroscopic tool for the investigation of the quantum Hall effect”. In: *Phys. Rev. B* 65 (7 2002), p. 075303. DOI: [10.1103/PhysRevB.65.075303](https://doi.org/10.1103/PhysRevB.65.075303). URL: <https://link.aps.org/doi/10.1103/PhysRevB.65.075303>.
 - [99] E. V. Deviatov and A. Lorke. “Separately contacted edge states at high imbalance in the integer and fractional quantum Hall effect regime”. In: *physica status solidi (b)* 245.2 (2008), pp. 366–377. DOI: [10.1002/pssb.200743341](https://doi.org/10.1002/pssb.200743341). eprint: <https://onlinelibrary.wiley.com/doi/pdf/10.1002/pssb.200743341>. URL: <https://onlinelibrary.wiley.com/doi/abs/10.1002/pssb.200743341>.
 - [100] Preden Roulleau et al. “Finite bias visibility of the electronic Mach-Zehnder interferometer”. In: *Phys. Rev. B* 76 (16 2007), p. 161309. DOI: [10.1103/PhysRevB.76.161309](https://doi.org/10.1103/PhysRevB.76.161309). URL: <https://link.aps.org/doi/10.1103/PhysRevB.76.161309>.
 - [101] L. V. Litvin et al. “Decoherence and single electron charging in an electronic Mach-Zehnder interferometer”. In: *Phys. Rev. B* 75 (3 2007), p. 033315. DOI: [10.1103/PhysRevB.75.033315](https://doi.org/10.1103/PhysRevB.75.033315). URL: <https://link.aps.org/doi/10.1103/PhysRevB.75.033315>.
 - [102] P-A. Huynh et al. “Quantum Coherence Engineering in the Integer Quantum Hall Regime”. In: *Phys. Rev. Lett.* 108 (25 2012), p. 256802. DOI: [10.1103/PhysRevLett.108.256802](https://doi.org/10.1103/PhysRevLett.108.256802). URL: <https://link.aps.org/doi/10.1103/PhysRevLett.108.256802>.
 - [103] A. Helzel et al. “Counting statistics and dephasing transition in an electronic Mach-Zehnder interferometer”. In: *Phys. Rev. B* 91 (24 2015), p. 245419. DOI: [10.1103/PhysRevB.91.245419](https://doi.org/10.1103/PhysRevB.91.245419). URL: <https://link.aps.org/doi/10.1103/PhysRevB.91.245419>.
 - [104] I. Neder et al. “Unexpected Behavior in a Two-Path Electron Interferometer”. In: *Phys. Rev. Lett.* 96 (1 2006), p. 016804. DOI: [10.1103/PhysRevLett.96.016804](https://doi.org/10.1103/PhysRevLett.96.016804). URL: <https://link.aps.org/doi/10.1103/PhysRevLett.96.016804>.
 - [105] Rolf Landauer. “Solid-state shot noise”. In: *Phys. Rev. B* 47 (24 1993), pp. 16427–16432. DOI: [10.1103/PhysRevB.47.16427](https://doi.org/10.1103/PhysRevB.47.16427). URL: <https://link.aps.org/doi/10.1103/PhysRevB.47.16427>.
 - [106] C. Beenakker and C. Schönenberger. “Quantum Shot Noise”. In: *Physics Today* 56.5 (May 2003), p. 37. DOI: [10.1063/1.1583532](https://doi.org/10.1063/1.1583532).
 - [107] R. C. Liu et al. “Quantum interference in electron collision”. English (US). In: *Nature* 391.6664 (Jan. 1998), pp. 263–265. ISSN: 0028-0836. DOI: [10.1038/34611](https://doi.org/10.1038/34611).
 - [108] E. Bocquillon et al. “Separation of neutral and charge modes in one-dimensional chiral edge channels”. In: *Nature Communications* 4 (2013), p. 11839. DOI: [10.1038/ncomms2788](https://doi.org/10.1038/ncomms2788).
 - [109] Carlo Jacoboni. *Theory of electron transport in semiconductors: A pathway from elementary physics to nonequilibrium Green functions*. Vol. 165. Springer Science & Business Media, 2010.

- [110] M. Kataoka et al. “Time-of-Flight Measurements of Single-Electron Wave Packets in Quantum Hall Edge States”. In: *Phys. Rev. Lett.* 116 (12 2016), p. 126803. DOI: [10.1103/PhysRevLett.116.126803](https://doi.org/10.1103/PhysRevLett.116.126803). URL: <https://link.aps.org/doi/10.1103/PhysRevLett.116.126803>.
- [111] Ady Stern. “Anyons and the quantum Hall effect—A pedagogical review”. In: *Annals of Physics* 323.1 (2008). January Special Issue 2008, pp. 204–249. ISSN: 0003-4916. DOI: <https://doi.org/10.1016/j.aop.2007.10.008>. URL: <http://www.sciencedirect.com/science/article/pii/S0003491607001674>.
- [112] Andrea Bertoni. “Charge-Based Solid-State Flying Qubits”. In: *Encyclopedia of Complexity and Systems Science*. New York, NY: Springer New York, 2009, pp. 1011–1027. ISBN: 978-0-387-30440-3. DOI: [10.1007/978-0-387-30440-3_67](https://doi.org/10.1007/978-0-387-30440-3_67). URL: https://doi.org/10.1007/978-0-387-30440-3_67.
- [113] E. Wigner. “On the Quantum Correction For Thermodynamic Equilibrium”. In: *Phys. Rev.* 40 (5 1932), pp. 749–759. DOI: [10.1103/PhysRev.40.749](https://doi.org/10.1103/PhysRev.40.749). URL: <https://link.aps.org/doi/10.1103/PhysRev.40.749>.
- [114] Haiyan Jiang, Wei Cai, and Raphael Tsu. “Accuracy of the Frensley inflow boundary condition for Wigner equations in simulating resonant tunneling diodes”. In: *J. Comput. Physics* 230 (Mar. 2011), pp. 2031–2044. DOI: [10.1016/j.jcp.2010.12.002](https://doi.org/10.1016/j.jcp.2010.12.002).
- [115] Remo Proietti Zaccaria and Fausto Rossi. “On the problem of generalizing the semiconductor Bloch equation from a closed to an open system”. In: *Phys. Rev. B* 67 (11 2003), p. 113311. DOI: [10.1103/PhysRevB.67.113311](https://doi.org/10.1103/PhysRevB.67.113311). URL: <https://link.aps.org/doi/10.1103/PhysRevB.67.113311>.
- [116] E. Colomés, Z. Zhan, and X. Oriols. “Comparing Wigner, Husimi and Bohmian Distributions: Which One is a True Probability Distribution in Phase Space?” In: *J. Comput. Electron.* 14.4 (Dec. 2015), pp. 894–906. ISSN: 1569-8025. DOI: [10.1007/s10825-015-0737-6](https://doi.org/10.1007/s10825-015-0737-6). URL: <http://dx.doi.org/10.1007/s10825-015-0737-6>.
- [117] N. C. Kluksdahl et al. “Self-consistent study of the resonant-tunneling diode”. In: *Phys. Rev. B* 39 (11 1989), pp. 7720–7735. DOI: [10.1103/PhysRevB.39.7720](https://doi.org/10.1103/PhysRevB.39.7720). URL: <https://link.aps.org/doi/10.1103/PhysRevB.39.7720>.
- [118] Carlo Jacoboni and Paolo Bordone. “The Wigner-function approach to non-equilibrium electron transport”. In: *Reports on Progress in Physics* 67 (June 2004), p. 1033. DOI: [10.1088/0034-4885/67/7/R01](https://doi.org/10.1088/0034-4885/67/7/R01).
- [119] Damien Querlioz, Philippe Dollfus, and Mireille Mouis. “The Wigner Monte Carlo Method for Nanoelectronic Devices”. In: Mar. 2013, pp. 1–56. ISBN: 9781848211506. DOI: [10.1002/9781118618479.ch1](https://doi.org/10.1002/9781118618479.ch1).
- [120] M. Wołoszyn and B. J. Spisak. “Dissipative transport of thermalized electrons through a nanodevice”. In: *Phys. Rev. B* 96 (7 2017), p. 075440. DOI: [10.1103/PhysRevB.96.075440](https://doi.org/10.1103/PhysRevB.96.075440). URL: <https://link.aps.org/doi/10.1103/PhysRevB.96.075440>.
- [121] M. Pascoli et al. “Wigner paths for electrons interacting with phonons”. In: *Phys. Rev. B* 58 (7 1998), pp. 3503–3506. DOI: [10.1103/PhysRevB.58.3503](https://doi.org/10.1103/PhysRevB.58.3503). URL: <https://link.aps.org/doi/10.1103/PhysRevB.58.3503>.
- [122] Z. Zhan, E. Colomés, and X. Oriols. “Unphysical Features in the Application of the Boltzmann Collision Operator in the Time-dependent Modeling of Quantum Transport”. In: *J. Comput. Electron.* 15.4 (Dec. 2016), pp. 1206–1218. ISSN: 1569-8025. DOI: [10.1007/s10825-016-0875-5](https://doi.org/10.1007/s10825-016-0875-5). URL: <https://doi.org/10.1007/s10825-016-0875-5>.

- [123] Damien Querlioz et al. “An improved Wigner Monte-Carlo technique for the self-consistent simulation of RTDs”. In: *Journal of Computational Electronics* 5.4 (2006), pp. 443–446. DOI: [10.1007/s10825-006-0044-3](https://doi.org/10.1007/s10825-006-0044-3). URL: <https://doi.org/10.1007/s10825-006-0044-3>.
- [124] Roberto Rosati et al. “Wigner-function formalism applied to semiconductor quantum devices: Failure of the conventional boundary condition scheme”. In: *Phys. Rev. B* 88 (3 2013), p. 035401. DOI: [10.1103/PhysRevB.88.035401](https://doi.org/10.1103/PhysRevB.88.035401). URL: <https://link.aps.org/doi/10.1103/PhysRevB.88.035401>.
- [125] D. Pandey et al. “Stochastic Schrödinger Equations and Conditional States: A General Non-Markovian Quantum Electron Transport Simulator for THz Electronics”. In: *Entropy* 21 (2019), p. 1148. DOI: [10.3390/e21121148](https://doi.org/10.3390/e21121148).
- [126] Lester Ingber, Marco Pappalepore, and Ronald R. Stesiak. “Electroencephalographic field influence on calcium momentum waves”. In: *Journal of Theoretical Biology* 343 (2014), pp. 138 –153. ISSN: 0022-5193. DOI: <https://doi.org/10.1016/j.jtbi.2013.11.002>. URL: <http://www.sciencedirect.com/science/article/pii/S0022519313005274>.
- [127] Fabrizio Buscemi, Paolo Bordone, and Andrea Bertoni. “Quantum teleportation of electrons in quantum wires with surface acoustic waves”. In: *Phys. Rev. B* 81 (4 2010), p. 045312. DOI: [10.1103/PhysRevB.81.045312](https://doi.org/10.1103/PhysRevB.81.045312). URL: <https://link.aps.org/doi/10.1103/PhysRevB.81.045312>.
- [128] Roberta Rodriguez et al. “Surface-acoustic-wave single-electron interferometry”. In: *Phys. Rev. B* 72 (8 2005), p. 085329. DOI: [10.1103/PhysRevB.72.085329](https://doi.org/10.1103/PhysRevB.72.085329). URL: <https://link.aps.org/doi/10.1103/PhysRevB.72.085329>.
- [129] F Buscemi, P Bordone, and A Bertoni. “Validity of the single-particle approach for electron transport in quantum wires assisted by surface acoustic waves”. In: *Journal of Physics: Condensed Matter* 21.30 (2009), p. 305303. DOI: [10.1088/0953-8984/21/30/305303](https://doi.org/10.1088/0953-8984/21/30/305303). URL: <https://doi.org/10.1088/0953-8984/21/30/305303>.
- [130] L. C. Lew Yan Voon and M. Willatzen. “Electromechanical phenomena in semiconductor nanostructures”. In: *Journal of Applied Physics* 109.3 (2011), p. 031101. DOI: [10.1063/1.3533402](https://doi.org/10.1063/1.3533402). eprint: <https://doi.org/10.1063/1.3533402>. URL: <https://doi.org/10.1063/1.3533402>.
- [131] I. Yahyaie et al. “High-resolution imaging of gigahertz polarization response arising from the interference of reflected surface acoustic waves”. In: *IEEE Transactions on Ultrasonics, Ferroelectrics, and Frequency Control* 59.6 (2012), pp. 1212–1218. DOI: [10.1109/TUFFC.2012.2311](https://doi.org/10.1109/TUFFC.2012.2311).